2024

Magnesium Technology

EDITED BY
Aeriel Leonard
Steven Barela
Neale R. Neelameggham
Victoria M. Miller
Domonkos Tolnai

TMS

Springer

The Minerals, Metals & Materials Series

Aeriel Leonard • Steven Barela •
Neale R. Neelameggham •
Victoria M. Miller • Domonkos Tolnai
Editors

Magnesium Technology 2024

TMS

Springer

Editors
Aeriel Leonard
The Ohio State University
Columbus, OH, USA

Steven Barela
Terves Inc./Magnesium-USA
Euclid, OH, USA

Neale R. Neelameggham
IND LLC
South Jordan, UT, USA

Victoria M. Miller
University of Florida
Gainesville, FL, USA

Domonkos Tolnai
Helmholtz-Zentrum Hereon
Geesthacht, Germany

ISSN 2367-1181 ISSN 2367-1696 (electronic)
The Minerals, Metals & Materials Series
ISBN 978-3-031-50239-2 ISBN 978-3-031-50240-8 (eBook)
https://doi.org/10.1007/978-3-031-50240-8

© The Minerals, Metals & Materials Society 2024

This work is subject to copyright. All rights are solely and exclusively licensed by the Publisher, whether the whole or part of the material is concerned, specifically the rights of translation, reprinting, reuse of illustrations, recitation, broadcasting, reproduction on microfilms or in any other physical way, and transmission or information storage and retrieval, electronic adaptation, computer software, or by similar or dissimilar methodology now known or hereafter developed.
The use of general descriptive names, registered names, trademarks, service marks, etc. in this publication does not imply, even in the absence of a specific statement, that such names are exempt from the relevant protective laws and regulations and therefore free for general use.
The publisher, the authors, and the editors are safe to assume that the advice and information in this book are believed to be true and accurate at the date of publication. Neither the publisher nor the authors or the editors give a warranty, expressed or implied, with respect to the material contained herein or for any errors or omissions that may have been made. The publisher remains neutral with regard to jurisdictional claims in published maps and institutional affiliations.

This Springer imprint is published by the registered company Springer Nature Switzerland AG
The registered company address is: Gewerbestrasse 11, 6330 Cham, Switzerland

Paper in this product is recyclable.

Preface

In recent decades, Magnesium (Mg) and its alloys have emerged as a sustainable structural material owing to their high strength-to-weight ratio, excellent vibration damping, low toxicity, and controllable corrosion rates in dissolvable applications. The possibility to traverse novel alloy designs that offer a distinctive combination of these properties as well as an improvement in ductility has ignited research and development throughout the world. And as many nations seek to reduce their carbon footprint, it is evident that Mg will play a crucial role in these efforts by forwarding the development of sustainable technology. In applications where light weighting is important, Mg has the potential to replace heavier conventional materials such as steel and aluminum leading to a reduction in greenhouse gas emissions.

Coalitions of researchers, scientists, and engineers from academic institutions, industry, and government laboratories have had tremendous success in addressing these challenges through innovative alloy designs and methods. These collaborations have and continue to develop roadmaps for next generation technologies that strengthen Mg as a premier structural material. The TMS Magnesium Committee has been actively involved in providing a platform for these institutions to disseminate the latest information, developments, and cutting-edge research and development, and to present the latest research and development trends related to magnesium and its alloys through the Magnesium Technology Symposium held each year at the TMS Annual Meeting & Exhibition.

The twenty-fifth volume in the series, *Magnesium Technology 2024*, is the proceedings of the Magnesium Technology Symposium held during the 153rd TMS Annual Meeting & Exhibition in Orlando, Florida, March 3–7, 2024. The volume captures full-length manuscripts and extended abstracts from 14 different countries. The papers have been categorized based on topics pertaining to alloy design, fundamentals of plastic deformation, primary production, recycling and ecological issues, characterization, joining, machining, forming, degradation and biomedical applications, corrosion and surface protection, and computational materials engineering.

The symposium began with keynote sessions that featured several distinguished invited-speakers from industry, government organizations, and academia, who provided their perspectives on the state of the art, goals, and opportunities in magnesium alloy research and development. Petra Maier from the University of Applied Sciences Stralsund discussed the role corrosion plays in performance of Mg alloys in biomedical applications. Alexander Grant, CEO of Magrathea Metals addressed the development of next generation electrolytic technology for making Mg metal. Ashley Bucsek of the University of Michigan spoke about the role 3D diffraction microscopy has in uncovering crystallographic texture development in Mg alloys. Jian-Feng Nie from Monash University discussed the progress made in the development of magnesium wheels. Maria Teresa Perez Prado, IMDEA Institute, spoke about the role alloy segregation has in suppressing deformation twinning during mechanical loading.

In conclusion, the 2023–2024 Magnesium Committee would like to thank and express its deep appreciation to all authors who contributed to the success of the symposium; our panel of distinguished keynote speakers for sharing the newest developments and valuable thoughts on the future of magnesium technology; all the reviewers for their best efforts in reviewing the manuscripts; and the session chairs, judges, TMS staff members, and other volunteers for their excellent support, which allowed us to develop a successful, high-quality symposium and proceedings volume.

Aeriel Leonard
Steven Barela
Neale R. Neelameggham
Victoria M. Miller
Domonkos Tolnai

Contents

Part I Corrosion and Coatings

Part II Microstructural Evolution and Phase Transformations

Part III Deformation Mechanisms

Part IV Advanced Processing

Part V Primary Production, Recycling, and Modeling

Part VI Biomedical Applications

Part VII Poster Session

About the Editors

Aeriel Leonard is an Assistant Professor in the Materials Science and Engineering Department at The Ohio State University. She was awarded the National Science Foundation CAREER Award in 2024, Department of Energy Early Career Award in 2022, and the Office of Naval Research Young Investigator Award in 2021. She earned her Bachelor's Degree in Metallurgical and Materials Engineering from the University of Alabama in 2012. In 2013, she began her Ph.D. journey at the University of Michigan in Materials Science and Engineering where she earned her Ph.D. in 2018. Dr. Leonard's Ph.D. work investigated real-time microstructural and deformation evolution in magnesium alloys using advanced characterization techniques such as high energy diffraction microscopy and electron back scatter diffraction. During her time at the University of Michigan she led and worked on many teams aimed at increasing the number of underrepresented minorities in engineering including developing and implementing a leadership camp for female engineering students in Monrovia, Liberia. Dr. Leonard was awarded an NRC Postdoctoral Fellowship at the US Naval Research Laboratory in Washington, DC where she worked for two years. During this time, she used advanced characterization techniques such as x-ray computed tomography and high energy diffraction microscopy to understand damage and texture evolution during in-situ loading in additive manufactured materials. She also runs a lifestyle blog titled Aeriel-Views aimed at young graduate and professional students.

Steven Barela is from Pueblo, Colorado, home to the Colorado Fuel & Iron Steel Mill (now Evraz). Driven by the need to resolve welding problems encountered when fabricating race cars, he attended the University of S. Colorado (now CSU-Pueblo) earning an A.A.S. in Metallurgical Engineering Technology. This led to a position at Rocky Flats/DOE nuclear assembly facility in the Non-Nuclear Joining R&D group as an Intern Engineer while simultaneously earning a B.S. in Metallurgical & Materials Engineering at the Colorado School of Mines (CSM) where he specialized in joining and was involved in the CSM Joining Research Center. Mr. Barela then went on to work at Martin Marietta Astronautics Group in the Advanced Manufacturing Technology Group which oversaw procedures and the production of the Titan family of launch vehicles, specifically all joining operations (braze, TIG, MIG, Variable Polarity Plasma) on aluminum, stainless steel, titanium, and metal matrix composites materials. He also participated in the development of Weldalite, a program to produce the Al-Li external tank for the NASA space shuttle program. In the late 1990s, Mr. Barela transitioned his career from welding metallurgy technology to marketing, product development, and sales of welding, forging, and fabricated products as a Technical Sales Engineer at Timminco Extruded Magnesium Products. He then worked for 10 years for Solikamsk Magnesium Works (Russia) by running the U.S. subsidiary Magnesium. com, Inc. During his tenure, Mr. Barela championed forged Magnesium (Mg) wheel projects, generating, and overseeing sales of various Mg products worldwide. Currently, Mr. Barela is with Terves Inc./Magnesium-USA overseeing marketing, product development, and technical sales for extruded and forged products. Over the 20+ years as a member of the TMS Magnesium Committee, Mr. Barela has brought practical industrial end-use knowledge, experience, and insight to the proceedings.

Neale R. Neelameggham, IND LLC, is involved in international technology and management licensing for metals and chemicals, thiometallurgy, energy technologies, Agricoal, lithium-ion battery, energy efficient low cost OrangeH2, Net-zero sooner with Maroon gas and Pink hydrogen, rare earth oxides, etc. He has more than 38 years of expertise in magnesium production and was involved in the process development of its startup company NL Magnesium to the present US Magnesium LLC, UT when he was instrumental in process development from thesolar ponds to magnesium metal foundry. His expertise includes competitive magnesium processes worldwide. In 2016, Dr. Neelameggham and Brian Davis authored the ICE-JNME award winning paper “Twenty-First Century Global Anthropogenic Warming Convective Model.” He is working on Agricoal® to greening arid soils, and at present energy efficient Orange hydrogen, and turbine generator electric car with hydrocarbons and steam. He authored *The Return of ManmadeCO2 to Earth: Ecochemistry*.

Dr. Neelameggham holds 16 patents and applications and has published several technical papers. He has served in the Magnesium Committee of the TMS Light Metals Division (LMD) since its inception in 2000, chaired in 2005, and since 2007 has been a permanent advisor for the Magnesium Technology Symposium. He has been a member of the Reactive Metals Committee, Recycling Committee, Titanium Committee, and Program Committee for LMD and LMD council. Dr. Neelameggham was the Inaugural Chair, when in 2008, LMD and the TMS Extraction and Processing Division (EPD) created the Energy Committee and has been a Co-Editor of the Energy Technology Symposium through the present. He received the LMD Distinguished Service Award in 2010. As Chair of the Hydrometallurgy and Electrometallurgy Committee, he initiated the Rare Metal Technology Symposium in 2014 and has been a co-organizer to the present. He organized the 2018 TMS Symposium on Stored Renewable Energy in Coal and initiated Light Elements Technology in 2023.

Victoria M. Miller is an Assistant Professor in the Department of Materials Science and Engineering at the University of Florida, a position she started in September 2019. She was previously an assistant professor at North Carolina State University from 2017 to 2019. Originally from Michigan, she received her B.S.E. in Materials Science and Engineering from the University of Michigan in 2011 and completed her Ph.D. in Materials at the University of California Santa Barbara in 2016. After graduate school, she worked for a year at UES, Inc. onsite in the Materials and Manufacturing Directorate of the Air Force Research Laboratory in Dayton, Ohio. She also previously worked at Ford Motor Company, Toyota Engineering and Manufacturing, and Lockheed Martin Aeronautics. Her primary research interest is microstructural evolution during thermomechanical processing of metals and alloys, particularly for those with low symmetry crystal structures. She has been researching Mg alloys since the age of 16. Professionally, Dr. Miller has served on many committees within TMS, is Associate Editor for *JOM*, and is a Key Reader for *Metallurgical and Materials Transactions A*. She was a recipient of the 2017 TMS Young Leaders Professional Development Award, the 2020 ASM Bronze Medal Award, and the 2022 TMS-JIMM Young Leaders International Scholar Award.

Domonkos Tolnai is a scientist with the Department of Functional Magnesium Materials at Helmholtz-Zentrum Hereon in Geesthacht, Germany. He earned his master's degree in engineering physics from the Eötvös University in Budapest, Hungary, where he investigated the fatigue behavior of Al based particle reinforced MMCs with synchrotron tomography. In 2007 he began his Ph.D. studies at the Vienna University of Technology in Vienna, Austria on investigating the solidification of Al alloys by in situ synchrotron tomography. After defending his thesis in 2011, he moved to Geesthacht, where he started as a post-doctoral fellow and then continued later as a scientist. His research focuses on the microstructural response of Mg based materials to thermo-mechanical and degradation load, and on the development of advanced in situ characterization environments based on synchrotron radiation.

Session Chairs

Magnesium Technology

Corrosion and Coatings

Aeriel Leonard, The Ohio State University
Domonkos Tolnai, Helmholtz-Zentrum Hereon

Microstructural Evolution and Phase Transformations

Tracy Berman, University of Michigan
Steven Johnson, Central Connecticut University

Deformation Mechanisms

Qianying Shi, University of Michigan
Victoria Miller, University of Florida

Advanced Processing

Sridhar Niverty, Pacific Northwest National Laboratory
Benjamin Schuessler, Pacific Northwest National Laboratory

Primary Productions, Recycling, and Modeling

Wim Silekens, European Space Agency
Vineet Joshi, Pacific Northwest National Laboratory

Biomedical Applications

Petra Maier, Stralsund University of Applied Sciences
Jonathan Weiler, Meridian Lightweight Technologies Inc.

Reviewer Pool

Aeriel Leonard, The Ohio State University, USA
Domonkos Tolnai, Helmholtz-Zentrum Hereon, Germany
Steven Johnson, Central Connecticut University, USA
Norbert Hort, Helmholtz-Zentrum Hereon, Germany
Petra Maier, Stralsund University of Applied Sciences, Germany
Wim Sillekens, European Space Agency, the Netherlands
Alok Singh, National Institute for Materials Science, Japan
Neale Neelameggham, IND LLC, USA
Scott Sutton, Mag Specialties Inc., USA
Jonathan Weiler, Meridian Lightweight Technologies Inc., Canada
Tracy Berman, University of Michigan, USA
Adam Griebel, Fort Wayne Metals, USA
Rajib Kalsar, Pacific Northwest National Laboratory, USA
Victoria Miller, University of Florida, USA
Benjamin Anthony, University of Florida, USA
Sridhar Niverty, Pacific Northwest National Laboratory, USA

Part I

Corrosion and Coatings

Different Analytical Methods to Determine the Influence of Pitting on the Residual Performance of Mg Alloys as Implant Materials

Petra Maier

Abstract

Mg alloys are prone to pitting due to their non-uniform protective corrosion layers, which can lead to an increase in stress intensity based on the notch effect, pit-to-crack transition, and thus premature failure. A small set of analytical methods to determine the extent of pitting and its effect on the resulting residual strength is presented. Micrographs, 3D microscopy, or 3D analysis using CT are used to determine the amount and geometry of pitting—each with advantages and disadvantages. The influence of the corrosion pits on the mechanical properties is tested by static, quasi-static, and cyclic test methods: by tensile, flexural, or fatigue testing—either after corrosion or overlapping. Knowledge about the critical pit is of general interest. Stress corrosion is discussed by applying static tests like C-ring testing, which also plays a role in slow strain rate tensile tests and stress corrosion cracking is more or less influenced by corrosion pits.

Keywords

Mg–RE alloys • Pitting corrosion • 3D-µCT analysis • Residual tensile strength • Corrosion fatigue

Extended Abstract

Mg alloys are susceptible to pitting due to their non-uniform protective corrosion layers, which can lead to an increase in stress intensity based on the notch effect, a transition from pitting to cracking, and thus premature failure. To quantify the influence of corrosion pits on residual strength, the corrosion pit should be described as completely as possible, see an example with a Mg–3Y–3RE alloy in Fig. 1. A pit with a depth of about 300 µm was found to have a residual force was found to be 90% [1]. A small set of analytical methods for determining the extent of pitting and its effect on the resulting residual strength is presented in this keynote presentation at the Magnesium Technology symposium at the TMS 2024. The Standard Guide for Examination and Evaluation of Pitting Corrosion provides a chart to describe the shape of pits [2]: critical are pits with a narrow and deep shape and undercutting, less harmful are elliptical pits that are wide and shallow. The pitting factor [3, 4] is calculated by dividing the deepest pit by the average penetration depth, which is usually determined by the corrosion rate (CR) based on weight loss. The deepest pit can be determined by 3D microscopy, see Fig. 2 for a 3D confocal image from a study on corrosion properties of extruded Mg10Gd modified with Nd and La [5]. The study in [5] and a similar study on Mg–Y–Nd–Gd–Dy alloys [6] show that large corrosion pits lead to a high PF when the CR is low and the protective corrosion layer is only very locally discontinuous. 3D laser confocal scanning [7] or 3D laser profilometer measurements [8] can also be used to determine the depth of the pits. However, the shape cannot be determined with these methods. Undercutting pits, of course, cannot be visualized with 3D microscopy in top view. Atomic force microscope analysis can also be used to determine the corrosion morphology and depth of corrosion pits, but the area and shape, according to undercutting appearance, are limited [9].

Micrographs, see Fig. 3a, provide 2D determination of shape and size, but only a 2D view—the selected cross-section need not present the most critical shape of a single pit. SEM, see image in Fig. 3c, offers imaging with a great depth of field, but has its limitations in terms of fully quantifying the size and shape. Cross-sectional micrographs, however, provide the ability to determine the average

---

P. Maier (✉)
School of Mechanical Engineering, University of Applied Sciences Stralsund, Stralsund, Germany
e-mail: petra.maier@hochschule-stralsund.de

Department of Engineering Sciences, Lund University, Lund, Sweden

A. Leonard et al. (eds.), *Magnesium Technology 2024*, The Minerals, Metals & Materials Series,
https://doi.org/10.1007/978-3-031-50240-8_1

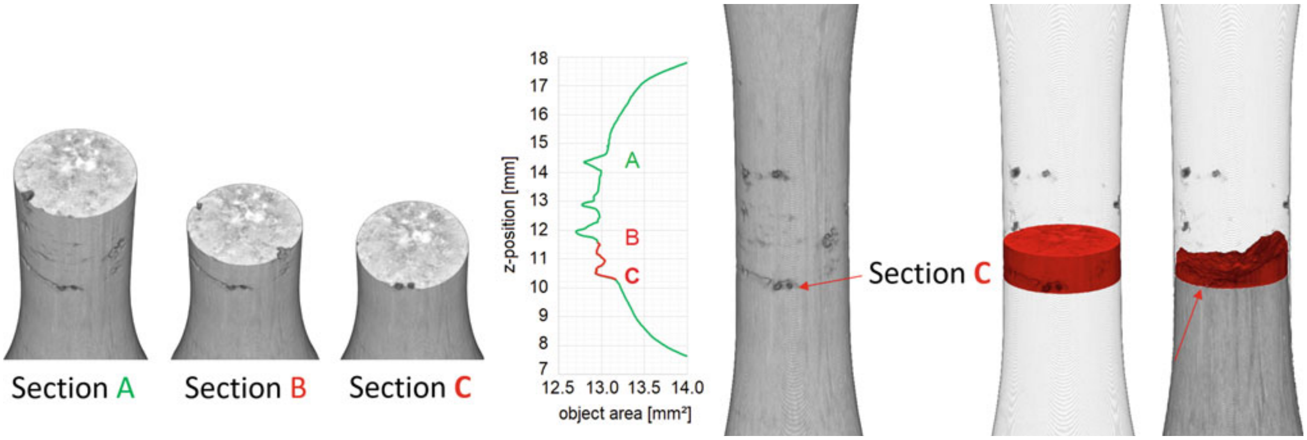

Fig. 1 Remaining cross-sectional area after corrosion of a Mg–3Y–3RE tensile sample after corrosion time of 24 h in Ringer solution at 37 °C (left: µCT cross-sections before tensile test, right: µCT before and after tensile test), red part of green curve (sample cross-sectional area) indicates the fractured area, based on [1]

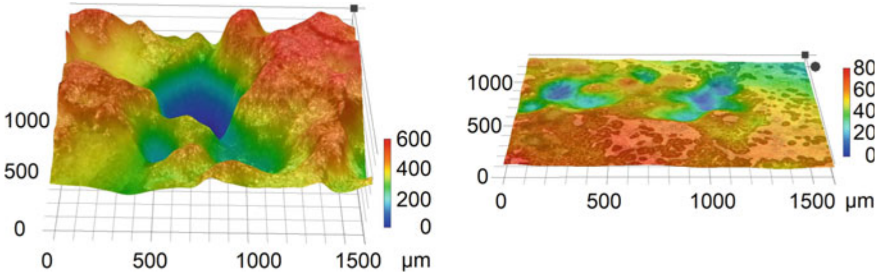

Fig. 2 3D height map by a confocal 3D microscope, showing a corrosion pit of significant size (left) and material with higher pitting resistivity (right)

penetration through the corroded area of individual slices independent of the volume (weight) loss, as described in [10]. The average penetration from corrosion rate based on weight loss will differ from the average penetration of cross-sections when the corrosion rate is not uniform—and severe pitting is obviously the clearest manifestation of non-uniform corrosion. In this case, the weight loss is a result of only a few local spots and distorts the evaluation.

Returning to the corrosion pits in Fig. 1, the larger of the two in Section C on the left has an elliptical shape in this cross-section. The longitudinal cross-section, on the other hand, shows a more pointed undercutting shape, resulting in a higher stress intensity increase. Only in complete 3D analysis using CT it is possible to assess the shape and size of a corrosion pit.

The influence of the corrosion pits on the mechanical properties is of interest under static, quasi-static, and especially under cyclic loading. Stress corrosion, slow strain rate tensile tests, flexural, and fatigue testing can be either applied after corrosion or simultaneously. The micrographs in Fig. 3a show corrosion pits on a Mg–RE alloy forming under stress corrosion [11]. It can be seen that these large

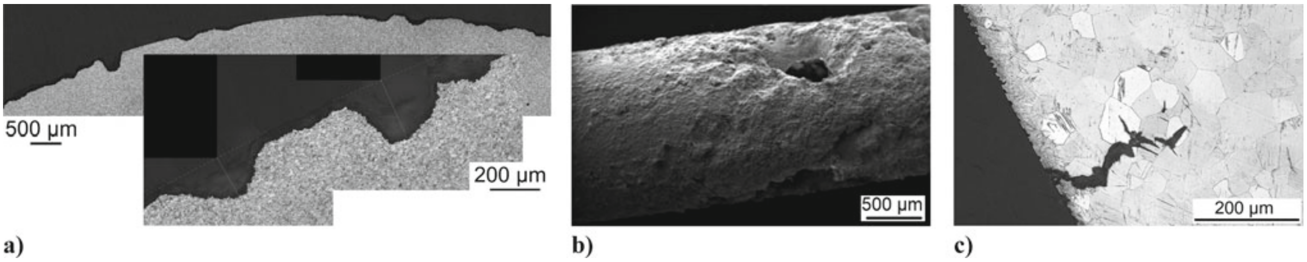

Fig. 3 Corrosion pits presented by **a** cross-sectional micrographs (based on [11]) and **b** SEM imaging [10] and **c** initiating stress cracks in stress corrosion (study presented in [12])

pits, which are elliptically formed and have a wide opening do not cause a crack initiation. Another is found when testing the wires shown in Fig. 3b in three-point bending after corrosion, the pits acting as crack initiation [10]. Under stress corrosion even small pits transits into cracks, see Fig. 3c [12]. In this study, it could be seen that the near-surface material of an Mg–Dy alloy is heavily twinned and, in combination with corrosion pits and tensile loading, cracks form. Twin boundaries strongly influence the crack propagation direction [12, 13]. The effect of surface roughness can reduce the fatigue strength to a high degree and corrosion fatigue cracks originate mainly from the corrosion pits [14, 15]. Knowledge about the critical pit is of general interest.

More and more effort is undertaken in automated detection of pitting corrosion and its effect on the mechanical integrity [16]. The identification and description of surface-based corrosion features are in main focus. CT analyses also offer to calculate the CR by volume loss; however, its segmentation is challenging. Machine learning is applied to define residual material, degradation/corrosion layers, bone/tissue, and background [17].

References

1. Clausius, B. et al. (2023). Influence of Corrosion Extent on Residual Tensile Strength and Corrosion Fatigue Properties of an Mg−Y−Nd Alloy Characterized by μCT. Magnesium Technology 2023. The Minerals, Metals & Materials Series. Springer, Cham.
2. Metals Handbook Ninth Edition (2008), Failure Analysis and Prevention, American Society for Metals, Standard Guide for Examination and Evaluation of Pitting Corrosion. ASTM G46-94 (Reapproved 2005); Materials Performance, 176.
3. Witte, F. et al. (2005) In vivo corrosion of four magnesium alloys and the associated bone response. Biomaterials 26 (17) 3557–3563.
4. Maier, P. et al. (2026) Degradation morphology and pitting factor compared to degradation rate, European Cells and Materials, 32, 6, 22.
5. Maier, P. et al. (2018) Precipitation hardening on mechanical and corrosion properties of extruded Mg10Gd modified with Nd and La. Metals 8 (640).
6. Maier, P. et al. (2019) Mechanical and corrosion properties of two precipitation hardened Mg–Y–Nd–Gd–Dy alloys with small changes in chemical composition. JOM 71 (4) 1426–1435.
7. Yuxiang L. et al. (2021) Improvement in corrosion resistance of micro-arc oxidized AZ91 alloy sealed with cement-mixed paraffin wax, Journal of Materials Research and Technology, 15, 6956–6973.
8. Holly J. et al. (2010) Comparison of corrosion pitting under immersion and salt-spray environments on an as-cast AE44 magnesium alloy, Corrosion Science, 52, 11, 3624–3638.
9. Quantong J. et al. (2015) Anisotropy of the crystallographic orientation and corrosion performance of high-strength AZ80 Mg alloy, Journal of Magnesium and Alloys, 3, 4, 309–314.
10. Maier, P. et al. (2017) Solid solution treatment on strength and corrosion of biodegradable Mg6Ag wires, Materials and Corrosion, 69, 2, 178–190.
11. Maier, P. et al. (2020) Influence of Solution Heat Treatment on the Microstructure, Hardness and Stress Corrosion Behavior of Extruded Resoloy®. JOM 72, 1870–1879.
12. Maier, P. et al. (2023). Effect of Deformation Speed on Stress Corrosion and Fracture Toughness of Extruded Mg10Dy and Mg10Dy1Nd Using C-Ring Tests. Magnesium Technology 2023, The Minerals, Metals & Materials Series. Springer, Cham.
13. Maier, P. et al. (2020) Characterization of an Extruded Mg–Dy–Nd Alloy during Stress Corrosion with C-Ring Tests. Metals, 10, 584
14. Raman, R.K.S.; Harandi, S.E. Resistance of Magnesium Alloys to Corrosion Fatigue for Biodegradable Implant Applications: Current Status and Challenges. Materials 2017, 10, 1316.
15. Maier, P. et al. (2019) Corrosion Bending Fatigue of RESOLOY® and WE43 Magnesium Alloy Wires. Magnesium Technology 2019. The Minerals, Metals & Materials Series. Springer, Cham.
16. Van Gaalen, K. et al. (2021) Automated ex-situ detection of pitting corrosion and its effect on the mechanical integrity of rare earth magnesium alloy - WE43. Bioact. Mater. 8, 545–558.
17. Baltruschat, IM. et al. (2021) Scaling the U-net: segmentation of biodegradable bone implants in high-resolution synchrotron radiation microtomograms. Science Report Dec 20;11(1):24237.

Effect of Heat Treatment on the Microstructure and Corrosion Properties of Mg–15Dy–1.5Zn Alloy with LPSO Phase

Genzhi Jiang, Yuanding Huang, Sarkis Gavras, Hui Shi,
and Norbert Hort

Abstract

The influence of the amount and type of long-period stacking ordered (LPSO) phase on the corrosion behavior of both the as-cast and heat-treated Mg–15Dy–1.5Zn alloys in 0.9% NaCl solution was investigated. It was found that the network structure 18R-LPSO phase is an effective barrier to further corrosion of the as-cast sample. After T4 treatment for 24 h, the dendrites disappeared and part of 18R-LPSO dissolved in the matrix, which weakened the corrosion protection. Meanwhile, such LPSO phase acts as a cathodic to accelerate the corrosion of the matrix because of its potential difference from the magnesium matrix. After T4 treatment for a longer time, 18R-LPSO phase could transform into 14H-LPSO phase which has a different effect on corrosion. The galvanic corrosion also occurs between the 14H-LPSO phase and the matrix. Its uniform and dense distribution results in the formation of continuous corrosion products on the surface, which is beneficial for corrosion resistance.

Keywords

Mg–Dy–Zn alloy • Heat treatment • Corrosion rate • LPSO phase • Microstructure

Introduction

Magnesium (Mg) alloys have long been an interesting research topic in the field of biomedical applications due to their low density, high specific strength, and good biocompatibility [1]. Nevertheless, the critical obstacle to their extensive application is how to balance their integral strength and degradation rate. Precipitation strength is one of the most popular methods to improve mechanical properties. Nevertheless, previous studies showed that the intermetallic phases can act as either a continuous network barrier to retard corrosion propagation, or as a galvanic cathode to accelerate the corrosion of the Mg matrix, or as a micro-anode to dissolve preferentially at the initial corrosion stage [2].

It was reported that optimizing the size, distribution, and morphology of long-period stacking ordered (LPSO) phases can change the corrosion behavior of Mg-RE alloys from pitting corrosion to uniform corrosion and reduce the corrosion rate to some extent [3, 4]. For example, the heat treatment of Mg alloy with LPSO phase influences the corrosion rate due to the phase transformation from the bulk reticular LPSO phase to the lamellar 14H-LPSO phase. The corrosion rate increased significantly after such heat treatment since the high volume fraction of 14H-LPSO phase changes the corrosion propagation paths and provides more galvanic corrosion points [5]. Magnesium alloys with the co-existence of the 18R and 14H-LPSO structures exhibited worse corrosion resistance than those with a single LPSO structure (either 18R or 14H), which could be attributed to the accumulation of stacking faults as well as the enrichment of solute atoms in the phase transition zone [6]. In this work, the effects of different LPSO phases on the corrosion behavior of Mg–15Dy–1.5Zn alloys have been investigated.

G. Jiang · Y. Huang (✉) · S. Gavras · H. Shi · N. Hort
Institute of Metallic Biomaterials, Helmholtz-Zentrum Hereon,
Max-Planck-Strasse 1, 21502 Geesthacht, Germany
e-mail: Yuanding.huang@hereon.de

N. Hort
Institute of Product Technology and Systems,
Leuphana University Lüneburg, Universitätsallee 1,
21335 Lüneburg, Germany

A. Leonard et al. (eds.), *Magnesium Technology 2024*, The Minerals, Metals & Materials Series,
https://doi.org/10.1007/978-3-031-50240-8_2

Experiments

The Mg–15Dy–1.5Zn alloy was prepared using permanent mould by direct chill casting [7]. High-purity Mg (Magnesium electron, Manchester, UK, 99.94 wt.%) was melted in a mild steel crucible under a protective atmosphere (Ar + 2% SF_6). Pure zinc (Zn) and pure dysprosium (Dy) were then added to the melt at 750 °C. The melt was stirred for 30 min at 200 rpm and then poured into a mold preheated at 680 °C and covered with a release agent (boron nitride) [2]. Then the filled crucible was held at 680 °C for 15 min with gas protection (Ar + 2% SF_6). Finally, the melt was solidified by lowering the crucible into cooling water at a rate of 10 mm/s. When the melt was fully immersed in the water, the solidification finished. Then, the as-cast Mg–15Dy–1.5Zn alloy was heat treated at 500 °C for 24, 48, and 264 h, followed by immediate quenching in water. These treated alloys are thereafter termed AC, 24HT, 48HT, and 264HT

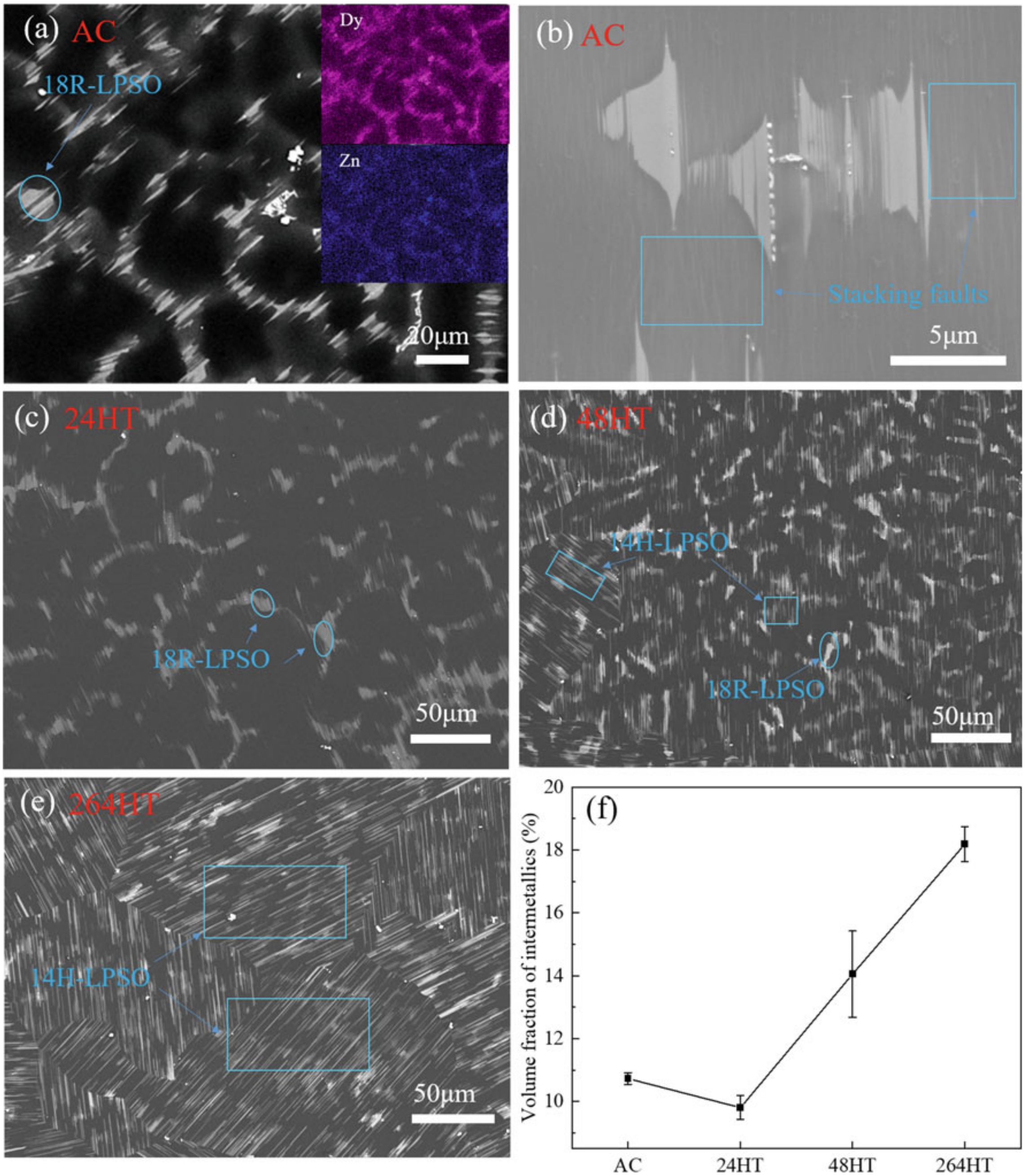

Fig. 1 BSE images of Mg–15Dy–1.5Zn alloys with different T4 treatment time at 500°C: **a** AC, **b** local magnified image of AC, **c** 24HT, **d** 48HT, **e** 264HT alloys, together with **f** their corresponding measured volume fraction of intermetallics

alloys, respectively. Corrosion products and characterization morphology were characterized by scanning electron microscope (SEM, Tescan Vegas3 SB) equipped with energy dispersive spectroscopy (EDS). The micrographs were obtained in backscatter electron (BSE) mode using an accelerating voltage of 15 kV.

Hydrogen evolution tests were performed using eudiometers (Art. Nr. 2591-10-500 from Neubert-Glas, Germany; as described in Ref. [8]), for 60 h. Metallic chips (0.3 g) were placed in a bottle containing 400 ml of electrolyte (0.9% NaCl). The electrolyte was constantly agitated by a magnetic stirrer but not refreshed during the test period. Electrochemical test was performed by Gamry interface 1010 potentiostat/galvanostat in 0.9% NaCl solution at 25 °C using Mg specimens with an area of 1 cm^2 exposed. Electrochemical impedance spectroscopy (EIS) tests were conducted by three-electrode systems, for which the prepared sample, saturated calomel electrode, and platinum plate were used as the working electrode, reference electrode, and counterelectrode, respectively [9].

The volume fraction of the LPSO phase was statistically measured using BSE micrographs captured from different regions and calculated by ImageJ software (National Institutes of Health, Version 1.51k).

Results and Discussion

Microstructure

Figure 1a–e presents the BSE images of the as-cast and T4-treated Mg–15Dy–1.5Zn alloys. Bulk 18R-LPSO [10] (labeled by the blue circle), dispersed and precipitated in the grain interiors, with dendrites and stacking faults around 18R-LPSO phase together form a network structure in the AC alloy as shown in Fig. 1a, b. The brighter contrast of the dendritic regions indicates the segregation of heavier elements at those places, which is consistent with the enrichment of the remaining melt with Zn and Dy during solidification, as proved by EDS mapping analysis in Fig. 1a. After solid solution for 24 h, the dendrite disappeared and a few lamellar 14H-LPSO [11] (labeled by the blue rectangle) formed near the α-Mg/18R interfaces. This could be due to the migration of Dy/Zn solute atoms, which were enriched at dendrites and the α-Mg/18R interfaces in the AC alloy. With the extension of the T4 treatment time to 48 and 264 h, more lamellar 14H-LPSO phases were precipitated within the grain interiors, as shown in Fig. 1c. The volume fractions of the LPSO phase in these alloys are shown in Fig. 1e.

Corrosion Behavior

Figure 2a shows the relationship between immersion time and hydrogen evolution volumes, demonstrating the increment of hydrogen evolution volume for all alloys. The corrosion rates of as-cast and heat-treated Mg–15Dy–1.5Zn alloys after the immersion in 0.9% NaCl for 2 h and 60 h in Fig. 2b show that the 24HT alloy has the highest corrosion rate while having the lowest volume fraction of intermetallics. Furthermore, the volume fraction of the lamellar LPSO phase for Mg–15Dy–1.5Zn alloys increases when the T4 treatment time is extended from 48 to 264 h, resulting in a continuously decreasing corrosion rate. The AC alloy with a network structure here showed the lowest corrosion rate.

The EIS plots show three loops, two capacitive loops in the high-frequency and mid-frequency range and one inductive loop in the low-frequency range. The mid-

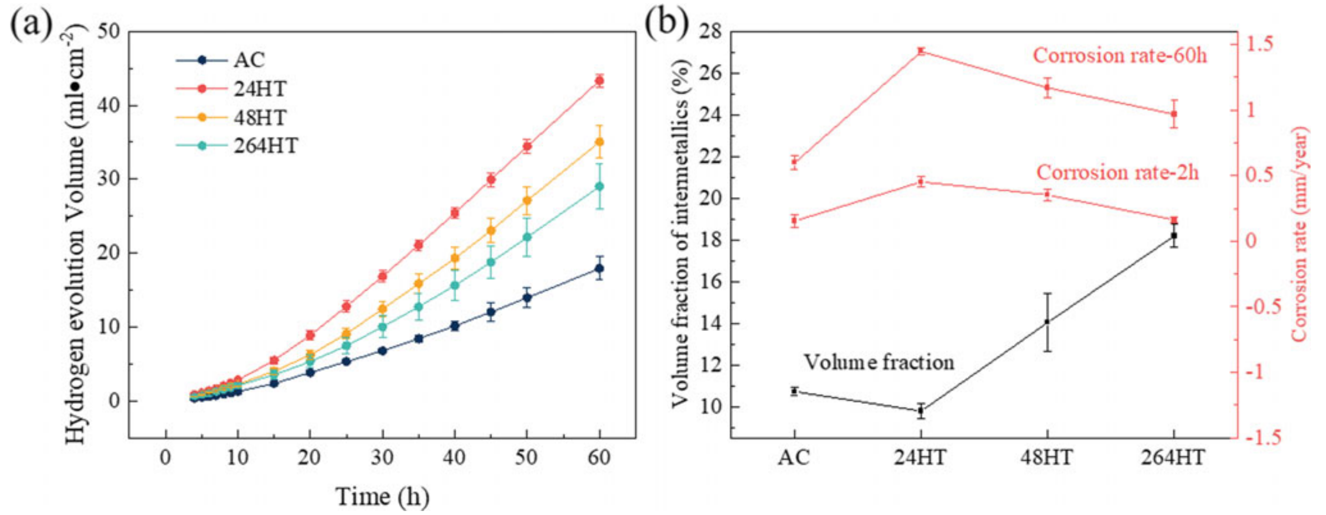

Fig. 2 **a** Relationship between immersion time and hydrogen evolution volumes, and **b** corrosion rates after immersing for 2 and 60 h in 0.9% NaCl solution and volume fraction of intermetallics in Mg–15Dy–1.5Zn alloys after T4 treatment for different time

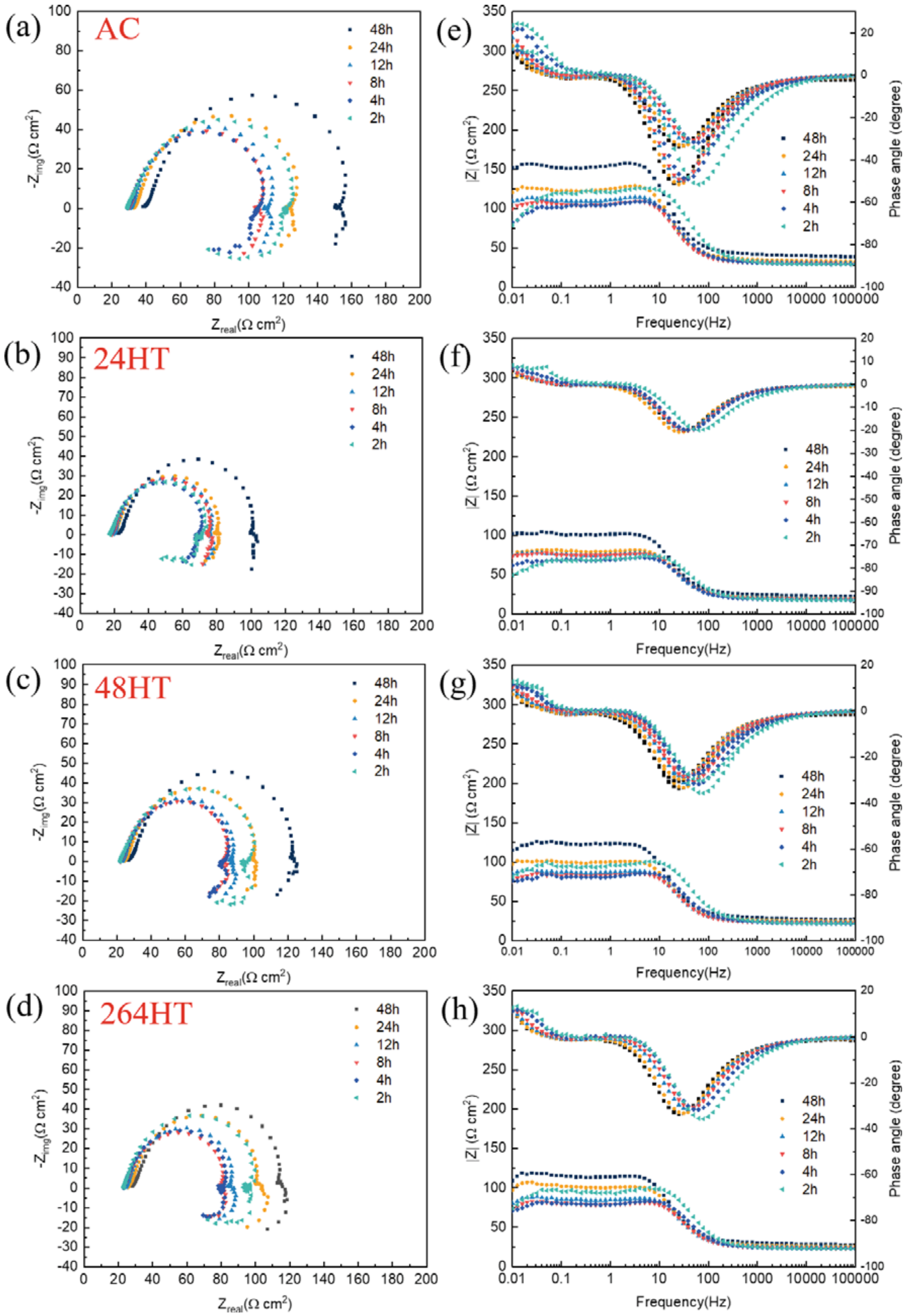

Fig. 3 Electrochemical impedance spectra and fitted equivalent circuit: Nyquist diagrams (**a**–**d**), Bode diagrams (**e**–**h**) in **a**, **e** AC alloy, **b**, **f** 24HT alloy, **c**, **g** 48HT alloy, **d**, **h** 264HT alloy

frequency range represents the relaxation of the corrosion product film formed on the Mg alloy surface. The existence of the low-frequency induction loop results from the insufficient protection of the surface film, indicating that local corrosion occurred [5]. In addition, the inductive loop implies that all four alloys suffered from localized corrosion. The largest capacitive loop diameter (Fig. 3a) and the highest impedance modulus (Fig. 3e) in the AC alloy reveal that this alloy possesses better corrosion resistance than other alloys. In the AC alloy, the network structure provides a barrier to corrosion [5, 12, 13]. In contrast, after solid solution for 24 h, the decreased protection due to the disappearance of the network structure and the galvanic corrosion between the LPSO phase and the matrix together lead

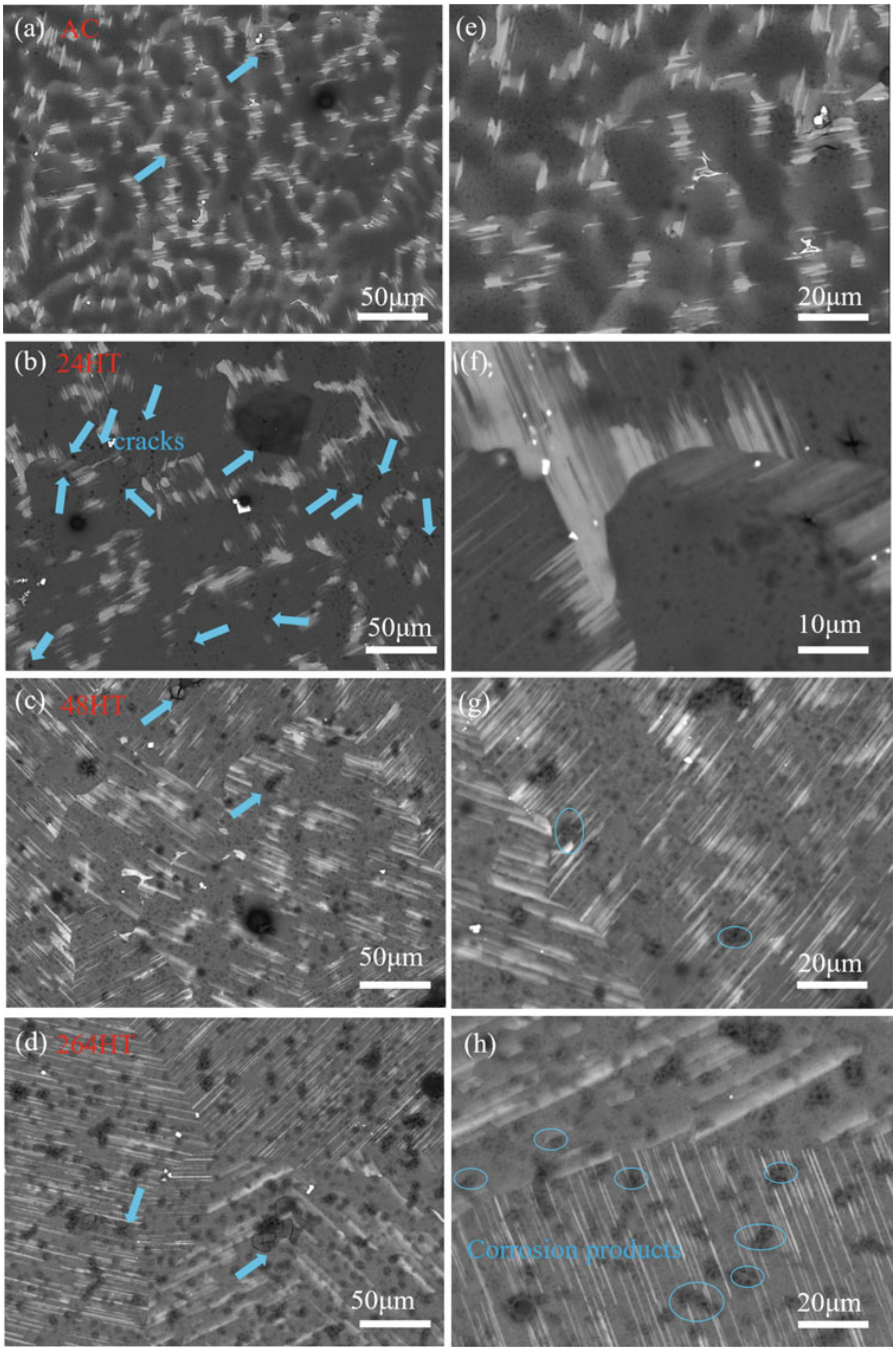

Fig. 4 BSE micrographs and magnified images of Mg–15Dy–1.5Zn alloys after immersed in 0.9%NaCl solution for 2 h: **a**, **e** AC alloy, **b**, **f** 24HT alloy, **c**, **g** 48HT alloy, **d**, **h** 264HT alloy

to corrosion deterioration. Meanwhile, the Bode phase angle and impedance plots in Fig. 3f illustrate that the 24HT alloy has the lowest peak value, the smallest half width of the phase angle, and the lowest impedance modulus than other alloys, representing its largest capacitance, the smallest polarization resistance, and the worst corrosion protection. The AC alloy has the best corrosion protection.

The T4 treatment time affects the corrosion behavior of Mg–15Dy–1.5Zn alloy (Fig. 4). BSE micrographs demonstrate that the corrosion cracks were observed on the surfaces of all specimens (labeled by blue arrows) after the immersion for 2 h. Among all the T4-treated samples, the 24HT alloy had the highest amount of corrosion cracks. In this specimen, the amount of 14H-LPSO phase is the lowest. The resultant corrosion layer was not continuous, and the corrosion products existed on the surface, covering the matrix rather than 14H-LPSO phase. Thus, there may have been the most inhomogeneous tensile stress inside such a corrosion product film. This result is in agreement with that obtained by EIS. With the solution treatment time increasing to 48 and 264 h, more corrosion products were observed on the surfaces. Such corrosion products even cover 14H-LPSO phase. Moreover, when compared with the 24HT alloy, fewer cracks were found on the surfaces of the 48HT alloy and 264HT alloys (labeled by blue circles) (Fig. 4g–h).

Figure 5 shows the cross-sectional BSE micrographs of T4-treated alloys following immersion for 60 h. The network structure in the corrosion product of the AC alloy still maintains almost complete distribution, further confirming the protection of the network structure in corrosion resistance as illustrated in Fig. 5a. The occurrence of cracks (labeled by blue arrows) near the matrix in the corrosion

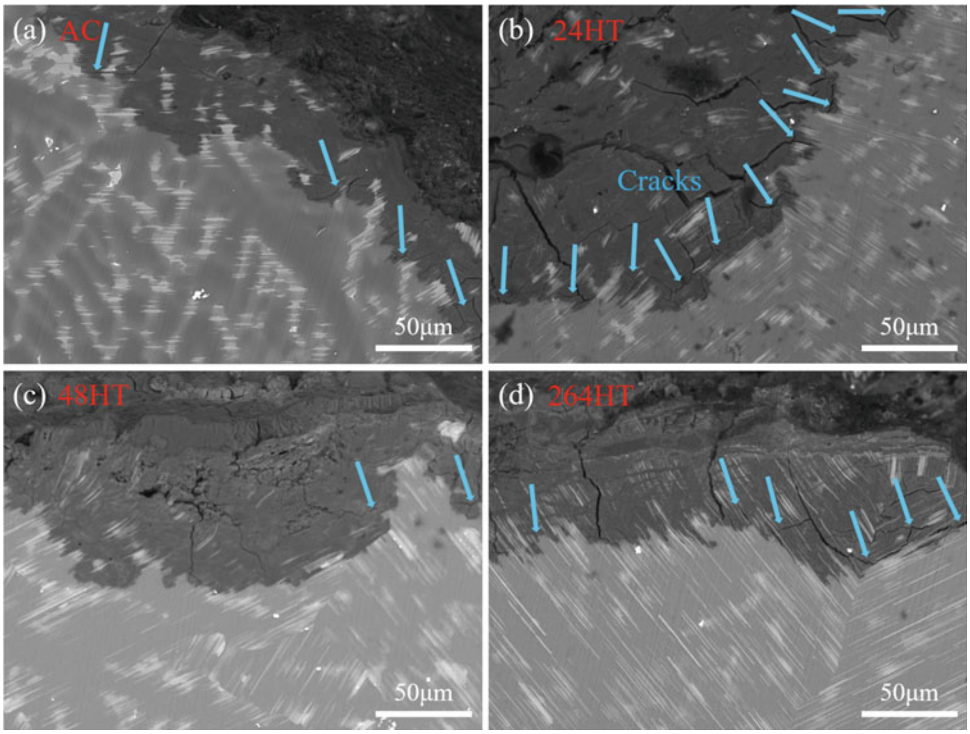

Fig. 5 BSE micrographs of cross section of Mg–15Dy–1.5Zn alloys after immersed in 0.9% NaCl solution for 60 h: **a** AC alloy, **b** 24HT alloy, **c** 48HT alloy, **d** 264HT alloy

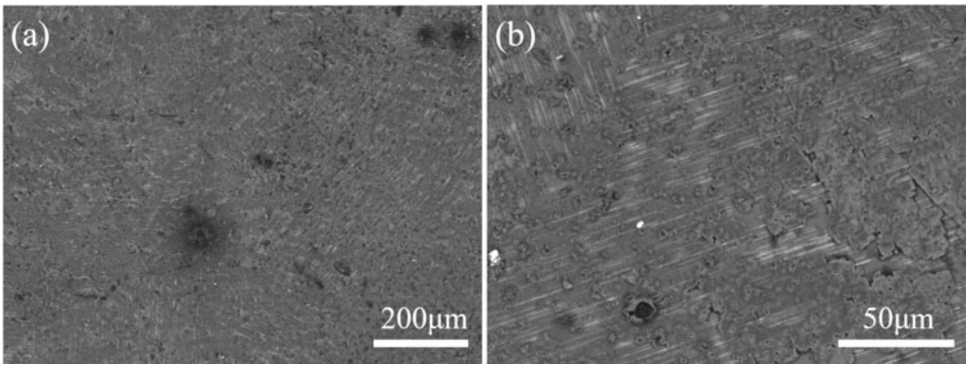

Fig. 6 **a** BSE micrograph and **b** local magnified image of the 264HT alloy after immersed in 0.9% NaCl solution for 14 h

product was significantly more pronounced in the 24HT alloy when compared to the other three alloys. This observation aligns with the results obtained from the aforementioned two-hour immersion test.

As shown by Fig. 2b, the corrosion rate decreased with increasing the T4 treatment time to more than 48 h. It seems that the formation of 14H-LPSO favors the improvement of corrosion resistance. In order to clarify the responsible mechanism, further SEM observations were performed on the surface corrosion products of the 264HT alloy. Figure 6 presents the BSE images of the 264HT alloy after the immersion in 0.9% NaCl solution for 14 h. It could be observed that a uniform and continuous corrosion layer was formed on the surface of the 264HT alloy. Such corrosion layer could prevent the corrosion medium from further penetrating the 264HT alloy matrix. As aforementioned, the 264HT alloy has the highest volume fraction of 14H-LPSO phase. Under such a high amount of 14H-LPSO, the formation of corrosion products was enhanced. As a result, the formed corrosion products could cover more areas in the 264HT alloy than other alloys, such as 24HT.

Conclusion

Based on the experimental results, the following conclusions can be drawn:

1. The network structure of 18R-LPSO phase at the dendrites could act as an effective barrier for further corrosion in the as-cast Mg–15Dy–1.5Zn alloy.
2. Mg–15Dy–1.5Zn alloy with T4 treatment for 24 h has the worst corrosion resistance. Its lowest volume fraction of 14H-LPSO phase and resultant inhomogeneous corrosion layer deteriorate its corrosion resistance.
3. Mg–15Dy–1.5Zn alloy with T4 treatment for 264 h has the highest corrosion resistance. Its dense lamellar 14H-LPSO phase could benefit the formation of uniform and continuous corrosion film.

Acknowledgements The author Genzhi Jiang would like to thank the China Scholarship Council for the award of a fellowship and funding (No. 202106890013). Mr. Gert Wiese is also gratefully acknowledged for the technical support.

References

1. L. Yang, L. Ma, Y. Huang, F. Feyerabend, C. Blawert, D. Hoche, R. Willumeit-Romer, E. Zhang, K.U. Kainer, N. Hort, Influence of Dy in solid solution on the degradation behavior of binary Mg–Dy alloys in cell culture medium, Mater Sci Eng C Mater Biol Appl 75 (2017) 1351–1358.
2. Y. Zhang, Y. Huang, F. Feyerabend, C. Blawert, W. Gan, E. Maawad, S. You, S. Gavras, N. Scharnagl, J. Bode, C. Vogt, D. Zander, R. Willumeit-Romer, K.U. Kainer, N. Hort, Influence of the amount of intermetallics on the degradation of Mg–Nd alloys under physiological conditions, Acta Biomater 121 (2021) 695–712.
3. Q. Zhu, Y. Li, F. Cao, D. Qiu, Y. Yang, J. Wang, H. Zhang, T. Ying, W. Ding, X. Zeng, Towards development of a high-strength stainless Mg alloy with Al-assisted growth of passive film, Nat Commun 13(1) (2022) 5838.
4. X. Zhang, Z. Ba, Q. Wang, Y. Wu, Z. Wang, Q. Wang, Uniform corrosion behavior of GZ51K alloy with long period stacking ordered structure for biomedical application, Corrosion Science 88 (2014) 1–5.
5. C. Dai, J. Wang, Y. Pan, K. Ma, Y. Peng, J. Ren, Y. Wang, D. Wang, J. Wang, Y. Ma, Tailoring the microstructural characteristic and improving the corrosion rate of Mg–Gd–Ni alloy by heat treatment with different volume fraction of LPSO phase, Corrosion Science 210 (2023).
6. L. Wang, J. Jiang, H. Liu, B. Saleh, A. Ma, Microstructure characterization and corrosion behavior of Mg–Y–Zn alloys with different long period stacking ordered structures, Journal of Magnesium and Alloys 8(4) (2020) 1208–1220.
7. F.R. Elsayed, N. Hort, M.A. Salgado Ordorica, K.U. Kainer, Magnesium Permanent Mold Castings Optimization, Materials Science Forum 690 (2011) 65–68.
8. S.V. Lamaka, B. Vaghefinazari, D. Mei, R.P. Petrauskas, D. Höche, M.L. Zheludkevich, Comprehensive screening of Mg corrosion inhibitors, Corrosion Science 128 (2017) 224–240.
9. C. Wang, X. Liu, D. Mei, M. Deng, Y. Zheng, M.L. Zheludkevich, S.V. Lamaka, Local pH and oxygen concentration at the interface of Zn alloys in Tris–HCl or HEPES buffered Hanks' balanced salt solution, Corrosion Science 197 (2022).
10. C.Q. Li, D.K. Xu, Z.R. Zeng, B.J. Wang, L.Y. Sheng, X.B. Chen, E.H. Han, Effect of volume fraction of LPSO phases on corrosion and mechanical properties of Mg–Zn–Y alloys, Materials & Design 121 (2017) 430–441.
11. Y. Yang, C. Ling, Y. Li, S. Peng, D. Xie, L. Shen, Z. Tian, C. Shuai, Microstructure development and biodegradation behavior of additively manufactured Mg–Zn–Gd alloy with LPSO structure, Journal of Materials Science & Technology 144 (2023) 1–14.
12. W. Du, Y. Du, Z. Yang, B. Ma, Y. Ge, B. Jiang, Effects of Long-Period Stacking-Order Phase on the Corrosion Behavior of an Mg–Gd–Y–Zn–Zr Alloy, Journal of Materials Engineering and Performance (2022).
13. Y. Nie, J. Dai, X. Li, X. Zhang, Recent developments on corrosion behaviors of Mg alloys with stacking fault or long period stacking ordered structures, Journal of Magnesium and Alloys 9(4) (2021) 1123–1146.

Dissolution Rate Change of Dissolving Magnesium in a Deoxygenated Environment

Tim Dunne, Lei Zhao, Jiaxiang Ren, Peng Cheng, Yu Liu, Xuefeng Cui,
Bing Zhu, and Qingjiang Wang

Abstract

The corrosion rate of dissolvable magnesium for frac plugs must maintain integrity for the duration of the operation and dissolve fully thereafter. This study compared water bath corrosion testing to testing in an autoclave with and without a nitrogen purge with the same temperature (95 °C) and salinity (1 wt% KCl). The water bath test dissolution rate fell within the range of the unpurged autoclave. There was a substantial decrease in the dissolution rate of the autoclave where the nitrogen was used for purging entrapped air. The delayed dissolution rate of the material in the purged autoclave appears to be more representative of the deoxygenated downhole environment. The possible reasons for the dissolution rate reduction of magnesium in the deoxygenated environment will be explained in the paper.

Keywords

Dissolvable magnesium • Corrosion •
Dissolution testing • Frac plugs

Introduction

Hydraulic fracturing has unlocked hydrocarbon resources that were considered uneconomical until the Shale Revolution of the past two decades [1]. Advancements in geo-steering allow for horizontal wells to be drilled within the hydrocarbon-bearing formation rather than through it [2, 3]. The increased wellbore contact with the formation increases the production from the well. Shale formation has very low permeabilities and porosities of > 1000 nanodarcies and > 5%, respectively, which still requires further techniques to increase production [4]. Chief among these is hydraulic fracturing, a method by which pressurized fluid creates fractures in the formation that are subsequently held open by proppants such as sand [5]. Multiple zones within a horizontal well are fractured, further increasing the surface area of the reservoir in contact with the wellbore. Operators use temporary wellbore isolation devices called frac plugs to individually isolate the zones, after which they are removed. Historically, these were cast iron or composite plugs that were drilled out with coiled tubing after concluding operations. The coiled tubing operation added extra time, cost, and risk of accidentally drilling through the wellbore casing [6].

Degradable materials for frac plugs were developed as intervention-less solutions for hydraulic fracturing operations [7]. These decrease cost and time associated with milling through plugs with coiled tubing leave little debris due to the materials degrading when in contact with the wellbore fluids [8]. Magnesium alloys are the prevailing material selected due to strength and tailorable dissolution rate for the selected reservoir's temperature, fluid, and composition. Localized galvanic cells created by the intentional addition of impurities induce corrosion within or along the grain boundaries in the material. Generally, increasing salinity and temperature increase the dissolution rate of an alloy, producing magnesium hydroxide and hydrogen gas as a byproduct. Manufacturers of dissolvable magnesium alloys advertise alloys providing reliable, controlled dissolution rates over a range of temperatures that dissolve in a known time [9]. Extensive laboratory qualification testing of the developed alloys in a range of fluids and temperatures provides the data necessary to measure the dissolution rate at a given condition. Typically, a cylindrical sample of dissolvable alloy weighing less than 50 g will be immersed in a 1 L beaker of solution, which is heated to the desired temperature with a water bath. After

---

T. Dunne (✉) · L. Zhao · J. Ren · P. Cheng · Y. Liu
CNPC USA Corporation, 2901 Wilcrest Dr, Houston, TX 77042, USA
e-mail: tim.dunne@cnpcusa.com

X. Cui · B. Zhu · Q. Wang
Daqing Oilfield Company Limited, Daqing, China

A. Leonard et al. (eds.), *Magnesium Technology 2024*, The Minerals, Metals & Materials Series,
https://doi.org/10.1007/978-3-031-50240-8_3

an immersion of appropriate duration is completed, the weight and dimensions are recorded, allowing the dissolution rate to be calculated by dividing the mass difference by the surface area difference by the time elapsed. Repeating testing with fixed temperature and varied salinity, or fixed salinity and varied temperature, provides dissolution rate curves that assist with alloy selection for a given application [10]. These curves are used to predict how long the plug will take to dissolve downhole.

Field experience has shown that dissolvable magnesium plugs take longer than expected to dissolve, with some not dissolving completely. Previous efforts have shown a measurable difference in prediction versus performance for dissolvable aluminum [11]. Oxygen scavengers are commonly used in completion brines to minimize the corrosive effects of dissolved oxygen in the well [12]. All known reported dissolvable magnesium testing is performed in oxygenated environments, motivating this effort to compare typical laboratory conditions to a downhole environment.

Material Testing

Samples of a commercial alloy were machined into 0.6 × 0.8 × 1″ rectangular prisms as depicted in Fig. 1. The individual widths, lengths, heights as well as mass were measured and recorded before and after testing. Residue was gently brushed off with a nylon bristle brush after a heat gun was used to dry the specimen. Two samples were tested in separate beakers placed in a water bath, suspended in a perforated Teflon cup in 1 L of 95 °C 1.05 wt% KCl for 6 h as seen in Fig. 2. A glass viewing lens placed over the beaker eliminated evaporation of the fluid, maintaining the salinity for the duration of the test.

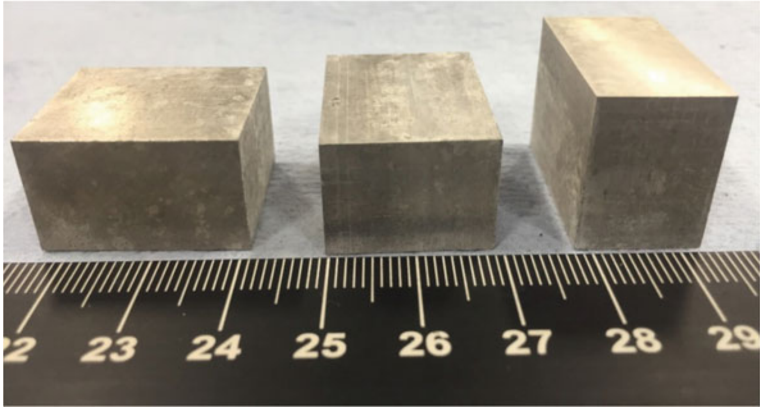

Fig. 1 Machined dissolvable magnesium samples

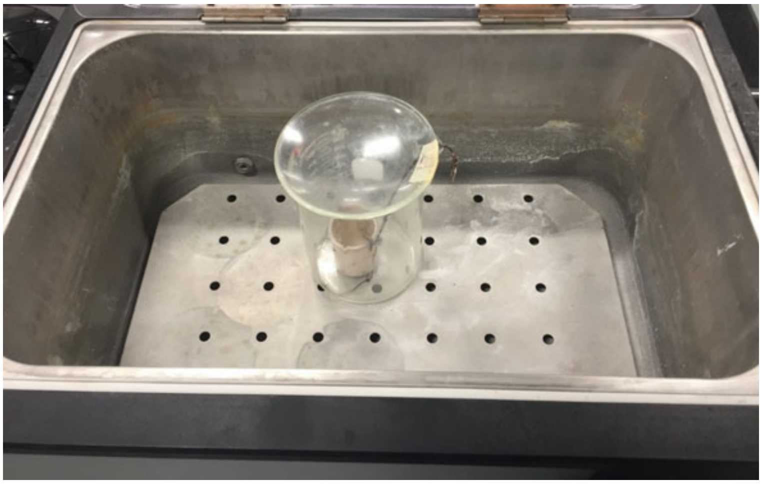

Fig. 2 Water bath setup for dissolution testing without water added. Note the Teflon beaker with a Teflon string to suspend the sample in the fluid

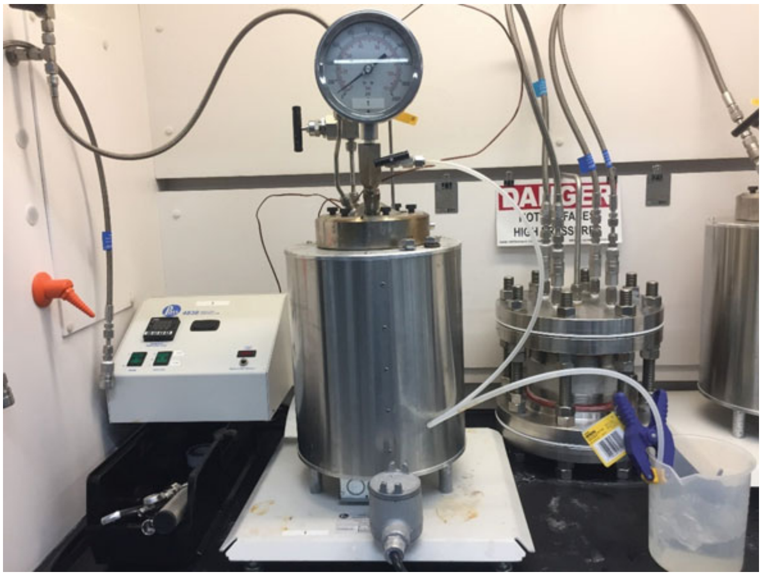

Fig. 3 Autoclave setup for dissolution testing in the N_2 purging configuration

Autoclave samples were tested in a 2 L non-stirred autoclave (Parr 4600-2000 mL-T-HC-1/8) controlled by a temperature controller (Parr 4838). An inert glass liner was placed within the autoclave to prevent any coupling with the Hastelloy body. A perforated Teflon cup suspended the sample, allowing fluid circulation and preventing byproducts from building up around it. Two samples were sequentially tested in 95 °C 1.05 wt% KCl for 6 h without purging the autoclave. Two samples were sequentially tested in 95 °C 1.05 wt% KCl for 6 h after purging the autoclave with nitrogen for 10 min as portrayed in Fig. 3.

Results and Discussion

Dissolution Results

Terves reports dissolution rates of its TervAlloy 3241 in 1% KCl up to 90 °C [13]. A linear fit of the data determines a dissolution rate of 35.3 mg/cm^2/h at 95 °C in 1 wt% KCl (Table 1).

The calculated value from Terves' reported data is comparable with results measured in both the water bath testing and the unpurged autoclave with a maximum of an 8% difference between the values. Despite the autoclave preventing atmospheric oxygen from entering the brine, there is only a 1% difference between the unpurged autoclave and the water bath. However, the purged autoclave results were 42% different from the unpurged autoclave, substantially outside of the range of differences for the previous measurements that can be ascribed to material heterogeneity, alloy batch variation, fluid compositional differences, extrapolation from reported values, or measuring techniques. The significant decrease in the purged autoclave dissolution rate is a significant finding (Table 2).

Table 1 Terves reported dissolution rate for TervAlloy 3241 (TAx100E)

Temperature (°C)	Dissolution rate, mg/cm^2/h
30	3
45	10
60	18
75	25
90	33

Table 2 Summary of reported and measured values for a commercial alloy at 95 °C

Condition (1 wt% KCl, 95 °C)	Rate, mg/cm^2/h (average)	Range, mg/cm^2/h (±)
Reported*	35.3	–
Water bath	32.6	1.0
Autoclave, air	33.0	1.5
Autoclave, N_2 purge	21.5	1.5

*Maximum reported data was 90 °C, so that the 95 °C data from the vendor was calculated from a curve fit

To understand the decrease in corrosion rate, an understanding of the role of oxygen must be understood in the context of the reaction. The typical mechanism is galvanic corrosion between the lower open corrosion potential (OCP) α phase magnesium matrix and the secondary phases with higher OCP. A reaction product layer of magnesium hydroxide forms, with the brine acting as the electrolyte. The typically presented electrochemical reaction is as follows (Fig. 4):

$$Mg \rightarrow Mg^{2+} + 2e^- \qquad (1)$$

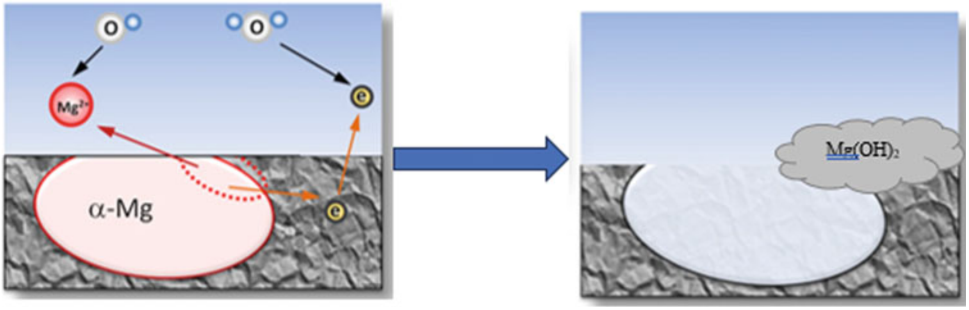

Fig. 4 Schematic of how the dissolution reaction of dissolvable magnesium is typically viewed [14]

$$2H_2O + 2e^- \rightarrow H_2 + 2OH^- \quad (2)$$

$$2H^+ + 2e^- \rightarrow H_2 \quad (3)$$

$$Mg + 2H_2O \rightarrow Mg(OH)_2 + H_2 \quad (4)$$

A review of literature discussing dissolvable magnesium seems to overlook the role dissolved oxygen plays in the corrosion process [15, 16]. The disconnection between lab conditions and the well environment has led to consistent overestimation of the dissolution rate for dissolvable magnesium plugs in the field. The data suggests an intermediate species being generated first through oxidation, which is either re-deposited or reacts with the environment. Experimentally, it is observed the typical reaction (Eqs. 1–4) is not the only one. The dissolved oxygen acts as a cathodic depolarizer of the cathode surface, stripping the adsorbed hydrogen ion film away, thus allowing for accelerated corrosion. Additionally, dissolved oxygen will oxidize magnesium.

$$2Mg + O_2 \rightarrow 2\left[Mg^{2+}\right]\left[O^{2-}\right] \quad (5)$$

$$Mg \rightarrow Mg^{2+} + 2e^- \quad (6)$$

$$O_2 + 4e^- \rightarrow 2O^{2-} \quad (7)$$

$$O_2 + 4e^- + 2H_2O \rightarrow 4OH^- \quad (8)$$

Recently, some workers have found the oxygen reduction reaction (Eq. 8) is underappreciated in its role in corrosion [17–19]. Dissolved oxygen was found to be depleted on the surface in one work, suggesting oxygen reduction is active. Work performed by Höche et al. suggests impurities such as copper will redeposit, which would accelerate the reaction in Eq. 2. The oilfield magnesium alloys contain relatively high amounts of impurities avoided in commercial alloys. Water bath testing benefits from the accelerated dissolution due to the impurity deposition which would not be seen in a downhole environment (Fig. 5).

Conclusions

Dissolvable magnesium alloys are extensively tested in a variety of fluids at different temperatures to inform end users of the expected downhole life of products machined from the alloy. Testing is predominately performed in fluid containing dissolved oxygen, where the downhole completion fluids are deoxygenated. Dissolvable magnesium alloys experience a considerable decrease in dissolution rate when the solution is purged with an inert gas. Dissolved oxygen modifies the passivation layer, increasing the reaction kinetics.

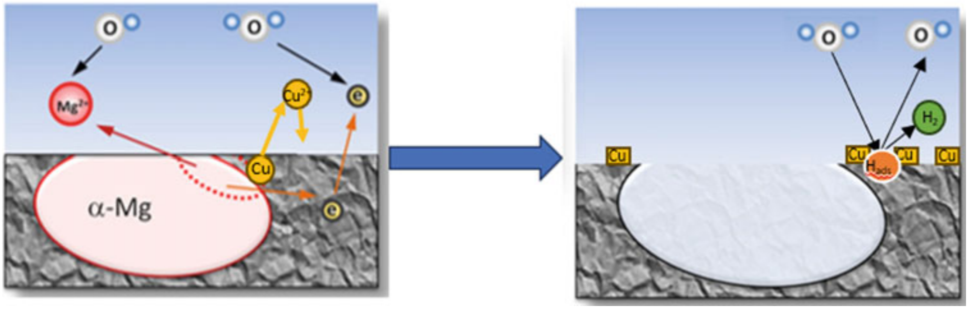

Fig. 5 Schematic with speculated deposition of copper impurity due to dissolved oxygen, contributing to accelerated reaction only seen in laboratory measurements

Dissolvable magnesium alloys should be qualified in a purged environment to inform end users of the dissolution rate more accurately in a downhole environment. Operators should consider higher dissolution rate materials for a given set of conditions.

Acknowledgements The authors thank the management of CNPC USA for granting permission to publish this work.

References

1. S. Brown and M. Yucel, “The Shale Gas and Tight Oil Boom: U.S. States’ Economic Gains and Vulnerabilities,” *Council on Foreign Relations* (October 2013).
2. R. R. Hansen and J. White, “Features of Logging-While-Drilling (LWD) in Horizontal Wells,” *SPE/IADC Drilling Conference*, Amsterdam, Netherlands, March 1991.
3. M.R. Islam and M.E. Hossain, “Chapter 3—Advances in directional drilling,” In *Sustainable Oil and Gas Development Series, Drilling Engineering*, Gulf Professional Publishing, 2021, Pages 179–316, ISBN 9780128201930.
4. J. Goral, P. Panja, M. Deo et al., “Confinement Effect on Porosity and Permeability of Shales,” *Sci Rep 10, 49* (2020).
5. U.S. Government Accountability Office, “Oil and Gas Information on Shale Resources, Development, and Environmental and Public Health Risks,” 2012.
6. Z. Walton, M. Fripp, J. Porter, G. Vargus, “Evolution of Frac Plug Technologies—Cast Iron to Composites to Dissolvable”, *SPE Middle East Oil and Gas Show and Conference*, March 2019.
7. J. Wang; X. He; J. Wang; et al., “New Dissolvable Isolation Tool Eliminating Plug and Perf Operation Challenges and Reduce Completion Costs,” *Gas & Oil Technology Showcase and Conference*, Dubai, UAE, March 2023.
8. D. Hutabarat, J. Ray, C. Frazier, A. Haines, “Coil Tubing Drillout Efficiency Gains Utilizing Dissolvable Plug Technology.” *SPE/ICoTA Well Intervention Conference and Exhibition*, The Woodlands, Texas, USA, March 2019.
9. T.R. Dunne, W. Yue, L. Zhao et al., “Addressing Corrosion Stress Cracking Issue of Magnesium Frac Plugs Used in Ultra HPHT Shale Well Development,” *Abu Dhabi International Petroleum Exhibition & Conference*, Abu Dhabi, UAE, November 2021.
10. T. Dunne, J. Ren, L. Zhao et al., “Enhancement of Mechanical and Dissolution Properties of a Cast Magnesium Alloy via Equal Angular Channel Processing,” *International Journal of Materials and Metallurgical Engineering 15 (4)*, 103–108, 2021.
11. H. Tu; I. Aviles; M. Dardis, “Degradable Materials for Multi-Stage Stimulation”, *Offshore Technology Conference*, Houston, Texas, May 2019.
12. D. Chappell, “Corrosion and Oxygen Control”, *Waterflooding: Chemistry*.
13. Terves, TervAlloy 3241|TAx100E Factsheet, https://www.tervesinc.com/media/ProductSheet_TervAlloy_3241_TAx100E.pdf
14. L. Bao, Z. Zhang, Q. Le et al., “Corrosion behavior and mechanism of Mg–Y–Zn–Zr alloys with various Y/Zn mole ratios,” *Journal of Alloys and Compounds 712*, 15–23, 2017.
15. G. Baril, N. Pebere, “The corrosion of pure magnesium in aerated and deaerated sodium sulphate solutions”, Corrosion Science, Volume 43, Issue 3, 2001, Pages 471–484
16. T. Beldjoudi, C. Fiaud, L. Robbiola, “Influence of Homogenization and Artificial Aging Heat Treatments on Corrosion Behavior of Mg-Al Alloys”, CORROSION 1 September 1993; 49 (9): 738–745.
17. C. Wang, W. Xu, D. Höche, M.L. Zheludkevich, S.V. Lamaka, “Exploring the contribution of oxygen reduction reaction to Mg corrosion by modeling assisted local analysis”, Journal of Magnesium and Alloys, Volume 11, Issue 1, 2023, Pages 100–109.
18. D. Höche, C. Blawert, S.V. Lamaka, N. Scharnagl, C. Mendis, M. L. Zheludkevich, “The effect of iron re-deposition on the corrosion of impurity-containing magnesium.” Phys Chem Chem Phys. 2016 Jan 14;18(2):1279–91.
19. E.L. Silva, S.V. Lamaka, D. Mei, M.L. Zheludkevich, “The Reduction of Dissolved Oxygen During Magnesium Corrosion,” Chemistry Open. 2018 Aug 30, 7(8):664–668.

Evaluation of Corrosion Performance of Friction Stir Processed Magnesium Alloys Using Multimodal Analysis Across Length Scales

Sridhar Niverty, Rajib Kalsar, Shuai Tan, Venkateshkumar Prabhakaran,
Hrishikesh Das, Piyush Upadhyay, David Garcia,
Mageshwari Komarasamy, Lyndi Strange, Glenn J. Grant,
Darrell R. Herling, and Vineet V. Joshi

Abstract

Friction stir processing (FSP) homogenizes and refines the microstructure through severe plastic deformation. Previous studies have demonstrated that the processed zone is more corrosion-resistant as compared to the base Mg alloy. However, the corrosion behavior of the microstructure immediately adjacent to the processed zone, and how it affects the base material under corrosive environments has received little attention. In this study, we have used a multimodal corrosion measurement system to investigate the corrosion behavior of the surface and cross section of FSP AZ31 and AZ91 Mg alloy plates by imaging the sample, acquiring electrochemical data, and collecting evolved hydrogen. Additionally, scanning electrochemical cell microscopy (SECCM) was employed to study variations in localized corrosion behavior from the base metal into the stir zone from the advancing and retreating sides. Microscopy was employed to identify the microstructural cause for the enhanced susceptibility to corrosion in the heat-affected zone and base material.

Keywords

Friction stir processing (FSP) • Magnesium alloys • Multimodal analysis

Extended Abstract

Magnesium (Mg) alloys offer exceptional potential for automotive applications due to their remarkable specific strength. However, their susceptibility to corrosion has historically posed a challenge to their widespread use. To address this concern, friction stir processing (FSP), a solid-phase processing technique, has emerged as a promising solution. FSP locally enhances the microstructure, leading to significant grain refinement and improved chemical homogenization [1–3]. Previous research has demonstrated that in saltwater solutions, the processed zone exhibits superior corrosion resistance and is more cathodic when compared to the base metal [4, 5]. However, FSP also generates an interface between the processed zone and the base metal, comprising a heat-affected zone (HAZ) and a thermo-mechanically affected zone (TMAZ). The role of these microstructural features along with the base and stirred regions on the overall corrosion performance is yet to be investigated. By doing so, we can gain a comprehensive understanding of how these regions interact and contribute to the enhanced corrosion performance of FSP'd Mg alloys.

In this study, we have investigated the corrosion performance of FSP AZ91 Mg alloy immersed in 0.6 wt% NaCl solution under open circuit potential. A newly designed multimodal corrosion measurement system was utilized to image the sample over a 24 h corrosion duration [6, 7]. The FSP AZ91 sample was epoxy mounted to analyze the cross section and polished to a 1 μm diamond finish prior to corrosion. Figure 1 shows snippets of corrosion occurring on the cross section of a FSP AZ91 sample, and their corresponding time stamps in hours. Half of the sample is shown in the figures wherein the stir zone is on the left and the base metal is on the right as shown in Fig. 1a. The approximate transition region/interface between these zones is highlighted using a dashed line. The ratio of the area of the stir zone

---

S. Niverty (✉) · R. Kalsar · S. Tan · V. Prabhakaran · H. Das ·
P. Upadhyay · D. Garcia · M. Komarasamy · L. Strange ·
G. J. Grant · D. R. Herling · V. V. Joshi
Energy and Environment Directorate, Pacific Northwest National Laboratory, 902 Battelle Boulevard, Richland, WA 99354, USA
e-mail: sridhar.niverty@pnnl.gov

A. Leonard et al. (eds.), *Magnesium Technology 2024*, The Minerals, Metals & Materials Series,
https://doi.org/10.1007/978-3-031-50240-8_4

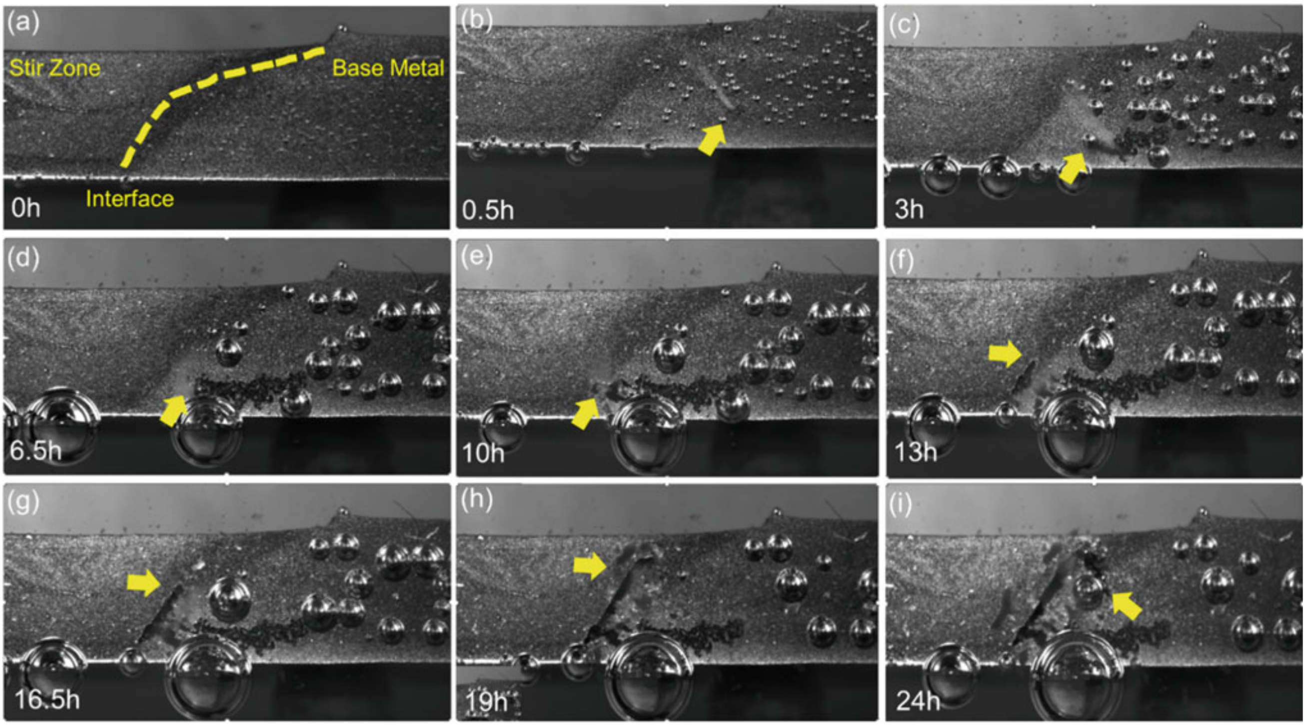

Fig. 1 Corrosion of cross section of FSP AZ91 in 0.6 wt% NaCl solution—snippet images of ongoing corrosion over the 24 h of corrosion duration showing the initiation of corrosion at the pore cluster and progress of filiform corrosion towards the stir zone. Redirection of corrosion front and progress along the interface can also be seen. Corrosion front is shown with a yellow arrow

(cathode) to the ratio of the base metal (anode) in this sample was approximately 0.33.

First, filiform corrosion initiates from a pre-existing cluster of pores within the base metal. With increase in corrosion time, the filiform corrosion propagates towards the transition region between the stir zone and the base metal. Upon reaching this region, the corrosion progresses towards the interface between these zones and later traces upwards towards the top face of the FSP sample. This interfacial attack is accompanied by material removal as can be seen in Fig. 1g–i, respectively. Additionally, the corrosion front can be identified by tracking the release of hydrogen bubbles from the corroding surface and is shown with an arrow in all the images. It is interesting to note that the primary region of the sample where rapid hydrogen bubbling is seen is at the corrosion front near the stir zone. Regions within the FSP stir zone show no hydrogen release over the 24 h duration indicating that it is not undergoing corrosion. Additionally, regions within the base metal show hydrogen bubble release and signs of localized corrosion attack, albeit at a very slow rate which leads to the growth of hydrogen bubbles slowly over the 24 h duration. Figure 2a, b shows post-corrosion optical micrographs of the corroded regions.

Note the magnitude of corrosion in the stir zone-base metal interface compared to the rest of the base metal. Depth profile measurements show that the depth of corrosion attack is greatest at the interface between the sir zone and base metal (Fig. 2c). To further probe this observed phenomenon, we utilized scanning electrochemical cell microscopy (SECCM) to study the variation in the localized corrosion behavior from the base metal into the stir zone from both the advancing and retreating sides [8]. Finally, correlative microscopy was employed to identify the microstructural cause for the enhanced susceptibility to corrosion in the heat-affected zone and the base material. In summary, our observations indicate the interface between the stir zone and base metal is particularly susceptible to preferential corrosion attack as compared to the base metal and stir zone, upon exposure to a saltwater solution.

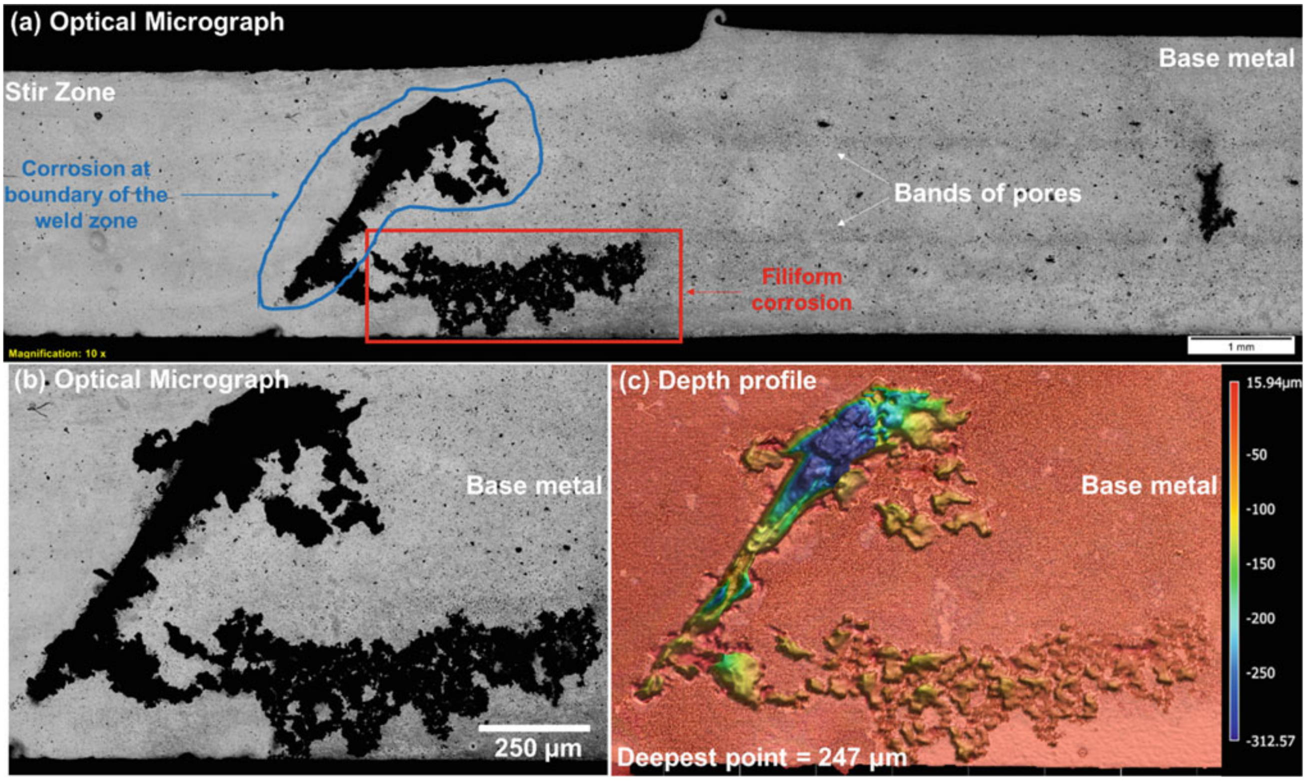

Fig. 2 **a** Large field of view optical micrograph showing preferential corrosion attack at the interface, absence of attack in the stir zone, and mild corrosion attack within the base metal, **b** optical micrograph showing a high-resolution optical micrograph of the corrosion attack at the interface, **c** surface depth profile map showing shallow filiform corrosion attack at the location of origin of corrosion and deeper corrosion attack at the interface region

References

1. R.S. Mishra, Z.Y. Ma, Friction stir welding and processing, Mater. Sci. Eng. R Reports. 50 (2005) 1–78. https://doi.org/10.1016/J.MSER.2005.07.001.
2. Z.Y. Ma, Friction stir processing technology: A review, Metall. Mater. Trans. A Phys. Metall. Mater. Sci. 39 A (2008) 642–658. https://doi.org/10.1007/S11661-007-9459-0.
3. D. Garcia, H. Das, K. Sadayappan, P. Newcombe, D. Herling, G. J. Grant, M. Komarasamy, Solid-Phase Processing of Mg-Al-Mn-Ca for High Strength and Ductility, in: Magnesium Technology 2023: pp. 131–133. https://doi.org/10.1007/978-3-031-22645-8_27.
4. Q. Liu, G. qiang Chen, S. bo Zeng, S. Zhang, F. Long, Q. yu Shi, The corrosion behavior of Mg-9Al-xRE magnesium alloys modified by friction stir processing, J. Alloys Compd. 851 (2021). https://doi.org/10.1016/J.JALLCOM.2020.156835.
5. Z. Zeng, M. Zhou, M. Esmaily, Y. Zhu, S. Choudhary, J.C. Griffith, J. Ma, Y. Hora, Y. Chen, A. Gullino, Q. Shi, H. Fujii, N. Birbilis, Corrosion resistant and high-strength dual-phase Mg-Li-Al-Zn alloy by friction stir processing, (n.d.). https://doi.org/10.1038/s43246-022-00245-3.
6. S. Niverty, R. Kalsar, L. Strange, V. Prabhakaran, V. V. Joshi, Integrating Multimodal Corrosion with Correlative Microscopy Across Multiple Length Scales, (2023) 63–64. https://doi.org/10.1007/978-3-031-22645-8_15/COVER.
7. S. Niverty, R. Kalsar, R. J. Seffens, A. D. Guzman, T. J. Roosendaal, L. Strange, V. V Joshi, Probing corrosion using a simple and versatile in situ multimodal corrosion measurement system, Sci. Reports. 13 (2023) 16695. https://doi.org/10.1038/s41598-023-42249-0.
8. V. Prabhakaran, R. Kalsar, L. Strange, O.A. Marina, R. Prabhakaran, V. V. Joshi, Understanding Localized Corrosion on Metal Surfaces Using Scanning Electrochemical Cell Impedance Microscopy (SECCIM), J. Phys. Chem. C. 126 (2022) 12519–12526. https://doi.org/10.1021/acs.jpcc.2c03807.

Improved Formability and Corrosion Resistance of Pure Magnesium by Parts-Per-Million-Level Addition of Copper and Calcium

Mingzhe Bian, Isao Nakatsugawa, Xinsheng Huang,
and Yasumasa Chino

Abstract

Poor cold formability, poor corrosion resistance, and high cost of alloying elements are longstanding barriers to the widespread use of magnesium (Mg) and its alloys. In this study, we demonstrated that both the room temperature (RT) stretch formability and corrosion resistance of commercially used pure Mg could be significantly improved by adding trace amounts of copper (Cu) and calcium (Ca). Owing to the addition of trace amounts of the alloying elements, the resultant alloy also showed excellent thermal conductivity, which is almost two times higher than that of the most commonly used Mg alloy (AZ31) and even higher than that of a commercial Al alloy (A5052). These findings are expected to stimulate the development of high-performance Mg alloys that can be used in portable electronic devices, automobile electronics, and household appliances.

Keywords

Magnesium • PPM-level alloying: formability • Corrosion • Thermal conductivity

Introduction

In recent years, lightweight, corrosion-resistant, and thermal conductive materials have gained increasing attention, driven by the growing demand for portable electronic devices, automobile electronics, and household appliances [1]. Magnesium (Mg) is the lightest structural metal, and its thermal conductivity is as high as ~ 160 W/(m K). However, the strength and formability at room temperature (RT) are low, and the corrosion resistance of commercially available pure Mg is very poor [2]. In contrast, a commercial Mg alloy AZ31 (Mg–3Al–1Zn–0.3Mn in wt%) has adequate strength and moderate corrosion resistance [3], but low thermal conductivity [~ 85 W/(m K)] due to the large solid solubility of Al in Mg [4]. In addition, the RT formability is poor, which can be ascribed to the development of a strong basal texture [5]. Recently developed Mg–Zn–Ca-based alloys such as Mg–3Zn–0.5Ca–0.5Al–1Mn (wt%) and Mg–1.6Zn–0.5Ca–0.4Zr (wt%) show attractive mechanical properties [6, 7]. Unfortunately, their thermal conductivity is still rather low compared to that of commercial Al alloys such as A5052 (138 W/(m K)) and A6061 [T4: 154 W/(m K), T6: 167 W/(m K)] [8].

Recently, we found that the RT formability and corrosion resistance of commercially available pure Mg could be significantly improved by adding trace amounts of Cu and Ca [9]. Due to the addition of extremely small amounts of the alloying elements, the resultant alloy showed excellent thermal conductivity. The purpose of this paper is thus to report the mechanical properties, corrosion resistance, and thermal conductivity of Mg–Cu–Ca ternary alloys with different Cu and Ca contents.

Experimental Procedure

Pure Mg, Mg–0.03wt%Cu, Mg–0.1wt%Ca, and Mg–Cu–Ca ingots were prepared by an induction melting furnace under an inert argon atmosphere. The ingots were then extruded at 400 °C with an extrusion ratio of 6 and a ram speed of 5 mm/min to produce 5-mm thick plates. Prior to rolling, the extruded Mg–0.03Cu–0.5Ca, Mg–0.03Cu–1Ca, and Mg–0.03Cu–2Ca (all in wt%) plates were homogenized at 450 °C for 24 h, while the other plates were directly rolled without the homogenization treatment. The plates were rolled from 5 to 1 mm in 7 passes with ~ 21% thickness reduction per pass. The rollers were heated to 90 °C during

---

M. Bian (✉) · I. Nakatsugawa · X. Huang · Y. Chino
Multi-Material Research Institute, National Institute of Advanced Industrial Science and Technology (AIST), Nagoya, 463-8560, Aichi, Japan
e-mail: mingzhe.bian@aist.go.jp

A. Leonard et al. (eds.), *Magnesium Technology 2024*, The Minerals, Metals & Materials Series,
https://doi.org/10.1007/978-3-031-50240-8_5

rolling. The sheets were quenched in water immediately after each pass and reheated to 350 °C before subsequent rolling. The as-rolled sheets were finally annealed at 300 °C for 2 h.

To evaluate the stretch formability of annealed sheets, Erichsen cupping tests were carried out on the circular blanks with a diameter of 60 mm and a thickness of 1 mm using a hemispherical punch with a diameter of 20 mm at RT. The punch speed and the blank-holder force were 5 mm/min and 10 kN, respectively. To evaluate corrosion resistance, the test pieces were immersed in 1 L of 3.5 wt% NaCl aqueous solution at 25 °C for 72 h (6 h for pure Mg and 24 h for Mg–0.03Cu, Mg–0.03Cu–0.01Ca, and Mg–1.5Cu–0.1Ca alloys). The thermal diffusivity (α), density (ρ), and specific heat capacity (C_p) were measured using a laser flash thermal constant measurement system TC-9000, mass dimension method, and PerkinElmer DSC7 differential scanning calorimetry, respectively. The thermal conductivity (λ) at RT was calculated using the following equation:

$$\lambda = \alpha.\rho.\mathrm{C_p} \tag{1}$$

(0002) basal pole figures were measured at the mid-layers of annealed sheets by X-ray texture analyses using a Rigaku RINT Ultima III operated at 40 kV and 40 mA. The TEM observation was carried out on a spherical aberration-corrected JEM-ARM200F instrument operated at 200 kV.

Results and Discussion

Figure 1 shows RT formability of annealed Mg, Mg–0.1Ca, Mg–0.03Cu, and Mg–Cu–Ca sheets. As expected, pure Mg had a low Index Erichsen (IE) value of 2.9 mm. The addition of 0.03 wt% Cu or 0.1 wt% Ca to pure Mg did not improve the RT formability significantly (3.3 and 4.3 mm). However, the addition of small amounts of Cu to the Mg–0.1Ca alloy or small amounts of Ca to the Mg–0.03Cu alloy significantly enhanced the RT formability. It is noteworthy that the chemically optimized Mg–0.03Cu–0.05Ca alloy showed a large IE value of 7.7 mm, which is more than twice that of pure Mg.

Figure 2a, b plots the average grain size and phase fraction of Mg_2Cu and Mg_2Ca as a function of Cu and Ca contents. The average grain size decreased dramatically with the addition of parts-per-million (PPM) levels of Ca and Cu of pure Mg. The 'tipping point' of Cu and Ca content in Mg–xCu–0.1Ca and Mg–0.03Cu–yCa alloys was approximately 0.03 wt% (300 PPM) and 0.05 wt% (500 PPM), respectively, after which the change in the grain size was much less pronounced. Instead, coarse Mg_2Cu second-phase particles were formed in the Mg–0.1Cu–0.1Ca alloys, and their volume fraction increased with increasing the Cu content. Similarly, Mg_2Ca second-phase particles were

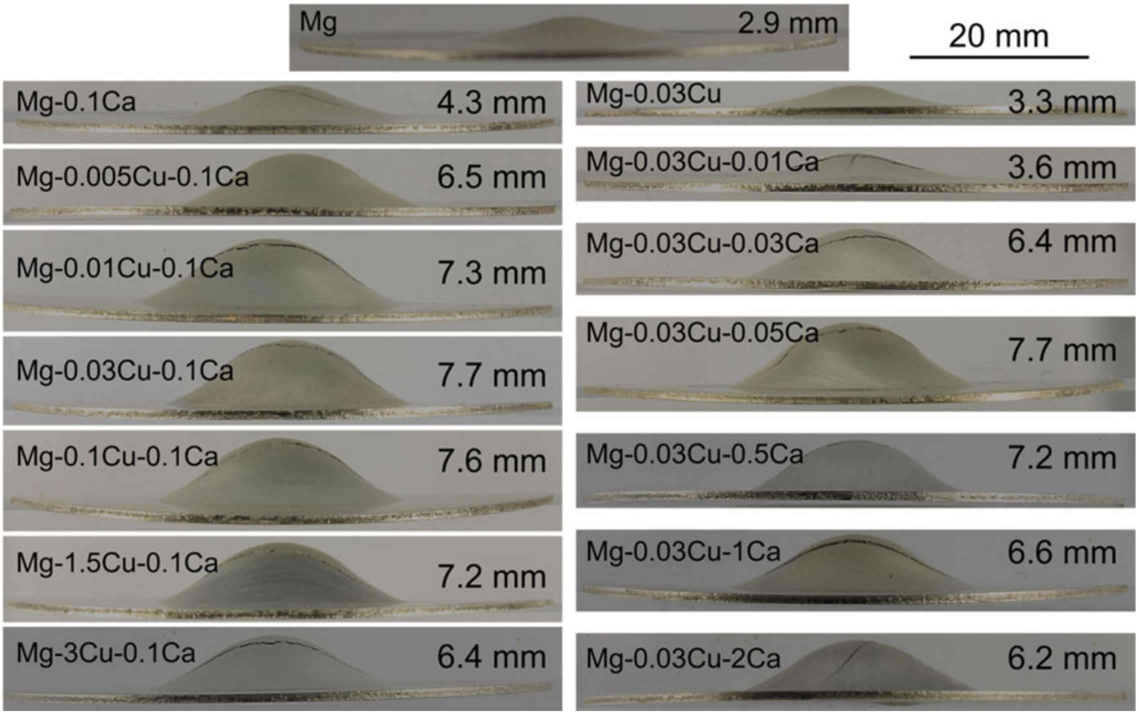

Fig. 1 Index Erichsen values of annealed Mg, Mg–0.1Ca, Mg–0.03Cu, and Mg–Cu–Ca sheets

formed in the Mg–0.03Cu–0.1Ca alloys, and their volume fraction increased with increasing the Ca content. In order to understand the reasons for the substantial decrease in the grain size by the PPM levels of Cu and Ca addition, the microstructure of Mg–0.03Cu–0.05Ca alloy was observed by TEM, as shown in Fig. 2c–e. From the high-angle annular dark-field scanning transmission electron microscopy (HAADF-STEM) image and corresponding energy-dispersive spectroscopy (EDS) elemental maps, it can be seen that Cu and Ca co-segregated along the grain boundaries (GBs). Therefore, it is believed that the co-segregation of Cu and Ca effectively retarded the growth of recrystallized grains, resulting in the formation of a finer-grained microstructure in the PPM-level alloyed Mg.

Figures 3 and 4 show the (0002) basal pole figures obtained from the as-rolled and annealed sheets of pure Mg, Mg–0.1Ca, Mg–0.03Cu, Mg–xCu–0.1Ca, and Mg–0.03Cu–yCa. All as-rolled sheets showed the rolling direction (RD) split textures with double peaks in which the maximum intensity of basal poles was located at 15–20° from the normal direction (ND) towards the RD. After annealing at 300 °C for 2 h, the distribution and intensity of (0002) basal pole figures varied with the chemical composition. Pure Mg exhibited a typical strong basal texture (16.3 m.r.d.). Therefore, poor stretch formability of pure Mg can be ascribed to the formation of strong basal texture. The 0.1 wt% Ca addition resulted in a significant reduction in the texture intensity (4.1 m.r.d.), which is consistent with the results reported in the literature [10]. On the other hand, the addition of 0.03 wt% Cu also decreased the texture intensity to 8.2 m.r.d., as shown in Fig. 4. However, the RD-split texture was retained after annealing for both Mg–0.1Ca and Mg–0.03Cu binary alloys. In the case of Mg–Cu–Ca ternary alloys, a transverse direction (TD) component started to appear when the Cu content increased to 0.03 wt% in the Mg–xCu–0.1Ca alloys, and when the Ca content increased to 0.03 wt% in the Mg–0.03Cu–yCa alloys. A typical TD-split texture with a low intensity of 2.6 m.r.d. was developed in the Mg–0.03Cu–0.05Ca alloy. This kind of texture is usually developed in RT formable Mg–Zn–Ca/RE [11–14], Mg–Ag–Ca [15], and

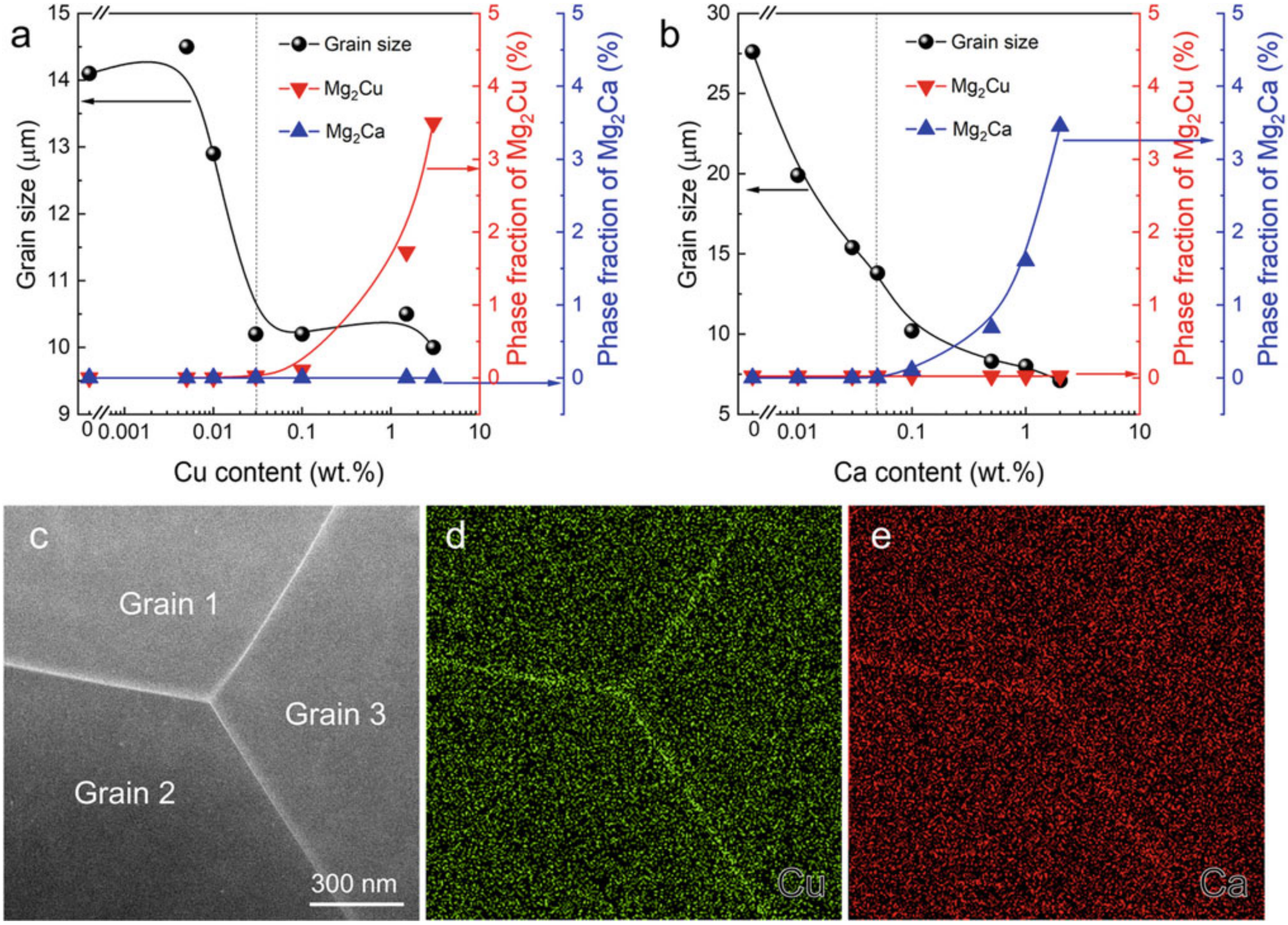

Fig. 2 Grain size and phase fraction of Mg_2Cu and Mg_2Ca as a function of **a** Cu content in Mg–xCu–0.1Ca alloys and **b** Ca content in Mg–0.03Cu–yCa alloys. **c–e** HAADF-STEM image and corresponding EDS elemental maps showing the distribution of Cu and Ca in Mg–0.03Cu–0.05Ca alloy

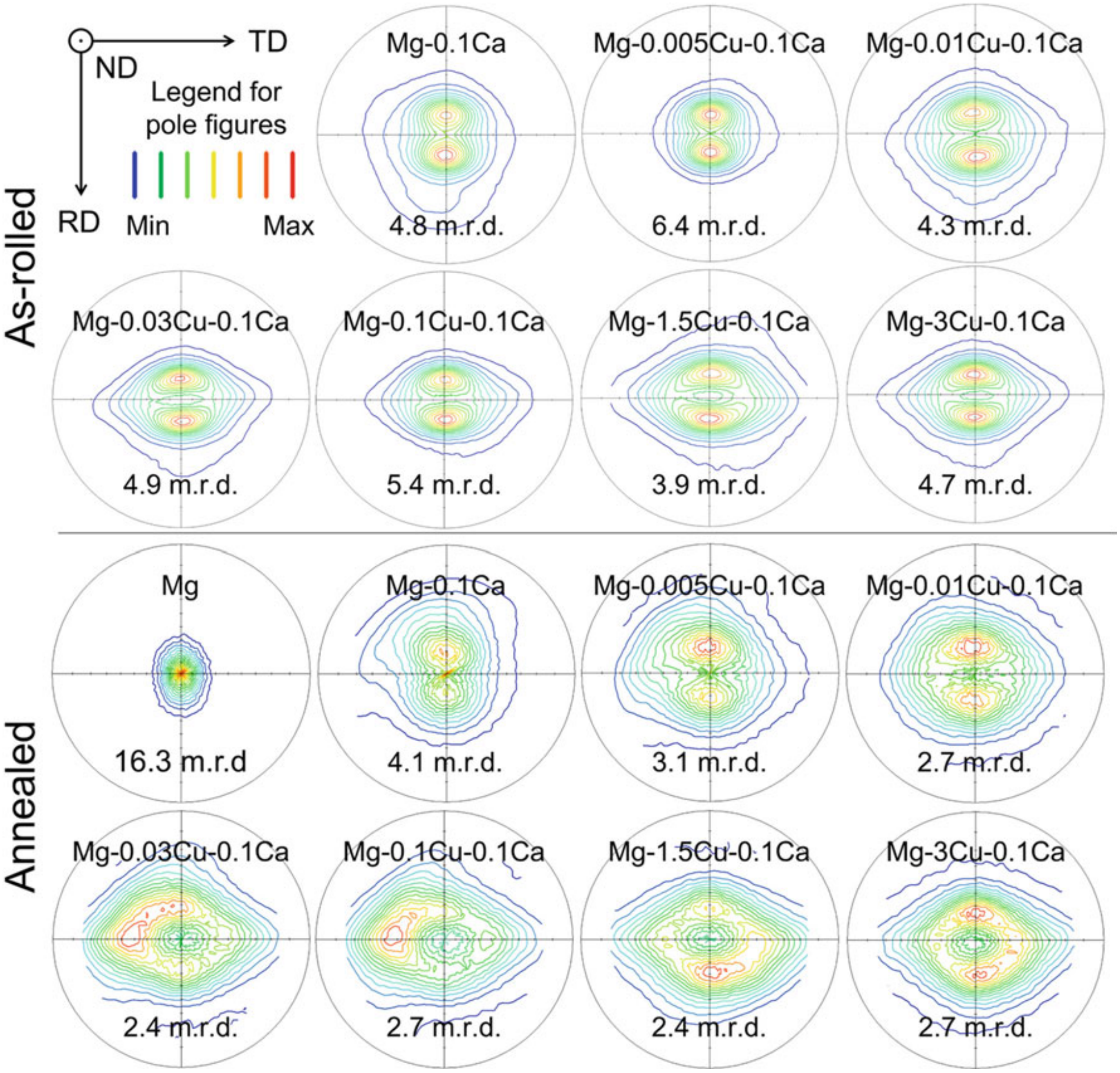

Fig. 3 (0002) basal pole figures showing the textures of as-rolled and annealed Mg, Mg–0.1Ca, and Mg–xCu–0.1Ca sheets

Mg–Ni–Ca [16] alloys. Therefore, the good RT formability obtained from the Mg–0.03Cu–0.05Ca alloy is mainly due to the development of the weak TD-split texture. Further increase in the Cu or Ca content did not lead to further decrease in the texture intensity. Instead, a typical quadruple texture was developed in the high Cu- and high Ca-containing alloys, particularly in the high Ca-containing alloys. Therefore, the decrease in the RT formability of high Cu- and high Ca-containing alloys can be mainly ascribed to the increased fraction of coarse Mg_2Cu and Mg_2Ca second-phase particles, as shown in Fig. 2.

Figure 5 shows the corrosion rate of Mg–Cu–Ca alloys as a function of Cu or Ca content. Obviously, the co-addition of Cu and Ca also resulted in the improvement in the corrosion resistance of pure Mg. It is worth pointing out that the corrosion rate of pure Mg was as high as 436 mg/(cm^2 day). To our surprise, the addition of 0.03 wt% Cu to pure Mg also decreased the corrosion rate to about 41.4 mg/(cm^2·day). Further addition of Ca, even at the PPM levels, to the binary Mg–0.03Cu alloy also resulted in a significant decrease in the corrosion rate. The corrosion rate of a 500 PPM Ca-containing Mg–0.03Cu alloy, i.e., Mg–0.03Cu–0.05Ca, with the highest IE value of 7.7 mm, showed a low corrosion rate of 1.79 mg/(cm^2·day), which is even lower than that of a commercial AZ31 alloy [2.23 mg/(cm^2·day)]. The detrimental effect of Cu on the corrosion resistance of Mg and its alloys is well known. However, a closer look at the tolerance limit of Cu in pure Mg indicates that it is about 0.1 wt% [17]. In other words, if the Cu concentration is less than 0.1 wt%, corrosion is not a big issue for Mg. In this study, we found that the corrosion rate of Mg–xCu–0.1Ca alloys is lower than 5 mg/(cm^2/day) when the Cu concentration is less

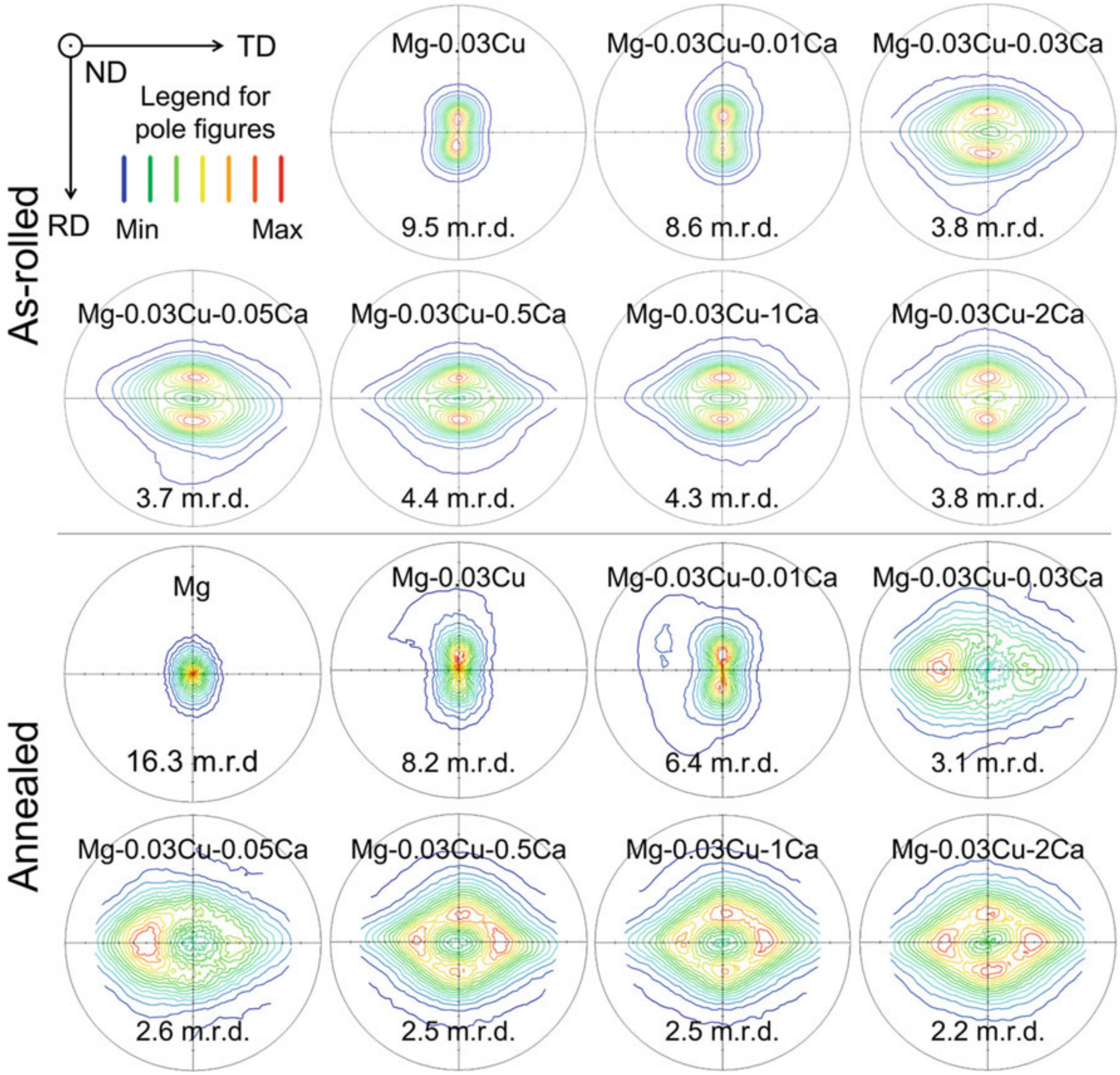

Fig. 4 (0002) basal pole figures showing the textures of as-rolled and annealed Mg, Mg–0.03Cu, and Mg–0.03Cu–yCa sheets

than 0.1 wt%. Therefore, the tolerance limit of Cu in Ca-containing Mg alloys is believed to be about 0.1 wt%.

Figure 6 presents the thermal conductivity of the newly developed Mg–0.03Cu–0.05Ca alloy. For comparison purpose, thermal conductivity of pure Mg, commercial Mg alloy AZ31, and commercial Al alloy A5052 was included. Benefiting from the addition of an extremely small amount of the alloying elements, the Mg–0.03Cu–0.05Ca alloy exhibited an excellent thermal conductivity of 157 W/(m·K), which is close to that of pure Mg [167 W/(m·K)]. It is to be noted that the thermal conductivity of Mg–0.03Cu–0.05Ca alloy is approximately two times higher than that of the AZ31 [87 W/(m·K)] and even higher than that of the A5052 [138 W/(m·K)].

Considering the combination of good formability, superior corrosion resistance, excellent thermal conductivity, and low cost of Cu and Ca, alloying them with Mg is believed to be particularly attractive for portable electronic devices, automobile electronics, and household appliances.

Summary

In this study, we demonstrated that the RT stretch formability of commercially available pure Mg could be remarkably improved from 2.9 to 7.7 mm by adding 300 PPM of Cu and 500 PPM of Ca. The (0002) basal pole figure intensity was substantially weakened from 16.3 to 2.6 m.r.d by the PPM-level addition of Cu and Ca of pure Mg. The improved RT stretch formability can be mainly attributed to the weakened basal texture. In addition, we found that the corrosion rate of the PPM-level alloyed Mg was 1.79 mg/(cm^2·day), which is almost two orders of magnitude lower than that of pure Mg [436 mg/(cm^2·day)]. Due to the

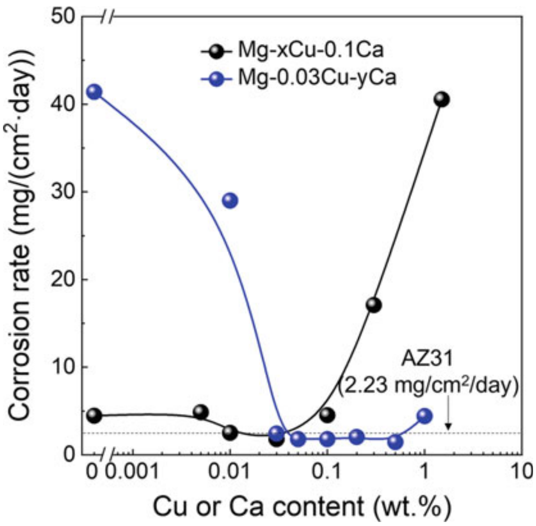

Fig. 5 Corrosion rate measured by the weight loss method as a function of Cu or Ca content. The figure is reproduced from Ref. [9]

Fig. 6 Thermal conductivity of a newly developed Mg–0.03Cu–0.05Ca alloy. Thermal conductivity of pure Mg, commercial Mg alloy AZ31 and commercial Al alloy A5052 was included for comparison purpose

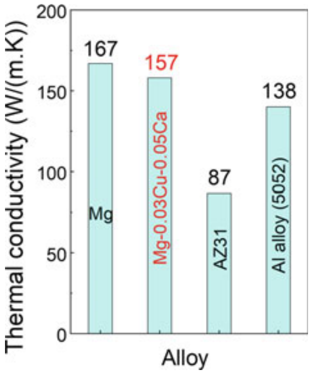

PPM-level addition of Ca and Cu, the resultant Mg–0.03 Cu–0.05Ca alloy showed an excellent thermal conductivity of 157 W/(m·K), which is approximately two times higher than that of the most widely used Mg alloy AZ31 and even higher than that of a commercial Al alloy A5052.

Acknowledgements This study was partially supported by JSPS KAKENHI Grant numbers JP20K15067, JP21K04716, and JP21K04687.

References

1. Li, S., Yang, X., Hou, J., and Du, W. (2020) A review on thermal conductivity of magnesium and its alloys. *J. Magnes. Alloy.*, **8** (1), 78–90.
2. Hirsch, J., and Al-Samman, T. (2013) Superior light metals by texture engineering: Optimized aluminum and magnesium alloys for automotive applications. *Acta Mater.*, **61** (3), 818–843.
3. Chino, Y., Kimura, K., and Mabuchi, M. (2009) Deformation characteristics at room temperature under biaxial tensile stress in textured AZ31 Mg alloy sheets. *Acta Mater.*, **57** (5), 1476–1485.
4. Lee, S.H., Ham, H.J., Kwon, S.Y., Kim, S.W., and Suh, C.M. (2013) Thermal Conductivity of Magnesium Alloys in the Temperature Range from −125 °C to 400 °C. *Int. J. Thermophys.*, **34** (12), 2343–2350.
5. Huang, X.S., Suzuki, K., Watazu, A., Shigematsu, I., and Saito, N. (2009) Improvement of formability of Mg–Al–Zn alloy sheet at low temperatures using differential speed rolling. *J. Alloys Compd.*, **470** (1–2), 263–268.
6. Huang, X., Bian, M., Nakatsugawa, I., Chino, Y., Sato, M., Yamazaki, K., Kido, F., Ueda, H., and Inoue, M. (2021) Simultaneously achieving excellent mechanical properties and high thermal conductivity in a high Mn-containing Mg–Zn–Ca–Al–Mn sheet alloy. *J. Alloys Compd.*, **887**, 161394.
7. Li, Z.H., Sasaki, T.T., Shiroyama, T., Miura, A., Uchida, K., and Hono, K. (2020) Simultaneous achievement of high thermal conductivity, high strength and formability in Mg–Zn–Ca–Zr sheet alloy. *Mater. Res. Lett.*, **8** (9), 335–340.
8. J.R. Davis, and Davis & Associates. (1993) *Aluminum and aluminum alloys*, ASM International.
9. Bian, M., Nakatsugawa, I., Matsuoka, Y., Huang, X., Tsukada, Y., Koyama, T., and Chino, Y. (2022) Improving the mechanical and corrosion properties of pure magnesium by parts-per-million-level alloying. *Acta Mater.*, **241**, 118393.
10. Tachi, H., Suzuki, K., Huang, X., Tsukada, Y., Koyama, T., and Chino, Y. (2021) Relationship between calculated segregation, texture and room temperature formability of binary magnesium alloys. *J. Japan Inst. Met. Mater.*, **85** (10), 382–390.
11. Chino, Y., Huang, X., Suzuki, K., and Mabuchi, M. (2010) Enhancement of stretch formability at room temperature by addition of Ca in Mg-Zn alloy. *Mater. Trans.*, **51** (4), 818–821.
12. Chino, Y., Huang, X., Suzuki, K., Sassa, K., and Mabuchi, M. (2010) Influence of Zn concentration on stretch formability at room temperature of Mg–Zn–Ce alloy. *Mater. Sci. Eng. A*, **528** (2), 566–572.
13. Chino, Y., Sassa, K., and Mabuchi, M. (2009) Texture and stretch formability of a rolled Mg–Zn alloy containing dilute content of Y. *Mater. Sci. Eng. A*, **513–514**, 394–400.
14. Bian, M., Huang, X., Mabuchi, M., and Chino, Y. (2020) Compositional optimization of Mg–Zn–Sc sheet alloys for enhanced room temperature stretch formability. *J. Alloys Compd.*, **818**, 152891.
15. Bian, M., Huang, X., and Chino, Y. (2020) A combined experimental and numerical study on room temperature formable magnesium–silver–calcium alloys. *J. Alloys Compd.*, **834**, 155017.
16. Bian, M., Matsuoka, Y., Huang, X., Ishiguro, Y., Tsukada, Y., Koyama, T., and Chino, Y. (2023) Insights into the microstructures and mechanical properties of magnesium–calcium–transition elements: A combined experimental and simulation study. *Acta Mater.*, **254**, 118958.
17. Hanawalt, J.P. (1942) Corrosion studies of magnesium and its alloys. *Trans. AIME*, **147**, 273–299.

Investigating the Corrosion Response of Cast and Extruded ZK60 Magnesium Alloy Processed via Shear Assisted Processing and Extrusion

V. Beura, A. Sharma, S. Sharma, V. Joshi, and K. N. Solanki

Abstract

An increase in demand for high-strength and corrosion-resistant magnesium alloys in transportation sectors has driven the development of new processing techniques. Towards this, in this work, cast and extruded ZK60 magnesium alloys were processed using a novel solid-state process i.e., Shear Assisted Processing and Extrusion (ShAPE). Processing-induced microstructure were characterized using Scanning Electron Microscopy (SEM) and Energy Dispersive Spectroscopy (EDS) techniques, which revealed an extensive refinement in grain size, distribution of solutes (Zn and Zr) and second phases, and overall texture. Comparative corrosion analysis of ShAPE and feedstock alloys was performed using various electrochemical measurements such as potentiodynamic polarization, electrochemical impedance spectroscopy (EIS), and atomic emission spectroelectrochemistry analysis (AESCE) that indicate an improvement in corrosion resistance with ShAPE processing for cast feedstock but not for extruded ZK60. Post-corrosion microstructures were analyzed to elucidate the underlying corrosion mechanism.

Keyword

Cast and extruded ZK60 magnesium alloy • Shear Assisted Processing and Extrusion (ShAPE) • Corrosion

Extended Abstract

Magnesium alloys are widely sought for their high strength to weight ratio, machinability, and low cost in light weight engineering for automotive, aerospace, industrial, and commercial applications [1, 2]. One of these alloys is formed by additions of zinc and zirconium to the balance, commercially known as ZK60. The intended increased mechanical properties, as a result of these additions, are in turn due to the developments in the grain variations, second phase particles, and micro- or nano-scale precipitates etc. However, along with the increased strength in ZK60, high susceptibility of corrosion also comes in play as a result of the second phase particles (MgZn and/or $MgZn_2$) which could either act as galvanic corrosion sites or corrosion blocking sites based on their distribution and quantities. Many studies have shown the involvement of the alloy microstructure and the second phase particles detrimental in deciding the corrosion behavior. Variations in the formation of second phase particles in ZK60 have been extensively investigated in the literature and so are the techniques which could vary the alloy microstructure completely such as heat treatment, solid phase processing, and others.

Recently, an abundance of literature is focusing towards newer processing techniques under the major umbrella of solid phase processing which are constantly re-designed to upgrade the conventional thermo-mechanical processing techniques [1–6]. One of the solid phase processing techniques is Shear Assisted Processing and Extrusion (ShAPE) which has been developed by the co-authors to achieve high extrusion ratio and large output diameter at a more economical rate to the conventional counterparts [3, 7–9]. Various grain size reduction processes like ShAPE have been observed to both improve and deteriorate the corrosion response of the alloys [10–14]. However, the reasoning behind such a behavior against a ShAPE processing technique is not so evident yet. Therefore, it becomes imperative to figure out how the widely used commercial high-strength

---

V. Beura · A. Sharma · S. Sharma · K. N. Solanki (✉)
School for Engineering of Matter, Transport, and Energy, Arizona State University, Tempe, AZ 85287, USA
e-mail: kiran.solanki@asu.edu

V. Joshi
Pacific Northwest National Laboratory, Richland, WA, USA

A. Leonard et al. (eds.), *Magnesium Technology 2024*, The Minerals, Metals & Materials Series,
https://doi.org/10.1007/978-3-031-50240-8_6

ZK60 alloy would behave if processed by ShAPE technique. This study aims to investigate the corrosion response of ZK60 processed by conventional cast and extrusion techniques against the ones processed by an additional post ShAPE technique.

In this work, four processing conditions, namely cast (C), extruded (E), cast followed by ShAPE (C + S) and extruded followed by ShAPE (E + S) were investigated against the corrosion behavior of ZK60 magnesium alloy. All the corrosion measurements were performed on the surface perpendicular to the direction of ShAPE processing and the tests were performed at room temperature in an open air condition and 0.1 M sodium chloride (NaCl) was used as the testing solution. Potentiodynamic polarization experiments were performed on all the samples using a GAMRY Reference 600 Potentiostat. A standard three-cell electrode system was used with SCE as the reference electrode for the electrochemical testing. Surface of the samples was carefully coated by a non-conductive coating such that only the desired area of the sample stays exposed to the solution during experiment and a 1800s open circuit potential was set before initializing the polarization.

It is evident by the results shown in Fig. 1 that changes occur in the fundamental behavior of the alloys after being processed by ShAPE. Adding ShAPE process to either cast or extruded ZK60 results in an improvement in corrosion potential (E_{corr}) and corrosion current density (I_{corr}), but this trend is opposite in the case of cathodic current density (I_{cath}). Another change observed was in terms of the pitting potential ($E_{pitting}$). E_{pit} for cast ZK60 increased after adding ShAPE as a post process but in case of Extruded ZK60, a decline in $E_{pitting}$ can be seen in Fig. 2. We intend to understand this changed behavior further with other electrochemical experiments, spectroscopy, and imaging techniques.

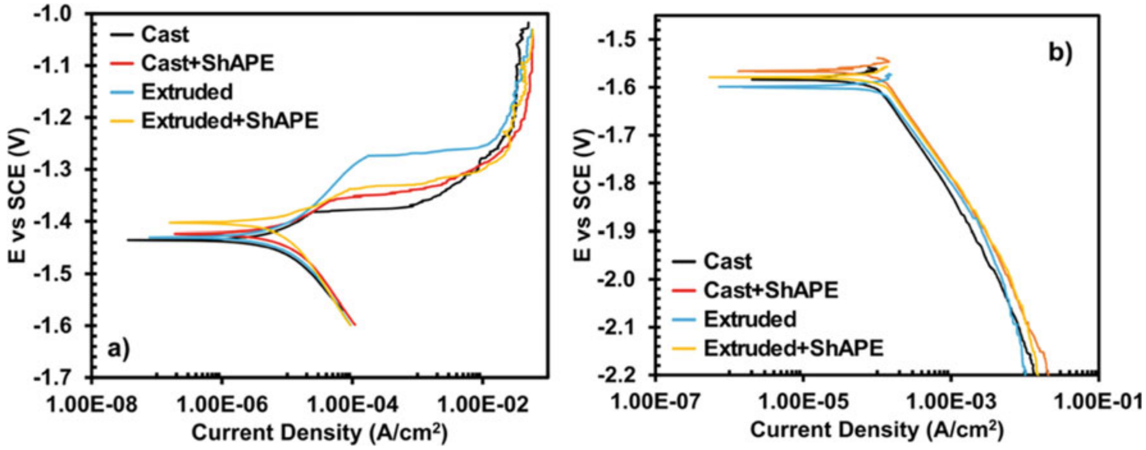

Fig. 1 **a** Anodic and **b** cathodic potentiodynamic polarization curves

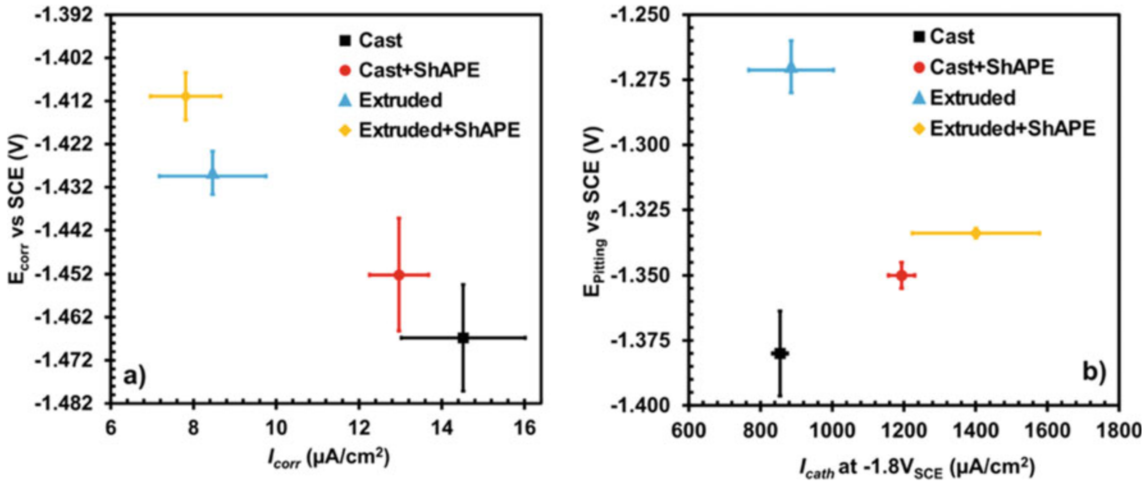

Fig. 2 **a** E_{corr} versus I_{corr} and **b** $E_{pitting}$ versus I_{cath} results from polarization plots

References

1. Huo, W. T., Zhang, W., Lu, J. W. & Zhang, Y. S. Simultaneously enhanced strength and corrosion resistance of Mg–3Al–1Zn alloy sheets with nano-grained surface layer produced by sliding friction treatment. *J. Alloys Compd.* **720**, 324–331 (2017).
2. Song, D. *et al.* Simultaneously improving corrosion resistance and mechanical properties of a magnesium alloy via equal-channel angular pressing and post water annealing. *Mater. Des.* **166**, 107621 (2019).
3. Darsell, J. T., Overman, N. R., Joshi, V. V., Whalen, S. A. & Mathaudhu, S. N. Shear Assisted Processing and Extrusion (ShAPE^{TM}) of AZ91E Flake: A Study of Tooling Features and Processing Effects. *J. Mater. Eng. Perform.* **27**, 4150–4161 (2018).
4. Liu, Q. *et al.* Enhanced corrosion resistance of AZ91 magnesium alloy through refinement and homogenization of surface microstructure by friction stir processing. *Corros. Sci.* **138**, 284–296 (2018).
5. Nazeer, F., Long, J., Yang, Z. & Li, C. Superplastic deformation behavior of Mg alloys: A-review. *J. Magnes. Alloys* **10**, 97–109 (2022).
6. Bahmani, A., Arthanari, S. & Shin, K. S. Improved corrosion resistant and strength of a magnesium alloy using multi-directional forging (MDF). *Int. J. Adv. Manuf. Technol.* **105**, 785–797 (2019).
7. Whalen, S. *et al.* Magnesium alloy ZK60 tubing made by Shear Assisted Processing and Extrusion (ShAPE). *Mater. Sci. Eng. A* **755**, 278–288 (2019).
8. Whalen, S. *et al.* Scaled-Up Fabrication of Thin-Walled ZK60 Tubing Using Shear Assisted Processing and Extrusion (ShAPE). in *Magnesium Technology 2017* (eds. Solanki, K. N., Orlov, D., Singh, A. & Neelameggham, N. R.) 315–321 (Springer International Publishing, 2017). https://doi.org/10.1007/978-3-319-52392-7_45.
9. Beura, V. *et al.* Enhanced mechanical behavior and corrosion resistance of AZ31 magnesium alloy through a novel solid-phase processing. *Corros. Sci.* **197**, 110074 (2022).
10. Song, D. *et al.* Corrosion behaviour of bulk ultra-fine grained AZ91D magnesium alloy fabricated by equal-channel angular pressing. *Corros. Sci.* **53**, 362–373 (2011).
11. Alvarez-Lopez, M. *et al.* Corrosion behaviour of AZ31 magnesium alloy with different grain sizes in simulated biological fluids☆. *Acta Biomater.* **6**, 1763–1771 (2010).
12. Aung, N. N. & Zhou, W. Effect of grain size and twins on corrosion behaviour of AZ31B magnesium alloy. *Corros. Sci.* **52**, 589–594 (2010).
13. Birbilis, N., Ralston, K. D., Virtanen, S., Fraser, H. L. & Davies, C. H. J. Grain character influences on corrosion of ECAPed pure magnesium. *Corros. Eng. Sci. Technol.* **45**, 224–230 (2010).
14. Song, D. *et al.* Corrosion behavior of equal-channel-angular-pressed pure magnesium in NaCl aqueous solution. *Corros. Sci.* **52**, 481–490 (2010).

Corrosion Rates by Immersion and Calorimetry on the Example of Extruded Mg10Gd(1Nd)1La

Petra Maier, Benjamin Clausius, Thea-Simone Tegtmeier, Lars Wadsö, and Dmytro Orlov

Abstract

This study is a follow-up investigation of the influence of the alloying elements Nd and La on the corrosion by immersion of an extruded and heat-treated Mg10Gd. The previous study made clear that the age-hardened condition has the lowest corrosion rate but high pitting corrosion susceptibility. The extruded Mg10Gd(1Nd) 1La shows the lowest pitting factors based on severe corrosion. In this study, the corrosion morphology and corrosion rates are discussed based on calorimetric data and 3D-analysis by µCT and compared to the results from the immersion tests. Thermal power and enthalpy readings from the isothermal calorimetry offer information on the reaction kinetics. The corrosion rate values are discussed based on the evaluation method—in general agreement alloying with Nd reduces the corrosion rate. The pitting factor is found to be very dependent on the reference average penetration: weight or volume loss, or evaluation by 3D volume or by 2D cross-sections.

Keywords

Mg-Gd alloys • Corrosion rate • Immersion • Calorimetry

Extended Abstract

This study is a follow-up investigation of the influence of the alloying elements Nd and La on the corrosion by immersion of an extruded and heat-treated Mg10Gd [1]. Mg10Gd1Nd is considered as a potential candidate for biodegradable implant materials, and La is being investigated as a substitute alloying element [1, 2]. The most widely used techniques for exploring the corrosion behavior of Mg alloys involve immersing the samples in a corrosive solution [3]. The previous study in [1] made clear that the age-hardened condition has the lowest corrosion rate (CR) but high pitting corrosion susceptibility, when corroding in Ringers Solution at 37 °C over 168 h (sample size: 10 mm in diameter and 7 mm of height, 500 ml of electrolyte). The as-extruded alloys Mg10Gd1Nd and Mg10Gd1Nd1La show the lowest pitting factors (PF) based on severe corrosion, see Fig. 1. In general, severe pitting corrosion should be prevented during alloy development, as corrosion pits can lead to stress increase and thus to premature failure. Mg10Gd1La has with 36.67 mm/a the highest CR and a PF of 2.0. The addition of Nd reduced the CR slightly to 29.99 mm/a; the PF was also found to be rather low at 2.1 [1]. Figure 2 shows the cross-section of corroded Mg10Gd1La1Nd. The white frames indicate the average corrosion, and the deepest pits appearing to be double as deep as the average corrosion. The pits are wide and shallow and start overlapping during progressing corrosion.

In this study, the corrosion morphology and CR are discussed based on isothermal calorimetry, see [4] for methodology, and 3D-analysis by µCT and compared to the results from the immersion tests presented in Figs. 1 and 2 and repeated immersion tests with the same volume of electrolyte as in calorimetric measurements, 17 ml, as well as the same sample size of 1 mm height and 10 mm diameter. The measurement of pH-values was only done in these additional immersion tests. As seen before in [1], the addition of Nd reduces the CR from approx. 50 mm/a to approx. 27 mm/a (Fig. 3a). Thermal power and enthalpy readings from the isothermal calorimetry offer information on the reaction kinetics. As seen for the CR, the addition of Nd lowers the thermal power release, which is increasing over 24 h (Fig. 3b). The thermal power values are normalized by

---

P. Maier (✉) · B. Clausius · T.-S. Tegtmeier
School of Mechanical Engineering, University of Applied Sciences Stralsund, Stralsund, Germany
e-mail: petra.maier@hochschule-stralsund.de

P. Maier · L. Wadsö · D. Orlov
Department of Engineering Sciences, Lund University, Lund, Sweden

A. Leonard et al. (eds.), *Magnesium Technology 2024*, The Minerals, Metals & Materials Series,
https://doi.org/10.1007/978-3-031-50240-8_7

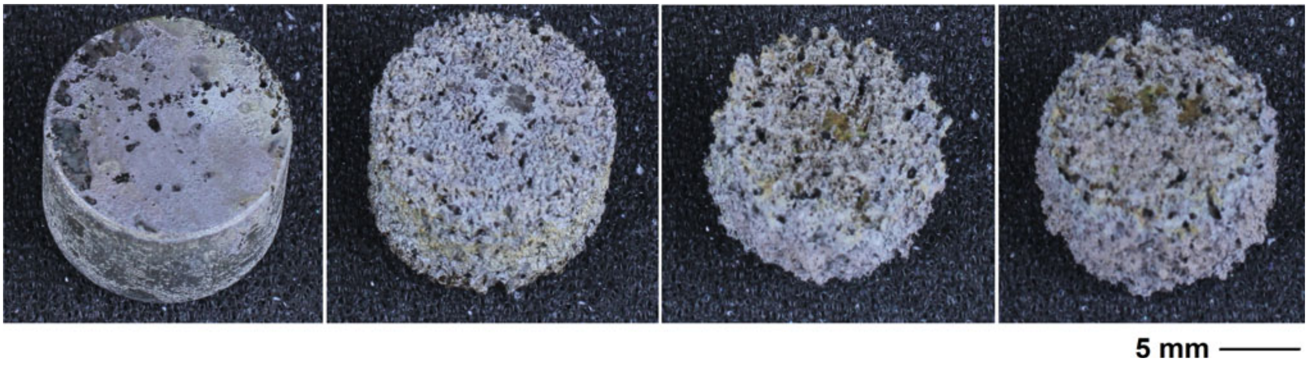

Fig. 1 Photograph of samples after immersion over 168 h: **a** Mg10Gd, **b** Mg10Gd1Nd, **c** Mg10Gd1La, and **d** Mg10Gd1La1Nd

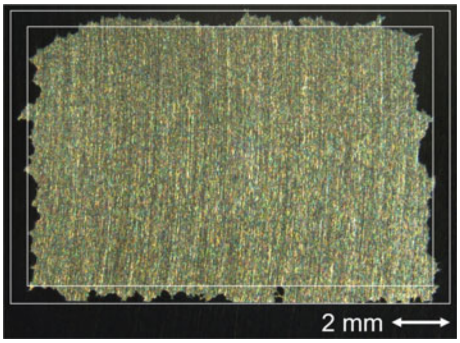

Fig. 2 Cross-section of corroded Mg10Gd1La1Nd

the surface area, but the sample of the largest area (brown curve) stands out. The pH-value (see Fig. 3c) reaches the highest value between 7 and 8 h, decreases, but stays above 10. It seems that the CR in agreement with the reaction kinetics increases to a higher level when the pH-value reaches its maximum. The enthalpy values (Fig. 3d) are unexpectedly low, the reaction Mg to $Mg(OH)_2$ produces approximately 350 kJ/mol in 0.9% NaCl. Whether the lower enthalpy is a result of using Ringer's solution and therefore more compounds than just $Mg(OH)_2$ will form compared to pure Mg needs to be discussed. A protective layer from passivated corrosion products reduces the interaction between electrolyte and corroding sample and therefore might reduce the enthalpy values re-calculated from hydrogen evolution rate and heat release in this study.

Figure 4 shows µCT images and cross-sectional micrographs of the Mg10Gd1La1Nd and Mg10Gd1La samples after removing the corrosion product either by segmentation or by chromic acid during metallographic preparation. Both have been applied to calculate the corrosion rate, by volume loss and by weight loss, respectively. Both alloys show strong pitting—in contrast to the immersion tests with a much higher volume of electrolyte in [1], which kept the pH-value below 8.5. Also interesting is that the upper surface (Fig. 4c, e) of the samples hardly shows corrosion pits, even the corrosion product, which is known from [1] not to remain attached, cannot fall off. This has been seen differently in [5], where underneath loose corrosion product on the upper sample surface the deepest pits form. The hydrogen bubbles forming all-around the sample are expected to cause this behavior. They might shelter large parts of the surface, allowing local corrosion.

The CR values are shown based on each evaluation method in Fig. 5. In general agreement with the results from [1], it can be seen that alloying with Nd reduces the corrosion rate, 4 of 6 CR values support this statement, see also Table 1. How good the methods will determine the difference in CR will be discussed in the following.

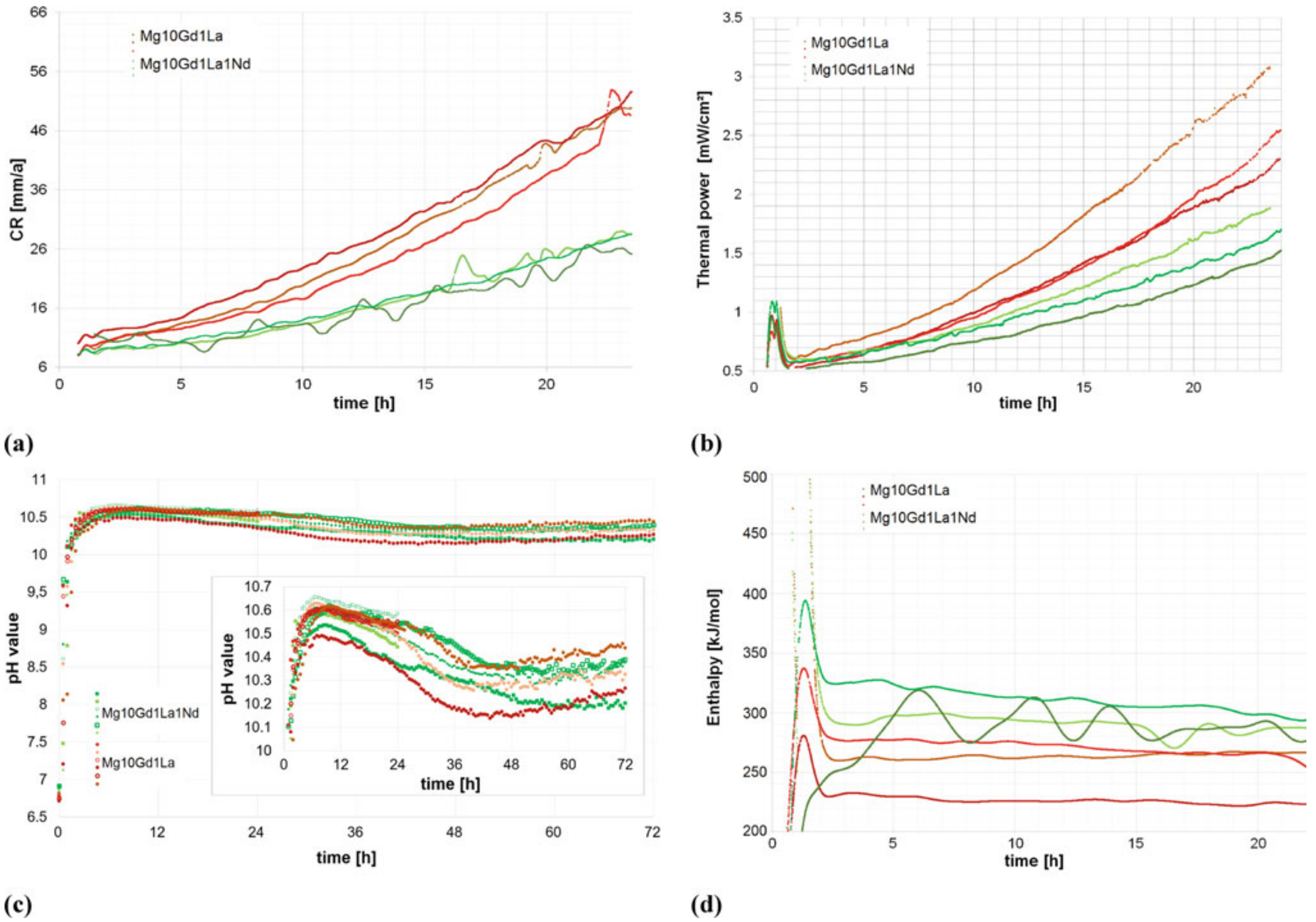

Fig. 3 **a** CR by hydrogen development/isothermal calorimetry over 24 h, **b** thermal power by isothermal calorimetry over 24 h, **c** ph-value development during immersion and **d** enthalphy by isothermal calorimetry over 24 h

The most significant difference can be seen by hydrogen evolution (calorimetry), the CR_{cal24} of Mg10Gd1La shows the highest value. However, evaluating the same samples by weight loss or volume loss, the results differ. The CR by weight loss CR_{cal24_WL} shows a small difference and much smaller values, and the CR by volume loss by segmentation grey values in 3D-µCT analysis CR_{cal24_VL} shows no difference. The sample size of 1 mm height and 10 mm diameter is too small to get meaningful values for weight loss after 24 h—the values do not differ much and are very small compared to all other results, and segmentation of µCT slides is not conclusive; however, these values are much higher. The repeated immersion tests underline the conclusion that the calculation of the CR by weight loss is not accurate enough at small sample weight and short times, the $CR_{imm17/24\_WL}$ is even higher for Mg10Gd1La1Nd. After 72 h, the higher CR of Mg10Gd1La can be picked up: $CR_{imm17/72\_WL}$ is almost double as high—the same as has been seen for CR_{cal24}. Immersion over 168 h (CR_{imm168_WL} of Mg10Gd1La1Nd close to CR by hydrogen evolution CR_{cal24} and CR_{imm168_WL} of Mg10Gd1La close to the CR_{cal24_VL}) shows a difference in CRs, allowing to say that alloying Nd reduces the CR, but the difference is smaller than for CR_{cal24_WL}. That shows that calculating the CR from hydrogen evolution in isothermal calorimetry is an adequate method which already allows to discuss CR in an early stage of corrosion, after 24 h. The micrographs in Fig. 4 clearly show a higher PF than 2. PF up to 10 can be seen along the circumference and up to 5 on the bottom surface areas. For determining the corrosion morphology larger samples sizes and higher electrolyte volume are recommended, here the values in [1] give a more appropriate statement on the pitting resistivity, coming back to the conclusion that higher corrosion rates due to a less protective corrosion layer, and therefore, overlapping pitting corrosion leads to smaller PFs.

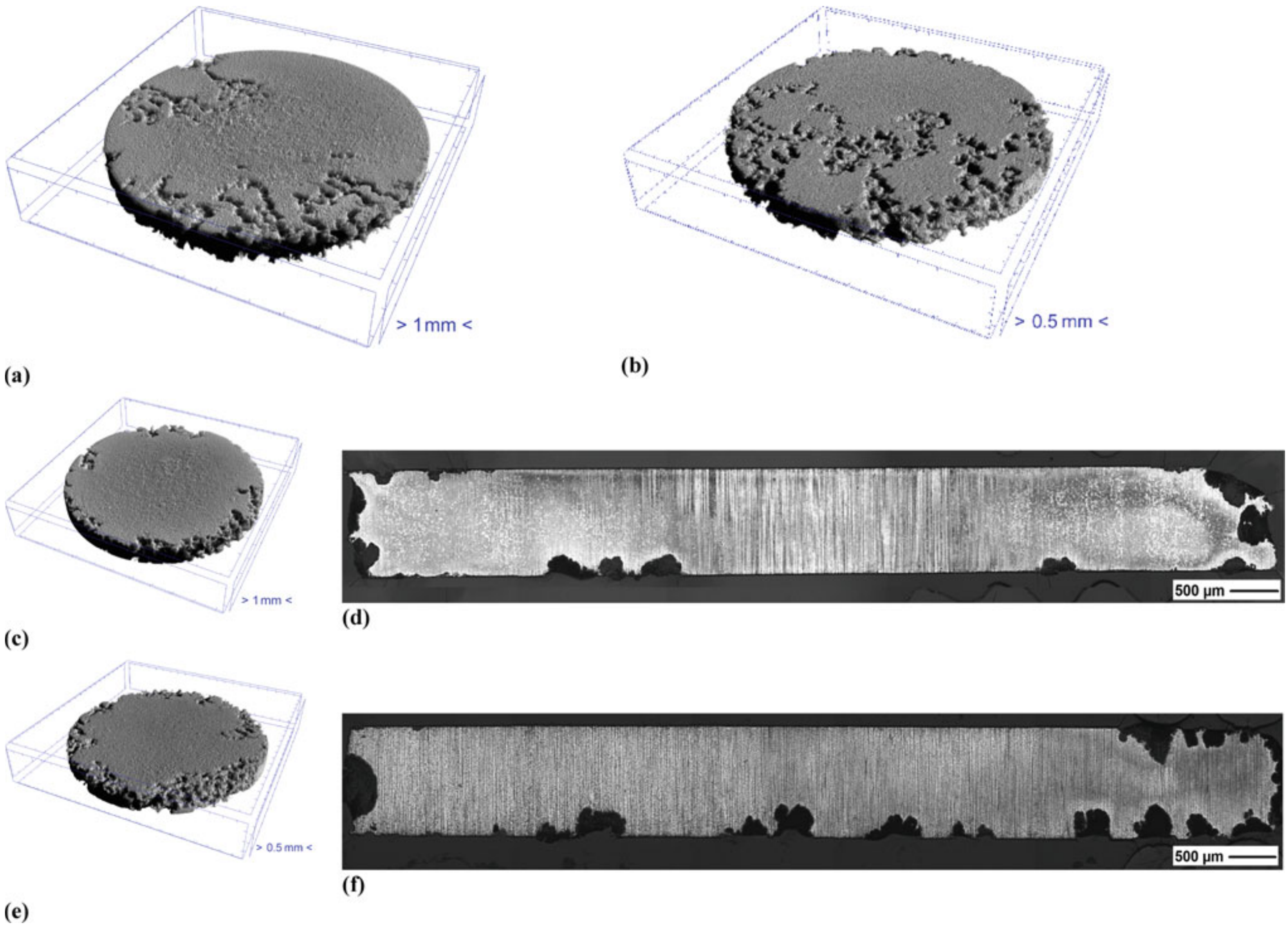

Fig. 4 µCT analysis (**a**, **b**, **c**, **e**) and cross-sectional micrographs (**d**, **f**) of Mg10Gd1La1Nd (**a**, **c**, **d**) and Mg10Gd1La (**b**, **e**, **f**)

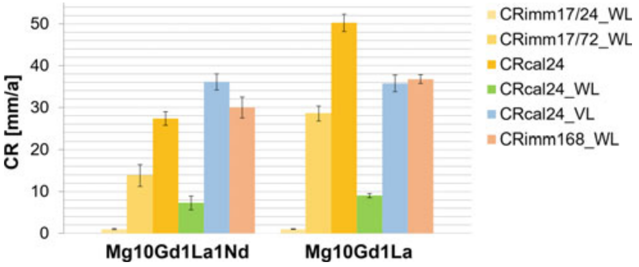

Fig. 5 CRs of various methods ($CR_{imm17/24\_WL}$: immersion in 17 ml over 24 h, weight loss, $CR_{imm17/72\_WL}$: immersion in 17 ml over 72 h, weight loss, CR_{cal24}: in calorimeter in 17 ml over 24 h, hydrogen evolution, CR_{cal24_WL}: in calorimeter in 17 ml over 24 h, weight loss, CR_{cal24_VL}: in calorimeter in 17 ml over 24 h, volume loss, CR_{imm168_WL}: immersion in 500 ml over 168 h, weight loss)

Table 1 Comparison of the two alloys in terms of CR

Method	Comparison			Conclusion
$\mathrm{CR}_{\mathrm{imm17/24\_WL}}$	Mg10Gd1La1Nd	>	Mg10Gd1La	Mg10Gd1La1Nd < Mg10Gd1La
$\mathrm{CR}_{\mathrm{imm17/72\_WL}}$	Mg10Gd1La1Nd	<	Mg10Gd1La	
$\mathrm{CR}_{\mathrm{cal24}}$	Mg10Gd1La1Nd	<	Mg10Gd1La	
$\mathrm{CR}_{\mathrm{cal24\_WL}}$	Mg10Gd1La1Nd	<	Mg10Gd1La	
$\mathrm{CR}_{\mathrm{cal24\_VL}}$	Mg10Gd1La1Nd	∼=	Mg10Gd1La	
$\mathrm{CR}_{\mathrm{imm168\_WL}}$	Mg10Gd1La1Nd	<	Mg10Gd1La	

References

1. Willumeit, R., Möhring, A., Feyerabend, F. Optimization of Cell Adhesion on Mg Based Implant Materials by Pre Incubation under Cell Culture Conditions. Int. J. Mol. Sci. 2014, 15, 7639–7650.
2. Maier, P. et al. (2018) Precipitation hardening on mechanical and corrosion properties of extruded Mg10Gd modified with Nd and La. Metals 8 (640).
3. Esmaily, M. et al. (2017) Fundamentals and advances in magnesium alloy corrosion, Progress in Materials Science, 89, 92–193.
4. Wadsö, L., Orlov, D. (2018). Adding Dimensions to the Immersion Testing of Magnesium Corrosion. Magnesium Technology 2018. The Minerals, Metals & Materials Series. Springer, Cham., 31–36.
5. Maier, P., Gentzsch, L., Hort, N. (2017). Voltammetric Studies of Extruded Pure Magnesium in Different Electrolytes and Its Corrosion Morphology. Magnesium Technology 2017. The Minerals, Metals & Materials Series. Springer, Cham, 429–437.

Part II

Microstructural Evolution and Phase Transformations

Understanding the Influence of Ca and Zn on the Microstructure and Texture Evolution of Mg-(Ca, Zn) Alloys During Static Recrystallization

Rogine A. Gomez and Aeriel Leonard

Abstract

Magnesium suffers from anisotropy and strong basal texture due to its hexagonal close-packed (HCP) structure. Additionally, twinning acts as the major deformation mode during mechanical loading. Alloying with Ca and Zn has shown to weaken texture and encourage slipping as a deformation mode. In this study, the microstructural and texture evolution of Mg-(Zn, Ca) alloys during static recrystallization were quantified using in-situ heating, EBSD, and electron microscopy. The objective is to understand the influence of Ca and Zn on the twin formation mediation and texture weakening of Mg. SEM and EBSD were utilized to quantify recrystallization behavior and texture, and TEM was used to understand the dislocation structure near and within various twin interfaces. It was determined that binary Mg–Zn retain twinning as a major deformation mode and strong basal texture after static recrystallization while ternary Mg–Ca–Zn exhibit slipping and weaker texture after static recrystallization.

Keywords

Magnesium alloys • Recrystallization • Microstructure • Texture

Extended Abstract

Magnesium is the lightest structural metal on earth and it is renowned for its excellent mechanical properties, high strength-to-weight ratio, and good castability [1]. However, its hexagonal close-packed (HCP) structure brings intrinsic anisotropy that causes poor low-temperature formability [1]. This is due to the limited slip systems, which results in twinning as the major deformation mode [2]. These deformation twins play a significant role in the nucleation and growth mechanisms that occur during recrystallization (RX). Recent studies have shown that interfaces associated with deformation twins serve as preferred nucleation sites of strain-free grains as they hinder dislocation motion during thermo-mechanical processing [3–5].

Texture weakening through alloying can improve low-temperature formability and ductility. Due to the low CRSS of basal slip, most Mg alloys develop a strong basal texture during thermo-mechanical processing that can be retained during subsequent heat treatments or static recrystallization (SRX). Recently, Mg alloys that contain both Ca and Zn show great promise in weakening the strong basal texture [6–8]. In this study, binary alloy Mg–2Zn (wt%) and ternary Mg–2Zn–0.5Ca (wt%) were studied to understand the influence of Ca and Zn on the mechanisms of deformation, crystallographic texture formation, and nucleation and growth of strain-free grains during SRX. The microstructural and texture evolution was quantified using quasi-in-situ heating experiments that combined both electron backscatter diffraction (EBSD) and scanning electron microscopy imaging. Transmission electron microscopy was used to characterize the interactions between dislocations and boundaries associated with crystallographic grains and deformation twins.

The Mg–2Zn and Mg–2Zn–0.5Ca alloys were provided by CanMet materials in the form of extruded rods. The Mg–2Zn rod was extruded from a cast billet that is 85 mm in diameter at 413 ºC at 63.5 mm/min to a final diameter of 15 mm. The Mg–2Zn–0.5Ca rods were extruded from a cast billet that is 85 mm in diameter at 350 °C at 63.5 mm/min. A solution treatment process was employed for the alloys to ensure homogenization of Zn and Ca contents into the material. The Mg–2Zn alloy was solution treated at 350 °C

R. A. Gomez (✉) · A. Leonard
The Ohio State University, Columbus, OH 43210, USA
e-mail: gomez.370@osu.edu

A. Leonard
e-mail: leonard.649@osu.edu

A. Leonard et al. (eds.), *Magnesium Technology 2024*, The Minerals, Metals & Materials Series,
https://doi.org/10.1007/978-3-031-50240-8_8

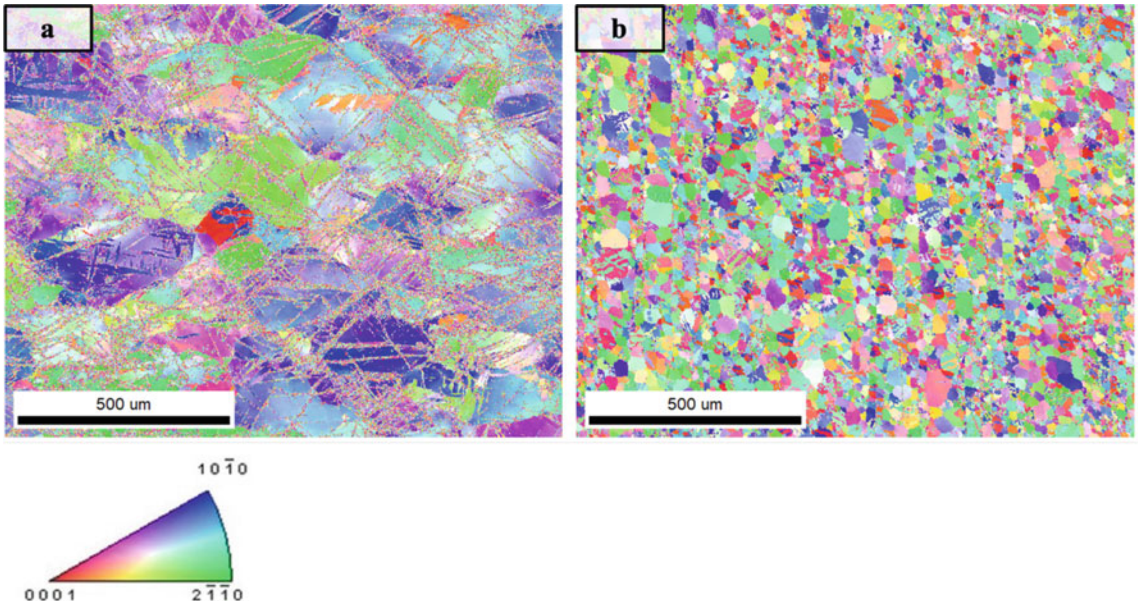

Fig. 1 IPF maps of as-compressed **a** Mg–2Zn and **b** Mg–2Zn–0.5Ca

for 4 h, and the Mg–2Zn–0.5Ca alloy was solution treated at 375 °C for 6 h. After solution treatment, the rods were water-quenched to retain the homogenized microstructure.

Room-temperature, uniaxial, compressive loading was performed along the working direction to initiate deformation twinning in the material. Figure 1 shows the microstructure of Mg–2Zn and Mg–2Zn–0.5Ca after deformation. It was found that twinning was a major deformation mode in Mg–2Zn. It was determined that {10–12} extension twins are the most prevalent twinning system in this alloy as characterized by the orientation of the basal poles 90º from the compression direction. These twins formed to accommodate for the c-axis extension of the crystal [9]. On the other hand, Mg–2Zn–0.5Ca exhibited basal dislocation slip as the predominant deformation mode. Although {10–12} extension twins are present, they do not contribute significantly to the deformation behavior of this material given their smaller area fraction. While Mg–2Zn showed that 60% of the scanned area consisted of twins, Mg–2Zn–0.5Ca exhibited only 3%. This behavior suggested that alloying with Ca and Zn can reduce twin formation, making basal dislocation slip as the predominant deformation mode for Mg alloys [10, 11].

After room-temperature deformation, ex-situ annealing was performed to determine appropriate time and temperature parameters for in-situ SEM heating experiments. At 350 °C, RX is instantaneous where late-stage RX can be observed as early as 30 s. This indicates that this temperature is sufficient in consuming deformed grains and driving RX.

In-SEM heating experiments were performed to determine preferred nucleation sites and their effect on the crystallographic texture evolution of the recrystallized grains. Figure 2 shows the microstructural evolution of a grain in Mg–2Zn. It can be observed that newly recrystallized grains preferentially nucleated along grain boundaries and twins. Additionally, as RX proceeded, the strong basal texture formed during deformation was retained throughout the RX process.

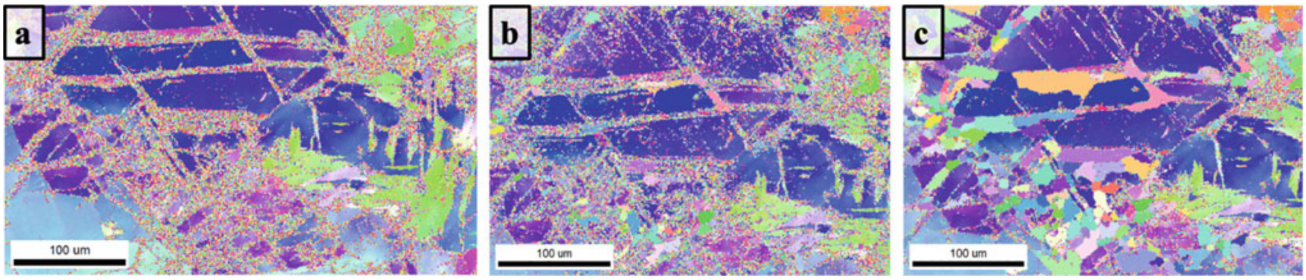

Fig. 2 IPF maps of Mg–2Zn showing nucleation and early-stage recrystallization occurring within twins and grain boundaries during in-situ heating

In Mg–2Zn–0.5Ca, it was determined that triple junctions and twin-grain boundary interfaces serve as preferred nucleation sites. With Ca addition, the recrystallized texture exhibits a large angle distribution, indicating a wider spread in the crystallographic orientation and a weaker overall texture [11, 12]. Combining Ca and Zn in Mg alloys shows potential in reducing twin formation during deformation and weakening the basal texture during SRX.

References

1. Powell, B. R., Krajewski, P. E., & Luo, A. A. (2021). Magnesium alloys for lightweight powertrains and automotive structures. *Materials, Design and Manufacturing for Lightweight Vehicles*, 125–186. https://doi.org/10.1016/b978-0-12-818712-8.00004-5
2. Yang, Z., Li, J., Zhang, J., Lorimer, G., & Robson, J. (2008). Review on research and development of magnesium alloys. *Acta Metallurgica Sinica (English Letters)*, *21*(5), 313–328. https://doi.org/10.1016/s1006-7191(08)60054-x
3. Li, L., Liu, W., Qi, F., Wu, D., & Zhang, Z. (2022). Effects of deformation twins on microstructure evolution, mechanical properties and corrosion behaviors in magnesium alloys - a review. *Journal of Magnesium and Alloys*, *10*(9), 2334–2353. https://doi.org/10.1016/j.jma.2022.09.003
4. Guan, D., Rainforth, W. M., Ma, L., Wynne, B., & Gao, J. (2017). Twin recrystallization mechanisms and exceptional contribution to texture evolution during annealing in a magnesium alloy. *Acta Materialia*, 126, 132–144. https://doi.org/10.1016/j.actamat.2016.12.058
5. Humphreys, F. J., & Hatherly, M. (2004). *Recrystallization and related annealing phenomena* (2nd ed.). Elsevier
6. Berman, T. D., & Allison, J. E. (2021). Coupling thermomechanical processing and alloy design to improve textures in Mg-Zn-CA Sheet Alloys. JOM, 73(5), 1450–1459. https://doi.org/10.1007/s11837-021-04630-0
7. Su, J., Sanjari, M., Kabir, A. S., Jonas, J. J., & Yue, S. (2016). Static recrystallization behavior of magnesium az31 alloy subjected to high speed rolling. Materials Science and Engineering: A, 662, 412–425. https://doi.org/10.1016/j.msea.2016.03.047
8. Guan, D., Liu, X., Gao, J., Ma, L., Wynne, B. P., & Rainforth, W. M. (2019). Exploring the mechanism of "rare earth" texture evolution in a lean mg–zn–ca alloy. *Scientific Reports*, *9*(1). https://doi.org/10.1038/s41598-019-43415-z
9. Russell, W. D., Bratton, N. R., Paudel, Y., Moser, R. D., McClelland, Z. B., Barrett, C. D., Oppedal, A. L., Whittington, W. R., Rhee, H., Mujahid, S., Paliwal, B., Vogel, S. C., & El Kadiri, H. (2020). In Situ Characterization of the Effect of Twin-Microstructure Interactions on {1 0 1 2} Tension and {1 0 1 1} Contraction Twin Nucleation, Growth and Damage in Magnesium. *Metals*, *10*(11), 1403. https://doi.org/10.3390/met10111403
10. Wang, J., Chen, Y., Chen, Z., Llorca, J., & Zeng, X. (2021). Deformation mechanisms of Mg-Ca-Zn alloys studied by means of micropillar compression tests. *Acta Materialia*, *217*, 117151. https://doi.org/10.1016/j.actamat.2021.117151
11. Zheng, R., Bhattacharjee, T., Gao, S., Gong, W., Shibata, A., Sasaki, T., Hono, K., & Tsuji, N. (2019). Change of deformation mechanisms leading to high strength and large ductility in Mg-Zn-Zr-CA alloy with fully recrystallized ultrafine grained microstructures. *Scientific Reports*, *9*(1). https://doi.org/10.1038/s41598-019-48271-5
12. Zeng, Z. R., Zhu, Y. M., Xu, S. W., Bian, M. Z., Davies, C. H. J., Birbilis, N., & Nie, J. F. (2016). Texture evolution during static recrystallization of cold-rolled magnesium alloys. *Acta Materialia*, *105*, 479–494. https://doi.org/10.1016/j.actamat.2015.12.045

Microstructural Evolution Near Microcrack in AZ31 Mg Alloy Under Electropulses

Jinyeong Yu, Seong Ho Lee, Seho Cheon, Mooseong Mun,
Jeong Hun Lee, and Taekyung Lee

Abstract

Electropulsing treatment (EPT) is a novel method utilizing the Joule effect for efficient metal heating. EPT's advantages over traditional furnace methods have led to growing interest, particularly its defect-repair potential at sub-melting temperatures. Our study introduces an alternative EPT process using direct current (DC) for reduced energy consumption and enhanced scalability. The research involves applying square wave pulses with varying current densities to AZ31 magnesium, examining microstructural changes in pre-cracked sheets under EPT. Subsequent fatigue tests induce controlled pre-cracks, revealing localized welding around the cracks post-EPT. The study diverges by proposing a “current detour effect” and a point-wise current source amplifying the Joule effect for defect repair. Observed {10−12} extension twins support the hypothesis, attributed to the compressive stress from EPT. However, calculated thermal compressive stress remains below the CRSS for the {10−12} twin. Distinct recrystallization kinetics, such as continuous static recrystallization, might be influential around the entire crack regions.

Keywords

Magnesium • Electropulsing • Defect repair

Extended Abstract

Electropulsing treatment (EPT) offers an alternative approach to heat metals, utilizing the Joule heating mechanism. EPT has gained significant attention due to its improved energy efficiency and rapid heating capabilities compared to traditional furnace-based heating methods [1, 2]. Recent research has demonstrated its potential to rectify existing defects, even at temperatures below the material's melting point. However, previous studies primarily employed a capacitor discharge technique, which resulted in considerable power consumption [3–6]. In contrast, our study introduces an alternative EPT process using a direct current (DC) power supply, with a focus on reducing power consumption and peak current density, indicating potential for broader industrial applications.

The experimental procedure involved applying square wave pulses to the designated material for five seconds while varying current densities. Our investigation explores the microstructural changes in an as-rolled AZ31 magnesium sheet subjected to the developed EPT regimen. Before EPT application, a high-cycle fatigue test induced a pre-existing crack of approximately 1 mm in length within the sheet sample. The cyclic loading direction was aligned parallel to the material's rolling direction (RD). EPT resulted in noticeable localized welding near the pre-existing crack, occurring notably at a peak temperature of around 523 K, which is below the melting point of magnesium. The ensuing fatigue crack was divided into tip, central, and opening sections, each meticulously examined using SEM and EBSD.

Diverging from previous research, our investigation into pre-existing crack restoration reveals a discontinuous nature, suggesting the activation of distinct healing mechanisms. The primary concept centers around the “current detour effect,” proposing that applied current diverts upon encountering the defect, intensifying Joule heating in proximity to the pre-existing defects, particularly at the crack tip

---

J. Yu · S. H. Lee · S. Cheon · M. Mun · T. Lee (✉)
School of Mechanical Engineering, Pusan National University,
Busan, 46241, Korea
e-mail: taeklee@pnu.edu

M. Mun · J. H. Lee
Advanced Forming Process R&D Group, Korea Institute
of Industrial Technology, Ulsan, 44413, Korea

A. Leonard et al. (eds.), *Magnesium Technology 2024*, The Minerals, Metals & Materials Series,
https://doi.org/10.1007/978-3-031-50240-8_9

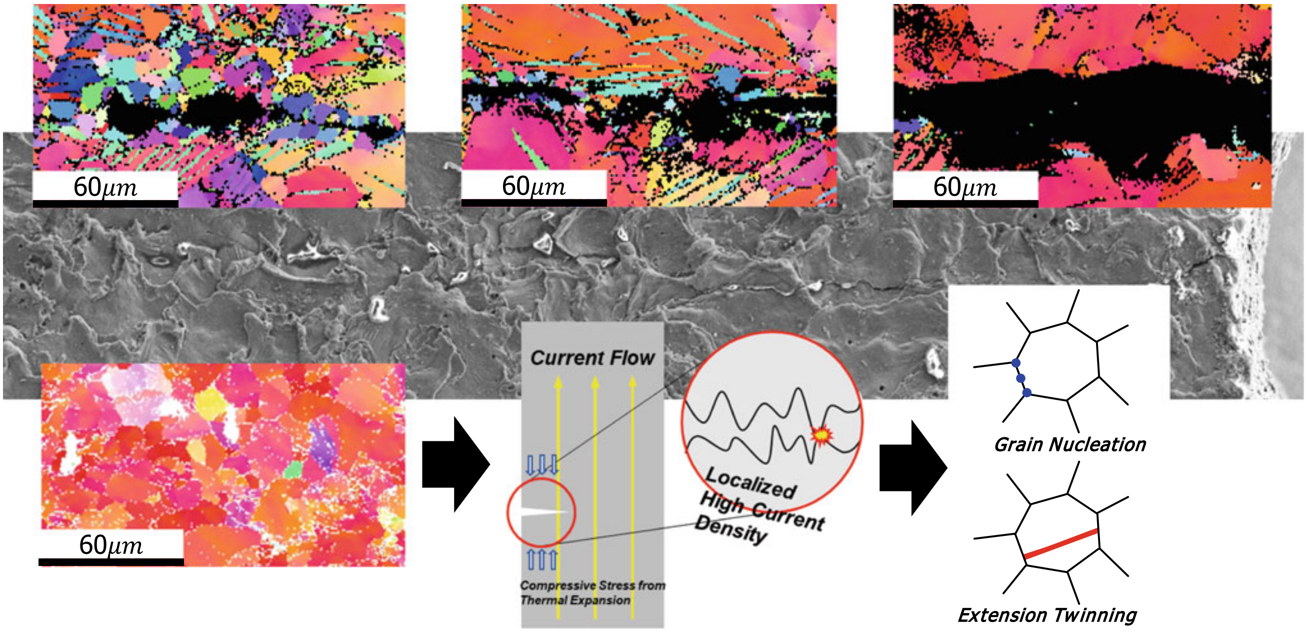

Fig. 1 Schematic illustration of the microstructure evolution process of electropulsing treatment

section. This intensified Joule effect contributes to progressive defect repair. Alternatively, our study suggests the existence of a current source capable of amplifying the Joule effect at localized contact points spread across the entire crack section. The credibility of our hypothesis is substantiated by the observation of {10−12} extension twins within the non-uniform crack region (see Fig. 1). Consistent with the rolled texture and cyclic loading conditions (i.e., the fully reversed pattern applied along the RD), these {10−12} extension twins are prone to form in regions experiencing compressive stress where c-axis extension occurs. The thermal compressive stress arising from the EPT process appears to underlie the genesis of these {10−12} extension twins.

Calculations indicate that the thermal compressive stress generated by the peak temperature of the EPT process (523 K) remains below 10 MPa, a value lower than the critical resolved shear stress (CRSS) for the {10−12} twins [7]. It is also noteworthy that distinct recrystallization kinetics attributed to the compressive stress, such as continuous static recrystallization (CSRX), may be at play in the vicinity of the crack regions [8]. The investigation into recrystallization kinetics was conducted through quasi-in-situ EBSD analysis, by capturing images immediately after the application of individual pulses. Confirmation was provided that each pulse application resulted in the formation of {10−12} twins and the subsequent twin propagation within neighboring grains was also validated.

References

1. M. Lee, J. Yu, M.H. Bae, J.W. Won, T. Lee, Journal of Materials Research and Technology 15 (2021) 5706–5711.
2. J. Yu, M. Lee, Y.H. Moon, Y. Noh, T. Lee, Korean J. Met. Mater. 58(6) (2020) 413–422.
3. D. Ben, H. Yang, Y. Ma, Q. Wang, Y. Tian, P. Zhang, Q. Duan, Z. Zhang, Advanced Engineering Materials 21(7) (2019) 1801345.
4. T. Yu, D. Deng, G. Wang, H. Zhang, Journal of Cleaner Production 113 (2016) 989–994.
5. Y. Zhou, J. Guo, M. Gao, G. He, Materials Letters 58(11) (2004) 1732–1736.
6. H. Song, Z.-J. Wang, X.-D. He, J. Duan, Scientific Reports 7(1) (2017) 7097.
7. N.M. Della Ventura, S. Kalácska, D. Casari, T.E.J. Edwards, A. Sharma, J. Michler, R. Logé, X. Maeder, Materials & Design 197 (2021) 109206.
8. S.J. Oh, J. Yu, S. Cheon, S.H. Lee, S.-Y. Lee, T. Lee, Journal of Materials Research and Technology 26 (2023) 3322–3331.

Data Science Approach for EBSD Data Processing and Materials Design for Magnesium Alloy

Haoran Yi, Xun Zeng, and Dikai Guan

Abstract

Electron backscatter diffraction method is widely adopted in metal fields. However, despite the abundant data sources, sufficient analysis covering all features is often absent. Especially with the emerging in-situ techniques, data processing is time-consuming, where access to every bit of data is imperative. In this work, a toolkit is developed with the aim of processing EBSD data automatically and efficiently. Two parts of toolkits are developed with Matlab and Mtex. One is used to correlate two maps, with simple implementation, results will generate within few minutes, indicating the grains correlation between two maps. The other correlates a series of in-situ datasets, making each individual grain become trackable. With the assistance of the toolkits, a large dataset containing pixels, digital information, and grains properties through an in-situ process can be created. Thus, the microfeatures and grain behaviors are studied using novel data science methods, especially machine learning and deep learning.

Keyword

Electron backscatter diffraction (EBSD) • Data processing • Magnesium alloy

Extended Abstract

The electron backscatter diffraction (EBSD) technique is extensively utilized for microanalysis in metallurgy field, for its ability of extracting grain features from sample surface. However, despite the abundant information stored in EBSD maps, sufficient analysis covering all data is often absent. Especially with the emerging in-situ [1] and quasi-in-situ [2] methods, data processing becomes time-consuming. In this study, a new approach is investigated aiming to process in-situ EBSD maps comprehensively and efficiently. The result obtained reflects the dataset statistically and provides potential for data science application.

A demonstration is presented here to exhibit this approach clearly, using quasi-in-situ EBSD maps. Figure 1 is the example data of WE43 Mg alloy under different annealing time, sample details, and experimental procedure can be found in reference [3]. Between these two maps, recrystallization and grain growth can be observed but cannot be quantified, because each map contains thousands of grains, which are labelled in chaos. In two maps, a same grain can exhibit different IDs and coordinates, making it challengeable to calibrate manually. In case of multiple in-situ maps, it is extremely difficult to process the data in a statistical way.

A dynamic correlation algorithm is designed to solve the above problem, as shown in Fig. 2. Starting with a manually matched grain, input its IDs from two maps as the initial 'reference', the coordinate difference 'displacement vector' of this grain between two maps is then calculated. The neighbour grains of 'reference' in the first map (EBSD1) is extracted and used to match grains in the second map (EBSD2), within the searching range decided by the 'displacement vector'.

The algorithm is realized by a script toolbox developed with MATLAB and MTEX. Starting with simple inputs (two IDs), the script will begin iterating and renewing the 'reference' and 'displacement vector' dynamically, while

---

H. Yi · X. Zeng · D. Guan (✉)
University of Southampton, University Road,
Southampton, SO171BJ, UK
e-mail: dikai.guan@soton.ac.uk

H. Yi
e-mail: hy1v22@soton.ac.uk

X. Zeng
e-mail: x.zeng@soton.ac.uk

A. Leonard et al. (eds.), *Magnesium Technology 2024*, The Minerals, Metals & Materials Series,
https://doi.org/10.1007/978-3-031-50240-8_10

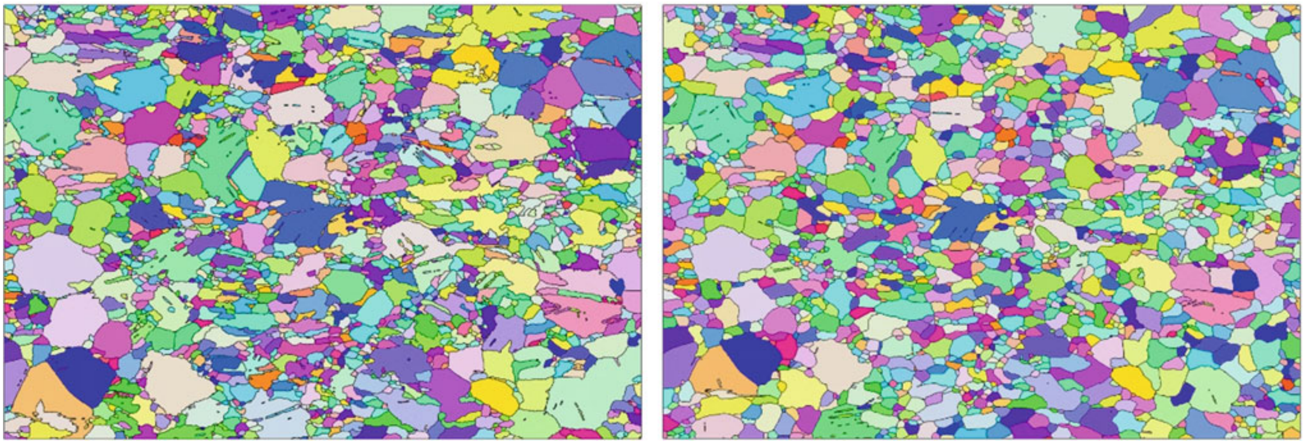

Fig. 1 Cold rolled WE43 Mg alloy under 490 °C annealing for (left) 39 min (right) 90 min [3]

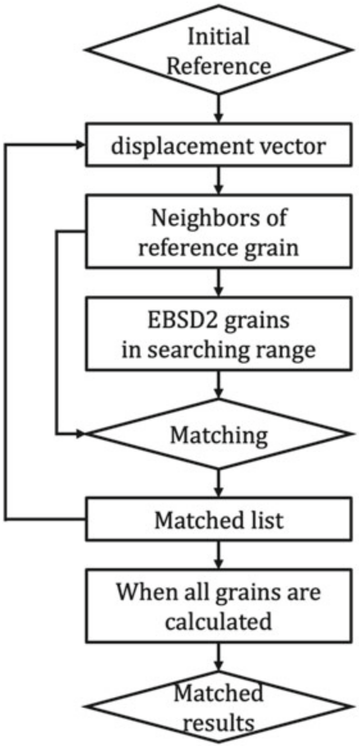

Fig. 2 Dynamic correlation algorithm

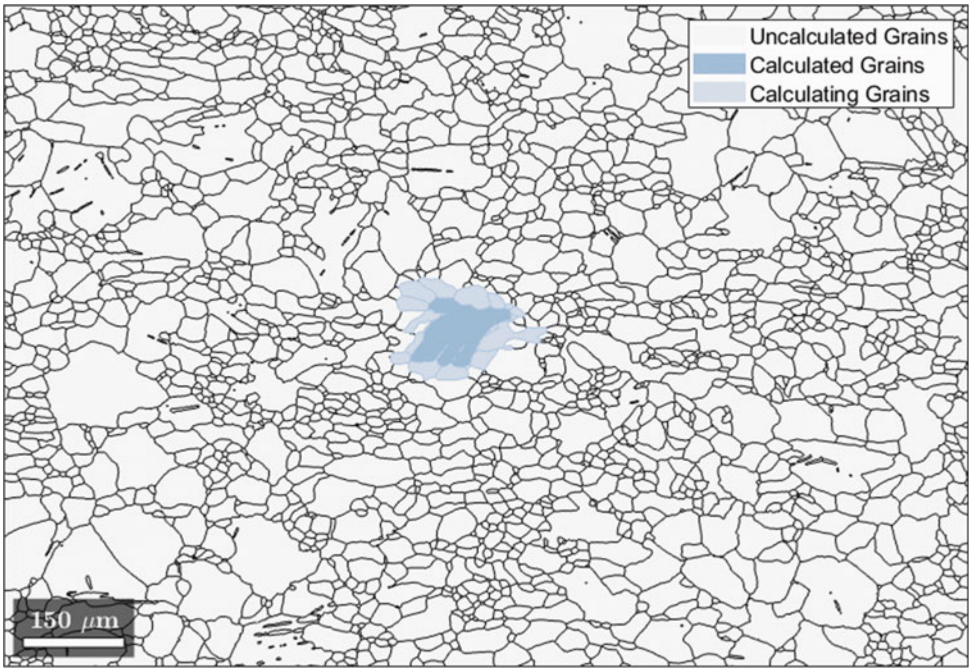

Fig. 3 Calculation process in EBSD1, white for not calculated grains; gray for grains being calculate; blue for grains have been calculated

conducting the correlation. The general workflow has a layer-by-layer structure, and the first layer is the initial input reference grain. Calculation process will finish when all the grains have been included, which normally within 20 min depending on the data size.

Figure 3 is the iterating calculation process of the example WE43 quasi-in-situ data. In this demonstration, approximately five thousand grains were calculated within 15 min, which significantly reduced data processing time. Moreover, the toolbox gave high quality results, with the support of dynamic algorithm.

Figure 4 shows the calculation results. Top row is the correlation result between example maps. All grains here are divided into three groups, which is 'Maintained Grains' that exist in both maps (red colour), 'Consumed Grains' that exist only in EBSD1 (grey colour), 'Newly Formed Grains' that exist only in EBSD2 (blue colour). Since in-situ and quasi-in-situ maps are sequentially arranged in time series, these three groups could reflect the changes between EBSD maps along with time. It is noticeable that some grains with irregular shape might affect their centroid coordinate, and further effect the correlation results. These irregular grains normally have bigger grain size, therefore easy to calibrate manually.

The three groups of grains are stored as subsets to original data, which provides convenience for further analysis. Figure 4 shows the grain size distribution and texture analysis. For maintained grains, size has barely changed between two maps, and the orientation is evolving towards a basal texture. For consumed grains, they tend to have smaller size and randomly distributed orientation comparing with maintained grains in EBSD1. For newly formed grains, their size is much smaller comparing with maintained grains in EBSD2 and exhibit a stronger basal texture. Further to the correlation between two maps, multiple maps can be processed by this approach. Firstly, each two following maps need to be correlated, then implement another specifically developed script which does not require user intervention. Individual grain can be tracked through the dataset. For example, 8 maps are processed and selecting a grain α in stage 3, its IDs in all 8 stages will be given in a time sequence.

In conclusion, the presented approach has proved the capability regarding to the task of processing EBSD data comprehensively and efficiently. The results give a statistical reflection upon the evolution during in-situ and quasi-in-situ experiments. For example, tracking grains behaviour during recrystallisation process within magnesium alloys. With simple implementation, connections can be created throughout multiple EBSD maps, and individual grain become trackable along the heat treatment process. The results here create a dataset containing pixels, digital information, individual grains & their properties, which is inspirational for data science methods like machine learning and deep learning [4–6]. In the presenting work, a deep learning model is under developing, with an objective of predicting 'the next step result' of the in-situ dataset. Suitable algorithms, formats, workflows are under investigating and should be available soon.

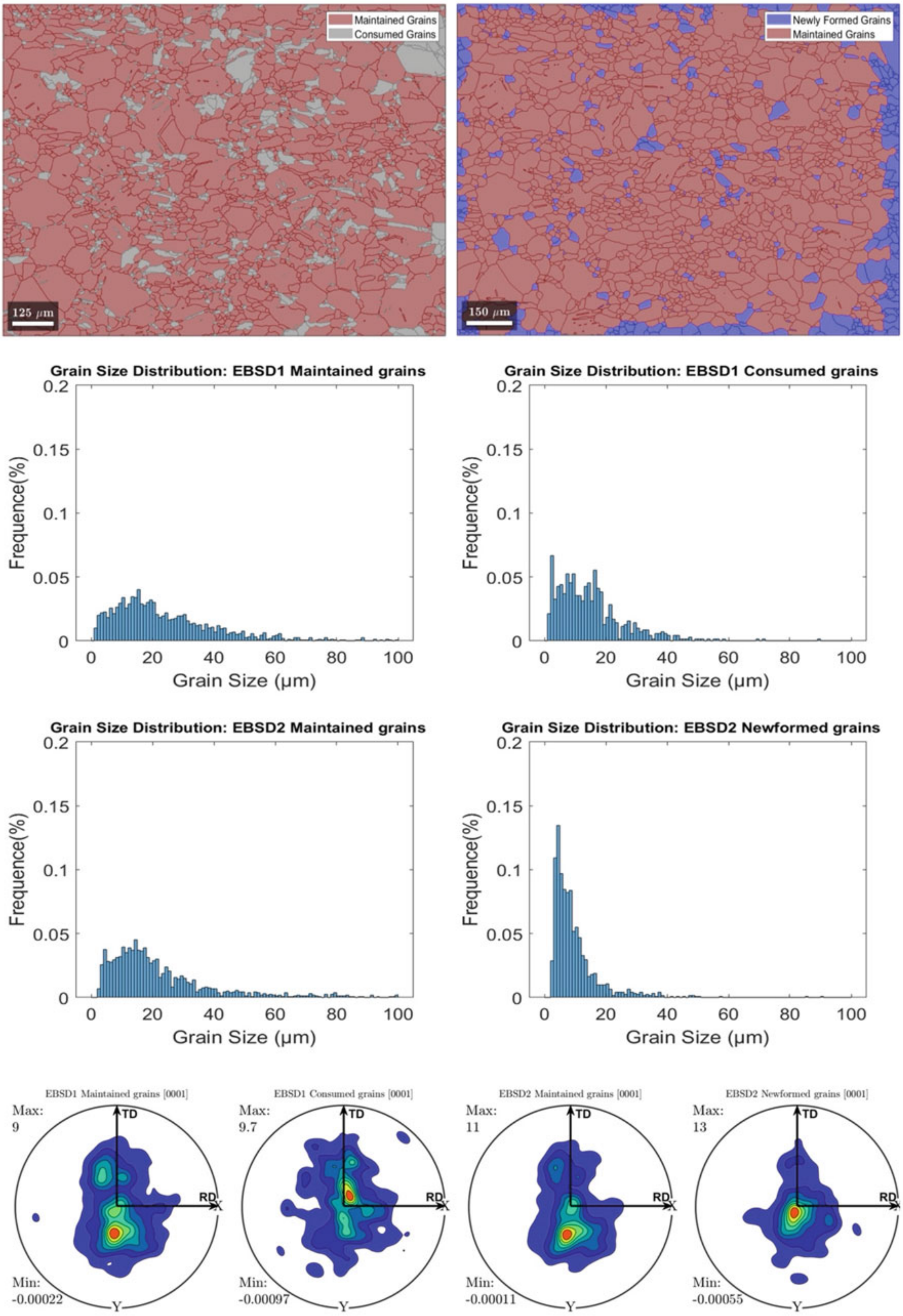

Fig. 4 Calculation results (top left) 39 min annealing (top right) 90 min annealing, different colour indicates different grains type: Consumed Grains; Maintained Grains; Newly formed Grains. Together with grain size distribution and texture evolution

References

1. S. Nagarajan, R. Jain, and N. P. Gurao, 'Microstructural characteristics governing the lattice rotation in Al–Mg alloy using in-situ EBSD', *Mater Charact*, vol. 180, p. 111405, Oct. 2021, doi: https://doi.org/10.1016/j.matchar.2021.111405.
2. Y. Zhu, D. Hou, and Q. Li, 'Quasi in-situ EBSD analysis of twinning-detwinning and slip behaviors in textured AZ31 magnesium alloy subjected to compressive-tensile loading', *Journal of Magnesium and Alloys*, vol. 10, no. 4, pp. 956–964, Apr. 2022, doi: https://doi.org/10.1016/j.jma.2021.08.025.
3. D. Guan, W. M. Rainforth, J. Gao, J. Sharp, B. Wynne, and L. Ma, 'Individual effect of recrystallisation nucleation sites on texture weakening in a magnesium alloy: Part 1- double twins', *Acta Mater*, vol. 135, pp. 14–24, Aug. 2017, doi: https://doi.org/10.1016/j.actamat.2017.06.015.
4. B. Nenchev *et al.*, 'Evaluating data-driven algorithms for predicting mechanical properties with small datasets: A case study on gear steel hardenability', *International Journal of Minerals, Metallurgy and Materials*, vol. 29, no. 4, pp. 836–847, Apr. 2022, doi: https://doi.org/10.1007/s12613-022-2437-0.
5. Y. Chen *et al.*, 'Machine learning assisted multi-objective optimization for materials processing parameters: A case study in Mg alloy', *J Alloys Compd*, vol. 844, Dec. 2020, doi: https://doi.org/10.1016/j.jallcom.2020.156159.
6. Y. Liu *et al.*, 'Accelerated Development of High-Strength Magnesium Alloys by Machine Learning', *Metall Mater Trans A Phys Metall Mater Sci*, vol. 52, no. 3, pp. 943–954, Mar. 2021, doi: https://doi.org/10.1007/s11661-020-06132-1.

Alloy Development, Microstructural, and Mechanical Behaviour of Mg–Ce Based Alloys

Hemant Kumar, Chandra Shekhar Perugu, and Surendra Kumar Makineni

Abstract

Lightweight magnesium (Mg) alloys attract great attention for automotive applications, especially in power train components. It acknowledges the potential of rare earth elements, specifically cerium (Ce), as an alloying addition to enhance the mechanical properties of Mg alloys at both room and high temperatures. However, its precise role is not yet well understood, particularly regarding nano-scale phase transformations, interface-solute segregations, and their effect on mechanical behaviour. To address this knowledge gap, the study focuses on design of Mg–Ce based alloys with further alloying additions of Dy, Gd, and Zr for high temperature applications. More specifically, we investigate the evolution of strengthening metastable and stable precipitates and their influence on their mechanical properties. A thorough microstructural analysis of the alloys using Transmission Electron Microscopy (TEM), and Atom Probe Tomography (APT) will be presented.

Keywords

Magnesium alloys • Mg–Ce based alloys • Transmission electron microscopy • Atom probe tomography

Extended Abstract

Lightweight magnesium (Mg) alloys attract great attention for automotive applications, especially in power train components [1]. It acknowledges the potential of rare earth elements, specifically cerium (Ce), as an alloying addition to enhance the mechanical properties of Mg alloys at both room and high temperatures [2]. However, its precise role is not yet well understood, particularly regarding nano-scale phase transformations, interface-solute segregations, and their effect on mechanical behaviour. Additionally, the literature suggests that dilute Mg–Ce alloys are not precipitation hardenable. To address this knowledge gap, the present work focuses on design of dilute Mg–Ce based alloys with further alloying additions of Dy, Gd, and Zr for high temperature applications. More specifically, we investigate the structural evolution of strengthening metastable and stable precipitates and their influence on their mechanical properties.

Figure 1 shows back-scattered-electron images of extruded Pure Mg and Mg–Ce alloys. It clearly reveals Ce rich bright precipitates distributed mainly along the grain boundaries. These precipitates led to a significant grain refinement as shown through the EBSD maps below respectively. The binary alloy showed and increase in yield strength to ~175 MPa as compared to ~110 MPa for pure Mg also with an increase in ductility by ~10%. Additionally, creep tests reveal a nearly two fold increase in activation energy at 80 MPa of stress with a significant increase in creep life up to 200 °C. The binary alloys found not to be precipitation hardenable on aging at intermediate temperatures. However, with the addition of Dy and Gd, these alloys show extensive hardening on aging at 200 °C [3, 4]. A detailed microstructural analysis by TEM and APT shows partitioning of Dy and Gd along with the Ce to the strengthening precipitates, grain boundaries and twins. The obtained results are discussed based on the measured mechanical and creep properties of the alloys.

H. Kumar · C. S. Perugu · S. K. Makineni (✉)
Materials Engineering, Indian Institute of Science Bangalore, Bangalore, 560012, India
e-mail: skmakineni@iisc.ac.in

A. Leonard et al. (eds.), *Magnesium Technology 2024*, The Minerals, Metals & Materials Series,
https://doi.org/10.1007/978-3-031-50240-8_11

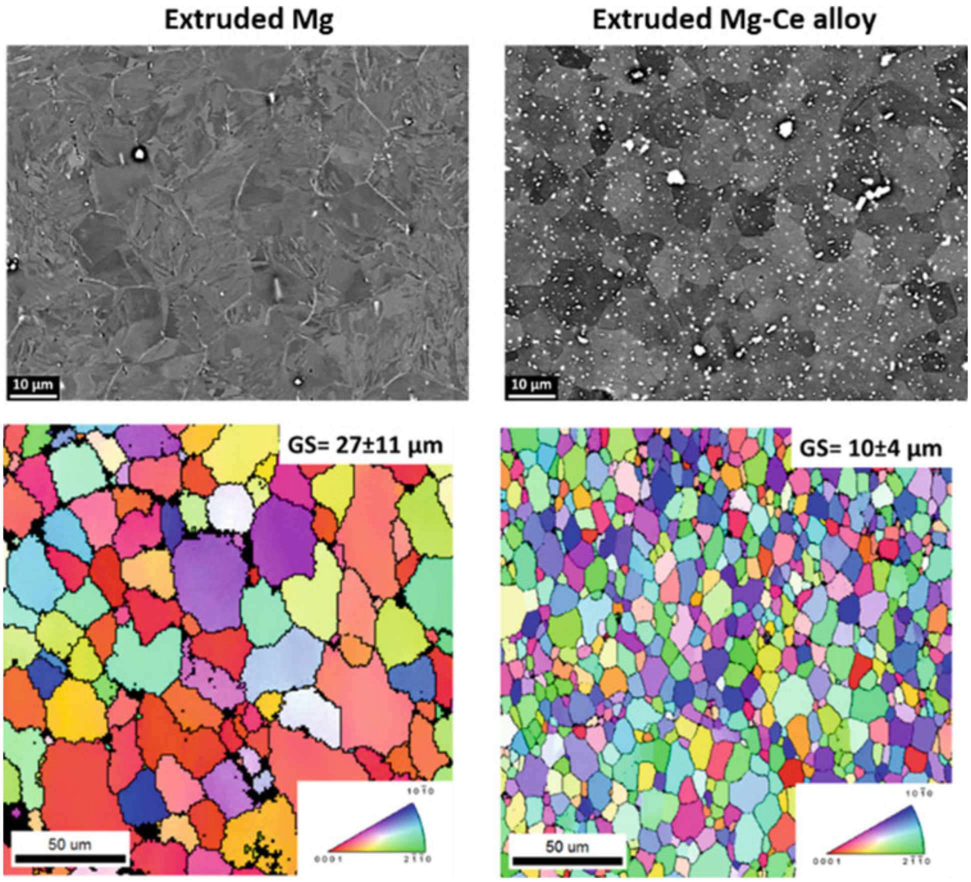

Fig. 1 Comparison of microstructure and grain size of extruded pure Mg and Mg–Ce alloys

References

1. Pollock TM, (2010) Weight loss with magnesium alloys, Science. 328:986–987.
2. Sabat RK, Brahme AP, Mishra RK, Inal K, Suwas S (2018) Ductility enhancement in Mg-0.2% Ce alloys, Acta Materialia. 161:246–257.
3. Saito K, Yasuhara A, Nishijima M, Hiraga K, (2011) Structural changes of precipitates by aging of an Mg-4 at %Dy solid solution studied by atomic-scaled transmission electron microscopy, Materials Transactions. 52:1009–1015.
4. Nishijima M, Hiraga K, (2007) Structural changes of precipitates in an Mg-5at%Gd alloy studied by transmission electron microscopy, Materials Transactions. 48: 10–15.

The Multi-Solute Solid Solution Behaviour of Magnesium Alloys and Their Application on Materials Design

Yuan Yuan, Tao Chen, Xianhua Chen, and Fusheng Pan

Abstract

The low-density magnesium (Mg) alloys are attractive for the application in aerospace, transportation, and other weight-saving-required fields. It is noteworthy that the solid solution of alloying elements in the α-Mg phase can have multi-effects on the properties of Mg alloys, e.g. solid solution strengthening, solid solution corrosion-resistance-enhancing, etc. And it is also notably the functional properties, e.g. damping capacities, magnetic shielding properties can also be tailored by controlling the solution in the matrix. It is promising that by selected proper multi-alloying-elements (with optimal ratio) solid solution in the α-Mg phase, the comprehensive properties of Mg alloys can be synergy improved. In this work, the solid solution behaviour of Mg alloys and the followed solid solution property-enhancing effects were studied. Three types solution behaviour in the ternary magnesium alloy systems were proposed and the application for the materials design for specified functions were proposed.

Keyword

Magnesium alloys • Solution behavior • Materials design

Extended Abstract

The low-density magnesium (Mg) alloys are attractive for the application in aerospace, transportation, and other weight-saving-required fields [1, 2]. Additionally, the magnesium alloys also have some unique properties, such as good biocompatibility and biodegradability, high damping capacity, good magnetic shielding properties and etc., which can provide plus functional properties for the structural applications [3–5]. Therefore, the green, eco-friendly Mg alloys attract a new round of attentions under the zero-CO_2 Policy.

However, the mass production and application of Mg alloys are still quite limited. Firstly, different with Fe alloys or Ti alloys, there is no martensitic phase transformation in Mg alloys and the strength of normally Mg alloys is not so high. Secondly, due to the hpc structure of primary Mg phase and the lack of the slip systems, the low room-temperature formability and ductility of Mg alloys lead a high cost for the manufacture of Mg alloys. Thirdly, the corrosion resistance of Mg alloy is not good enough and the further surface-treatment of the Mg alloys is needed for most of applications [6]. Fourthly, there is always dilemma between the high mechanical property and high functional property for the functional and structural integrated Mg alloys.

Consequently, there are many studies on these aspects and the effects of alloying elements are always the most basic study points. It is noteworthy, as being Mg alloys, the most important phase is inevitably the primary Mg phase. Hence, the solid solution strengthening and softening mechanism [7, 8], solid solution anti-oxidation mechanism [9, 10], solid solution corrosion-resistance-enhancing mechanism [11, 12], are proposed for Mg alloys and also wildly approved and applied in various Mg alloy design, etc. [1]. Additionally, it is also notably, the functional properties, e.g. damping capacities [3], magnetic shielding property, can also be tailored by controlling the alloying element solution in the matrix. To be concluded, the solution and precipitation behavior of alloying elements in Mg alloys are quite fundamental and important for the magnesium alloy design. Based on extensive review, it is found the multi-alloying-element-solution in primary Mg phase may bring cocktail effects and deliver the balanced comprehensive properties [1].

Y. Yuan (✉) · T. Chen · X. Chen · F. Pan
National Engineering Research Center for Magnesium Alloys,
College of Materials Science and Engineering,
Chongqing University, Chongqing, 400044, China
e-mail: yuanyuan17@cqu.edu.cn

T. Chen · X. Chen · F. Pan
Lanxi Magnesium Materials Research Institute,
Lanxi, 321100, China

A. Leonard et al. (eds.), *Magnesium Technology 2024*, The Minerals, Metals & Materials Series,
https://doi.org/10.1007/978-3-031-50240-8_12

Early at 1934, Hume-Rothery [13] has proposed the basic rules of the multi-solution behavior of binary alloys. In this work, the detailed effects of alloying elements on the lattice parameters, inherited chemical and physical properties of primary Mg phase (including lattice distortion, solution energy, work functions, etc.) have been calculated. And the correlation between the alloying elements' features and solubility in primary Mg phase has been proposed [14]. Further, the two different alloying elements solution in the primary Mg phase has been studied, including the element's interactions, the change of the properties of primary Mg phase, and etc. [15]. Specially, the relatively substitution sites of the two different alloying elements have been considering in this calculation, where dozen pair-sites have been selected. It is observed, the similarity of the elements can significantly affect the relatively substitution sites in the lattice.

Based on the above work, the solution behavior of two alloying elements in the primary Mg phase have been thermodynamic calculated, where some of typical systems were also experimental studied. With study on dozens ternary Mg-based systems, it is observed the solution behavior of two alloying elements in the primary Mg phase are with quite typical features. Here the calculated solution curves of Mg–Sc–X ternary systems using current available thermodynamic database TCMg have been selected as the example, as shown in Fig. 1, where the solution curves of Mg–Sc–In, Mg–Sc–Li, and Mg–Sc–Er systems show quite different features. Considering the precision of the database, series alloy experiments have been performed and these solution behavior features have been validated. Combining those typical solution behaviour features and physical relation between varied properties and the matrix, the basic alloy design principles of varied targeted magnesium alloys have been proposed. With the design concept, we designed the ultrahigh damping magnesium alloy [3] and the low degradation rate of Mg–Sr–Y alloy [11].

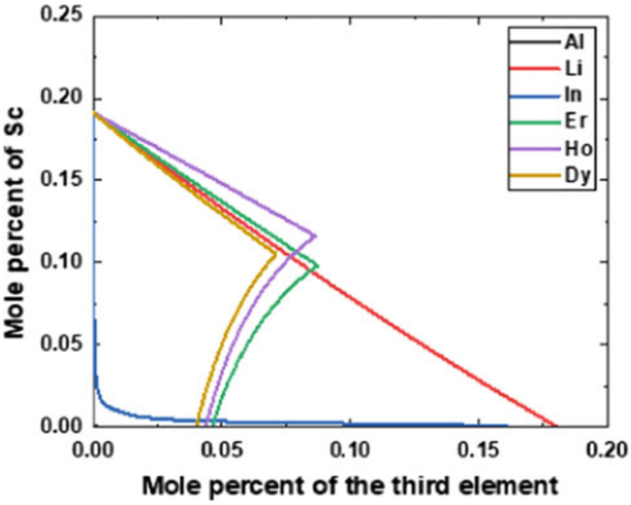

Fig. 1 The solubility curves of primary Mg phase of Mg–Sc-based ternary system at 500 °C

It is promising that by selected proper multi-alloying-elements (with optimal ratio) solid solution in the α-Mg phase, the comprehensive properties of Mg alloys with targeted performance can be synergy improved. The describing of the solution behavior and the proposed material design principles can also be applied into other alloy systems.

Acknowledgements This work is financially supported by National Key R&D Program of China (grant number: 2021YFB3701100) and National Natural Science Foundation of China (grant numbers: 52171100, 51971044, U20A20234, U1910213).

References

1. J. Wang, Y. Yuan, T. Chen, L. Wu, X. Chen, B. Jiang, J. Wang, F. Pan, Multi-solute solid solution behavior and its effect on the properties of magnesium alloys, Journal of Magnesium and Alloys 10(7) (2022) 1786–1820.
2. F. Pan, B. Jiang, J. Wang, Y. Hu, S. Luo, High Plasticity Magnesium Alloys, Elsevier 2022, 1–45.
3. L. Zhang, Y. Yuan, J. Wang, T. Chen, J. Wang, F. Pan, The ultrahigh damping capacity of Mg–Sn–Y alloy, Scripta Materialia 233 (2023) 115514.
4. J. Ye, X. Chen, Z. Luo, J. Li, Y. Yuan, J. Tan, F. Pan, Improving Strength and Electromagnetic Shielding Effectiveness of Mg–Sn–Zn–Ca–Ce Alloy by Sn Addition, Advanced Engineering Materials 23(9) (2021) 2100166.
5. T. Tu, X. Chen, T. Chen, Y. Yuan, F. Pan, New high-modulus and high-strength Mg–Gd–Ag–Mn–Ge alloys, Materials Science and Engineering: A 805 (2021) 140559.
6. Y. Chen, L. Wu, W. Yao, J. Wu, M. Serdechnova, C. Blawert, M. L. Zheludkevich, Y. Yuan, Z. Xie, F. Pan, "Smart" micro/nano container-based self-healing coatings on magnesium alloys: A review, Journal of Magnesium and Alloys (2023) DOI: https://doi.org/10.1016/j.jma.2023.06.006.
7. J. Wang, Y. Yuan, X. Cheng, Y. Li, S. Jiang, T. Chen, A. Tang, L. Wu, J. Wang, F. Pan, First-principle study of the basal-plane stacking fault energies of ternary Mg alloys, Journal of Materials Science 57(39) (2022) 18417–18436.
8. S. Zhou, A. Tang, T. Liu, P. Peng, J. Zhang, J. She, F. Pan, Ductility enhancement by activating non-basal slip in as-extruded Mg alloys with dilute Sc addition, Journal of Materials Research and Technology 22 (2023) 3362-3374.
9. J. Wu, Y. Yuan, L. Yang, T. Chen, D. Li, L. Wu, B. Jiang, M. Steinbrück, F. Pan, The oxidation behavior of Mg-Er binary alloys at 500 °C, Corrosion Science 195 (2022) 109961.
10. J. Wu, Y. Yuan, X. Yu, T. Chen, D. Li, L. Wu, B. Jiang, A. Atrens, F. Pan, The high-temperature oxidation resistance properties of magnesium alloys alloyed with Gd and Ca, Journal of Materials Science 56(14) (2021) 8745–8761.
11. Y. Li, Y. Yuan, J. Wang, L. Wu, F. Cao, L. Zhang, F. Pan, Controllable degradation behavior of Mg-Sr-Y alloys for the bio-applications, npj Materials Degradation 7(1) (2023) 45.
12. T. Chen, Y. Yuan, J. Wu, T. Liu, X. Chen, A. Tang, F. Pan, Alloy Design Strategies of the Native Anti-corrosion Magnesium Alloy, Magnesium Technology 2019 (2019), pp. 169–173.

13. W. Hume-Rothery, G.W. Mabbott, K.M. Channel-Evans, The Freezing Points, Melting Points, and Solid Solubility Limits of the Alloys of Silver, and Copper with the Elements of the B Sub-Groups, Philosophical Transactions of the Royal Society of London, Series A 233 (1934) 1–97.
14. T. Chen, Q. Gao, Y. Yuan, T. Li, Q. Xi, T. Liu, A. Tang, A. Watson, F. Pan, Coupling physics in machine learning to investigate the solution behavior of binary Mg alloys, Journal of Magnesium and Alloys 10(10) (2022) 2817–2832.
15. T. Chen, Y. Yuan, X. Mi, J. Wu, A. Tang, J. Wang, N. Moelans, F. Pan, Interaction of elements in dilute Mg alloys: a DFT and machine learning study, Journal of Materials Research and Technology 21 (2022) 4512–4525.

Microstructural Evolution of Hot-Rolled AZ31 Mg Plate Induced by Electropulsing Treatment

Seho Cheon, Jinyeong Yu, Seong Ho Lee, Sung Hyuk Park, and Taekyung Lee

Abstract

Mg alloys need to be thermomechanically treated at elevated temperatures due to the limited formability at room temperature. Electropulsing treatment (EPT) is a new method of heat treatment that utilizes Joule heating directly through electric current to a metal specimen. The process has various advantages, such as rapid heating and energy efficiency, in comparison to the conventional heating method. The authors' recent study suggested the anisotropic nature of EPT, namely electropulsing anisotropy. Specifically, AZ31 Mg alloy exhibits distinct kinetics of microstructural evolution depending on the direction of electropulsing. As the following study, this present work further investigates the electropulsing anisotropy excluding the effect of grain boundaries. EPT was applied in three directions using AZ31 Mg plate composed of equiaxed grains, which allow for a detailed study of the sole effect of texture on the anisotropy.

Keywords

Magnesium • Electropulsing • Anisotropy

Extended Abstract

Mg alloys require a thermomechanical treatment at elevated temperatures due to their limited formability at room temperature. When an electric current is applied to a metal, heat is generated due to the Joule effect. This concept forms the basis of electropulsing treatment (EPT), which involves directly administering electric current to the metal to induce a microstructural evolution through thermal effect [1]. The process offers several advantages, notably rapid heating and heightened energy efficiency, as compared to conventional furnace heat treatment (FHT).

There have been a number of researchers suggesting an athermal effect of EPT [2–4], which is not the Joule heating but the influence of electric current itself. For example, Jin et al. [2] compared FHT and EPT with respect to a rolled ZK60 Mg alloy, revealing that EPT remarkably enhanced recrystallization and grain growth behavior despite the similar processing conditions. This improvement was attributed to the additional free energy introduced by the electropulse, thereby intensifying the driving force of recrystallization. Our recent study [5] suggested an anisotropic nature of EPT, denoted as electropulsing anisotropy. Extruded ZK60 alloy exhibited distinct microstructural evolution depending on the direction of electropulse. Electropulsing along the extrusion direction resulted in a larger recrystallized area compared to those subjected to either FHT or electropulsing along the transverse direction, despite the lower temperature.

However, the previous study could not separate the effects of grain structure and texture owing to the nature of extruded alloy. The present work further investigates the electropulsing anisotropy excluding the effect of grain boundaries. For this purpose, AZ31 Mg alloy underwent hot rolling to include completely equiaxed grains and typical basal texture where basal poles were aligned with the normal direction (ND). EPT was applied along three directions: ND, rolling direction (RD), and 45°-inclined direction from ND to RD, namely diagonal direction (DD), respectively. This signifies an electropulsing applied in the parallel, perpendicular, and 45°-inclined to the basal pole, as illustrated in Fig. 1.

Under the identical condition, RD sample showed the highest temperature, followed by the DD and ND samples.

S. Cheon · J. Yu · S. H. Lee · T. Lee (✉)
School of Mechanical Engineering, Pusan National University,
Busan, 46241, Korea
e-mail: taeklee@pnu.edu

S. H. Park
School of Materials Science and Engineering,
Kyungpook National University, Daegu, 41566, Korea

A. Leonard et al. (eds.), *Magnesium Technology 2024*, The Minerals, Metals & Materials Series,
https://doi.org/10.1007/978-3-031-50240-8_13

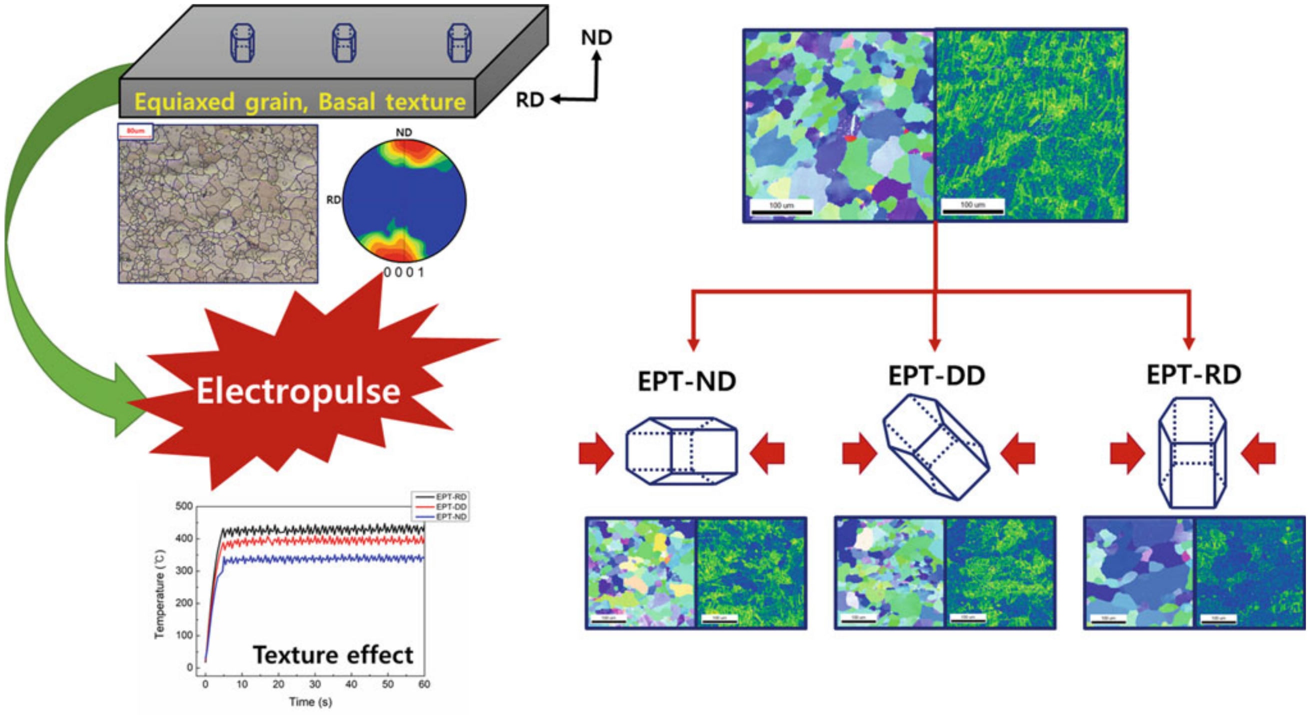

Fig. 1 Schematic of the experiment to observe the effect of texture on EPT

The trend of grain size exhibited the same sequence. Compared to the as-received sample, where the grain size was 34.84 um, it increased to 70.73 um in RD and 46.04 um in DD, but did not show a meaningful change in ND at 36.13 um. Similarly, KAM values decreased to 0.55 in RD, and 0.74 in DD compared to the as-received sample (0.81), but ND did not change significantly at 0.83. These results imply the presence of electropulsing anisotropy, even after excluding the effect of grain morphology. This phenomenon is caused by the difference in electrical resistivity depending on the atomic orientation (i.e., the texture). According to the Joule heating theory [6], the temperature elevation resulting from a electropulse is proportional to the electrical resistivity. The resistivity was higher in order of ND, RD, and DD when measuring the resistivity based on direction. Therefore, the microstructural differences depending on the electropulsing direction can be attributed to the thermal effect. In addition, an athermal effect also contributed to microstructural evolution. EPT specimens showed a more rapid grain growth and lower strain energy compared to the FHT counterparts.

References

1. M. Lee, J. Yu, M.H. Bae, J.W. Won, T. Lee, Electropulsing has various engineering benefits compared with the traditional heating l P of, Journal of Materials Research and Technology (2021).
2. W. Jin, J. Fan, H. Zhang, Y. Liu, H. Dong, B. Xu, Microstructure, mechanical properties and static recrystallization behavior of the rolled ZK60 magnesium alloy sheets processed by electropulsing treatment, Journal of Alloys and Compounds 646 (2015) 1–9.
3. K. Jeong, S.-W. Jin, S.-G. Kang, J.-W. Park, H.-J. Jeong, S.-T. Hong, S.H. Cho, M.-J. Kim, H.N. Han, Athermally enhanced recrystallization kinetics of ultra-low carbon steel via electric current treatment, Acta Materialia 232 (2022).
4. X. Li, X. Li, J. Zhu, X. Ye, G. Tang, Microstructure and texture evolution of cold-rolled Mg-3Al-1Zn alloy by electropulse treatment stimulating recrystallization, Scripta Materialia 112 (2016) 23–27.
5. S.J. Oh, J. Yu, S. Cheon, S.H. Lee, S.-Y. Lee, T. Lee, Anisotropic microstructural evolutions of extruded ZK60 Mg alloy subjected to electropulsing treatment, Journal of Materials Research and Technology 26 (2023) 3322–3331.
6. J. Yu, M. Lee, Y.H. Moon, Y. Noh, T. Lee, Prediction of Electropulse-induced nonlinear temperature variation of Mg alloy based on machine learning, Journal of Korean Institute of Metals and Materials 58(6) (2020) 413–422.

An Integrated Computational and Experimental Study of Static Recrystallization in the Mg–Zn–Ca Alloy System

T. D. Berman, D. Montiel, M. Pilipchuk, M. Yaghoobi, K. Thornton, V. Sundararaghavan, and J. E. Allison

Abstract

The PRISMS Center is utilizing both experimental studies and simulations to better understand the effect of alloying on static recrystallization in alloys in the Mg–Zn–Ca system. The kinetics and mechanisms of recrystallization are characterized using electron backscatter diffraction on annealed Gleeble plane-strain compression samples. This data is used to inform the computational models. In order to simulate alloying effects on static recrystallization, a sequentially integrated PRISMS-PF/PRISMS-Plasticity framework is employed. PRISMS-Plasticity calculates the dislocation density distribution within a microstructure after deformation. PRISMS-PF reads both the microstructure and the average dislocation density per grain as inputs and then computes the evolution of recrystallized grains by taking into account the differences in stored energy between grains. This capability can be used to predict the volume fraction and distribution of recrystallized grains as a function of time which will be compared to an experimentally determined Johnson–Mehl–Avrami–Kolmogorov (JMAK) relationship.

Keyword

Recrystallization • ICME • Texture

Extended Abstract

Producing affordable, formable magnesium alloy sheet is a long-standing technological challenge that limits widespread use of magnesium. It has been established that alloying Mg with Zn and Ca can lead to relatively weak recrystallization textures [1–5] and improved formability [6–8] but the mechanisms responsible are still not fully understood [9]. This limits the development of predictive models for alloy design. The PRISMS Center is utilizing both experimental studies and simulations to better understand the effect of alloying on static recrystallization in alloys in the Mg–Zn–Ca system.

The kinetics of recrystallization were characterized using electron backscatter diffraction (EBSD) on annealed plane-strain compression samples prepared using a Gleeble 3500 thermomechanical processing simulator. Four different alloys were studied, Mg–0.1Ca, Mg–3Zn, Mg–1Zn–0.1Ca, and Mg–3Zn–0.1Ca (in wt%). Compression was performed at a temperature of 200ºC using a strain rate of 0.5 s^{-1}. Immediately following deformation, the specimen temperature was ramped to the desired annealing temperature at a rate of 5 ºC per second. Following annealing, the specimens were quenched in the Gleeble using forced air. EBSD was used to characterize the grain size, grain morphology, crystallographic texture, and the extent of recrystallization. Grains with a grain orientation spread $< 1°$ were considered to be recrystallized.

A comparison between the recrystallization kinetics of the four alloys when annealed at 350 °C following a 17 pct reduction in height is shown in Fig. 1a, where the percentage of recrystallization vs. annealing time is plotted for each alloy. None of the alloys exhibited signs of recrystallization in the as-deformed state. The Mg-3Zn binary alloy exhibited the fastest kinetics, with more than half of the area recrystallized within 20 s of deformation (at which point the temperature had increased from 200 to 300 °C). The addition of 0.1Ca to Mg–3Zn retarded the static recrystallization process; this alloy was approximately 20% recrystallized by the time the specimen reached the desired annealing temperature of 350 °C. Decreasing or removing Zn also decreased the kinetics of static recrystallization.

T. D. Berman (✉) · D. Montiel · M. Pilipchuk · M. Yaghoobi · K. Thornton · V. Sundararaghavan · J. E. Allison
Department of Materials Science and Engineering, University of Michigan, Ann Arbor, MI 48109, USA
e-mail: tradiasa@umich.edu

A. Leonard et al. (eds.), *Magnesium Technology 2024*, The Minerals, Metals & Materials Series,
https://doi.org/10.1007/978-3-031-50240-8_14

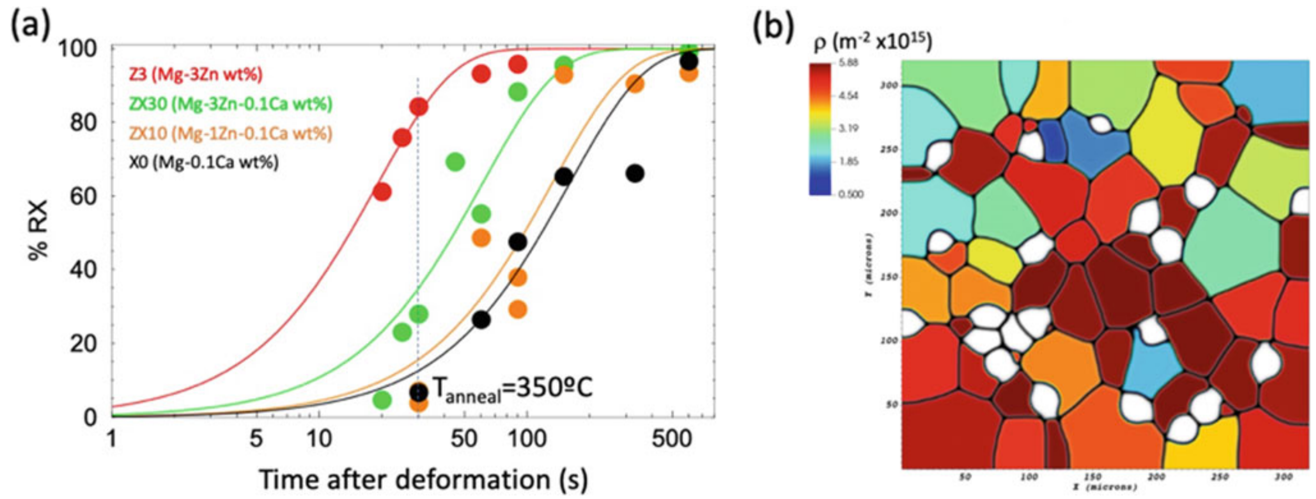

Fig. 1 **a** Kinetics T the area fraction of recrystallized grains in each alloy as a function of the time after deformation in specimens subjected to a compressive pass of 0.2 true strain at 200 °C using a strain rate of 0.5 s^{-1} and subsequently annealed at 350 °C. **b** An example of the evolution of nuclei in the microstructure of the Mg–3Zn–0.1 alloy after a simulated deformation pass of 0.2 true strain at 200 °C. (For interpretation of the figure legends, the reader is referred to the web version of this article.)

In order to simulate static recrystallization, a sequentially integrated PRISMS-PF/PRISMS-Plasticity framework was employed. The Taylor model pipeline in PRISMS-Plasticity [10] is used to simulate the response of the magnesium alloys during deformation. The Gleeble stress–strain curves were used to calibrate the crystal plasticity model, which calculates the dislocation density distribution within a microstructure after deformation. PRISMS-PF reads both the microstructure (an experimentally equivalent reconstruction generated using Dream.3D) and the average dislocation density per grain as inputs. PRISMS-PF then computes the evolution of recrystallized grains by considering the differences in stored energy between grains using the same approach as Gentry et al. [11]. Currently, all nuclei are seeded at the beginning of the simulation and they are placed preferentially at grain boundaries and triple junctions. This capability can be used to predict the volume fraction and distribution of recrystallized grains as a function of time, which will be compared to the experimentally determined kinetics. An example of a 2D simulation is shown in Fig. 1b. Current work in the PRISMS Center includes applying the model to simulate 3D microstructures and incorporating inputs from molecular dynamic grain boundary energy and mobility models to better capture alloying effects.

Acknowledgements This work was supported by the U.S. Department of Energy, Office of Basic Energy Sciences, Division of Materials Sciences and Engineering under Award#DE-SC0008637 as part of the Center for Predictive Integrated Structural Materials Science (PRISMS Center) at University of Michigan. We also acknowledge the financial cost-share support of University of Michigan College of Engineering and Office of the Vice President for Research, as well as computational resources from the National Energy Research Scientific Computing Center (NERSC), award BES-ERCAP0023763.

References

1. J. Bohlen, J. Wendt, M. Nienaber, K.U. Kainer, L. Stutz, D. Letzig, Calcium and zirconium as texture modifiers during rolling and annealing of magnesium-zinc alloys, Mater. Charact. 101 (2015) 144–152. https://doi.org/10.1016/j.matchar.2015.02.002.
2. T.D. Berman, J.E. Allison, Coupling Thermomechanical Processing and Alloy Design to Improve Textures in Mg–Zn–Ca Sheet Alloys, JOM. 73 (2021) 1450–1459. https://doi.org/10.1007/s11837-021-04630-0.
3. Q. Li, G.J. Huang, X.D. Huang, S.W. Pan, C.L. Tan, Q. Liu, On the texture evolution of Mg–Zn–Ca alloy with different hot rolling paths, J. Magnes. Alloy. 5 (2017) 166–172. https://doi.org/10.1016/j.jma.2017.06.001.
4. Z.R. Zeng, Y.M. Zhu, S.W. Xu, M.Z. Bian, C.H.J. Davies, N. Birbilis, J.F. Nie, Texture evolution during static recrystallization of cold-rolled magnesium alloys, Acta Mater. 105 (2016) 479–494. https://doi.org/10.1016/j.actamat.2015.12.045.
5. J. Victoria-Hernández, S. Yi, D. Klaumünzer, D. Letzig, Recrystallization behavior and its relationship with deformation mechanisms of a hot rolled Mg–Zn–Ca–Zr alloy, Mater. Sci. Eng. A. 761 (2019) 138054. https://doi.org/10.1016/j.msea.2019.138054.
6. M. Zhou, X. Huang, Y. Morisada, H. Fujii, Y. Chino, Effects of Ca and Sr additions on microstructure, mechanical properties, and ignition temperature of hot-rolled Mg–Zn alloy, Mater. Sci. Eng. A. 769 (2020). https://doi.org/10.1016/j.msea.2019.138474.
7. J. Bohlen, P. Dobron, J. Swiostek, D. Letzig, F. Chmelik, P. Lukac, K.U. Kainer, On the influence of the grain size and solute content on the AE response of magnesium alloys tested in tension and compression, Mater. Sci. Eng. A. 462 (2007) 302–306. https://doi.org/10.1016/j.msea.2006.02.470.
8. Y. Chino, T. Ueda, Y. Otomatsu, K. Sassa, X. Huang, K. Suzuki, M. Mabuchi, Effects of Ca on Tensile Properties and Stretch Formability at Room Temperature in Mg-Zn and Mg-Al Alloys, Mater. Trans. 52 (2011) 1477–1482. https://doi.org/10.2320/matertrans.M2011048.

9. M.T. Pérez-Prado, J. Bohlen, S. Yi, D. Letzig, T. Al-Samman, J. Robson, M. Barnett, W. Poole, C. Mendis, S. Agnew, N. Stanford, Emerging Hot Topics and Research Questions in Wrought Magnesium Alloy Development, JOM. 72 (2020) 2561–2567. https://doi.org/10.1007/s11837-020-04051-5.
10. M. Yaghoobi, S. Ganesan, S. Sundar, A. Lakshmanan, S. Rudraraju, J.E. Allison, V. Sundararaghavan, PRISMS-Plasticity: An open-source crystal plasticity finite element software, Comput. Mater. Sci. 169 (2019) 109078. https://doi.org/10.1016/j.commatsci.2019.109078.
11. S.P. Gentry, K. Thornton, Sensitivity analysis of a phase field model for static recrystallization of deformed microstructures, Model. Simul. Mater. Sci. Eng. 28 (2020). https://doi.org/10.1088/1361-651X/ab9751.

Part III

Deformation Mechanisms

An Experimental Study on Twinning Behavior in Mg Alloys with Different Solute Elements

Qianying Shi and John Allison

Abstract

Twinning is an important deformation mode in magnesium alloys; however, the influence of different solute elements remains a topic of active research. In this study, the influence of solute elements on twinning activity during monotonic and cyclic loading has been investigated in Mg alloys containing the rare earth elements Nd and Y as well as non-rare earth elements Al, Zn, and Ca. In-situ EBSD was used at multiple load steps to quantify the level of deformation twinning and twin variants. In addition, high-resolution TEM has been used to study twin characteristics. Our results indicate that a high level of Y addition significantly retards twin activity and, in addition to the more common $\{10\bar{1}2\}$ extension twins, also promotes a second type of tension twins $\{11\bar{2}1\}$. Similarly, the addition of Nd leads to a reduction in twin activity. These results will be compared with twin activity in non-rare earth alloys.

Keywords

Magnesium alloys • Rare earth • Y • Twinning • Twin boundary segregation

Extended Abstract

Since the available slip deformation modes are inherently restricted by the hexagonal close-packed structure of Mg, twinning is an important deformation mode in Mg and Mg alloys to accommodate the deformation along the *c*-axis [1–3]. However, the influence of different solute elements remains a topic of active research. In this study, Mg alloys containing the rare earth elements Nd and Y as well as the non-rare earth elements Al, Zn, and Ca were studied to understand the alloying effect on twinning activity during monotonic and cyclic loading.

Y is of great interest in terms of its effect on the deformation behavior in Mg alloys, which has been found to activate non-basal slip, i.e., a higher activity of pyramidal $\langle c + a \rangle$ dislocations, resulting in a significant improvement of the ductility at room temperature [4–6]. Two Mg–Y alloys with different Y additions, Mg–1wt%Y and Mg–7wt%Y, were used in this study to investigate the Y effect on twinning behavior. Figure 1a, b compares the fraction of twins formed in these two alloys after a compression test with approximately 1% plastic strain. It is clearly seen that the twin fraction in Mg–7wt%Y alloy is much lower than that in Mg–1wt%Y alloy, indicating a high level of Y addition significantly retards twinning activity. In addition, all twins formed in Mg–1wt%Y alloy were identified as the commonly activated $\{10\bar{1}2\}$ extension twin (Type I), while a second type of extension twin (Type II, $\{11\bar{2}1\}$ twins) was also observed in Mg–7wt%Y alloy. As shown in Fig. 1c, twins with boundaries outlined in white lines are $\{11\bar{2}1\}$ extension twins, which appears in a more narrow and straight morphology compared to $\{10\bar{1}2\}$ twins outlined in black lines.

Two types of atomic arrangement at the twin boundary for Type I $\{10\bar{1}2\}$ extension twin were reported in previous studies [7–10]. The classical coherent twin boundary (CTB), where the twin boundary is perfectly straight and the atoms from twin and matrix crystals are symmetrical, and basal-prismatic (BP) interface, which is in a stair-steps shape with random size or length of stairs. The twin boundary structure in current studied Mg–Y alloys was characterized using high-resolution STEM and EDS to compare the effect of different Y additions. Both CTB and BP interface were observed in two Mg–Y alloys after compression with a plastic strain of ∼ 5%. Significant Y segregation was

---

Q. Shi (✉) · J. Allison
Department of Materials Science and Engineering, University of Michigan, 2300 Hayward Street, Ann Arbor, MI 48109, USA
e-mail: shiqiany@umich.edu

A. Leonard et al. (eds.), *Magnesium Technology 2024*, The Minerals, Metals & Materials Series,
https://doi.org/10.1007/978-3-031-50240-8_15

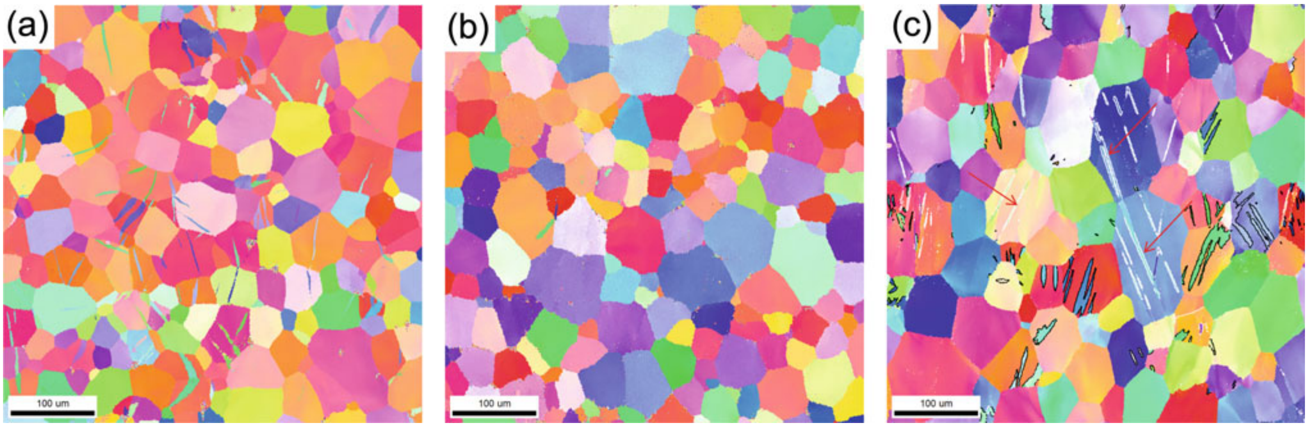

Fig. 1 EBSD IPF maps to characterize the microstructures of Mg–Y alloys after compression deformation. **a** Mg–1wt%Y alloy, ~ 1% plastic strain; **b** Mg–7wt%Y alloy, ~ 1% plastic strain; **c** Mg–7wt%Y alloy, ~ 5% plastic strain

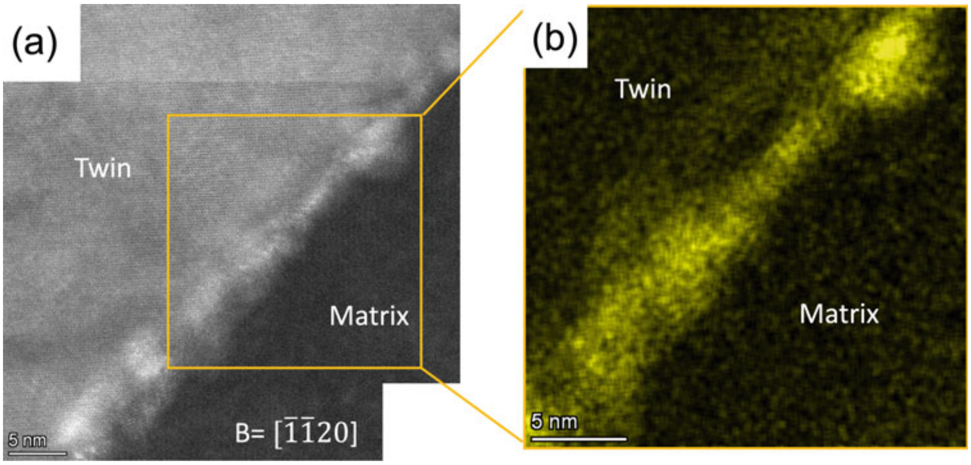

Fig. 2 High-resolution STEM-HAADF image (**a**) and EDS map of Y concentration (**b**) in Mg–7wt%Y alloy after approximately 5% plastic strain compression

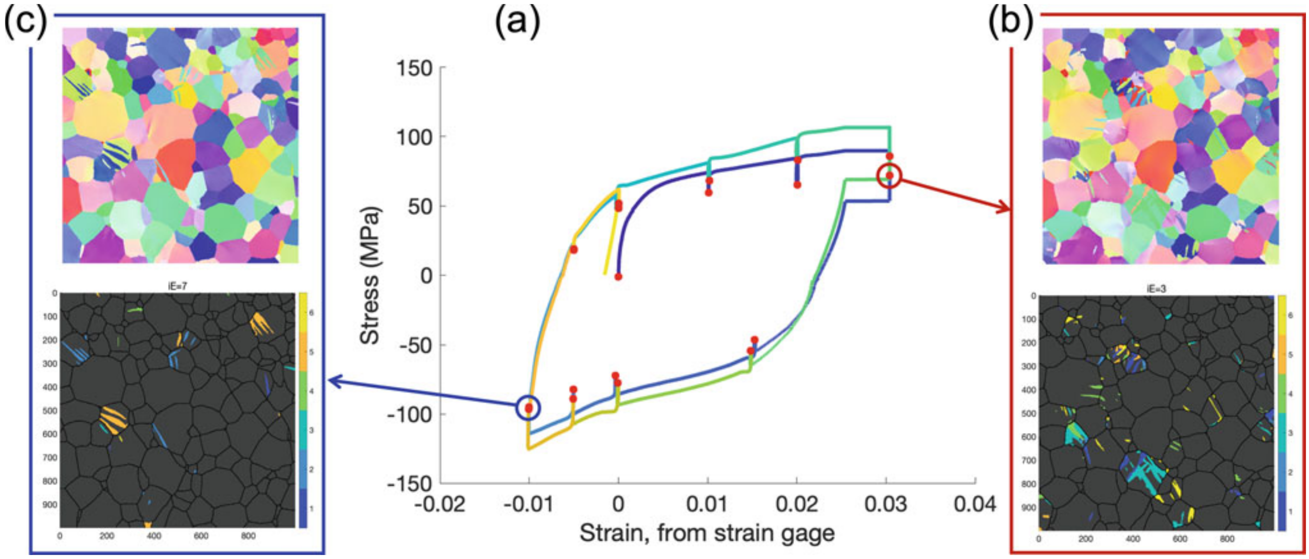

Fig. 3 In-situ EBSD test to quantify the level of deformation twinning and twin variants. **a** Stress versus strain plot of one Mg–2.4wt%Nd sample; **b** EBSD IPF map and twin variant map at load step 3 (tension cycle); **c** EBSD IPF map and twin variant map at load step 7 (compression cycle)

observed in $\{10\bar{1}2\}$ twin boundaries in Mg–7wt%Y alloy, while no clear TB segregation was detected in Mg–1wt%Y alloy. As shown in Fig. 2, Y segregated at the twin boundary in the form of clusters instead of being continuously distributed. More BP stairs were observed in Mg–7wt%Y alloy, which were believed to be associated with the Y segregation.

In-situ mechanical tests were applied in SEM equipment with EBSD detector to collect data at multiple load steps during cyclic loading [11]. The level of deformation twinning and twin variants were identified and quantified. The alloys with rare earth elements Y and Nd were found a reduction in twin activity compared to pure Mg and Mg–Al alloys. Additionally, it is interesting to find that twinning occurs in both tension and compression loading in Mg-2.4wt%Nd alloy, as shown in Fig. 3, which is attributed to the weak rotated basal texture. Different $\{10\bar{1}2\}$ extension twin variants were observed during tension and compression loading. More in-depth analysis is being conducted to investigate the alloying effect on twinning behavior.

Acknowledgements This work was supported by PRedictive Integrated Structural Materials Science (PRISMS) center which is located at the University of Michigan and funded by the US Department of Energy, Office of Basic Energy Science, Division of Materials Science and Engineering (Grant award number DE-SC0008637). We acknowledge the access to and the support from the Michigan Center for Materials Characterization (MC2) at the University of Michigan. We also acknowledge Bruce Williams from CanmetMATERIALS, Natural Resources Canada who provided the materials used in this investigation.

References

1. M.R. Barnett, Twinning and the ductility of magnesium alloys. Part I: "Tension" twins, Materials Science and Engineering A. 464 (2007) 1–7. https://doi.org/10.1016/j.msea.2006.12.037.
2. M.R. Barnett, Twinning and the ductility of magnesium alloys. Part II. "Contraction" twins, Materials Science and Engineering A. 464 (2007) 8–16. https://doi.org/10.1016/j.msea.2007.02.109.
3. M.R. Barnett, N. Stanford, P. Cizek, A. Beer, Z. Xuebin, Z. Keshavarz, Deformation mechanisms in Mg alloys and the challenge of extending room-temperature plasticity, JOM. 61 (2009) 19–24. https://doi.org/10.1007/s11837-009-0115-6.
4. S. Sandlöbes, M. Friák, J. Neugebauer, D. Raabe, Basal and non-basal dislocation slip in Mg–Y, Materials Science and Engineering A. 576 (2013) 61–68. https://doi.org/10.1016/j.msea.2013.03.006.
5. S. Sandlöbes, S. Zaefferer, I. Schestakow, S. Yi, R. Gonzalez-Martinez, On the role of non-basal deformation mechanisms for the ductility of Mg and Mg–Y alloys, Acta Mater. 59 (2011) 429–439. https://doi.org/10.1016/j.actamat.2010.08.031.
6. Z. Wu, R. Ahmad, B. Yin, S. Sandlöbes, W.A. Curtin, Mechanistic origin and prediction of enhanced ductility in magnesium alloys, Science. 359 (2018) 447–452. https://www.science.org.
7. K.Y. Xie, K. Hazeli, N. Dixit, L. Ma, K.T. Ramesh, K.J. Hemker, Twin boundary migration mechanisms in quasi-statically compressed and plate-impacted mg single crystals, Sci Adv. 7 (2021) 1–7. https://doi.org/10.1126/sciadv.abg3443.
8. Y. He, B. Li, C. Wang, S.X. Mao, Direct observation of dual-step twinning nucleation in hexagonal close-packed crystals, Nat Commun. 11 (2020) 1–8. https://doi.org/10.1038/s41467-020-16351-0.
9. B.Y. Liu, Z.W. Shan, E. Ma, Non-dislocation based room temperature plastic deformation mechanism in magnesium, Magnesium Technology. (2016) 199–201. https://doi.org/10.1002/9781119274803.ch40.
10. S. Wang, M. Gong, R.J. McCabe, L. Capolungo, J. Wang, C.N. Tomé, Characteristic boundaries associated with three-dimensional twins in hexagonal metals, Sci Adv. 6 (2020). https://doi.org/10.1126/sciadv.aaz2600.
11. Z. Chen, C. Torbet, J. Allison, In Situ Characterization of Deformation Twinning in Magnesium During Cyclic Loading via Electron Backscatter Diffraction, JOM. 74 (2022) 2577–2591. https://doi.org/10.1007/s11837-022-05335-8.

In Situ Tomographic Investigation of the Combined Effect of Mechanical Load and Degradation on Mg2Y1Zn(Gd, Ag, Ca)

P. dos Santos Mallmann, B. Hindenlang, S. Bruns, J. Bohlen,
D. C. F. Wieland, F. Wilde, and D. Tolnai

Abstract

The mechanical properties of Mg can be substantially improved by the addition of Y and Zn. Further, alloying elements modify the secondary phases formed by the former, enabling to tailor the properties. Samples of pure Mg1.8Y0.6Zn and modified with 1.6 wt% Gd, 1 wt% Ag, or 0.4 wt% of Ca were subjected to in situ tensile testing with a strain rate of 10^{3} s^{-1} and 10^{-4} s^{-1} in air and submerged in NaCl solution and SBF, respectively. During testing, synchrotron tomographies were acquired to follow the crack evolution and the interaction of mechanical and corrosion damage until failure. The results show that the degradation media has a drastic effect on the mechanical properties in all the alloys, changing the brittle fracture in air to a more ductile behaviour in media. Lower strain rates, due to the longer duration of the experiment, enable the degradation to have a more profound effect.

Keywords

Mg–Y–Zn alloys • In situ synchrotron tomography • Tensile test • Degradation

Extended Abstract

Due to its similar elastic modulus to cortical bone and degradation under physiological conditions, magnesium is considered as an implant material. The matching mechanical properties allow the implants to provide optimal support, while the degradation and the obsolete removal surgery increase patient comfort and reduce risk and medical costs [1]. The mechanical properties of Mg can be substantially improved by the addition of Y and Zn. Favourable processing conditions lead to the formation of a long periodic stacking-ordered structure (LPSO) that provides superior strength without deteriorating the ductility [2]. Further, alloying elements modify the secondary phases, enabling to tailor the property profile. Complemented with the biocompatibility of Mg–Y–Zn (WZ) alloys makes them suitable as biodegradable implant materials [3, 4]. For this purpose, the degradation process and the influence of the surrounding tissue have been targeted by numerous investigations [5]. This complex process is effected by many parameters, e.g., material composition, processing, and production of the implant, the mechanical load during and after the implantation, but also the ionic composition of the corrosive media and the content of organic molecules in the environment [6]. In corrosive environment mechanical loads even at moderate stress levels can lead to crack formation resulting in stress corrosion cracking (SCC) [7]. Several parameters influence the SCC (e.g., environment, microstructure, strain, strain rate, etc.), whereas the strain and degradation rates play a pivotal role. SCC occurs, when both the degradation and the mechanical load simultaneously contribute to the failure process.

Synchrotron-based X-ray tomography is a well-suited tool to follow damage evolution in the material subjected to simultaneous degradation and mechanical load conditions as it allows in situ investigations with the needed resolution [8]. In the frame of this project, we aimed to follow the crack evolution and the interaction of mechanical and corrosion

---

P. dos Santos Mallmann · B. Hindenlang · S. Bruns ·
D. C. F. Wieland · D. Tolnai (✉)
Institute of Metallic Biomaterials, Helmholtz-Zentrum Hereon,
Max-Planck Strasse 1, 21502 Geesthacht, Germany
e-mail: domonkos.tolnai@hereon.de

J. Bohlen
Institute of Material and Process Design, Helmholtz-Zentrum
Hereon, Max-Planck Strasse 1, 21502 Geesthacht, Germany

F. Wilde
Institute of Materials Physics, Helmholtz-Zentrum Hereon,
Max-Planck Strasse 1, 21502 Geesthacht, Germany

A. Leonard et al. (eds.), *Magnesium Technology 2024*, The Minerals, Metals & Materials Series,
https://doi.org/10.1007/978-3-031-50240-8_16

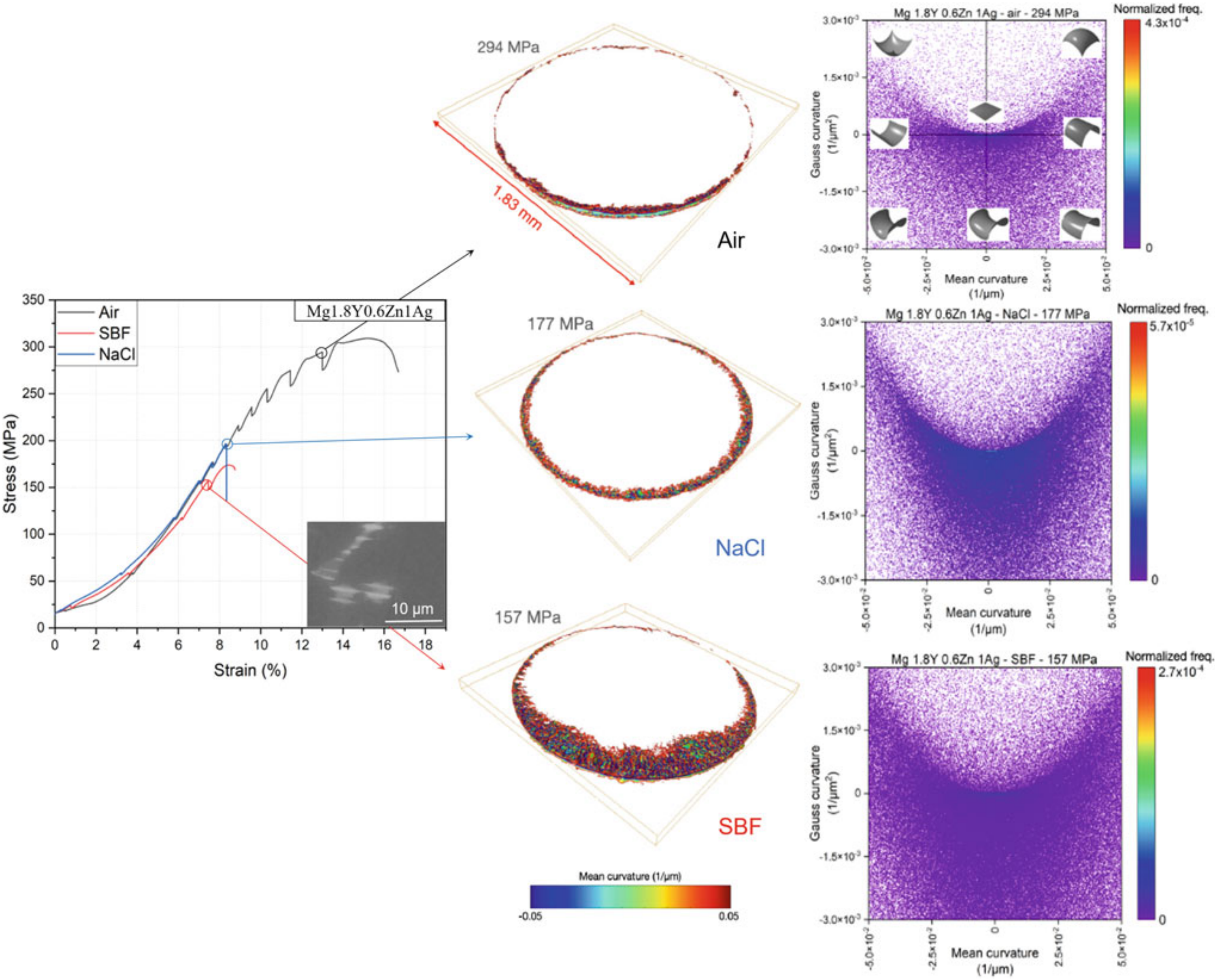

Fig. 1 Experimental results of the in situ tensile test in air, SBF, and NaCl for Mg1.8Y0.6Zn1Ag, with the crack shown in the last scan before failure, and the shape distribution of the crack surfaces

damage until failure in 3D in order to retrieve deeper knowledge on the SCC phenomena.

Mg1.8Y0.6Zn in pure form and modified with 1.6 wt% Gd, 1 wt% Ag, or 0.4 wt% of Ca, were produced by permanent mould indirect chill casting [9]. The ingots were homogenized at 400 °C for 24 h and subsequently quenched in water. Indirect extrusion was carried out at 400 °C with an extrusion speed of 1 mm·s^{-1} from round bars with a diameter of 10 mm corresponding to an extrusion ratio of 1:25. Cylindrical tensile samples with a notch, to reduce the region of interest, were subjected to in situ tensile testing with an initial strain rate of 10^{-3} and 10^{-4} s^{-1} in air and submerged in NaCl solution and SBF. The tests were stopped at certain forces to perform the tomographic tests. During these periods, 4000 radiographies were recorded with a monochromatic beam at an energy of 38 keV and an acquisition time of 230 ms per radiogram at the nearest possible sample-to-detector distance of 60 mm at the P05 (IBL) beamline of Petra III, DESY (Deutsches Elektronen-Synchrotron), operated by Helmholtz-Zentrum Hereon [10, 11]. The radiographies were then reconstructed into tomographic volumes with a voxel size of (1.8 µm)^3. As an example, the results of the analysis of the alloy with 1 wt% Ag are shown in Fig. 1.

The sample tested in air exhibited a UTS of 309 MPa and an elongation of 15%. The corrosive environment substantially deteriorated the mechanical properties in the case of both media. The test in NaCl resulted in a UTS of 196 MPa and an elongation of 8.3% while the one in SBF resulted in a UTS of 174 MPa and 8.4% elongation. In air, a brittle fracture has developed, as the crack is relatively small even at the last stage of the tensile test. The crack shape was characterised by the curvature values of its surface. The analysis shows that the maximum of the shape distribution can be attributed to a planar surface, suggesting that an intragranular crack causes the failure of the sample. In the case of the tensile test in NaCl, the sample also breakes in a brittle manner; however unlike the one tested in air, the curvature analysis shows that the distribution extends towards shapes that are saddle-like. This suggests that the crack propagation is more intergranular as the crack surface follows the shapes of the grains. In SBF the sample showed a ductile behavior as the crack is substantially larger than in the samples tested in other media. The quantitative analysis also indicates an intergranular fracture of the alloy, as the distribution extends towards non-planar shapes. The results show that besides the alloy composition, there are also remarkable differences in the damage evolution and fracture behavior among the tests performed in different media.

Acknowledgements The authors acknowledge the Deutsches Elektronen-Synchrotron for the provision of beamline facilities in the framework of the proposal I-20220208.

References

1. H. Hermawan, D. Dubé, D. Mantovani, *Acta Biomaterialia* 6 (2010) 1693–1697.
2. K. Horváth et al., Magnesium Technology 2017. The Minerals, Metals & Materials Series. Springer, Cham. https://doi.org/10.1007/978-3-319-52392-7_8.
3. T. Kraus et al., Acta Biomaterialia 66 (2018) 109–117.
4. T.A. Grünewald et al., Acta Biomaterialia 31 (2016) 448–457.
5. B. Zeller-Plumhoff et al., Adv. Eng. Mater., vol. n/a, no. n/a, p. 2100197, May 2021, https://doi.org/10.1002/adem.202100197.
6. R. Willumeit-Römer et al., TMS 2018 147th Annual Meeting & Exhibition Supplemental Proceedings, Cham, 2018, pp. 275–284.
7. Y. Gao et al., Acta Biomaterialia, vol. 83, pp. 477–486, Jan. 2019, https://doi.org/10.1016/j.actbio.2018.11.019.
8. B. Zeller-Plumhoff et al., Sci. Rep. 10 (2020) 16101.
9. F.R. Elsayed et al., Materials Science Forum 690 (2011) 65–68.
10. F. Wilde et al., AIP Conference Proceedings 1741, 030035, (2016), https://doi.org/10.1063/1.4952858.
11. J. Moosmann et al., Proceedings Volume 11113, Developments in X-Ray Tomography XII; 1111318 (2019), https://doi.org/10.1117/12.2530445.

Quantifying the Role of Coarse Intermetallic Particles on Deformation Behavior

Benjamin T. Anthony and Victoria M. Miller

Abstract

Deformation twinning is a mechanism of critical interest in magnesium alloys and other HCP metals, both due to its ability to accommodate strain and its tendency to contribute to failure by providing a preferential crack pathway along twin boundaries. This deleterious behavior is worsened by instances of twin transmission, where a twin impinging on a grain boundary nucleates an adjacent, connected twin in the neighboring grain due to intense local stresses. Many commercial Mg alloys feature coarse grain boundary intermetallic particles in their as-produced state which potentially impede or exacerbate the localized stresses that play a role in both twin transmission and twinning behavior. Combined EDS-EBSD is used to analyze grain boundary particles, deformation twins, and transmission events to determine how particle morphology, position, and grain orientation modify twinning behavior and transmission likelihood, and how these findings compare to computational results from crystal plasticity—fast Fourier transform modeling.

Keywords

Texture • Deformation twinning • Intermetallic phases

Extended Abstract

Controlling the evolution of crystallographic texture is key to promoting ductility and formability in magnesium alloys. A number of different avenues of texture control have been researched, including novel deformation processes [1, 2], alloying to alter the balance of deformation mode activities [3–6], and microstructural engineering via grain size reduction [7–11]. One under-studied strategy for control of texture evolution is the introduction of intermetallic particles.

Previous research into the role of coarse, micron-scale intermetallic particles during deformation has indicated that they may promote a more diffuse deformation texture when compared to a similar alloy with a lower volume fraction of particles [12, 13]. Additionally, Berman et al. found that, while the intermetallic particles may fracture, they did not cause premature failure; fractography indicated that most microvoids originated at grain boundaries rather than at particles [14].

In the present work, the role of intermetallic particles on the active deformation modes and the texture evolution of thixomolded and thermomechanically processed (TTMP) AM60 was studied. Hot-rolled and flattened thixomolded AM60 was subsequently heat treated at 250 °C for 48 h followed by 100 °C for 24 h to homogenize the microstructure and grow the β-$Mg_{17}Al_{12}$ intermetallic phase at the grain boundaries. Samples in this as-TTMP condition were compared to samples subsequently heat treated at 450 °C for 15 min to partially solutionize the β phase. These two microstructural conditions will be referred to as the “high particle fraction” and “low particle fraction” samples, respectively. While the low particle fraction samples admittedly contain a greater fraction of Al in solid solution, Al solute has not generally been found to significantly weaken the formation of a basal texture. Tensile specimens were produced from each of the microstructural conditions along both the rolling and transverse directions (RD and TD). These samples were pulled in tension to strains of 5%, and then the as-deformed specimens were characterized via combined electron backscatter diffraction (EBSD) and electron dispersive spectroscopy (EDS). While EBSD identified the orientations of the grains, EDS identified the locations of the intermetallic particles.

B. T. Anthony · V. M. Miller (✉)
University of Florida, 100 Rhines Hall, Gainesville,
FL 32611-0001, USA
e-mail: victoria.miller@ufl.edu

A. Leonard et al. (eds.), *Magnesium Technology 2024*, The Minerals, Metals & Materials Series,
https://doi.org/10.1007/978-3-031-50240-8_17

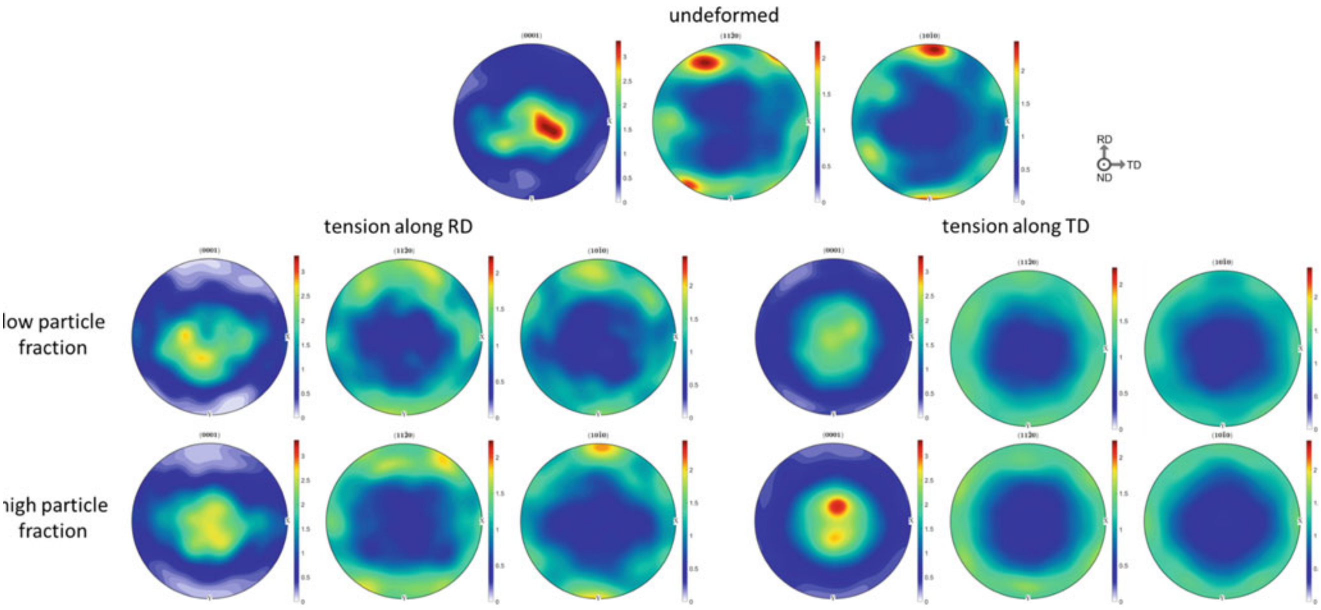

Fig. 1 EBSD-measured textures of the as-TTMP undeformed AM60 and the low versus high particle fraction specimens pulled in tension along the RD or the TD

The viscoplastic self-consistent polycrystal plasticity model (VPSC) [15] was used to predict the tensile behavior along the RD and the TD based on the starting textures. Based on the VPSC modeling results, tension along the TD is predicted to result in deformation dominated by extension twinning, while tension along the RD is more favorable for dislocation slip.

The textures of the undeformed as-TTMP material and specimens pulled in tension are shown in Fig. 1. The as-TTMP material has a moderate basal texture with significant TD spread. Tension along the RD resulted in the weakening of the basal texture and an increase in the extent of TD spread. This evolution was more pronounced in the high particle fraction specimen. In the low particle fraction specimen pulled along the TD, the basal peak weakened but became more symmetrical. In the high particle fraction specimen, a clear split basal texture was produced.

In this talk, twinning analysis and intragranular misorientation analysis conducted using the MTEX toolbox for MATLAB [16] are used to examine the microstructural mechanisms that result in this disparate texture evolution. The implications for alloy design and microstructural engineering of magnesium alloys are discussed.

References

1. Mathaudhu, S. *et al.* Novel Magnesium Alloy Processing via Shear-Assisted Processing and Extrusion (ShAPE). in *Magnesium Technology 2019* (eds. Joshi, V. V., Jordon, J. B., Orlov, D. & Neelameggham, N. R.) 65–67 (Springer International Publishing, 2019). doi: https://doi.org/10.1007/978-3-030-05789-3_11.
2. Zhang, D., Darsell, J., Overman, N., Herling, D. R. & Joshi, V. V. Eliminating Yield Asymmetry and Enhancing Ductility in Mg Alloys by Shear Assisted Processing and Extrusion. in *Magnesium Technology 2021* (eds. Miller, V. M., Maier, P., Jordon, J. B. & Neelameggham, N. R.) 91–99 (Springer International Publishing, 2021). doi: https://doi.org/10.1007/978-3-030-65528-0_15.
3. Hantzsche, K. *et al.* Effect of rare earth additions on microstructure and texture development of magnesium alloy sheets. *Scr. Mater.* **63**, 725–730 (2010).
4. Hadorn, J. P. *et al.* Role of Solute in the Texture Modification During Hot Deformation of Mg-Rare Earth Alloys. *Metall. Mater. Trans. A* **43**, 1347–1362 (2011).
5. Al-Samman, T. & Li, X. Sheet texture modification in magnesium-based alloys by selective rare earth alloying. *Mater. Sci. Eng. A* **528**, 3809–3822 (2011).
6. Jin, Z.-Z. *et al.* Alloying design and microstructural control strategies towards developing Mg alloys with enhanced ductility. *J. Magnes. Alloys* **10**, 1191–1206 (2022).
7. Xu, J. *et al.* A weak texture dependence of Hall-Petch relation in a rare-earth containing magnesium alloy. *J. Mater. Sci. Technol.* (2021) doi: 10/gmdfd2.
8. Wang, Y. & Choo, H. Influence of texture on Hall–Petch relationships in an Mg alloy. *Acta Mater.* **81**, 83–97 (2014).
9. Yamashita, A., Horita, Z. & Langdon, T. G. Improving the mechanical properties of magnesium and a magnesium alloy through severe plastic deformation. *Mater. Sci. Eng. A* **300**, 142–147 (2001).
10. Liao, J., Hotta, M., Kaneko, K. & Kondoh, K. Enhanced impact toughness of magnesium alloy by grain refinement. *Scr. Mater.* **61**, 208–211 (2009).
11. Somekawa, H. & Mukai, T. Effect of grain refinement on fracture toughness in extruded pure magnesium. *Scr. Mater.* **53**, 1059–1064 (2005).
12. Decker, R. F. *et al.* Alloy Design and Processing Design of Magnesium Alloys Using 2nd Phases. *JOM* **71**, 2219–2226 (2019).
13. Miller, V. M. & Pollock, T. M. Texture Modification in a Magnesium-Aluminum-Calcium Alloy During Uniaxial Compression. *Metall. Mater. Trans. A* **47**, 1854–1864 (2016).

14. Berman, T. D., Pollock, T. M. & Jones, J. W. Texture, Second-Phase Particles, and the Anisotropy of Deformation Behavior in TTMP AZ61. *Metall. Mater. Trans. A* **46**, 2986–2998 (2015).
15. Lebensohn, R. A. & Tomé, C. N. A self-consistent anisotropic approach for the simulation of plastic deformation and texture development of polycrytsals: application to zirconium alloys. *Acta Metall. Mater.* **41**, 2611–2624 (1993).
16. Bachmann, F., Hielscher, R. & Schaeben, H. Texture Analysis with MTEX—Free and Open Source Software Toolbox. *Solid State Phenom.* **160**, 63–68 (2010).

Investigations on Creep Behavior of Extruded Mg–Ca–Al Alloys

S. Gneiger, J. A. Nietsch, and N. Papenberg

Abstract

In modern vehicle concepts, lightweight materials that can withstand elevated temperatures are of great importance, e.g., for battery trays and motor housings. Despite their low density, high specific strength, and good thermal conductivity, magnesium alloys are of limited use because they often exhibit unsatisfactory creep behavior at temperatures above 100 °C. Wrought products are particularly affected, as they exhibit pronounced recrystallisation and grain growth in such environments. To mitigate this behavior, Ca can be used to improve the creep resistance of Mg–Al alloys. Here we have used short-term creep experiments to evaluate the performance of multiple extruded Mg–Ca–Al alloys at 150 °C. Our mechanical investigations and microstructural analysis show that the Ca-containing alloys have superior properties at elevated temperatures compared to AZ31.

Keywords

Magnesium • Creep resistance • Mechanical properties • Characterization

Introduction

With their high strength-to-weight ratio, magnesium alloys are promising materials for reducing the weight of automotive components and find use in steering wheels, instrument panel beams, and various housings. It is foreseeable that the ongoing shift from internal combustion engine-powered vehicles (ICEV) to electrically powered vehicles (EV) in our society will open further opportunities for Mg to be used as a structural material, such as battery housings. In addition, existing components that currently cannot be designed in Mg might also be utilized due to changing requirements. For example, the lower service temperatures of EVs in comparison with ICEVs mean that applications close to the power unit can be considered; nevertheless, temperatures as high as 150 °C are still common [1], posing a challenge to conventional Mg alloys.

Due to their cost efficiency and desirable room temperature properties, Mg–Al type alloys represent the main share of industrial applications. However, classical Mg alloys such as those of the AZ-type (Mg–Al–Zn, i.e., AZ31, AZ61, AZ80, and AZ91) are restricted to low-temperature structural components as their creep resistance is limited [2]. This is caused by the Al content present in the alloys, often up to approx. 10 weight percent (wt%), leading to the formation of a low-melting phase ($Mg_{17}Al_{12}$). This can be counteracted either by reducing the Al content or by adding elements to Mg–Al alloys which bind the Al into other, higher-melting intermetallic phases (IMPs). By doing so, the amount of $Mg_{17}Al_{12}$ is reduced and the grain boundaries can be stabilized by the simultaneous introduction of IMPs. This led to the development of special alloys where a higher creep resistance has been realized by additions of rare earth [3–5], alkaline earth [2, 6], and silicon additions [7–9].

Mg wrought alloys typically possess lower Al contents compared to cast alloys, therefore often showing better creep performance. At the same time, many of these alloys use finely distributed IMPs for precipitation hardening, further

---

S. Gneiger (✉) · J. A. Nietsch · N. Papenberg
Light Metals Technologies Ranshofen, AIT Austrian Institute of Technology, Lamprechtshausenerstraße 61, 5282 Ranshofen, Austria
e-mail: stefan.gneiger@ait.ac.at

J. A. Nietsch
e-mail: juergen.nietsch@otto-fuchs.com

N. Papenberg
e-mail: nikolaus.papenberg@ait.ac.at

J. A. Nietsch
Otto Fuchs KG, Derschlagerstrasse 26, 58540 Meinerzhagen, Germany

A. Leonard et al. (eds.), *Magnesium Technology 2024*, The Minerals, Metals & Materials Series,
https://doi.org/10.1007/978-3-031-50240-8_18

contributing to creep resistance. Mg–Al–Ca alloys exhibit exceptional strength at room temperature, and their production is straightforward without elaborate heat treatments or demanding processing steps [10, 11]. As a result, these alloys are promising candidates for structural applications. At the same time, the presence of temperature-stable intermetallic phases can play a crucial role in enhancing the creep resistance, consequently expanding their utility to applications characterized by elevated temperatures.

In this work, we investigated the performance of four extruded Mg–Al–Ca alloys at elevated temperatures and compared the results to a standard AZ31B according to ASTM B107 (from now on designated as AZ31). Short-time creep tests as well as tensile tests were conducted at 150 °C, and the microstructure was investigated in the extruded state.

Materials and Methods

Four different Mg–Ca–Al–Mn alloys (AX01, AX11, AX22, and AX55) as well as an Mg–Al–Zn alloy (AZ31), with their nominal chemical compositions given in Table 1, were prepared by gravity casting in a tempered steel mold. Round profiles with a diameter of 10 mm were produced by indirect extrusion at a temperature of 350 °C, and an extrusion ratio of 25:1. Ram speed was set at 0.45 mm/s. Further details on the material preparation are described in [10].

Circular tensile test samples according to DIN 50125 A8 × 40 were manufactured from the profiles and tested at 150 °C using a Zwick Z100 tensile testing machine. Short-time creep experiments based on DIN EN ISO 204 [12] were performed using a deformation dilatometer DIL 805T (Bähr Thermoanalyse GmbH, now TA instruments) on round samples with a cross section of 19.6 mm^2. The experiments were performed at a constant load and a temperature of 150 °C, with nominal stress levels between 48.8 and 152.2 MPa. Details on the test setup and the sample geometry can be found in [13]. The creep limit for 1% plastic elongation as well as the minimum creep rate were analyzed and shown in the results section. The Microstructure was investigated using an optical light microscope (OLM), and a Tescan MIRA3 field emission gun (FEG) scanning electron microscope (Brno, Czech Republic) operated at 15 kV, at a working distance of 15 mm and a beam intensity of 12 (Tescan internal value). A 4-quadrant solid-state backscattered electron (BSE) detector was used for creating the micrographs with different view fields (1000, 500, and 100 µm). Grain sizes of AX11 and AZ31 were measured using the line intersection method with five lines (440 µm long) per alloy. Thermodynamic calculations, using the software Thermo-Calc (Version 2023a) and database TCMG6 (Thermo-Calc Software AB, Solna, Sweden) based on the average values of the compositions given in Table 1, were performed.

Results

Figure 1 illustrates the outcomes of equilibrium thermodynamic calculations conducted for the Mg–Al–Ca alloys. The diagram in the figure presents the ternary Mg–Al–Ca diagram at 150 °C, while the accompanying table provides phase fractions in atomic percentage (at.%) at the same temperature. According to the calculations, all investigated AX alloys are in the α-Mg + C14 (Mg_2Ca) + C15 (Al_2Ca) phase field close to the α-Mg + C14 phase boundary. Therefore, the amount of C14 is somewhat limited, especially when compared to the C15 phase fractions. The amount of the Mn-containing phase (Al_8Mn_5) is solely determined on the Mn-content in the respective alloy. In contrast, the presence of Ca-containing phases (C14 and C15) is significantly dependent on the combined Al and Ca content, starting with 1.1 at.% in AX01 and reaching nearly 9 at.% in alloy AX55.

Figure 2 shows the microstructures of the investigated Mg–Al–Ca alloys and AZ31 in extrusion direction. In AZ31 (e), Al-rich precipitated phases are homogeneously distributed in the microstructure. In the Mg–Al–Ca alloys (a–d), the Ca-containing intermetallic phases (visible as dark particles in the images) are oriented along the extrusion direction. As the combined Al and Ca content rises, there is a corresponding increase in the quantity of these intermetallic phases, which confirms the calculations (Fig. 1). All alloys show a predominantly recrystallized microstructure. AX01 and AZ31 possess a larger grain size, while AX11, AX22, and AX55 consist of a high amount of fine dynamically recrystallized (DRX) grains with dispersed larger structures. This can be attributed to the higher amount of intermetallic

Table 1 Nominal chemical compositions of the investigated alloys; composition of AZ31B according to specification ASTM B107

Alloy	Al (wt%)	Ca (wt%)	Mn (wt%)	Zn (wt%)	Mg
AX01	0.50–0.70	0.55–0.70	0.20–0.30	–	Balance
AX11	1.00–1.10	1.00–1.10	0.20–0.30	–	Balance
AX22	2.20–2.40	2.10–2.40	0.35–0.45	–	Balance
AX55	4.50–5.00	4.40–5.00	0.35–0.47	–	Balance
AZ31	2.50–3.50	–	0.20–0.50	0.60–1.40	Balance

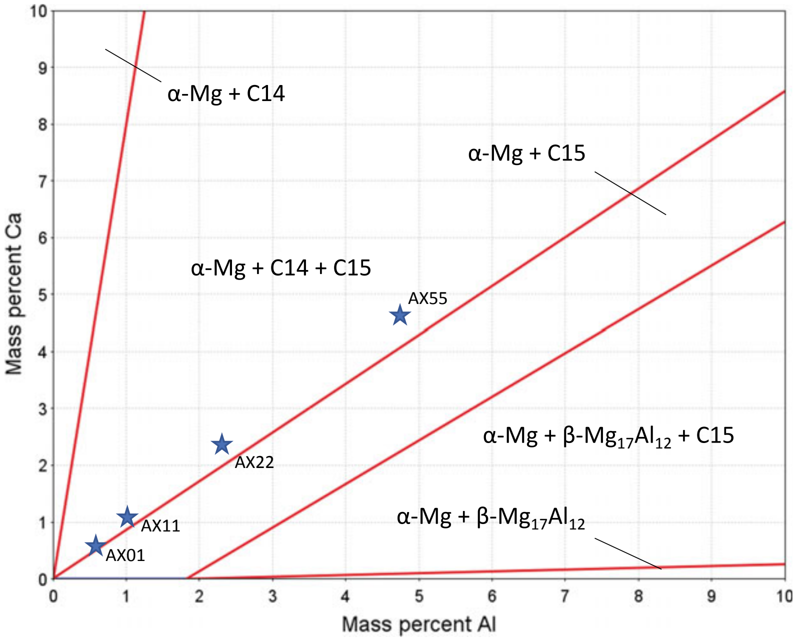

Fig. 1 Isothermal section of ternary Mg–Al–Ca phase diagram at 150 °C with investigated Mg–Al–Ca alloys marked and corresponding phase fractions at 150 °C given in the table

Alloy	α-Mg [at. %]	C14 [at. %]	C15 [at. %]	Al_8Mn_5 [at. %]
AX01	98.66	0.42	0.71	0.22
AX11	97.88	0.50	1.41	0.22
AX22	95.52	0.89	3.24	0.35
AX55	90.88	1.64	7.11	0.36

phases, i.e., Al_2Ca and Al_8Mn_5. The recorded grain sizes for AX01 and AZ31 were 15.6 µm and 14.8 µm, respectively. As for the average sizes of the recrystallized grains in AX11, AX22, and AX55, these values were obtained from the measurements conducted in [10] and are approximately between 2 and 2.5 µm.

Table 2 provides an overview of the tensile tests of the AX alloys performed at 150 °C. Among the alloys tested, the tensile yield strength (YS) ranged from 151.8 to 174.3 MPa, with AX11 achieving the highest YS. Interestingly, AX11 also exhibited the lowest ultimate tensile strength (205.1 MPa) in the same tests.

Figure 3 displays the 1% creep limits of the examined alloys at 150 °C. In the case of Mg–Al–Ca alloys, a distinct trend is visible: as the combined content of Al and Ca increases, the creep resistance decreases. Nevertheless, Mg–Al–Ca alloys exhibited notably high creep resistance across all tested nominal stresses, whereas AZ31 showed inferior performance. At 100 MPa, the time to reach 1% plastic elongation is nearly two orders of magnitude higher for AX01 and AX11 compared to AZ31. Under a stress of 100 MPa, AX01 reached 1% plastic elongation after 66.6×10^3 s. AX11, which is the alloy with the second-best creep resistance, endured 49.8×10^3 s at the same stress level, and AX55 only 6.0×10^3 s. By comparison, the Mg–Al–Zn alloy AZ31 would withstand such high stresses at 150 °C for only 143 s.

The minimum creep rate of the investigated alloys at different applied stresses is shown in Fig. 4. Analogous to the creep limits, AX01 shows the lowest minimum creep rate at all applied stresses, whereas AZ31 shows the highest minimum creep rate. However, all the investigated alloys displayed a similar trend in the minimum creep rate with respect to stress for the tested stress range. Consequently, the Norton–Bailey exponent varies between 6.34 and 6.81, which is an indicator for dislocation creep under the tested stress/temperature conditions.

Figure 5 shows micrographs of (a) AX11 and (b) AX22 after conducted creep tests in the vicinity of the fractured surface. Banded structures of broken and fractured intermetallic phases aligned in extrusion direction are visible for both alloys and are well-known features from the extrusion process. These IMPs are significantly larger in AX22, most likely stemming from the higher amount of alloying elements.

Fig. 2 Microstructures (OLM) of AX alloys and AZ31; extrusion direction (ED) horizontal

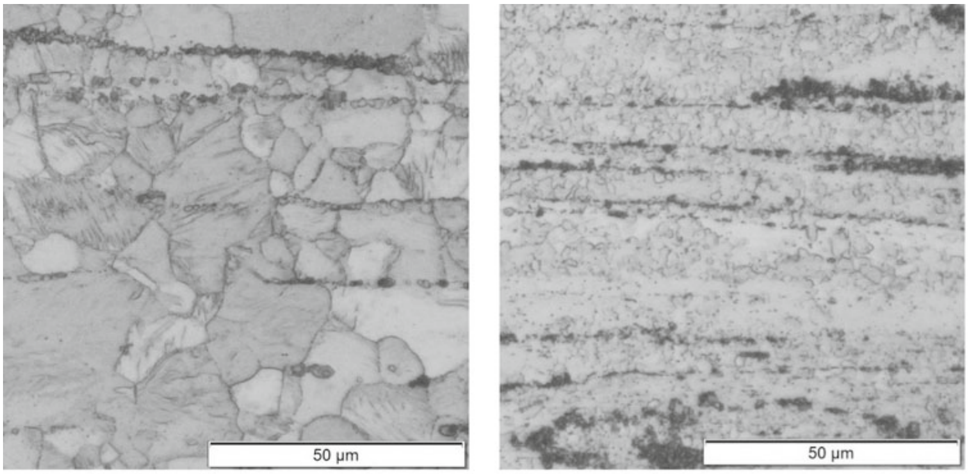

(a) AX01 (b) AX11

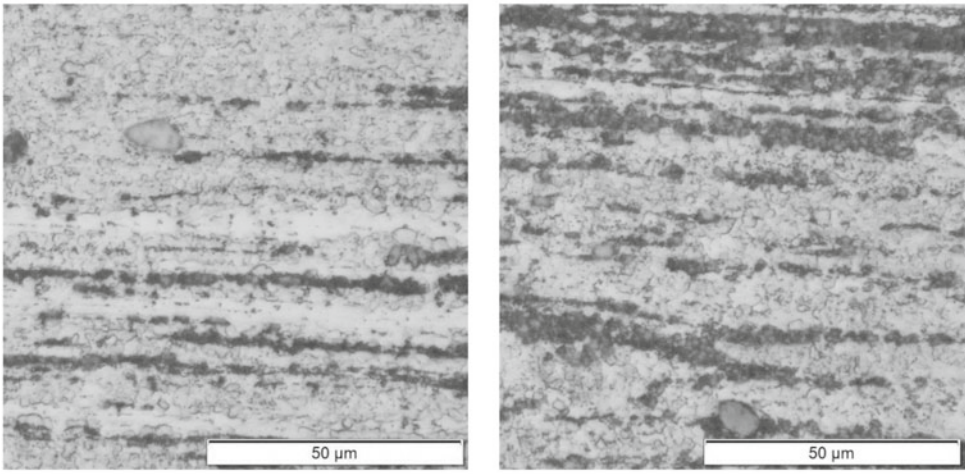

(c) AX22 (d) AX55

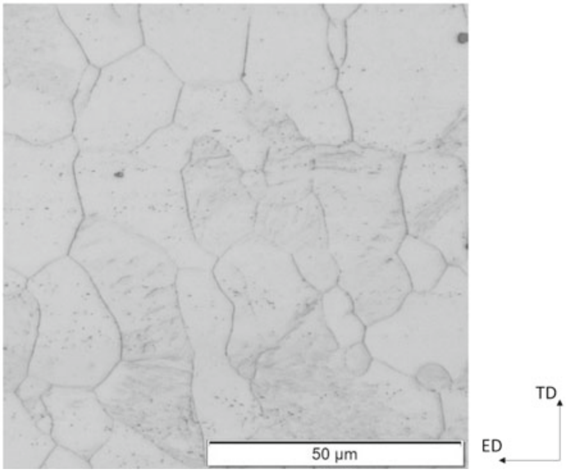

(e) AZ31

Table 2 Results of the elevated temperature tensile tests of Mg–Al–Ca alloys performed at 150 °C

Alloy	YS (MPa)	UTS (MPa)	ε_f (%)
AX01	165.7 ± 1.9	211.6 ± 1.6	28.3 ± 2.1
AX11	174.3 ± 2.1	205.1 ± 5.9	35.3 ± 2.8
AX22	151.8 ± 3.0	220.8 ± 2.6	37.9 ± 1.5
AX55	157.6 ± 1.9	220.2 ± 1.4	31.8 ± 1.9

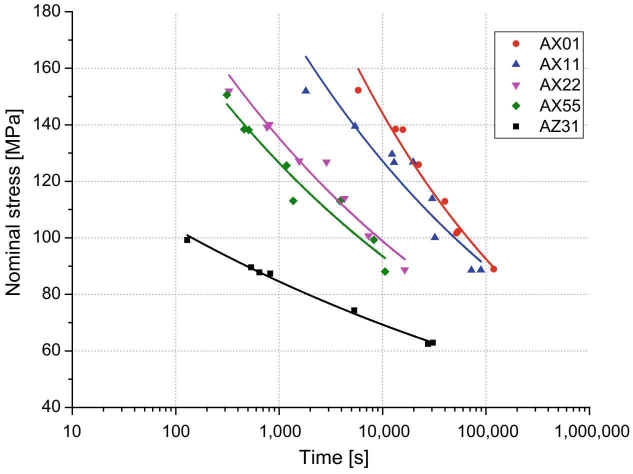

Fig. 3 Creep limits at 150 °C for 1% plastic elongation

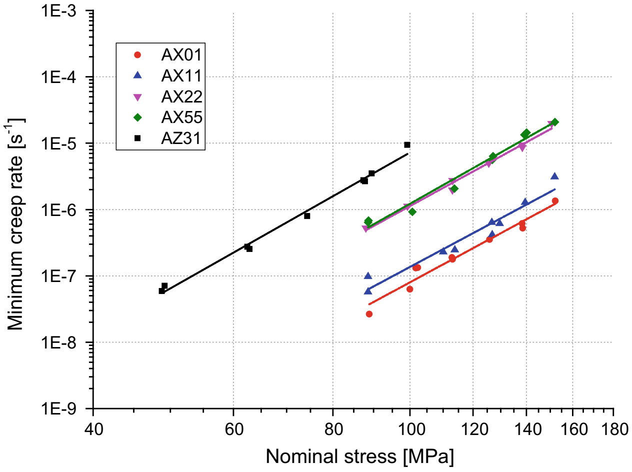

Fig. 4 Minimum creep rate at 150 °C

Discussion

It is well-established that when the grain size decreases, the material's susceptibility to creep increases. This is primarily due to the fact that grain boundaries facilitate grain boundary sliding [14]. Conversely, particles that act as barriers to dislocation glide can increase the creep resistance. Suzuki et al. [15] showed that the precipitation of Al_2Ca plates in the α-Mg matrix can enhance the creep resistance in an Mg–5Al–2–Ca alloy by the factor of ~ 1.5–2. Homma et al. showed the positive effect of an Mn addition (0.3 wt% Mn) to Mg–2Al–2Ca (in wt%) and attributed this to the increased formation of ordered GP zones on the basal plane during creep deformation [16]. Zhu et al. have shown that the addition of 0.32 wt% Mn to an Mg–Al–RE alloy increases the creep resistance significantly due to the formation of nanoscale Al–Mn particles [17]. Zhu et al. [5] implicated that the creep resistance of Mg alloys can be significantly increased by strengthening the α-Mg matrix by solid solution and/or precipitation hardening. However, they indicated that in Mg-RE alloys, the creep resistance is more dependent on the level of solute RE supersaturated in the α-Mg, compared to the effect of intermetallic phases reinforcing the grain boundaries.

Chu et al. [18] conducted a study on extruded Mg–Al–Ca–Mn alloys, including a Mg–5.1Al–5.2Ca–0.7Mn alloy, comparable to the AX55 investigated in our work. At 150 °C their material achieved a YS of 152 MPa, an UTS of 187 MPa, and an ε_f of 13%. While their YS is comparable to our measurements, their UTS and ε_f are noticeably lower. However, analysis of the creep rate (90 MPa and 150 °C) showed a distinct improvement when compared to our material, 26.5×10^{-8} versus $59.8 \times 10^{-8}\ s^{-1}$. These differences, i.e., the lower elongation, UTS, and creep rate, can be a result of the higher grain size (~ 4.5 µm) in this material, which is caused by differences in processing (higher extrusion temperature and lower extrusion ratio) compared to our approach.

Although the thermodynamic calculations shown in this work indicate that all the Ca and Al are bound into intermetallic phases, it is plausible that to some extent these two elements were also dissolved in the α-Mg solid solution. The differences in creep resistance shown in this work can be attributed to a combination of the described effects, as extensively discussed in previous studies [5, 15–17], including grain size, solute content, particle type, and particle size. An allocation of the contributions to the individual effects was not attempted; however, some observations were made:

Even though AX01 and AZ31 share a similar grain size, they exhibit notably different creep behaviors. This disparity can be solely attributed to the varying types and quantities of intermetallic phases present in each respective alloy.

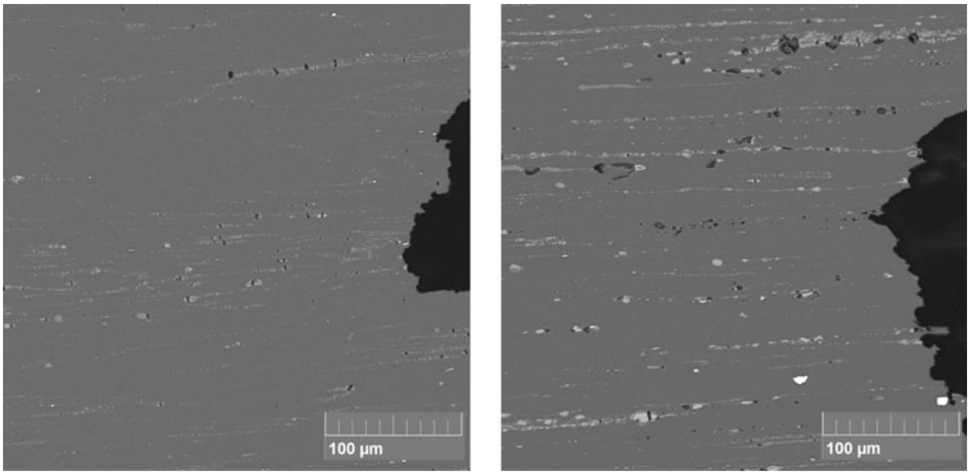

(a) AX11 (b) AX22

Fig. 5 Micrographs (SEM-BSE) of AX11 (**a**) and AX22 (**b**) samples after creep testing

In contrast to the investigations performed by Zhu et al. in [19], our investigations show that the creep resistance decreases with the increasing amount of intermetallic particles, and the Mg–Al–Ca alloy with the lowest amount of alloying elements (AX01) showed the highest creep resistance of all examined alloys. This different behavior can potentially be attributed to the different processes used: While the authors in [19] investigated die-casting alloys, we used extruded material. Due to the deformation during extrusion, the original phases are broken, leading to microcrack formation. These cracks tend to grow at applied stresses and elevated temperature conditions, therefore leading to increased creep. The higher the alloying content, the larger the intermetallic phases in the microstructure. An example for this can be found in the comparison of micrographs of AX11 and AX22 after creep testing (Fig. 5), where the phases in AX22 are larger and therefore provide larger microcracks causing increased crack growth and void coalescence during testing. This trend can be assumed to continue also for the alloys with higher combined Al and Ca content.

Conclusions

Despite their potential, Mg alloys face challenges, particularly in applications involving elevated temperatures. This is primarily due to their susceptibility to creep, an effect where materials deform under constant stress at elevated temperatures. To address this challenge, we investigated a series of extruded Mg–Al–Ca alloys with varying Al and Ca content and compared the results with an extruded AZ31 magnesium alloy. Our study revealed the following key findings:

1. With increasing alloying content, the quantity and size of the Ca-containing intermetallic phases in the Mg–Al–Ca alloys also increased.
2. Despite the very different chemical compositions, all alloys show similar tensile strengths at 150 °C.
3. The intermetallic phases (IMPs) found in the Mg–Al–Ca alloys are arranged along the extrusion direction, stabilizing the grains, and therefore contributing to improved creep behavior.
4. Remarkably, the creep resistance increased with decreasing Al and Ca content in the alloys. This is likely attributed to the larger size of IMPs resulting in the formation of larger microcracks in the higher alloyed materials.
5. The Mg–Al–Ca alloys demonstrated superior creep resistance when compared to AZ31.

In summary, our study highlights the influence of alloy composition, microstructure, and grain size in determining the creep resistance of magnesium alloys. While traditional Mg–Al–Zn alloys are constrained in their application due to limited creep resistance, our findings suggest that tailored Mg–Al–Ca alloys, especially those with lower alloying content, offer improved creep performance and promise for high-temperature applications.

Acknowledgements The authors thankfully acknowledge the work done by the technical staff at the LKR Ranshofen and Aurel Arnoldt for his assistance in making the SEM images.

Funding This research was performed within the project “Data-T-Rex” (Wi-2021-305676/13-Au), co-financed by research subsidies granted by the government of Upper Austria.

References

1. Rothe R, Hameyer K. Life expectancy calculation for electric vehicle traction motors regarding dynamic temperature and driving cycles. 2011 IEEE Int. Electr. Mach. Drives Conf. IEMDC, 2011, p. 1306–9. https://doi.org/10.1109/IEMDC.2011.5994793.
2. Pekguleryuz MO, Baril E. Creep Resistant Magnesium Diecasting Alloys Based on Alkaline Earth Elements. Mater Trans 2001;42:1258–67. https://doi.org/10.2320/matertrans.42.1258.
3. Powell BR, Rezhets V, Balogh MP, Waldo RA. Microstructure and creep behavior in AE42 magnesium die-casting alloy. JOM 2002;54:34–8. https://doi.org/10.1007/BF02711864.
4. Nami B, Shabestari SG, Razavi H, Mirdamadi Sh, Miresmaeili SM. Effect of Ca, RE elements and semi-solid processing on the microstructure and creep properties of AZ91 alloy. Mater Sci Eng A 2011;528:1261–7. https://doi.org/10.1016/j.msea.2010.10.004.
5. Zhu SM, Gibson MA, Easton MA, Nie JF. The relationship between microstructure and creep resistance in die-cast magnesium–rare earth alloys. Scr Mater 2010;63:698–703. https://doi.org/10.1016/j.scriptamat.2010.02.005.
6. Jing B, Yangshan S, Shan X, Feng X, Tianbai Z. Microstructure and tensile creep behavior of Mg–4Al based magnesium alloys with alkaline-earth elements Sr and Ca additions. Mater Sci Eng A 2006;419:181–8. https://doi.org/10.1016/j.msea.2005.12.017.
7. Dargusch MS, Dunlop GL, Bowles AL, Pettersen K, Bakke P. The effect of silicon content on the microstructure and creep behavior in die-cast magnesium AS alloys. Metall Mater Trans A 2004;35:1905–9. https://doi.org/10.1007/s11661-004-0099-3.
8. Mohammadi Mazraeshahi E, Nami B, Miresmaeili SM, Tabatabaei SM. Effect of Si on the creep properties of AZ61 cast magnesium alloy. Mater Des 2015;76:64–70. https://doi.org/10.1016/j.matdes.2015.03.021.
9. Blum W, Zhang P, Watzinger B, Grossmann B v, Haldenwanger HG. Comparative study of creep of the die-cast Mg-alloys AZ91, AS21, AS41, AM60 and AE42. Mater Sci Eng A 2001;319–321:735–40. https://doi.org/10.1016/S0921-5093(00)02016-5.
10. Gneiger S, Papenberg NP, Arnoldt AR, Schlögl CM, Fehlbier M. Investigations of High-Strength Mg–Al–Ca–Mn Alloys with a Broad Range of Ca+Al Contents. Materials 2021;14:5439. https://doi.org/10.3390/ma14185439.
11. Xu SW, Oh-ishi K, Kamado S, Uchida F, Homma T, Hono K. High-strength extruded Mg–Al–Ca–Mn alloy. Scr Mater 2011;65:269–72. https://doi.org/10.1016/j.scriptamat.2011.04.026.
12. DIN EN ISO 204:2019–04, Metallische Werkstoffe_- Einachsiger Zeitstandversuch unter Zugbeanspruchung_- Prüfverfahren (ISO_204:2018); Deutsche Fassung EN_ISO_204:2018. Beuth Verlag GmbH; n.d. https://doi.org/10.31030/2853768.
13. Nietsch JA, Papenberg NP, Cerny A, Ott AC, Grabner F, Gneiger S. Applicability of a deformation dilatometer for short time creep experiments of magnesium alloys. Mater Test 2023;65:652–61. https://doi.org/10.1515/mt-2022-0339.
14. Raynor GV. The physical metallurgy of magnesium and its alloys. New York: Pergamon Press; 1959.
15. Suzuki A, Saddock ND, TerBush JR, Powell BR, Jones JW, Pollock TM. Precipitation Strengthening of a Mg-Al-Ca–Based AXJ530 Die-cast Alloy. Metall Mater Trans A 2008;39:696–702. https://doi.org/10.1007/s11661-007-9455-4.
16. Homma T, Nakawaki S, Oh-ishi K, Hono K, Kamado S. Unexpected influence of Mn addition on the creep properties of a cast Mg–2Al–2Ca (mass%) alloy. Acta Mater 2011;59:7662–72. https://doi.org/10.1016/j.actamat.2011.08.049.
17. Zhu SM, Abbott TB, Gibson MA, Nie JF, Easton MA. The influence of minor Mn additions on creep resistance of die-cast Mg–Al–RE alloys. Mater Sci Eng A 2017;682:535–41. https://doi.org/10.1016/j.msea.2016.11.075.
18. Chu A, Zhao Y, Ud-Din R, Hu H, Zhi Q, Wang Z. Microstructure and Properties of Mg–Al–Ca–Mn Alloy with High Ca/Al Ratio Fabricated by Hot Extrusion. Materials 2021;14:5230. https://doi.org/10.3390/ma14185230.
19. Zhu S, Easton MA, Abbott TB, Nie J-F, Dargusch MS, Hort N, et al. Evaluation of Magnesium Die-Casting Alloys for Elevated Temperature Applications: Microstructure, Tensile Properties, and Creep Resistance. Metall Mater Trans A 2015;46:3543–54. https://doi.org/10.1007/s11661-015-2946-9.

Cryogenic Deformation Behavior of a Dual-Phase Mg–Li Alloy Investigated by In-Situ Neutron Diffraction

Wu Gong, Reza Gholizadeh, Takuro Kawasaki, Kazuya Aizawa,
and Stefanus Harjo

Abstract

Mg and its alloys commonly exhibit inadequate formability due to the limited availability of deformation modes in hcp phase. The addition of Li can stabilize a bcc phase in Mg alloys at room temperature, resulting in dual-phase (hcp + bcc) Mg–Li alloys that possess excellent formability. However, these Mg-Li alloys exhibit poor work-hardening ability due to the dislocation recovery resulting in the low strength at room temperature. Considering that the dislocation recovery can be suppressed at cryogenic temperatures and the deformation mechanisms may vary with temperature, we tried to investigate the deformation behavior of a commercial LZ91 alloy (Mg–9Li–1Zn, wt%) at cryogenic temperatures. In-situ neutron diffraction experiments during tensile deformation at 20, 77, and 298 K were performed by a time-of-flight engineering neutron diffractometer "TAKUMI" at J-PARC. The temperature-dependent deformation mechanisms in LZ91 alloy will be discussed based on the evolutions of phase stress, peak width, and texture during deformation.

Keywords

Cryogenic deformation behavior • Mg–Li alloys • Neutron diffraction

Extended Abstract

Mg and its alloys generally exist as a single hcp crystal structure at room temperature. It is widely recognized that the application of Mg alloys is hindered by their limited formability at room temperature, primarily attributable to the scarcity of readily activated deformation modes within the hcp phase. The addition of Li in Mg alloy can stable the bcc phase at room temperature [1], and these dual-phase (hcp + bcc) Mg–Li alloys exhibit excellent formability [2]. The Li-enriched bcc phase has been frequently considered as the origin for improving formability. However, these Mg-Li alloys show poor work-hardening ability and the resultant low strength at room temperature [3]. Considering that the dislocation recovery can be suppressed by decreasing the deformation temperature and the activity of deformation mode may be changed with temperature, we investigated the deformation behavior of a commercial LZ91 magnesium alloy at cryogenic temperatures using in-situ neutron diffraction.

The commercial LZ91 alloy (Mg–9wt%Li–1wt%Zn) in the extruded condition was used in this study. Cylindrical tensile specimens with a gage diameter of 6 mm and a length of 12 mm were cut from the as-extruded rods with the loading direction parallel to the extrusion direction for in-situ neutron diffraction experiments. *In-situ* neutron diffraction during monotonic tensile deformation at 20, 77, and 298 K with an initial strain rate of 2.2×10^{-5} s^{-1} was performed by a time-of-flight engineering neutron diffractometer "TAKUMI" at J-PARC [4]. Strains were evaluated precisely by the extensometer and the temperatures were monitored by two Cernox temperature sensors fixed at the two ends of the specimen.

Figure 1a shows the true stress–strain curves of the specimens deformed at 298 K, 77 K, and 20 K, respectively. Decreasing the deformation temperature resulted in an increase in yield stress (90 MPa → 130 MPa → 189 MPa). Moreover, a remarkable work hardening occurred at 77 and

---

W. Gong (✉) · T. Kawasaki · K. Aizawa · S. Harjo
J-PARC Center, Japan Atomic Energy Agency, Ibaraki, 319-1195, Japan
e-mail: wu.gong@j-parc.jp

R. Gholizadeh
Department of Materials Science and Engineering, Kyoto University, Kyoto, 606-8501, Japan

A. Leonard et al. (eds.), *Magnesium Technology 2024*, The Minerals, Metals & Materials Series,
https://doi.org/10.1007/978-3-031-50240-8_19

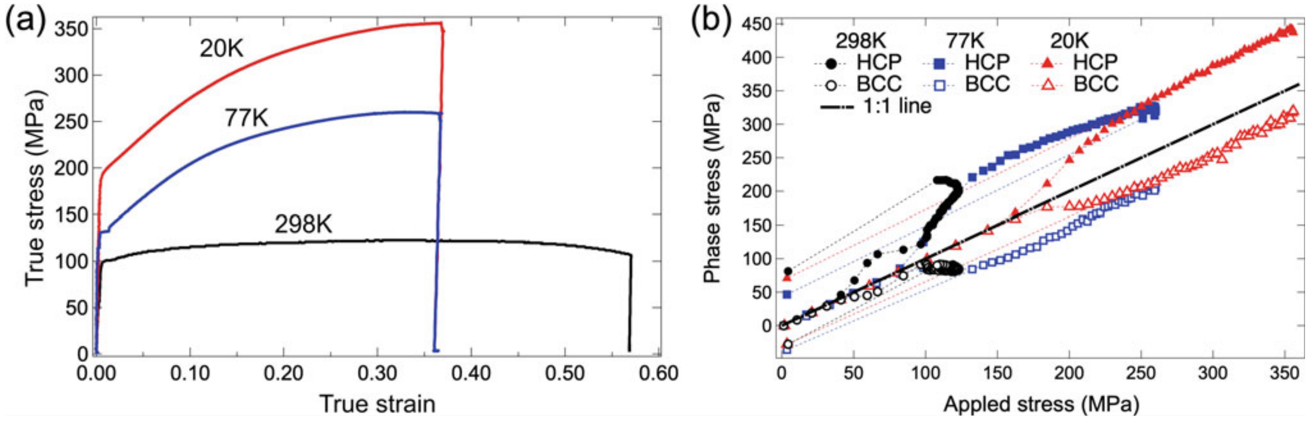

Fig. 1 **a** True stress–strain curves and **b** stress partitioning between hcp and bcc phases in LZ91 alloy deformed at 298, 77, and 20 K

20 K improved the ultimate stress and uniform elongation simultaneously as compared to 298 K. Figure 1b shows the stress partitioning between hcp and bcc at various temperatures, demonstrating the features as follows:

- The hcp phase shared higher stress than bcc phase, indicating the hcp phase to be the hard phase in LZ91 alloy, while the bcc phase played as the soft phase for accommodating more plastic strain.
- The stress partitioning occurred at the stress lower than the macroscopic yield stress at all temperatures.
- After macroscopic yielding, the phase stress of bcc phase hardly increased at 298 K, but increased consistently at 77 and 20 K. This suggests that the macroscopic work hardening can be attributed to the work-hardening capacity of bcc phase at cryogenic temperature.

The deformation temperature dependence of macroscopic stress–strain response can be attributed to the changes in lattice stress partitioning and evolutions of dislocation density and texture, which will be shown and discussed in the presentation.

References

1. Massalski, TB (1990) Binary Alloy Phase Diagrams, 2nd ed. ASM International, Materials Park, OH, p1487
2. Takuda H, Enami T, Kubota K, Hatta N (2000) The formability of a thin sheet of Mg–8.5 Li–1Zn alloy. J. Mater. Process. Technol. 101 (1–3): 281–286.
3. Peng X, Liu W, Wu G, Ji H, Ding W (2022) Plastic deformation and heat treatment of Mg-Li alloys: a review. J. Mater. Sci. Technol. 99: 193–206.
4. Harjo S, Ito T, Aizawa K, Arima H, Abe J, Moriai A, Iwahashi T, Kamiyama T (2011) Current status of engineering materials diffractometer at J-PARC. Mater. Sci. Forum. 681: 443–448

Experimental Observation of $\langle c+a \rangle$ Dislocations on $\{\bar{1}2\bar{1}1\}$ Plane in Submicron Magnesium

Fei Liu, Yu-Han Tian, Yao-Feng Li, Bo-Yu Liu, and Zhi-Wei Shan

Abstract

Pyramidal $\langle c+a \rangle$ dislocation slip is the major deformation mode for accommodating plastic strain along *c*-axis in magnesium. Understanding its fundamental behaviors is crucial for revealing the plastic deformation mechanisms of magnesium and its alloys. Pyramidal $\langle c+a \rangle$ dislocations are usually considered to glide on $\{10\bar{1}1\}$ and $\{11\bar{2}2\}$ planes. By conducting in-situ compression test on submicron single-crystal magnesium pillars and three-dimensional image reconstruction, we find that the configurations of $\langle c+a \rangle$ dislocations are complicated, even for a single dislocation, its different segments can locate on multiple planes. We also find that some segments of the $\langle c+a \rangle$ dislocations can locate on $\{\bar{1}2\bar{1}1\}$ planes, indicating $\{\bar{1}2\bar{1}1\}$ possible slip planes for $\langle c+a \rangle$ dislocations in magnesium.

Keywords

Magnesium • Dislocation • TEM • 3D reconstruction • Slip plane

Extended Abstract

In HCP metals, the major slip system for accommodating *c*-axis strain is $\langle c+a \rangle$ dislocation slip, which can provide five independent slip systems and coordinate the strain along the *c*-axis [1, 2]. However, $\langle c+a \rangle$ dislocations always exhibit very complicated structures, making the study on this important slip system difficult [3–6]. As we know that slip plane is one key element of a slip system, so precisely knowing the slip plane of $\langle c+a \rangle$ dislocations is important for us to understand the fundamental behaviors of these dislocations. During the past decades, many efforts have been made to determine whether $\langle c+a \rangle$ dislocation locates (or glides) mainly on $\{10\bar{1}1\}$ plane (Pyramidal I) or $\{\{11\bar{2}2\}$ plane (Pyramidal II).

In the early work, according to TEM and slip trace analysis, $\langle c+a \rangle$ dislocations were confirmed in magnesium under *c*-axis compression and considered as slipping on $\{11\bar{2}2\}$ plane [3, 7], which was supported by an in-situ neutron diffraction experiment in AZ31 Mg alloys [8]. Whereas for the same experimental results [3], Fan et al. [4] reanalyzed and thought that the slip plane is actually $\{10\bar{1}1\}$ plane. Pyramidal I slip was also observed in single-crystal magnesium compressed along the *c*-axis [9] and supported by simulations based on molecular dynamics (MD) [4], multiscale dislocation dynamics plasticity (MDDP) [10], and three-dimensional discrete dislocation dynamics (3D-DDD) [11]. Additionally, there were also some works thought that $\langle c+a \rangle$ dislocation probably cross-slip from Pyramidal I to Pyramidal II [12–14]. More interestingly, a recent atomistic simulation, by using the LAMMS code [15] and the revised MEAM potential [16], observed that $\langle c+a \rangle$ dislocations slip on $\{11\bar{2}1\}$, which has a low Peierls stress and generalized stacking fault energy (GSFE), indicating that the slip system might be an easy mode [17]. It was found that $\langle c+a \rangle$ dislocations on Pyramidal I or II not only cross-slip to Pyramidal I, but cross-slip to $\{\overline{11}21\}$ planes under stress [17].

F. Liu
Guizhou Key Laboratory of Materials Mechanical Behavior and Microstructure, National and Local Joint Engineering Laboratory for High-Performance Metal Structure Material and Advanced Manufacturing Technology, College of Materials and Metallurgy, Guizhou University, Guiyang, 550025, China

Y.-H. Tian · Y.-F. Li · B.-Y. Liu (✉) · Z.-W. Shan (✉)
Engineering Research Center for Magnesium-Based New Materials, Center for Advancing Materials Performance From the Nanoscale (CAMP-Nano), State Key Laboratory for Mechanical Behavior of Materials, Xi'an Jiaotong University, Xi'an, 710049, China
e-mail: boyuliu@xjtu.edu.cn

Z.-W. Shan
e-mail: zwshan@xjtu.edu.cn

A. Leonard et al. (eds.), *Magnesium Technology 2024*, The Minerals, Metals & Materials Series,
https://doi.org/10.1007/978-3-031-50240-8_20

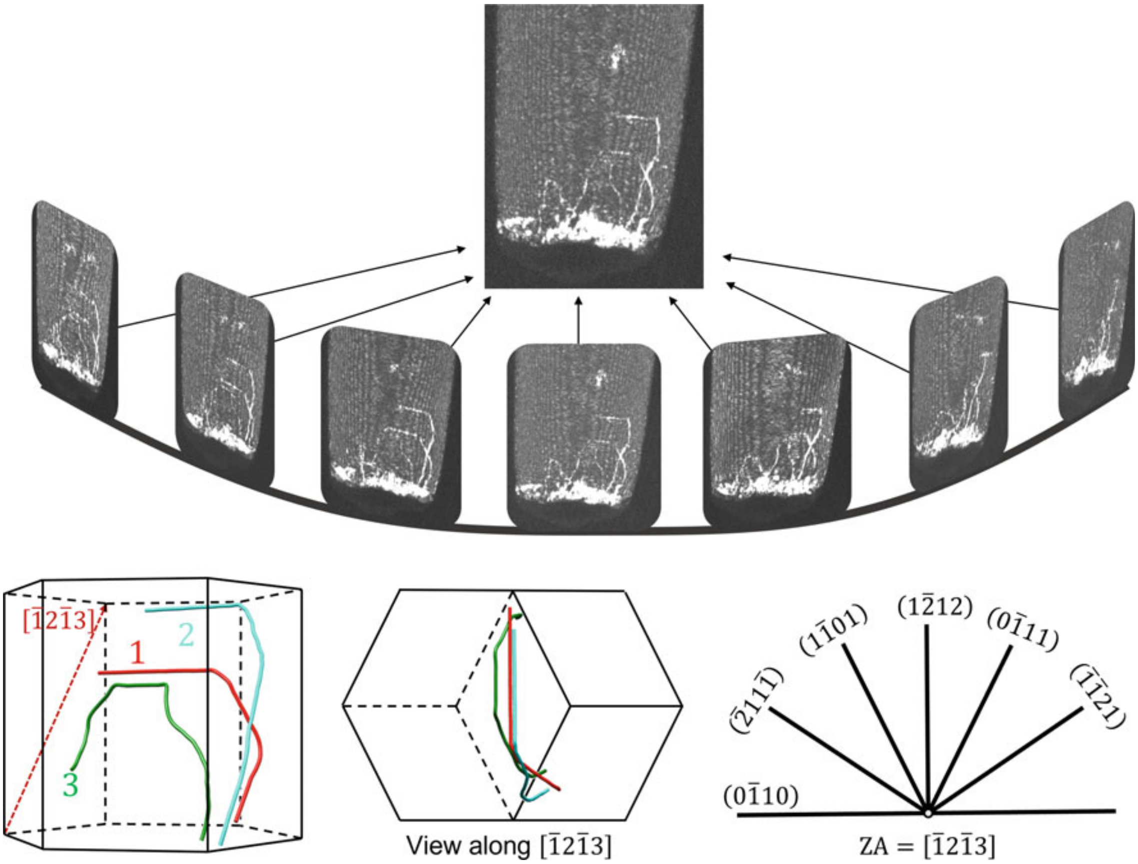

Fig. 1 3D image reconstruction for determining the slip plane of dislocations with complicated configuration. A series of weak beam dark field images under $\boldsymbol{g} = (0002)$ were acquired with tilt angle from − 32° to + 29° at the increment of 1°. These images were aligned and reconstructed by the IMOD software [18] and these reconstructed dislocations were visualized by UCSF Chimera [19]

However, $\{\overline{11}21\}$ slip systems and their cross-slip have hitherto $\{\overline{11}21\}$ not been considered and absence of direct experimental evidence. In addition, the mobility of $\langle c+a \rangle$ dislocations on $\{\overline{11}21\}$ is also unclear.

By conducting in-situ TEM tests on submicron magnesium pillars and 3D image reconstruction, we find that the configurations of $\langle c+a \rangle$ dislocations are very complicated. Even for a single $\langle c+a \rangle$ dislocation, its different segments can locate on different planes. More surprisingly, some segments of the $\langle c+a \rangle$ dislocations are found to locate on $\{\bar{1}2\bar{1}1\}$ planes, indicating that $\{\bar{1}2\bar{1}1\}$ plane can be a possible slip plane for $\langle c+a \rangle$ dislocations, which has never been experimentally observed in magnesium before.

Our findings can help to build a clearer image of this important slip system, and to better understand the complicated structure of $\langle c+a \rangle$ dislocations. Our methods combining in-situ TEM and 3D image reconstruction can be generalized to study the dislocation slip behavior in other materials, the dislocation-precipitate interaction, the dislocation-twinning interaction, or the dislocation-grain boundary interaction (Fig. 1).

Acknowledgements This work is supported by the National Natural Science Foundation of China (No. 52022076, 51971168, 52301137).

References

1. S. Agnew, D. Brown, C. Tome, Validating a polycrystal model for the elastoplastic response of magnesium alloy AZ31 using in situ neutron diffraction, Acta Materialia 54(18) (2006) 4841–4852.
2. M.H. Yoo, Slip, twinning, and fracture in hexagonal close-packed metals, Metallurgical Transactions A 12(3) (1981) 409–418.
3. T. Obara, H. Yoshinga, S. Morozumi, $\{11\bar{2}2\}\langle\overline{11}23\rangle$ Slip system in magnesium, Acta Metallurgica 21(7) (1973) 845–853.
4. H. Fan, J.A. El-Awady, Towards resolving the anonymity of pyramidal slip in magnesium, Materials Science and Engineering: A 644 (2015) 318–324.
5. B.Y. Liu, F. Liu, N. Yang, X.B. Zhai, L. Zhang, Y. Yang, B. Li, J. Li, E. Ma, J.F. Nie, Z.W. Shan, Large plasticity in magnesium mediated by pyramidal dislocations, Science 365(6448) (2019) 73–75.
6. B.-Y. Liu, F. Liu, B. Li, J.-F. Nie, Z.-W. Shan, In situ TEM investigation of ≺c + a≻ dislocations in magnesium, Magnesium Technology 2020 (2020) 135–139.
7. J.F. Stohr, J.P. Poirier, Electron-microscope study of pyramidal slip $\{11\bar{2}2\}\langle 11\bar{2}3\rangle$ in magnesium, Philos. Mag. 25(6) (1972) 1313–1329.

8. O. Muránsky, D.G. Carr, M.R. Barnett, E.C. Oliver, P. Šittner, Investigation of deformation mechanisms involved in the plasticity of AZ31 Mg alloy: In situ neutron diffraction and EPSC modelling, Materials Science and Engineering: A 496(1) (2008) 14–24.
9. K.Y. Xie, Z. Alam, A. Caffee, K.J. Hemker, Pyramidal I slip in c-axis compressed Mg single crystals, Scripta Materialia 112 (2016) 75–78.
10. M.A. Shehadeh, N.K. Shatarat, W. Jaber, Modeling the mechanical response and microstructure evolution of magnesium single crystals under c-axis compression, Computational Materials Science 138 (2017) 236–245.
11. K. Srivastava, J.A. El-Awady, Deformation of magnesium during c-axis compression at low temperatures, Acta Materialia 133 (2017) 282–292.
12. M. Itakura, H. Kaburaki, M. Yamaguchi, T. Tsuru, Novel cross-slip mechanism of pyramidal screw dislocations in magnesium, Physical Review Letters 116(22) (2016) 225501.
13. J. Geng, M.F. Chisholm, R.K. Mishra, K.S. Kumar, An electron microscopy study of dislocation structures in Mg single crystals compressed along [0001] at room temperature, Philos. Mag. 95 (35) (2015) 3910–3932.
14. J. Jain, P. Cizek, K. Hariharan, Transmission electron microscopy investigation on dislocation bands in pure Mg, Scripta Materialia 130 (2017) 133–137.
15. S. Plimpton, Fast Parallel Algorithms for Short-Range Molecular Dynamics, Journal of Computational Physics 117(1) (1995) 1–19.
16. Z. Wu, M.F. Francis, W.A. Curtin, Magnesium interatomic potential for simulating plasticity and fracture phenomena, Model. Simul. Mater. Sci. Eng. 23 (2015) 015004.
17. J. Zhang, Y. Zhang, J.A. El-Awady, T. Yizhe, The plausibility of dislocation slip on $\left\{\bar{1}2\bar{1}1\right\}$ planes in Mg, Scripta Materialia 156 (2018) 19–22.
18. J.R. Kremer, D.N. Mastronarde, J.R. McIntosh, Computer visualization of three-dimensional image data using IMOD, Journal of structural biology 116(1) (1996) 71–6.
19. E.F. Pettersen, T.D. Goddard, C.C. Huang, G.S. Couch, D.M. Greenblatt, E.C. Meng, T.E. Ferrin, UCSF Chimera—a visualization system for exploratory research and analysis, Journal of computational chemistry 25(13) (2004) 1605–12.

In-Situ Dynamic Investigation of Plastic Deformation Carriers in Magnesium and the Effects of Multifield

Bo-Yu Liu, Fei Liu, Jin Zhang, Yao-Feng Li, and Zhi-Wei Shan

Abstract

The processing of magnesium and its alloys, as well as the deformation and damage during service, are closely related to the behavior of plastic deformation carriers, such as dislocation nucleation and slip, twinning formation and growth, interface formation and migration, and the interaction between various deformation carriers. Meanwhile, the behavior of these deformation carriers is also significantly influenced by alloying elements, precipitates, as well as various environmental factors involved in processing and service, such as high temperature, atmosphere, and electric fields. In this study, in-situ transmission electron microscopy with quantitative nanomechanical testing was employed to investigate the behavior of dislocations, twins, and grain boundaries in magnesium, as well as their response to alloying elements, precipitates, temperature, hydrogen, and electric fields. The aim is to provide fundamental data for understanding of the deformation and damage mechanisms of magnesium and to contribute to the development of high-performance magnesium alloys.

Keywords

Magnesium • In-situ TEM • Multifield • Plastic deformation • Mechanical properties

Extended Abstract

Magnesium is the lightest metal structural material with broad applications in fields such as aerospace, transportation, and electronics [1–5]. The manufacturing and processing of magnesium and magnesium alloy products often involve deformation processes, and during service, deformation and damage are also commonly involved [6–11]. The deformation and damage of magnesium, as well as other metal structural materials, are closely related to the behavior of internal plastic deformation carriers, such as dislocation nucleation and glide [12], twin formation and growth [13, 14], interface/grain-boundary formation and migration [15], and interactions between various deformation carriers. Additionally, the behavior of these deformation carriers can be significantly influenced by alloying elements [16–18], precipitates [19, 20], and various environmental factors encountered during preparation and service, such as high temperature [21, 22], atmosphere [23], electric fields [24, 25] and their combinations.

In recent years, our research team has employed in-situ transmission electron microscopy with quantitative nanomechanical testing (based on Bruker Hysitron PicoIndenter series) to study the behavior of dislocations and twins, and other plastic deformation carriers in magnesium, and their responses to alloying elements, precipitates, high temperature, atmosphere, and electric fields. In the following, we demonstrate several typical examples.

For the effects of alloying elements on dislocation and twinning behaviors, we chose Mg–Y as model materials because Y is a typical alloying element that is believed can enhance plasticity but the underlying mechanism still requires further exploration, especially through experiment. By compressing Mg–Y nanopillars along c-axis that is the hardest orientation of Mg crystal, we found that the pyramidal $\langle c + a \rangle$ dislocations exhibit higher mobility and a more significant multiplication behavior compared to that in pure Mg, leading to increased strength, plasticity, and work

---

B.-Y. Liu (✉) · F. Liu · J. Zhang · Y.-F. Li · Z.-W. Shan (✉)
Engineering Research Center for Magnesium-Based New Materials, Center for Advancing Materials Performance From the Nanoscale (CAMP-Nano), State Key Laboratory for Mechanical Behavior of Materials, Xi'an Jiaotong University, Xi'an, 710049, China
e-mail: boyuliu@xjtu.edu.cn

Z.-W. Shan
e-mail: zwshan@xjtu.edu.cn

A. Leonard et al. (eds.), *Magnesium Technology 2024*, The Minerals, Metals & Materials Series,
https://doi.org/10.1007/978-3-031-50240-8_21

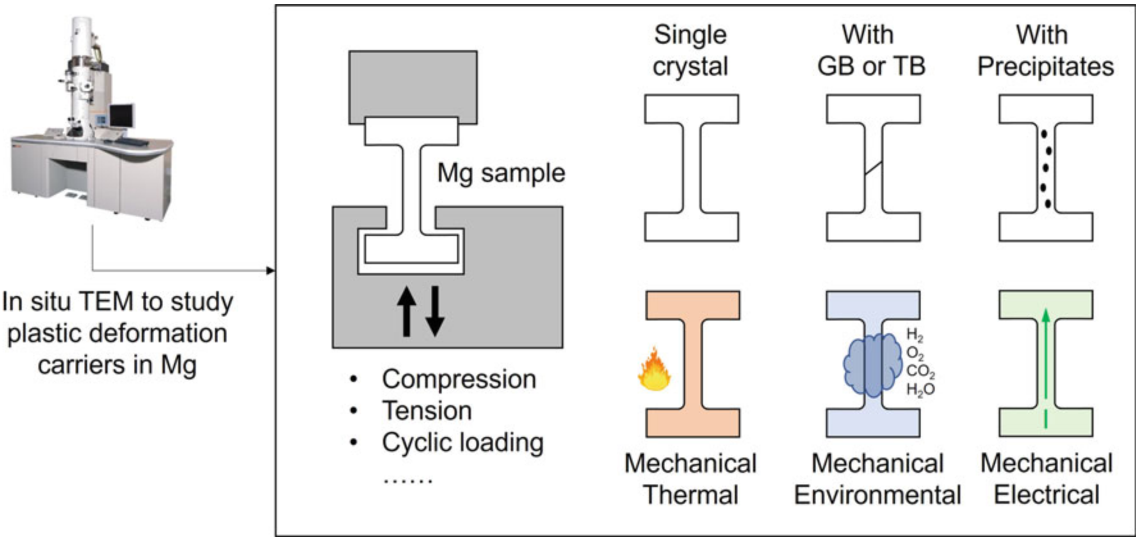

Fig. 1 In-situ study of the plastic deformation carriers in Mg under multi-field coupling. Transmission electron microscopy-based in-situ quantitative nanomechanical testing to study the behavior of dislocations and twins in magnesium, and their responses to alloying elements, precipitates, high temperature, atmosphere, and electric fields

hardening. For $\{10\bar{1}2\}$ twinning that is always largely activated under quite low stress and leads to low yield strength, we found that the stress required for the formation of $\{10\bar{1}2\}$ twins and twin boundary migration in Mg–Y pillar is higher than that in pure Mg, suggesting that Y can suppress deformation twinning in Mg.

Another typical result is about electric-pulse enhancing the plasticity of pure Mg. The application of electricity can significantly improve the formability of metals with limited room-temperature plasticity, which is known as electro-plasticity. For Mg, which has limited plasticity at room temperature, its processing can be benefited by electro-plasticity. However, there is still a lack of understanding on the behaviors of deformation carriers under electric current. The present work investigated the electro-plasticity of Mg by in-situ TEM compression along its c-axis. We found that electrical-pulses can facilitate the smooth and continuous glide of pyramidal $\prec c + a \succ$ dislocations, both for the edge and screw type dislocations. Those edge type pyramidal dislocations are difficult to move at room temperature without electrical-pulses. As a result, the yield strength and flow stress are reduced. Controlled experiments demonstrated that Joule heating and electron wind force are not the primary causes of dislocation motion, suggesting the existence of other electrical effects that require further investigation.

The results of the present study are expected to provide insights into the understanding of the deformation and damage mechanisms of magnesium, thereby contributing to the development of high-performance magnesium alloys Fig. 1.

Acknowledgements This work is supported by the National Natural Science Foundation of China (No. 52022076, 51971168).

References

1. Yang Y, Xiong X, Chen J, et al. Research advances in magnesium and magnesium alloys worldwide in 2020[J]. Journal of Magnesium and Alloys, 2021, 9(3): 705–747.
2. Song J, She J, Chen D, et al. Latest research advances on magnesium and magnesium alloys worldwide [J]. Journal of Magnesium and Alloys, 2020, 8(1): 1–41.
3. Pan H, Qin G, Huang Y, et al. Development of low-alloyed and rare-earth-free magnesium alloys having ultra-high strength [J]. Acta Materialia, 2018, 149: 350–363.
4. Feng X H, Jia H M, Luo T J, et al. Microstructures and mechanical properties of extruded high-purity magnesium [J]. Materials Science Forum, 2015, 816: 439–445.
5. Yu H, Xin Y, Wang M, et al. Hall-Petch relationship in Mg alloys: A review [J]. Journal of Materials Science and Technology, 2018, 34(2): 248–256.
6. Kelley E W, Hosford W F. Plane-strain compression of magnesium and magnesium alloy crystals [J], Trans Met Soc AIME, 1968, 242(1): 5–13.
7. Caceres C H, Rovera D M. Solid solution strengthening in concentrated Mg-Al alloys[J]. Journal of Light Metals, 2001.
8. Kula A, Jia X, Mishra R K, et al. Flow stress and work hardening of Mg–Y alloys [J]. International Journal of Plasticity, 2017, 92: 96–121.
9. Li L, Wang L Y, Wang J, et al. In situ synchrotron X-ray study of the mechanical properties of pure Mg produced by powder metallurgy [J]. Metals, 2020, 10(9): 1198.
10. Sukedai E, Yokoyama T. Investigation of tensile–compressive yield asymmetry and the role of deformation twin in extruded pure magnesium [J]. International Journal of Materials Research, 2010, 101(6): 736–740.

11. Yamashita A, Horita Z, Langdon T G. Improving the mechanical properties of magnesium and a magnesium alloy through severe plastic deformation [J]. Materials Science and Engineering: A, 2001, 300(1–2): 142–147.
12. Liu B Y, Liu F, Yang N, et al. Large plasticity in magnesium mediated by pyramidal dislocations [J]. Science, 2019, 365(6448): 73–75.
13. Liu B Y, Wang J, Li B, et al. Twinning-like lattice reorientation without a crystallographic twinning plane [J]. Nature Communications, 2014, 5(1): 3297.
14. Jeong J, Alfreider M, Konetschnik R, et al. In-situ TEM observation of $\{10\bar{1}2\}$ twin-dominated deformation of Mg pillars: Twinning mechanism, size effects and rate dependency [J]. Acta Materialia, 2018, 158: 407–421.
15. Liu B Y, Zhang Z, Liu F, et al. Rejuvenation of plasticity via deformation graining in magnesium [J]. Nature Communications, 2022, 13(1): 1060.
16. Wu Z, Ahmad R, Yin B, et al. Mechanistic origin and prediction of enhanced ductility in magnesium alloys [J]. Science, 2018, 359 (6374): 447–452.
17. Sandlöbes S, Zaefferer S, Schestakow I, et al. On the role of non-basal deformation mechanisms for the ductility of Mg and Mg–Y alloys [J]. Acta Materialia, 2011, 59(2): 429–439.
18. Nie J F, Zhu Y, Liu J, et al. Periodic segregation of solute atoms in fully coherent twin boundaries [J]. Science, 2013, 340(6135): 957–960.
19. Stanford N, Barnett M R. Effect of particles on the formation of deformation twins in a magnesium-based alloy [J]. Materials Science and Engineering A, 2009, 516: 226–234.
20. Nie J F. Precipitation and hardening in magnesium alloys [J]. Metallurgical and Materials Transactions A, 2012, 43: 3891–3939.
21. Chapuis A, Driver J H. Temperature dependency of slip and twinning in plane strain compressed magnesium single crystals [J]. Acta Materialia, 2011, 59(5): 1986–1994.
22. Tonda H, Ando S. Effect of temperature and shear direction on yield stress by $\{11\bar{2}2\}\langle\bar{1}\bar{1}23\rangle$ slip in HCP metals [J]. Metallurgical and Materials Transactions A, 2002, 33(3): 831–836.
23. Winzer N, Atrens A, Dietzel W, et al. Characterisation of stress corrosion cracking (SCC) of Mg–Al alloys [J]. Materials Science and Engineering: A, 2008, 488(1–2): 339–351.
24. Sun J, Zhang J, Liu D, et al. Inhibition behavior of edge cracking in the AZ31B magnesium alloy cold rolling process with pulsed electric current [J]. Metals, 2023, 13(2): 274.
25. Xu S, Xiao X, Zhang H, et al. Electroplastic effects on the mechanical responses and deformation mechanisms of AZ31 Mg foils [J]. Materials, 2022, 15(4): 1339.

Part IV

Advanced Processing

Investigations on the Forging Behavior of Mg–Ca–Al Alloys

Nikolaus Papenberg and Stefan Gneiger

Abstract

Mg parts for modern transport applications must compete with high performance materials such as 7xxx series Al alloys, making superior strength an important factor. Mg–Ca wrought alloys have shown promising results in this regard, exhibiting high strength and adequate ductility over a broad range of alloying contents. These properties originate from the forming process, creating a fine-grained microstructure in combination with stabilizing intermetallic phases. While extruded profiles made from these alloys have been well investigated, no studies on the forging behavior of Mg–Ca alloys have been published yet. Therefore, the forgeability of two Mg–Ca–Al alloys, XA22 and XA55, has been analyzed for extruded and cast stock alike. The processing steps and resulting material properties, based on microstructural analysis and mechanical testing at room temperature, are discussed in this work.

Keywords

Magnesium • Mechanical properties • Characterization

Introduction

The aim to reduce weight in transport applications causes raised interest in lightweight materials. Mg alloys, with their inherent low density, are good candidates for this purpose, i.e. cast parts have nowadays established a solid base of products and applications in the transport sector [1, 2]. Wrought alloys on the other hand are often at a disadvantage in the competition with established materials such as Al alloys and high strength steels. The material requirements in these applications regarding corrosion behavior and mechanical properties are high, but also other aspects such as forming and processing behavior as well as mechanical anisotropy make the use of Mg wrought alloys a challenging topic [3].

In recent years multiple Mg wrought alloys with high mechanical properties have been developed, especially alloys containing Ca combine a multitude of advantages [4]. The mostly discussed group of these alloys are part of the Mg–Ca–Al system (XA alloys), which show high strength and adequate ductility over a wide range of alloy compositions after processing by extrusion [5, 6]. As heat-treatments can be omitted in these alloys, time and energy consumption during production can be reduced. Forming operations are possible in a large temperature window, but care must be taken as processing temperature is known to influence the resulting mechanical properties [7]. Mg–Ca–Al high strength alloys usually show a bi-modal microstructure consisting of large deformed and small (dynamically) recrystallized grains, created during the forming operations [5].

Besides Mg itself Mg–Ca–Al alloys consist of three alloying elements, showing a good synergy: (i) Ca which improves slip behavior, increases the oxidation resistance and provides hardening phases in combination with Mg and/or Al [8]; (ii) Al is well known for solid solution strengthening and phase formation in Mg alloys [9]; (iii) Mn is used to improve the corrosion behavior and stabilize the microstructure by phase formation, e.g. β-Mn and AlMn phases [10].

As investigations on these alloys are near exclusively done on extruded material, this work investigates the forgeability of both as-cast as well as cast & extruded Mg–Ca–Al forging stock. Additionally, the suitability of the forging process to produce high strength Mg parts is discussed.

Material and Methods

Two different Mg–Al–Ca alloys, XA22 and XA55, with nominal compositions as provided in Table 1 were produced at

N. Papenberg (✉) · S. Gneiger
Light Metals Technologies Ranshofen, AIT Austrian Institute of Technology, Lamprechtshausenerstraße 61, 5280 Ranshofen, Austria
e-mail: nikolaus.papenberg@ait.ac.at

S. Gneiger
e-mail: stefan.gneiger@ait.ac.at

A. Leonard et al. (eds.), *Magnesium Technology 2024*, The Minerals, Metals & Materials Series,
https://doi.org/10.1007/978-3-031-50240-8_22

Table 1 Nominal composition of the used Mg–Ca–Al alloys in weight percent (wt%)

Alloy	Ca	Al	Mn	Mg	Ca/Al ratio
XA22	2.20–2.40	2.10–2.40	0.35–0.45	Bal.	0.98
XA55	4.50–5.00	4.40–5.00	0.35–0.47	Bal.	0.99

Ca/Al ratio was calculated from average contents

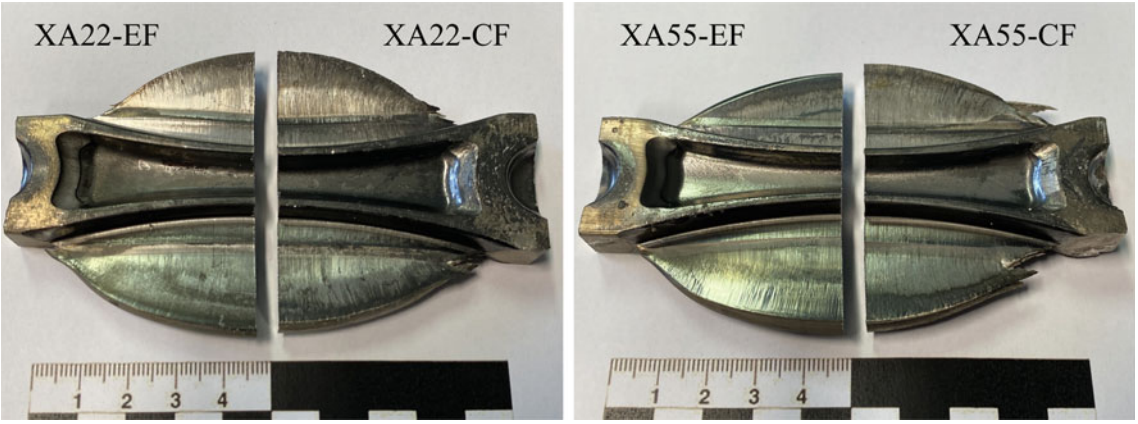

Fig. 1 Comparison of as-forged connecting rods made from different alloys (XA22 and XA55) and stock materials. The parts are designated as cast & forged (-CF) and extruded & forged (-EF), respectively. To provide a better overview, halved parts, separated by their alloy are shown

LKR Ranshofen. The material was gravity cast in the shape of round billets (∅ 63 × 240 mm) using a pre-heated steel mold and cooled at air. The billets were machined to round extrusion stock (∅ 48.5 × 180 mm) and square forging stock (90 × 12 × 25 mm) without any homogenization heat treatment. Extrusion took place on a 1.5 MN extrusion press (NEHP 1500.01, Müller Engineering), producing square profiles (12 × 25 mm) at 400 °C and 0.5 mm/s ram speed (extrusion ratio 1:6.5).

Forgings resembling the center part of a connecting rod were produced on a 160 t hydraulic forming press (NEFF DZP 160), using an isothermal two step forming process at 400 °C and a crosshead speed of 10 mm/s. After final forging the samples were cooled at air. The used part geometry allows for easy analysis of the microstructure, with varying degrees of local deformation, and measurement of mechanical properties via tensile testing.

The microstructure was characterized via optical microscopy (OM), on an Olympus BX60. Mechanical properties were analyzed by tensile testing at room temperature, using a Zwick Z100 testing machine with flat specimen (DIN 50125, E 3 × 8 × 25 mm).

Results and Discussion

In this Section the results of the forming trials and subsequent analyses are described and discussed. To avoid confusion concerning material and processing state, the samples are designated as follows: as-cast material (XA22-C, XA55-C), as-extruded material (XA22-E, XA55-E), forged parts made from cast stock (XA22-CF, XA55-CF) and forged parts made from extruded stock (XA22-EF, XA55-EF).

Forming Trials

Isothermal forging of the rods was done at 400 °C, corresponding to the production temperature of the as-extruded stock material. While forming might have also been possible at lower temperatures, this temperature was chosen to ensure an adequate forming behavior of the as-cast material during the forging process. Furthermore, the temperature related differences between extrusions and forgings were thereby minimized. Subsequent to pre-heating of the square forging stock (1 h at 400 °C) forming was done in a two-step forging die. This process takes ∼ 30 s for both forging steps and has been described in Ref. [11], using a comparable setup.

Both types of stock material, i.e. as-cast (-C) and as-extruded (-E), were successfully forged to the desired part geometry. While the connecting rods where fully formed in all cases, the extruded stock material showed better forming behavior for both alloys (XA22-EF and XA55-EF). This is evident in the rough flash surface and slight skewers visible in the XA22-CF and more obvious in the XA55-CF parts, see Fig. 1. It has been shown repeatedly [11, 12], that as-cast forging stock exhibits lower ductility and reduced performance when compared to extruded stock. This is confirmed by the forging trials done in this work, even though the processing parameters, i.e. isothermal forging at 400 °C, were chosen

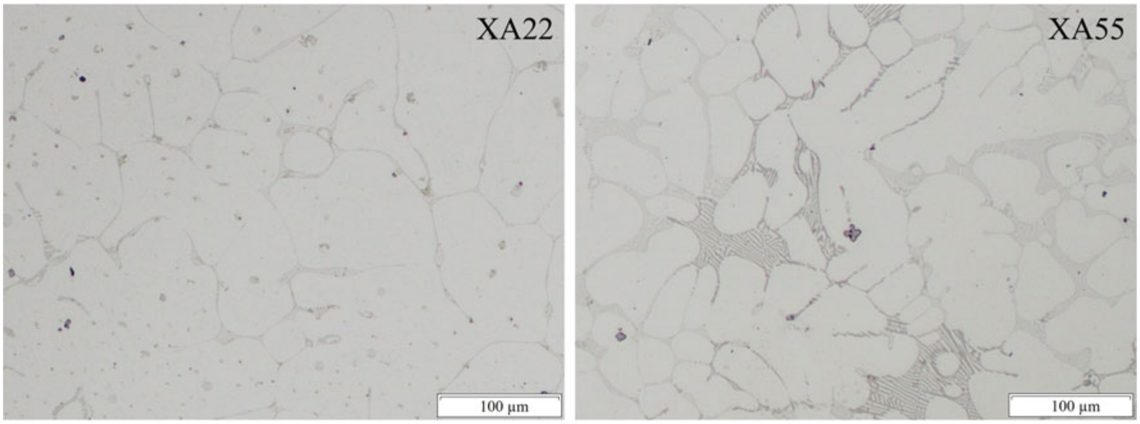

Fig. 2 Microstructure (OM-image) of as-cast XA22-C and XA55-C samples

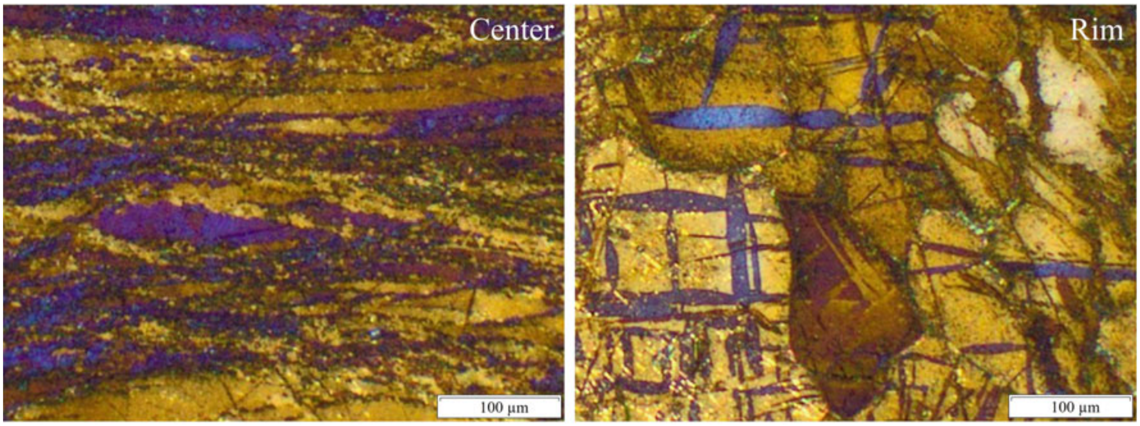

Fig. 3 Microstructure (OM-image) of XA22-CF samples of the center and rim areas

to ensure adequate forming behavior of all stock materials. When taking into account that industrial processes tend to use lower die temperatures as well as higher local deformations, which would further exacerbate the shortcomings of the cast material, the superior performance of extruded stock material is thereby affirmed.

Microstructural Investigations

The microstructure of all samples was analyzed via optical microscopy. The main difference between the investigated alloys is their combined Ca and Al content, which is $\sim$ 4 wt% and $\sim$ 10 wt% for XA22 and XA55, respectively. This markedly increases the formation of Ca and Al containing intermetallic phases (IMPs) in XA55, resulting in a higher fraction and larger size of the formed IMPs, which further influences the recrystallization behavior and mechanical properties.

The as-cast material of both alloys shows Ca-containing lamellar eutectic phases on the grain boundaries. These increase corresponding to the rising alloying content of Ca and Al in XA55. The size of the cast grains decreases at the same time [6]. The combination of Al and Mn can form blocky (primary-) phases, which can be found throughout both materials. Images of the XA22 and XA55 alloys in as-cast (-C) state are given in Fig. 2.

The microstructure of the cast & forged (-CF) rods is strongly dependent on the local degree of deformation applied during the forging process. Only the sections of a XA22-CF part are exemplarily shown in Fig. 3, as the XA55-CF sample shows similar behavior. While the sample center has a bimodal grain structure, consisting of large deformed and small dynamically recrystallized grains, the rim areas still show the remnants of the original cast microstructure. These large grains are deformed and pervaded by twins, but the degree deformation was too low to facilitate widespread recrystallization.

The extruded material, XA22-E and XA55-E, mostly consists of large deformed grains, separated by dynamically recrystallized (DRX) grains, see Fig. 4. The nucleation of DRX grains is enhanced in the vicinity of particles and

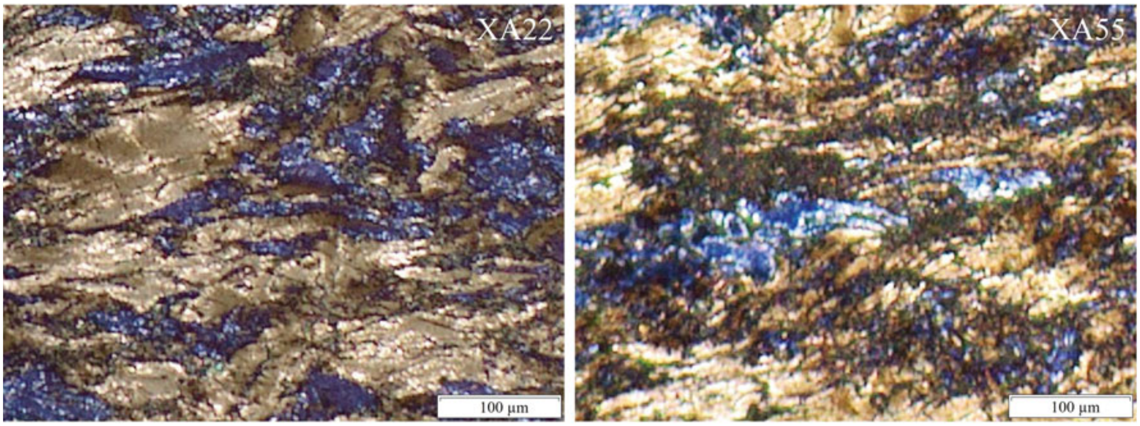

Fig. 4 Microstructure (OM-image) of extruded samples, showing XA22 and XA55 alloys

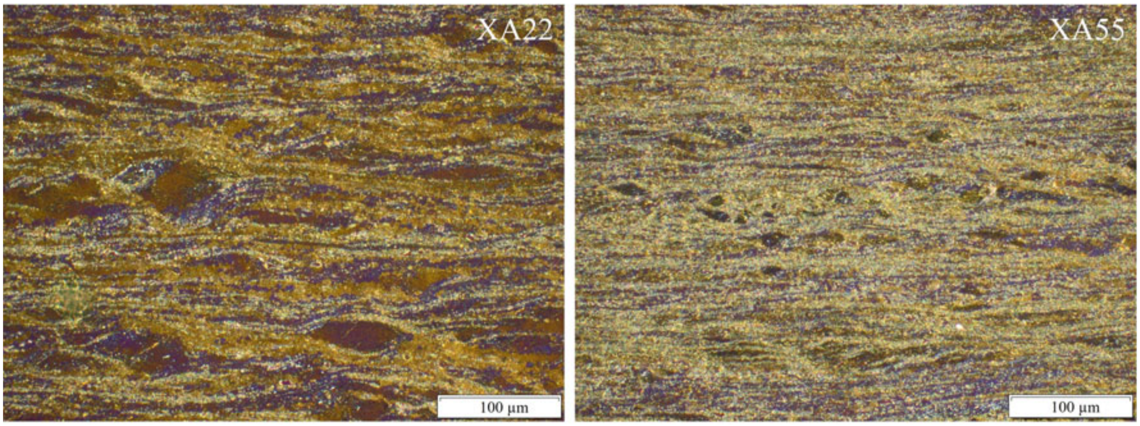

Fig. 5 Microstructure (OM-image) of the center area of extruded & forged samples, showing XA22 and XA55 alloys

twinned areas. This is visible in the XA55-E samples, which show a higher amount of DRX grain structure when compared to XA22-E.

While the low degree of deformation during the extrusion process (1:6.5) was not sufficient to provide a largely recrystallized microstructure, the subsequent forging process profited nevertheless. The combined deformation, applied during extrusion and forging, enhanced the amount of fine DRX grain markedly, see XA22-EF and XA55-EF in Fig. 5. The center areas of the investigated connecting rods predominately consist of fine DRX grains in banded structures. These are punctuated by remnants of large, deformed grains, stemming from the initial microstructure. Again XA55-EF shows an increased fraction of DRX areas and smaller deformed grains, which can be attributed to the already described interaction of particles and recrystallization behavior in this alloy.

Mechanical Properties

Tensile testing of the connecting rods was done at room temperature, using flat specimen of 3 mm thickness. As evident from the tensile curves illustrated in Fig. 6 the cast & forged samples (-CF) of both alloys exhibited lower performance, in both strength and elongation, when compared to the extruded & forged parts (-EF). The alloy XA22 showed better ductility in general, both for uniform elongation (ϵ_u) and elongation at break (ϵ_f), while XA55 samples achieved a higher yield (YS) and ultimate strength (UTS). In case of the XA55-EF parts ∼ 285 MPa and ∼ 320 MPa are reached for YS and UTS, respectively.

The sub-par mechanical properties from cast & forged (-CF) material is not surprising, as this type of alloy achieves its good mechanical properties mainly by a fine grained microstructure, which is prevalent neither in the XA22-CF nor XA55-CF samples. It is therefore of high interest to assess the performance of XA22-EF and XA55-EF samples in comparison to extruded material.

To increase the comparability of the -EF forgings with existing literature, round profiles were used as a benchmark. The profiles were extruded at a processing temperature of 400 °C with an extrusion ratio 1:25, based on the process described in [6]. Table 2 provides an overview of the tensile properties of both the -EF rods and the extruded

Table 2 Tensile properties of Mg–Ca–Al alloys processed at 400 °C comparing as-extruded[a] round profiles and extruded & forged (-EF) connecting rods

	Alloy	YS (MPa)	UTS (MPa)	ϵ_u (%)	ϵ_f (%)
as-extruded[a]	XA22	284.5 ± 4.9	312.4 ± 2.0	6.9 ± 0.2	12.3 ± 0.8
	XA55	280.2 ± 3.6	310.9 ± 1.9	3.8 ± 0.7	5.6 ± 1.6
extruded & forged	XA22	268.6 ± 5.6	303.2 ± 2.5	5.7 ± 0.3	6.7 ± 1.2
	XA55	284.7 ± 1.8	319.7 ± 1.7	4.3 ± 0.5	4.3 ± 0.5

[a] Profile and sample production was based on [6]

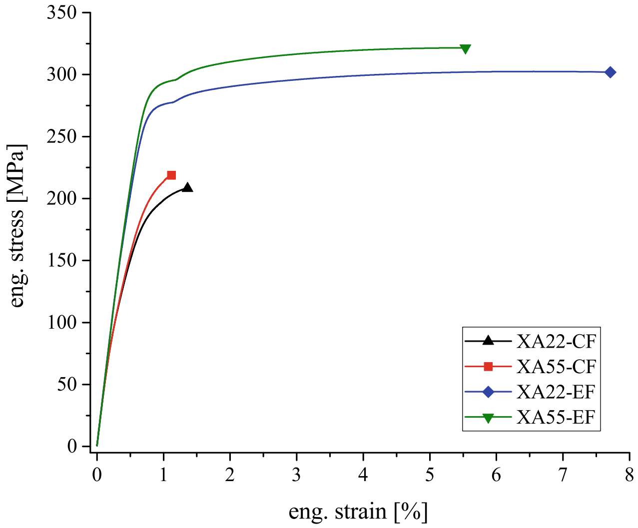

Fig. 6 Overview of the tensile measurements of the forged connecting rods, showing exemplary stress-strain curves

profiles. The performance of the analyzed samples varied slightly, the largest differences were noticeable in the measured elongation, where the XA22 alloy performed better, for both the profiles and the forgings. It can be assumed that this is a consequence of the substantially higher amount of intermetallic phases in the XA55 alloy, which contains ~ 10 wt% of alloying elements. The extruded profiles made from XA22 had the best overall values, i.e. good YS and UTS as well as the highest elongations (ϵ_u and ϵ_f). Interestingly the XA55-EF samples showed the highest strength (YS and UTS) of all tested materials, at still adequate elongations of ~ 4 %. This clearly shows the potential of forgings made from extruded stock. The combination of low complexity extrusion with the high variability of subsequent forging processes allow the production of complex parts with good mechanical properties.

Conclusion

In this work the forging behavior and mechanical properties of high-strength Mg–Ca–Al alloys were investigated. Forgings in the shape of connecting rods were used to analyze the performance of two alloys, XA22 and XA55, as well as different forging stock, i.e. extruded and cast material.

- The cast stock (-C) showed reduced forgeability compared to extruded material (-E). This is also reflected in the forgings themselves. The samples from extruded & forged (-EF) rods performed markedly better than the cast & forged (-CF) parts during tensile testing. This can be attributed to the higher amount of fine recrystallized grains in the both the extruded stock and the extruded & forged samples.
- The large difference in alloying content causes a substantial increase of Al and Ca containing intermetallic phases in the XA55 alloy. Thereby XA55 achieved higher strengths, while the alloy XA22 provided better ductility throughout.
- An assessment of extruded round profiles and forged parts(-EF) showed comparable tensile properties for both alloys, with XA55-EF rods achieving the highest overall strength.

It can be concluded, that the used forging process is not able to create the desired mechanical properties and microstructure when using cast stock. On the other hand, a good synergy can be achieved by using extruded stock material in the forging process. This combination allows for the production of complex Mg–Ca–Al parts with high mechanical properties.

Acknowledgements The authors would like to thankfully acknowledge the work done by the technical staff at the LKR Ranshofen. The funding of this work by the project 'Data-T-Rex' (Wi-2021-305676/13-Au), which is co-financed by research subsidies granted by the government of Upper Austria, is gratefully acknowledged.

References

[1] Tauber, M., Fischer, H., Just, M., Fackler, H.: Magnesium Parts in Serial Production: A Virtual Demonstrator. IMA Webinar (2020)

[2] D'Errico, F., Tauber, M., Just, M.: Magnesium Alloys for Sustainable Weight-Saving Approach: A Brief Market Overview, New Trends, and Perspectives. In: Sunkari, S. (ed.) Current Trends in Magnesium (Mg) Research. IntechOpen, London (2022). https://doi.org/10.5772/intechopen.102777

[3] Mordike, B., Ebert, T.: Magnesium: properties-applications-potential. Materials Science and Engineering: A **302**(1), 37–45 (2001) https://doi.org/10.1016/S0921-5093(00)01351-4

[4] Pan, H., Ren, Y., Fu, H., Zhao, H., Wang, L., Meng, X., Qin, G.: Recent developments in rare-earth free wrought magnesium alloys having high strength: A review. Journal of Alloys and Compounds **663**, 321–331 (2016) https://doi.org/10.1016/j.jallcom.2015.12.057

[5] Xu, S., Oh-Ishi, K., Kamado, S., Uchida, F., Homma, T., Hono, K.: High-strength extruded Mg–Al–Ca–Mn alloy. Scripta Materialia **65**(3), 269–272 (2011) https://doi.org/10.1016/j.scriptamat.2011.04.026

[6] Gneiger, S., Papenberg, N.P., Arnoldt, A.R., Schlögl, C.M., Fehlbier, M.: Investigations of high-strength Mg–Al–Ca–Mn alloys with a broad range of Ca+Al contents. Materials **14(18)**(5439), 1–15 (2021) https://doi.org/10.3390/ma14185439

[7] Papenberg, N., Simson, C., Gneiger, S.: Mg–Ca–X Alloys-A Brief Fact Sheet of High-Strength Mg Wrought Alloys. In: Magnesium Technology 2022, pp. 37–42. Springer, Cham (2022). https://doi.org/10.1007/978-3-030-92533-8_7

[8] Rao, K.P., Prasad, Y.V.R.K., Dharmendra, C., Suresh, K., Hort, N., Dieringa, H.: Review on Hot Working Behavior and Strength of Calcium-Containing Magnesium Alloys. Advanced Engineering Materials **20**(1701102), 1–19 (2018) https://doi.org/10.1002/adem.201701102

[9] Nie, J.-F.: Precipitation and hardening in magnesium alloys. Metallurgical and Materials Transactions A **43**(11), 3891–3939 (2012) https://doi.org/10.1007/s11661-012-1217-2

[10] Cihova, M., Schäublin, R., Hauser, L.B., Gerstl, S.S., Simson, C., Uggowitzer, P., Löffler, J.F.: Rational design of a lean magnesium-based alloy with high age-hardening response. Acta Materialia **158**, 214–229 (2018) https://doi.org/10.1016/j.actamat.2018.07.054

[11] Papenberg, N.P., Arnoldt, A., Trink, B., Uggowitzer, P.J., Pogatscher, S.: Closed die forging of a Mg–Al–Ca–Mn–Zn lean alloy. Materials Science and Engineering: A **857**(144079), 1–13 (2022) https://doi.org/10.1016/j.msea.2022.144079

[12] Gryguc, A., Behravesh, S.B., Shaha, S., Jahed, H., Wells, M., Williams, B., Su, X.: Low-Cycle Fatigue Characterization and Texture Induced Ratcheting Behaviour of Forged AZ80 Mg Alloys. International Journal of Fatigue **116**, 429–438 (2018) https://doi.org/10.1016/j.ijfatigue.2018.06.028

Ultrafine-Grained Magnesium Alloys Manufactured by Multi-axial Forging: Elucidating Mechanisms of Achieving Both High Strength and High Ductility

A. J. Maldonado, M. Weaver, and R. D. K. Misra

Abstract

Warm processing of magnesium (Mg) alloys is a challenge because Mg has a hexagonal close-packed (HCP) lattice with limited slip systems, which makes it difficult to plastically deform at low temperature. To address this challenge, a concept of combining annealing of as-cast alloy and multi-axial forging (MAF) was adopted for Mg alloys to obtain texture-free ultrafine-grained (UFG) structure with high strength-high ductility combination. We describe here the initial findings that indicated a distinct and fundamental transition in the deformation behavior of low strength coarse-grained (CG) rare earth element containing Mg alloy from twinning to strong and ductile UFG Mg alloy with basal and pyramidal dislocation slip. This implied the role of specific grain boundary states (grain boundary character distribution), grain orientation, and dislocation activity in governing the deformation mechanisms.

Keywords

Ultrafine-grained magnesium alloys • Multi-axial forging • Deformation behavior

Extended Abstract

Currently, there is a significant interest in magnesium alloys for structural and functional applications. Magnesium (Mg) alloys are light-weight materials (1.7–2.0 g/cm^3), whose density is significantly less than titanium alloys and stainless steels. Furthermore, from the perspective of biomedical devices, they are biodegradable, bioresorbable, and biocompatible. Irrespective of these characteristics, warm processing of magnesium alloys is a pressing challenge because Mg has a hexagonal close-packed (HCP) lattice with limited slip systems, which makes it difficult to plastically deform. To address the challenge of warm processing of magnesium (Mg) alloys, an ingenious concept of combining annealing of as-cast alloy and multi-axial forging (MAF) was adopted for Mg alloys to obtain texture-free ultrafine-grained (UFG) structure with high strength-high ductility combination (yield strength: ~ 227 MPa)—high ductility (% elongation: ~ 30%) combination. This combination of strength and ductility is excellent for the lean alloy, enabling an understanding of deformation processes in a formable high strength Mg-rare earth alloy [1–3].

The deformation behavior was studied via nanoindentation and electron microscopy and the behavior compared with its low strength (yield strength: ~ 46 MPa)—low ductility (% elongation: ~ 7%) coarse-grained (CG) counterpart. In the UFG alloy, extensive dislocation slip was an active deformation mechanism, while in the CG alloy, mechanical twinning occurred. The differences in the deformation mechanisms of UFG and CG alloys were reflected in the discrete burst in the load–displacement plots. The deformation of Mg–2Zn–2Gd alloys was significantly influenced by the grain structure, such that there was change in the deformation mechanism from dislocation slip (non-basal slip) to nanoscale twins in the CG structure. In summary, distinct and fundamental transition occurred in the deformation behavior of low strength coarse-grained (CG) rare earth element containing Mg alloy from twinning to strong and ductile UFG Mg alloy with basal and pyramidal dislocation slip. The high plasticity of UFG Mg alloy involved high dislocation activity and change in activation volume. This implied the role of specific grain boundary states (grain boundary character distribution), grain orientation, and dislocation activity in governing the deformation mechanisms. The grain size of UFG alloy was 416 ± 140 nm, which is smaller than the plastic zone size,

A. J. Maldonado · M. Weaver · R. D. K. Misra (✉)
Department of Metallurgical, Materials and Biomedical Engineering, University of Texas at El Paso, El Paso, TX 79968, USA
e-mail: dmisra2@utep.edu

A. Leonard et al. (eds.), *Magnesium Technology 2024*, The Minerals, Metals & Materials Series,
https://doi.org/10.1007/978-3-031-50240-8_23

while the grain size of CG alloy was significantly larger at 44 ± 5 µm. The UFG alloy exhibited multiple dislocation slips because of the need for compatibility near the grain boundaries. In the CG alloy, deformation twinning compensated for the lack of dislocation slip. However, less frequent observation of twinning in the CG alloy implied reduced elongation of ~ 7% as compared to the high elongation of ~ 30% in the UFG alloy. The UFG alloy with large number of grain boundaries promoted dislocation slip.

Thus, the deformation mechanism of UFG Mg–2Zn–2Gd alloy with "high strength-high ductility combination" was distinctly different from the CG counterpart, as documented via nanoindentation deformation experiments and transmission electron microscopy and is related to the grain size effect. In UFG alloy, extensive dislocation slip was attributed to excellent ductility, whereas ductility in the CG alloy was governed by the degree of twinning activity. The multi-axial forging of magnesium alloys is a potential and viable approach to process other hcp alloys with a limited number of slip systems, enabling superior mechanical properties to be obtained (Figs. 1 and 2).

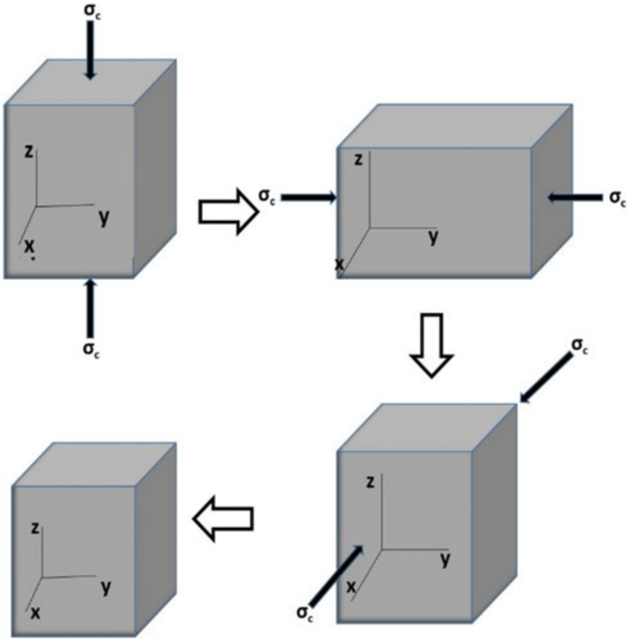

Fig. 1 Schematic of the multi-axial forging (MAF) process

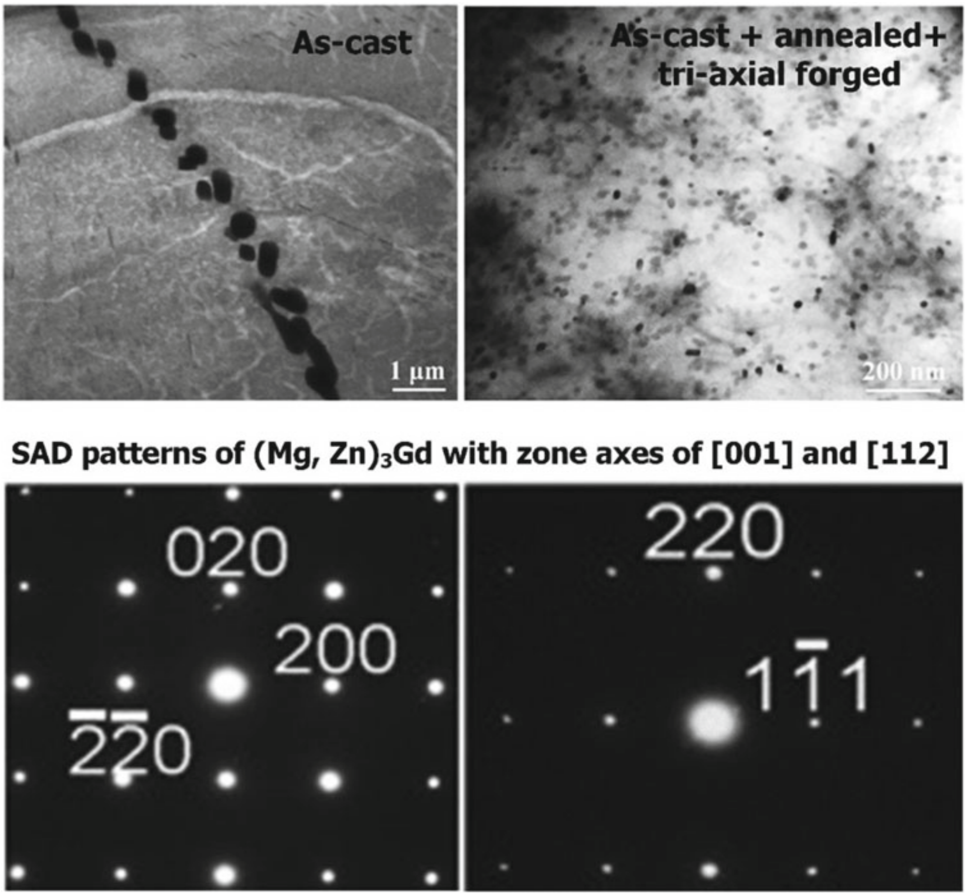

SAD patterns of $(Mg, Zn)_3Gd$ with zone axes of [001] and [112]

Fig. 2 Transmission electron micrographs and selected area diffraction patterns (SAD) of as-cast and as-cast+annealed +multi-axial forged Mg–2Zn–2Gd alloy

Acknowledgements The authors (M. R. Weaver, A. J. Maldonado, and R. D. K. Misra) are grateful to the National Science Foundation for financial support through grant # CMMI 2130586.

References

1. R.D.K. Misra, Materials Letters, 31 (2023) 133443.
2. R.D.K. Misra, Materials Technology: Advance Performance Materials, 38 (2023) 2189769.
3. M. R. Weaver A.J. Maldonado, J.L. Banueolos, R.D.K. Misra, Materials Technology: Advanced Performance Materials, 38 (2023) 2215038.

Enhancement of Mechanical Properties of Rolled AZ31 Alloy by Utilizing Ultrasonic Nano-crystalline Surface Modification (UNSM) Treatment and Heat Treatment

Hyun Ji Kim, Sumi Jo, Auezhan Amanov, and Sung Hyuk Park

Abstract

Mg alloys have great potential as lightweight structural materials due to their low density, but their application is limited due to lower mechanical properties compared to other lightweight alloys. The Ultrasonic Nano-crystalline Surface Modification (UNSM) technique, which induces severe plastic deformation on the material surface using ultrasonic impacts, can result in a gradient microstructure with a refined surface consisting of nano-sized grains, and an intermediate microstructure with residual strain, ultimately enhancing mechanical properties. While the nano-crystalline surface contributes to improved strength and ductility, the residual strain in the intermediate microstructure brings about a significant reduction in ductility. However, the residual strain can be beneficial for both strength and ductility through recovery and recrystallization, achieved through an appropriate annealing treatment. In this study, we applied the UNSM-treatment, followed by subsequent annealing at 200 °C, to a homogenized rolled AZ31 alloy to simultaneously improve strength and ductility by generating a gradient microstructure.

Keywords

AZ31 alloy • Ultrasonic Nano-crystalline Surface Modification (UNSM) • Gradient microstructure • Heat treatment

Introduction

Mg and its alloys are highly regarded as lightweight materials in various industries, including automotive and aerospace [1–5]. Mg offers excellent properties such as low density, high strength-to-weight ratio, castability, damping capacity, machinability, and recyclability, making it essential for the production of lightweight products. However, Mg and its alloys have weaknesses such as lower hardness, strength, formability, and corrosion resistance when compared to other lightweight materials, which can make their use challenging in certain industrial applications. Recently, the surface severe plastic deformations (SSPD) method, which imposes strong plastic deformation on the specimen surface, has been widely used as a way to overcome this problem [6–10]. Recently, a specific SSPD method known as Ultrasonic Nano-crystalline Surface Modification (UNSM) has been developed. This method not only significantly improves material strength but also offers advantages like ease of production, cost-effectiveness, and precise load control compared to conventional methods [11, 12]. Nevertheless, research conducted to date on the application of UNSM-treatment in Mg alloys is scarce. Therefore, in this study, we investigated the impact of UNSM-treatment on the mechanical properties of a commercial AZ31 Mg alloy. Furthermore, we applied post-UNSM heat treatment to induce recrystallization, aiming to eliminate the intense compressive residual strain formed on the surface and enhance ductility.

Materials and Experimental Methods

Sample preparation involved using a 3 mm thick rolled AZ31 plate (Mg–3.0Al–0.8Zn, wt%), which underwent homogenization heat treatment at 420 °C for 10 h, followed by air-cooling. The specimen was machined to dimensions of 125 mm (length) × 25 mm (width) × 3 mm (thickness)

H. J. Kim · S. Jo · S. H. Park (✉)
School of Materials Science and Engineering, Kyungpook National University, Daegu, 41566, Republic of Korea
e-mail: sh.park@knu.ac.kr

A. Amanov
Department of Mechanical Engineering, Sun Moon University, Asan, 31460, Republic of Korea

A. Leonard et al. (eds.), *Magnesium Technology 2024*, The Minerals, Metals & Materials Series,
https://doi.org/10.1007/978-3-031-50240-8_24

for UNSM-treatment, and the UNSM-treatment was performed in the normal direction. Then UNSM-treated specimens were annealed at 200 °C. Samples treated with UNSM in the as-rolled state and annealed after UNSM-treatment are referred to as UNSM and UNSMA samples, respectively. Microstructural observations were performed on each sample using optical microscopy (OM) and electron backscatter diffraction (EBSD). Samples were prepared by grinding and polishing, followed by etching with an acetic-picral solution (10 ml acetic acid, 3.0 g picric acid, 10 ml distilled water, and 100 ml ethanol). EBSD measurements were carried out, and the data was analyzed using Tex-SEM Laboratories orientation imaging microscopy (TSL OIM) analysis software. Mechanical testing included measuring Vickers hardness of surface for as-rolled, UNSM, and UNSMA samples.

Results and Discussion

Figure 1 shows the optical micrographs and SEM micrographs of the ND-RD plane of as-rolled, UNSM, and UNSMA samples. The as-rolled sample exhibits an equiaxed recrystallized grain structure with uniform grain size from the surface to the center. In contrast, after UNSM-treatment, a gradient microstructure is observed. The surface region shows significantly refined grain structure due to the strong severe plastic deformation applied, with nanoscale-sized grains observed near the surface and extending to ~ 650 μm depth. For the annealed UNSMA sample, newly recrystallized grains are observed on the surface, and residual twinned regions are observed from the region ~ 250 μm away from the surface to ~ 650 μm depth. The

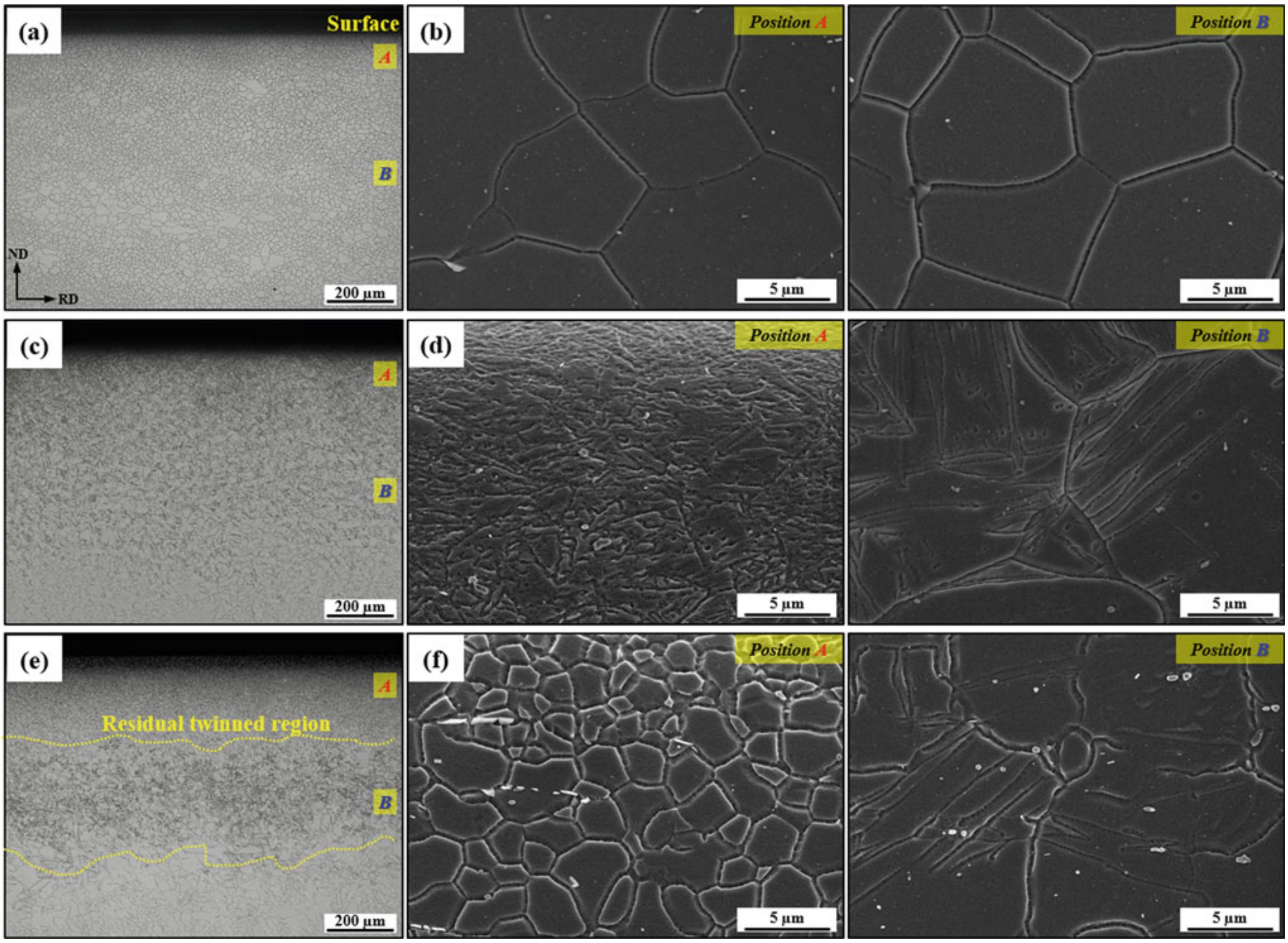

Fig. 1 Microstructural characteristics of **a** as-rolled, **c** UNSM, and **e** UNSMA samples: **a**, **c**, and **e** optical micrographs and **b**, **d**, and **f** SEM micrographs at positions A and B in each sample

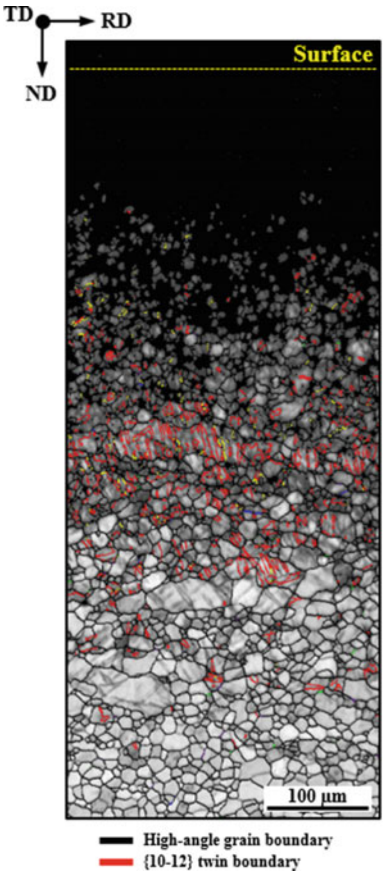

Fig. 2 EBSD grain boundary map of the UNSM sample. High-angle grain boundaries and {10–12} twin boundaries are shown in black and red, respectively

twin observed in UNSM and UNSMA samples is the most readily occurring {10–12} twin in Mg, as reported in previous studies [13, 14]. This is confirmed through analysis of the EBSD boundary map (Fig. 2).

The internal residual strain within the material subjected to the UNSM-treatment and subsequent annealing is indicated in Fig. 3 using the kernel average misorientation (KAM) values obtained from EBSD measurements. The KAM, employed in EBSD technique, quantifies the extent of localized deformation or misorientation within a crystalline material [15, 16]. A higher residual strain within the material is represented by green color, while a low strain is indicated by blue in the KAM map. Both UNSM and UNSMA samples exhibit a drastic increase in the KAM value of 0.95 and 0.73 respectively, comparing to the KAM value of 0.41 in the as-rolled sample. Surface area of the UNSM material was not indexed as indicated by the black-colored area, signifying that the UNSM-treatment causes highly concentrated internal strain on the surface. On the other hand, the concentrated strain on surface was distinctly relaxed through the annealing treatment at 200 °C, as confirmed by the recrystallized grains in blue color. Even though the UNSMA sample underwent annealing at a low temperature of 200 °C, recrystallization occurred readily due to the high residual strain in the surface region. These results indicate that the residual strain at the surface was significantly reduced after annealing, which is expected to improve the ductility degradation caused by high residual strain.

To investigate the mechanical properties of each sample, a Vickers hardness test was performed, and the corresponding hardness values on the surfaces of the three samples are shown in Fig. 4a. The results show that the as-rolled, UNSM, and UNSMA samples exhibit hardness values of 58.7 Hv, 112.2 Hv, and 78.1 Hv, respectively. After the UNSM-treatment, the hardness value was significantly increased by 91%. This is attributed to the high residual strain and twin induced by the UNSM-treatment. On the other hand, after annealing, the hardness value decreased compared to the UNSM sample; however, it exhibited a 33% increase when compared to the as-rolled sample. Recrystallization induced by the annealing reduces the internal strain on the surface and results in smaller grains compared to the as-rolled sample. As a result, the UNSMA sample exhibits lower hardness compared to the UNSM sample, while demonstrating higher hardness in contrast to the as-rolled sample. Figure 4b shows the grain size measurements from the surface to the center. The as-rolled sample exhibited a consistent grain size of 15 µm from the surface to the center, showing minimal variation across regions. In the UNSM sample, the grain size near the surface was too fine to measure, but at ~ 200 µm, the grain size was 2.8 µm. Toward the center region, the grain size becomes gradually larger until it is comparable to the grain size of the as-rolled sample. The UNSMA sample possessed the surface grain size of 8 µm and gradually approached the grain size comparable to that of the as-rolled sample in similar manner to the UNSM sample. These differences in grain size from the surface to the center in each sample are corresponded to the differences in hardness.

Conclusions

In this study, we investigated the effects of UNSM and subsequent annealing treatment on the microstructure and mechanical properties of AZ31 Mg alloy. After the utilization of UNSM-treatment, the gradient microstructure consisted of high residual strain and twin at the surface and intermediate layer was formed. This microstructural change significantly contributed to the remarkable surface hardness improvement by 91%. Meanwhile, the annealing treatment conducted as a post-UNSM-treatment resulted in the relaxation of internal strain and formation of fine recrystallized grains on the surface. This refined microstructure is advantageous for mitigating ductility degradation resulting from

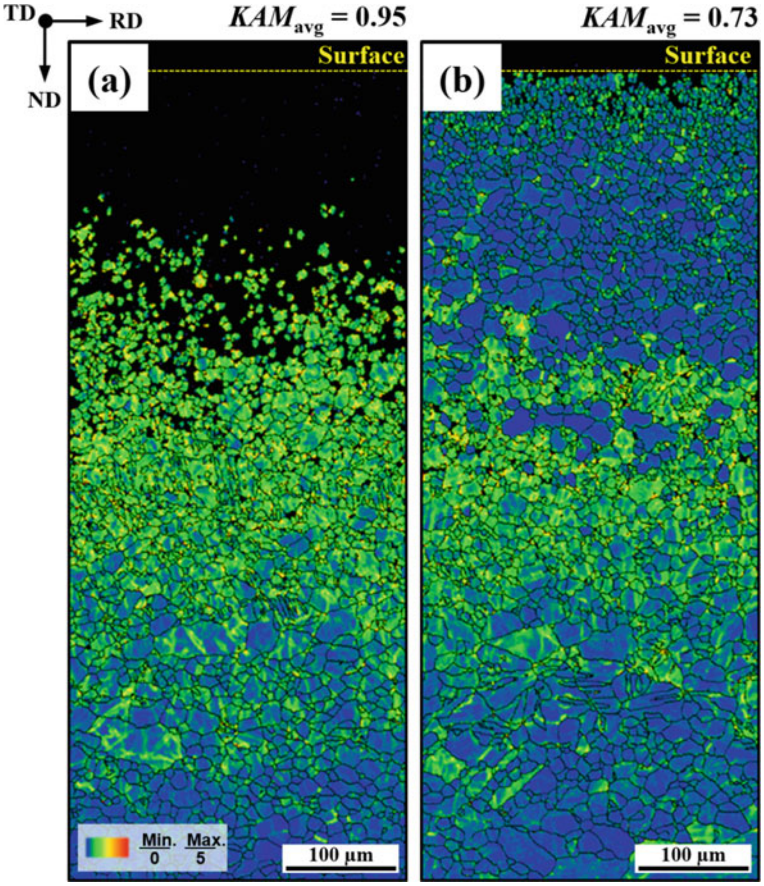

Fig. 3 EBSD results of kernel average misorientation (KAM) maps of **a** UNSM and **b** UNSMA samples

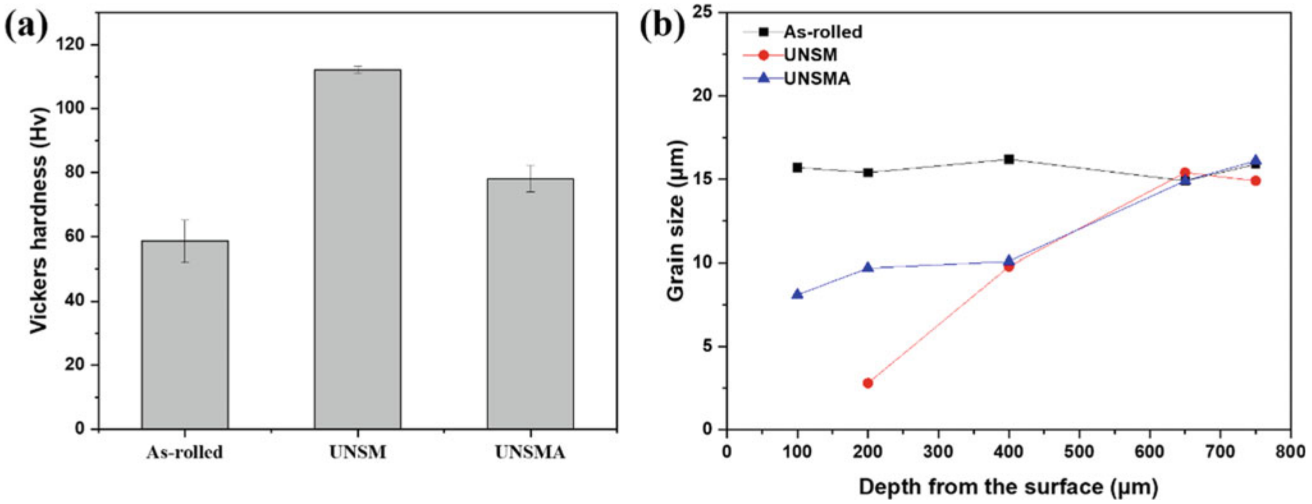

Fig. 4 **a** Vickers hardness of the surface and **b** grain size variation according to depth from the surface for as-rolled, UNSM, and UNSMA samples

the concentrated strain induced by UNSM-treatment, while also enhancing strength compared to the as-rolled sample. These findings highlight the potential of UNSM and subsequent annealing treatments in tailoring the microstructure and properties of Mg alloys, which are controllable depending on the various applications.

References

1. H. Yang, X. Wang, P. Ni, Z. Li, H. Liu, Met. Mater. Int. 28 (2022) 1938–1947.
2. M. Johari, S.H. Tabaian, S. Saeedi, Met. Mater. Int. 28 (2022) 1386–1400.
3. J.S. Suh, B.C. Suh, J.O. Choi, Y.M. Kim, B.S. You, Met. Mater. Int. 27 (2021) 2696–2705.
4. J. Zhao, J. Fu, B. Jiang, A. Tang, H. Sheng, T. Yang, G. Huang, D. Zhang, F. Pan, Met. Mater. Int. 27 (2021) 1403–1415.
5. V.V Ramalingam, P. Ramasamy, M.D. Kovukkal, G. Myilsamy, Met. Mater. Int. 26 (2020) 409–430.
6. H. Fu, X. Zhou, B. Wu, L. Qian, X.S. Yang, J. Mater. Sci. Technol. 82 (2021) 227–238.
7. M.Z. Ge, J.Y. Xiang, Z. Fan, Y.L. Lu, W.N. Lei, J. Alloy. Compd. 734 (2018) 266–274.
8. G. Chen, J. Gao, Y. Cui, H. Gao, X. Guo, S. Wu, J. Alloy. Compd. 735 (2018) 536–546.
9. C. Liu, H. Zheng, X. Gu, B. Jiang, J. Liang, J. Alloy. Compd. 770 (2019) 500–506.
10. H. Ye, X. Sun, Y. Liu, X. Rao, Q. Gu, Surf. Coat. Technol. 372 (2019) 288–298.
11. X. Hou, H. Qin, H. Gao, S. Mankoci, R. Zhang, X. Zhou, Z. Ren, G.L. Doll, A. Martini, N. Sahai, Y. Dong, C. Ye, Mater. Sci. Eng. C 78 (2017) 1061–1071.
12. A. Amanov, O.V. Penkov, Y.-S. Pyun, D.-E. Kim, Tribol. Int. 54 (2012) 106–113.
13. M.S. Kang, J.-H. Kang, H. Park, J.H. Kim, Y.-S. Pyoun, M. Baek, D.J. Lee, S.J. Lee, S. Park, H.M. Kim, S.H. Park, Y.S. Choi, Korean J. Met. Mater. 60 (3) (2022) 169–179.
14. B. Mao, B. Li, D. Lin, Y. Liao, Mater. Sci. Eng. A 756 (2019) 219–225.
15. H.J. Kim, Y.J. Kim, S.H. Park, J. Magnes. Alloy. 11 (2023) 671–683.
16. M. Kamaya, Mater. Charact. 66 (2012) 56–67.

Research Toward Sintering Improvement During Press and Sinter Processing of Mg and Mg Alloy Powders

Steven C. Johnson and William A. Caron

Abstract

Consolidation of magnesium (Mg) alloy powders by near shape forming methods offers significant opportunity for structural material light weighting. Experimental results to date indicate that Mg/Mg alloy powders can be consolidated using press and sinter processing to some extent. Attaining full density of Mg/Mg alloy powders using solid and liquid phase sintering is difficult apparently due to the presence of surface oxide layers impeding interparticle sintering. In this work, thermodynamic modeling was applied to determine the equilibrium phases formed at varying oxygen (O_2) concentrations for pure Mg and several Mg powder alloys. Complimentary sintering experiments in relatively O_2 free inert atmospheres were subsequently performed to investigate densification and interparticle neck formation during sintering. Additionally, all sintered powder compacts were characterized for density, microstructure, phase development, and microstructure composition. Results of this work are intended to increase understanding of solid and liquid state sintering of Mg/Mg alloy powders.

Keywords

Mg and AZ91D powder • Press and sinter processing • Thermodynamic modeling • Solid state sintering • Liquid phase sintering • Supersolidus liquid phase sintering • Surface oxide layer

Extended Abstract

Near and net shape fabrication of light alloy materials for potential structural applications represents critical materials and component fabrication methods for efficient and sustainable materials processing. Magnesium (Mg) alloys are exemplary light alloy structural materials with a density of ~ 1.8 gm/cm^3. However, near and net shape fabrication of Mg alloys specifically using conventional press and sinter processing is challenging primarily due to the presence of a powder particle surface magnesium oxide (MgO) layer. This surface oxide layer functions as a diffusion barrier to interparticle mass transport and impedes densification of Mg alloys when using conventional sintering. Methods other than conventional press + sintering of Mg, Mg alloy, and Mg alloy composite powders have been applied towards achieving full density. Vacuum hot pressing, high frequency spark plasma sintering, and susceptor assisted microwave sintering have all been applied to these powders and attained final densities approaching full density most likely due to disruption of the powder particle surface MgO layer during sinter processing [1–4]. For susceptor assisted microwave sintering of Mg alloy and Mg alloy composite powders, significant reduction in sintering time and increased sinter densification kinetics are achieved due to the mechanism of microwave coupling with green powders compacts. Results of ~ 93–95% theoretical density (ρ_{Th}) in the as-microwave sintered condition for solid state sintering have been achieved [4]. The work presented here combines thermodynamic modeling with complimentary sintering experiments in relatively O_2 free inert atmospheres to better understand and progress conventional, atmospheric pressure sintering of Mg and Mg alloys.

Modeling of the effect of trace O_2 content on equilibrium phase formation in Mg and Mg alloy AZ91D was performed using the thermodynamic modeling software Pandat™ and the associated Mg thermodynamic database PanMg2023. For the formation of equilibrium phases, Gibb's free energy

S. C. Johnson (✉) · W. A. Caron
Central Connecticut State University, 1615 Stanley Street,
New Britain, CT 06050, USA
e-mail: scjohnson@ccsu.edu

A. Leonard et al. (eds.), *Magnesium Technology 2024*, The Minerals, Metals & Materials Series,
https://doi.org/10.1007/978-3-031-50240-8_25

and fraction of phase(s) present were calculated from 0 to 1000 °C for O_2 contents of 1 (0.0001 wt%), 10, 100, and 1000 (0.1 wt%) parts per million (ppm). Modeling results are summarized as plots of Gibb's free energy versus temperature and phase fraction versus temperature. In this approach, the formation of the thermodynamically most stable phase(s) can be identified and the fractional quantity of these phase(s) determined.

Mg and AZ91D powder experimental characterization and compaction processing was previously described as in [5]. Based partially on thermodynamic modeling results, sintering of Mg and AZ91D powder compacts was performed using vacuum evacuation of the sintering tube furnace environment in an attempt to minimize any residual air or O_2 in the sintering atmosphere and high purity Argon (Ar) for inert furnace atmosphere. Specifically, 99.999% Ar (5-9Ar) containing less than of 1 ppm O_2, 3 ppm H_2O, and 0.5 ppm total hydrocarbons was used for the inert furnace atmosphere [6]. Prior to initiating the furnace sintering program, the sintering furnace chamber was sealed, backfilled and purged with 5-9Ar for ~ 5 min and subsequently a vacuum of ~ 10 Torr pulled on the sintering furnace chamber for ~ 5 min. This procedure of Ar backfill + vacuum pump was repeated 3 times to remove any residual air or O_2 and ensure that the furnace sintering atmosphere was relatively the purity of the 5-9Ar gas used. Mg and AZ91D green compacts were heated at 10 °C per minute for all sintering program ramps, a compaction lubricant removal dwell of 20 min. at 400 °C was performed for all samples, and sintering was performed for 60 min at temperatures below and above the melting temperature (T_m) or solidus temperature (T_s) to facilitate both solid state and liquid phase or supersolidus liquid phase sintering. After sintering, all samples were cooled within the furnace to 400 °C in the inert furnace atmosphere by shutting the furnace off and increasing the flow of Ar. Sintered samples were subsequently sectioned using a low speed Diamond saw with the sample for density determination removed from approximately the center of the sintered 30 mm diameter disc and of approximately 1800 mm^3 in volume. Density was determined following ASTM standard B962-17 [7].

Thermodynamic modeling results for Mg and AZ91D were reasonably similar in that for each of the O_2 contents modeled, MgO had the lowest modeled Gibb's free energy and was present from room temperature (T_R) to T_m of Mg or T_s of AZ91D in very small phase fractions. Figure 1a shows the phase fractions for AZ91D with 1 ppm O_2 from T_R to 700 °C with the fraction of MgO 0.0003%, shown as the red line along the *x*-axis of the plot. Similarly, Fig. 1b shows the phase fractions for AZ91D with 1000 ppm O_2 from T_R to 700 °C with the fraction of MgO 0.3%.

Modeled results clearly indicate that for any O_2 content at or above 1 ppm, MgO is the most thermodynamically stable phase for AZ91D and will be present in small quantities. Similar modeling results were obtained for pure Mg again with MgO present in small quantities for any O_2 content at or above 1 ppm. For modeled phase fractions of pure Mg, solid hexagonal closed-packed (HCP) Mg transitions to liquid Mg as a step function at the T_m of Mg as expected for a pure element. These results clearly imply that to eliminate the formation of MgO in Mg-based systems, a sintering atmosphere O_2 content of below 1 ppm must be achieved.

Experimental sintering of Mg and AZ91D samples was performed at temperatures below and above the T_m for Mg ($T_{m,Mg}$ = 645 °C) and the T_s for AZ91D ($T_{s,AZ91D}$ = 561 °C) to affect both solid and liquid phase sintering in a relatively low O_2 content Ar atmosphere. Experimental results of this effort are shown in Table 1. For both Mg and AZ91D, solid state sintering ~ 10 °C below T_m or T_s was ineffective in achieving 100% ρ_{Th}. Sintered density decreased

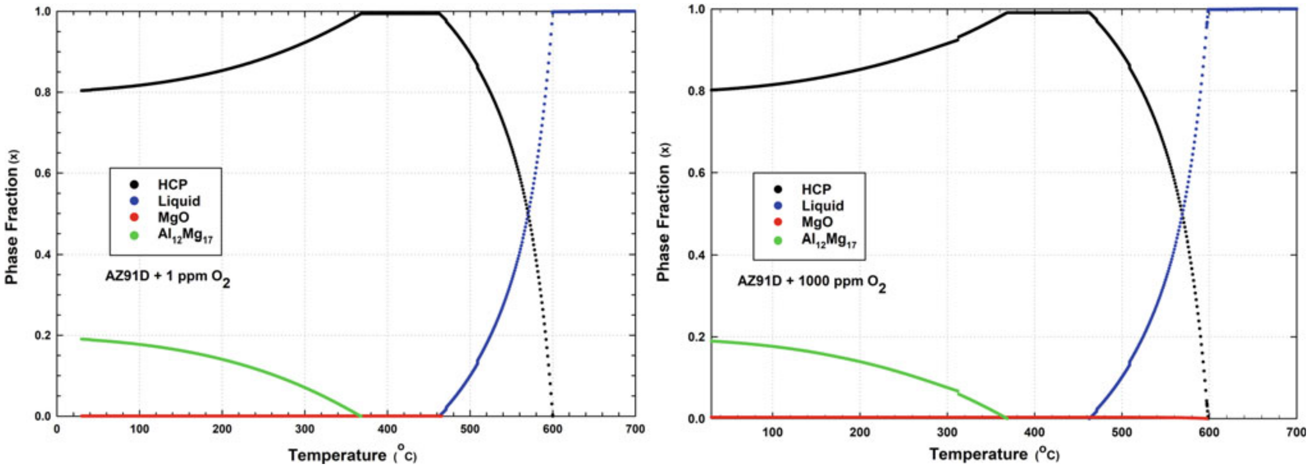

Fig. 1 **a** Modeled phase fractions for AZ91D with 1 ppm O_2 from T_R to 700 °C. **b** Modeled phase fractions for AZ91D with 1000 ppm O_2 from T_R to 700 °C

Table 1 Experimentally determined green and sintered densities for pure Mg and AZ91D

Powder material	Compaction stress (MPa)	Lubricant	Sinter T (°C)	Green density (% ρ_{Th})	Sinter density (% ρ_{Th})
Mg	570	1% ethylene bis stearamide admixed	635	96.26	91.67 ± 0.9
	522	1% ethylene bis stearamide admixed	655	97.03	90.16 ± 1.0
	518	1% ethylene bis stearamide admixed	670	96.99	89.12 ± 0.9
AZ91D	557	Zn stearate die wall	550	92.82	86.15 ± 0.5
	468	Zn stearate die wall	570	91.32	84.04 ± 3.0
	565	Zn stearate die wall	585	93.47	84.79 ± 2.6

compared to green density with a maximum sintered density of 91.67% ρ_{Th}. Similarly, liquid phase and supersolidus liquid phase sintering at ~ 10 and ~ 25 °C above T_m or T_s were also ineffective in achieving 100% ρ_{Th} again resulting in a decrease in density with a maximum sintered density of 90.16% ρ_{Th}. For solid state sintering, MgO occurs as a thin surface film on powder particles and functions as a diffusion barrier impeding solid state Mg transport and sinter densification of Mg and AZ91D [8]. For liquid phase and supersolidus liquid phase sintering, the mechanism of poor sinter densification appears to be due to a high contact angle and therefore poor wetting of any liquid formed with the surrounding solid [9]. For all samples liquid or supersolidus liquid phase sintered, liquid was observed to exude from the solid sample thus decreasing sample density.

Results of this work better define two fundamental impediments to atmospheric pressure sintering of Mg and Mg alloy powders. One impediment is the contribution of ppm level quantities of O_2 in sintering atmospheres. Thermodynamic modeling has shown that even these small quantities of O_2 result in formation of MgO specifically as a surface oxide layer on powder particles. This surface MgO layer functions as a diffusion barrier which impedes solid state diffusion and prevents solid state sinter densification of Mg. For example, Wolff and coworkers used very detailed processing methods such as glove box processing of Mg powders, use of a 99.9999% pure Ar sintering atmosphere, active gettering within the sintering atmosphere, and more but achieved only 85% ρ_{Th} sintered density for pure Mg which is lower than achieved in work presented here [10].

A second impediment is the presence of a pre-existing MgO layer that must be reduced or disrupted to facilitate solid or liquid phase sinter densification. In this work, liquid and supersolidus liquid phase sintering was performed to overcome any pre-existing MgO layer for sinter densification and was unsuccessful. The autogenous formed liquid phases were insufficient to cause sinter densification and some of the formed liquid exuded to the sample surfaces resulting in a decrease in sintered density.

From this work, approaches at successful conventional atmospheric pressure sintering of Mg and Mg alloy powders can be offered.

- Practice high levels of sample and sintering atmosphere cleanliness during handling and processing of Mg and Mg alloy powder compacts to minimize additional O_2 sources to the pre-exiting MgO layer. This practice will limit surface oxide growth and enhance sinterability of Mg and Mg alloy powders.
- Approach alloying Mg base alloys that form surface oxide layers more stable than MgO and better facilitate solid and liquid phase densification. Burke and Wolff have both approached alloying pure Mg with Ca or Y with varying levels of success and additional research of this approach is warranted [11, 12].

References

1. Yang, L *et. al* (2021) Microstructures and mechanical properties of AZ31 magnesium alloys fabricated via vacuum hot-press sintering. Journal of Alloys and Compounds 870:1–8. DOI: https://doi.org/10.1016/j.jallcom.2021.159473.
2. Liu, R *et. al.* (2019) Densification of pure magnesium by spark plasma sintering – discussion of sintering mechanism. Advanced Powder Technology 30:2649–2658. DOI: https://doi.org/10.1016/j.apt.2019.08.012.
3. Salehi, M *et. al.* (2021) Rapid densification of additive manufactured magnesium alloys via microwave sintering. Additive Manufacturing 37:1–11. DOI: https://doi.org/10.1016/j.addma.2020.101655.
4. Akinwekomi, AD *et. al* (2016) Rapid microwave sintering of carbon nanotube-filled AZ61 magnesium alloy composites. Composites Part B: Engineering 93:302–309. DOI: https://doi.org/10.1016/j.compositesb.2016.03.041.
5. Johnson, S and Caron, W (2021) Research into Near Shape Processing of Magnesium and Magnesium Alloy Powders. Paper presented at Powder Metallurgy & Particulate Materials - 2021, Orlando, Florida, 23 June 2021.
6. Praxair Specialty Gases, Product Specification AR 5.0UH, Ultra High Purity Argon, 2023, United States.

7. ASTM standard B962 – 17 (2017) Standard Test Methods for Density of Compacted or Sintered Powder Metallurgy (PM) Products Using Archimedes' Principle. ASTM International. West Conshohocken, PA.
8. Burke, P *et. al.* (2009) Sintering Fundamentals of Magnesium Powders. Canadian Metallurgical Quarterly 48(2):123–132. DOI: https://doi.org/10.1179/cmq.2009.48.2.123.
9. German, R *et. al.* (2009) Review: Liquid Phase Sintering. J. Mater. Sci. 44:1–39. DOI: https://doi.org/10.1007/s10853-008-3008-0.
10. Wolff, M *et. al.* (2010) Sintering of Magnesium. Adv. Eng. Mater. 12(9):829–836. DOI: https://doi.org/10.1002/adem.201000038.
11. Burke, P *et. al.* (2016) DSC and FIB/TEM investigation of calcium and yttrium additions in the sintering of magnesium powder. Can. Metall. Quart. 55(1):45–52. DOI: https://doi.org/10.1080/00084433.2015.1135535.
12. Wolff, M *et. al.* (2016) Magnesium Powder Injection Molding (MIM) of Orthopedic Implants for Biomedical Applications. JOM. 68 (4):1191–1197. DOI: https://doi.org/10.1007/s11837-016-1837-x.

Low Anisotropy and High Ductility of Mg–Zn–Ce Alloy Achieved by the Optimized Thermo-mechanical Process

Xiaoying Qian, Zhihua Dong, Bin Jiang, Cuihong Wang, Zhiying Zheng, and Fusheng Pan

Abstract

The effect of thermo-mechanical process involving different cold rolling reductions along extrusion direction combined with annealing treatment on plastic deformation and its anisotropy of Mg–1Zn–0.2Ce (wt%) alloy is studied. The results show that low anisotropy and exceptional ductility with the elongation up to 41.6% along rolling direction (RD) and 45.4% along perpendicular direction (TD) are achieved by one-passed cold rolling reduction of 19% in combination with the annealing at 350 °C for 1 h. The microstructure characterization by electron backscattered diffraction indicates that the mechanism behind this is closely related to the preferred nucleation and growth of grains characterized by the TD texture component during the annealing process, which contributes to the texture transformation from bimodal to ring-like type. The weakened anisotropy and improved ductility obtained by the optimized thermo-mechanical process can significantly increase the plastic deformation capacity and promote wider engineering applications of the alloys.

Keywords

Magnesium alloys • Plastic deformation • Thermo-mechanical process • Texture evolution

Introduction

The strong basal texture is generally observed in commercial wrought magnesium (Mg) alloys due to the hexagonal closed-packed structure, leading to relatively low ductility and formability at room temperature and further restricting the engineering applications of Mg alloys [1–3]. Weakened basal texture and even double peak texture could be obtained in Mg–Zn–Re alloys [4], such as Mg–Zn–Gd [5, 6], Mg–Zn–Ce [7–9], and Mg–Zn–Y [10] via high-speed extrusion or multidirectional impact forging. It contributes to their improved ductility and formability at room temperature. Nevertheless, the Mg–Zn–Re alloys generally exhibit evident plastic anisotropy when tension is conducted along various directions, because of numerous grains in one favourable orientation for basal slip and tensile twinning [11, 12].

Extensive processing technologies, such as multiple rolling [13, 14] and equal channel angular extrusion [15–17], have been proposed to reduce plastic anisotropy. For instance, Hoseini-Athar et al. [18] introduced the new $\langle \bar{1}2\bar{1}1 \rangle$ component texture to form non-basal extrusion direction-perpendicular direction (ED-TD) double split texture in Mg–Zn–Gd alloy by the constrained groove pressing. Shi et al. [19] revealed that the basal pole was tilted from ND (normal direction) toward TD by five-pass rolling with final heavy reduction rolling and the planar anisotropy in the mechanical response of Mg–Zn–Y–Zr alloy was significantly reduced. Nevertheless, these processes are relatively complex and costly for engineering applications [20]. In addition, the processing parameters highly depend on chemical composition and need to be optimized for different alloy systems. For the plastic Mg–Zn–Ce alloy, the influence of the one-passed cold-rolled process on its microstructure, plastic anisotropy, and ductility remains unclear.

In the present work, the effect of thermo-mechanical process involving different cold rolling reductions along extrusion direction combined with annealing treatment on texture modification, ductility, and anisotropy of as-extruded

---

X. Qian · Z. Dong (✉) · B. Jiang (✉) · C. Wang · Z. Zheng · F. Pan
National Engineering Research Center for Magnesium Alloys, College of Materials Science and Engineering, Chongqing University, Chongqing, 400044, China
e-mail: dzhihua@cqu.edu.cn

B. Jiang
e-mail: jiangbinrong@cqu.edu.cn

X. Qian · Z. Dong · B. Jiang · C. Wang · Z. Zheng
National Key Laboratory of Advanced Casting Technologies, College of Materials Science and Engineering, Chongqing University, Chongqing, 400044, China

A. Leonard et al. (eds.), *Magnesium Technology 2024*, The Minerals, Metals & Materials Series,
https://doi.org/10.1007/978-3-031-50240-8_26

Mg–Zn–Ce alloy is investigated. The mechanisms behind the improved mechanical properties are elaborated with detailed microstructure characterizations.

Experimental Procedures

The chemical composition of the studied alloy is shown in Table 1. As-extruded sheets with a thickness of 3 mm and a width of 56 mm were obtained by hot extrusion at 450 °C with an extrusion ratio of 30. Then, the as-extruded sheets were subjected to the one-passed cold rolling with different reductions of 5, 8, and 19%. The annealing treatment of the rolled sheets was conducted at 350 °C for 1 h.

Table 1 Chemical composition of studied Mg alloy (wt%)

	Mg	Zn	Ce
ZCe10	Bal	1.06	0.19

The mechanical properties of samples were tested at a tensile rate of 1.5 mm/min at room temperature. The tensile tests were performed along ED or rolling direction (RD) and TD, and three repeated measurements were carried out for accuracy. The tensile specimens with a cross-sectional area of 6 mm × 3 mm and a gauge length of 12 mm were used in the test. The microstructure characterization was conducted using electron backscattering diffraction (EBSD, JEOL JSM-7800F) after electrolytically polished by AC2 at − 20 °C with a voltage of 20 V and a current of 0.03 A.

Results and Discussion

Mechanical Properties

Figure 1 shows the engineering stress–strain curves along ED/RD and TD of as-extruded alloys and cold-rolled alloys with annealing. As can be seen, as-extruded Mg–Zn–Ce alloy

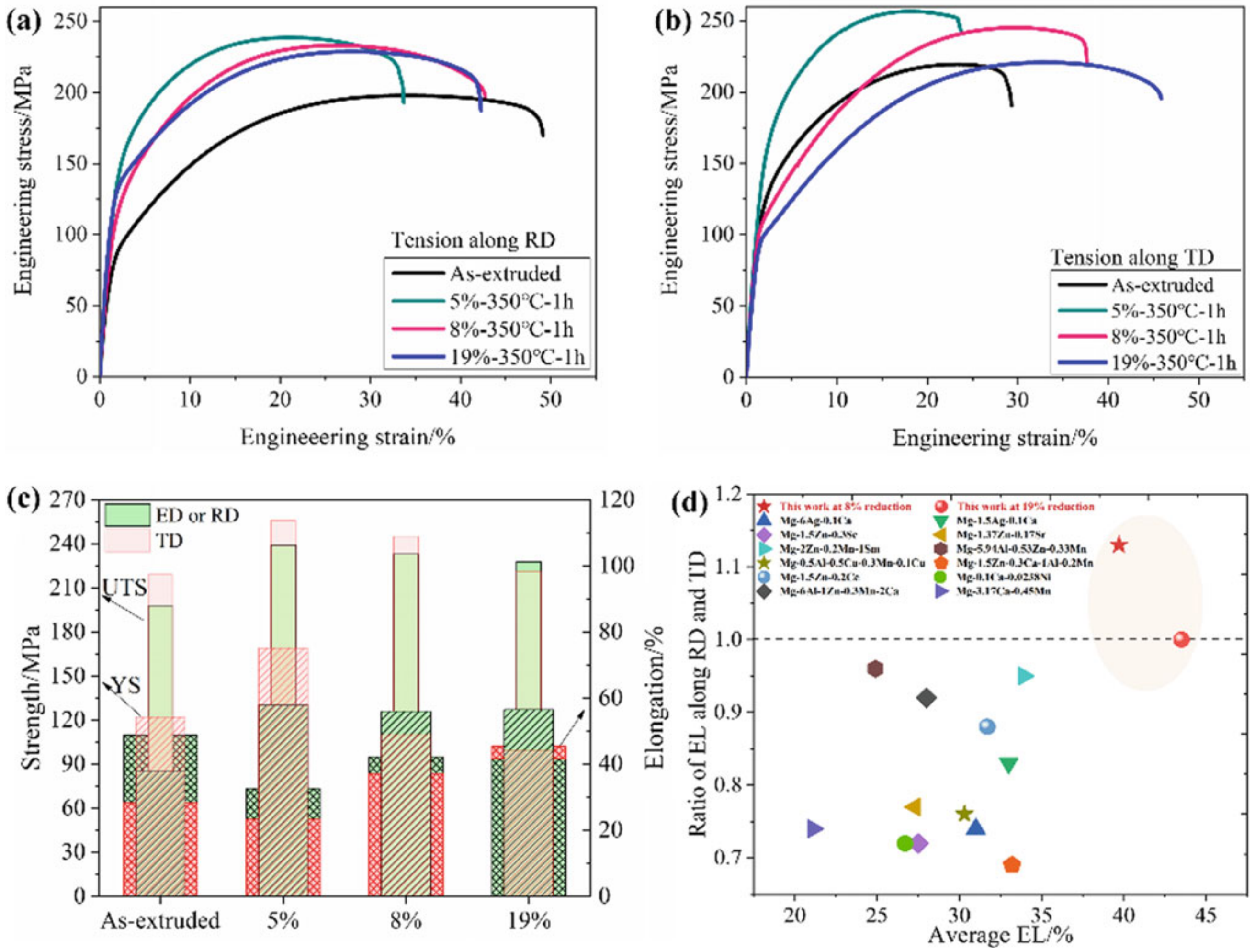

Fig. 1 Engineering stress–strain curve of alloys tension along **a** RD and **b** TD, with **c** critical mechanical parameters at different rolling reductions. A comparison of average elongation and plastic anisotropy among various rolled Mg alloys is shown in panel (**d**)

exhibits the elongation of 48.7 and 28.4% along ED and TD, respectively, indicating the large difference in terms of ductility, i.e., an obvious anisotropy in plasticity. After being subjected to the one-passed cold rolling reduction of 5% and the annealing process, the elongation decreases to ~ 32% along RD. With further increasing the rolling reduction to 8 and 19%, the elongation increases again to ~ 42%. For the tension along TD, the elongation decreases to 23.2% at 5% reduction and then gradually increases to 45.4% at annealing from the cold-rolled reduction of 19%. Accordingly, Mg–Zn–Ce alloy with the elongation of 41.6 and 45.4% along RD and TD, which is achieved at 19% cold-rolled reduction with annealing, shows a low anisotropy and high ductility. A comparison of ductility and anisotropy between the present findings with the available reports of the rolled Mg alloys [6, 21–31] is shown in Fig. 1d. It is clear that the studied alloy subjected to the extrusion and rolling process exhibits relatively high ductility and low plastic anisotropy, indicating an improved formability in engineering applications.

Microstructure Characterization

To understand the improvement of anisotropy and ductility, microstructure at as-extruded, cold-rolled, and annealed states are examined. Figure 2 shows the inverse polar figures (IPF), twin maps (TM), complete Kernel average misorientation (KAM) maps, and polar figures (PF) of as-extruded alloy and one-passed cold-rolled alloy with 5, 8, and 19% reduction. The as-extruded alloy shows complete dynamic recrystallization with the ED-split double peak texture. The average grain size of the dynamically recrystallized grains is estimated to be ~ 14 μm. Many high-angel grain boundaries are observed in twin maps without any twin variants. In addition, the KAM map exhibits that the strain is relatively homogeneous. After subjecting to a cold-rolled reduction of 5%, the number of tension twins increases, along with which a certain degree of low-angel grain boundaries appears. It is indicated that tension twinning is induced at small cold-rolled strains. With increasing the reduction to 8 and

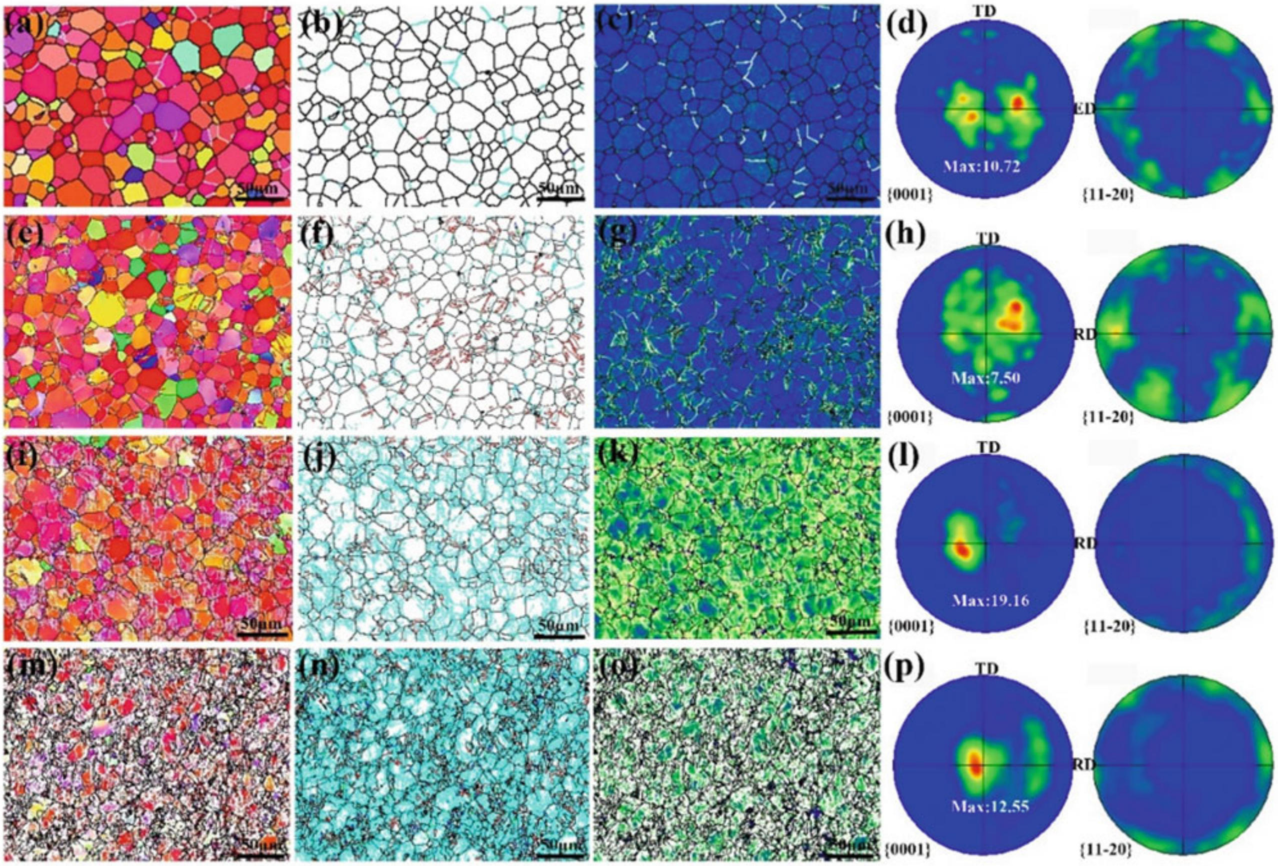

Fig. 2 Inverse pole figure, twin map, KAM, and pole figure of alloys at different rolling reductions: **a–d** 0%, **e–h** 5%, **i–l** 8%, and **m–p** 19%

19%, most grains exhibit a completely twinning structure. Namely, non-basal-orientated grains are rotated around 86° with the *c*-axis paralleling to normal direction, which ultimately leads to the enhanced basal texture component. Furthermore, the density of low-angel grain boundaries in the twin maps and geometrically necessary dislocation density in the KAM maps increase noticeably, indicating that dislocations slip also contributes to plastic deformation.

Furthermore, microstructure at annealing after different cold rolling reductions is shown in Fig. 3. It is observed that after annealing at 350 °C for 1 h, complete dynamic recrystallization occurs. The density of low-angel grain boundaries and the number of twins decrease significantly. Importantly, the type and component of texture are changed compared to the one of the as-extruded alloy. After annealing with 8 and 19% cold-rolled reduction, the double peak texture at the as-extruded state transforms to a ring-like texture with the maximum polar density decreasing from 10.72 m.r.d to 5.51 and 3.59 m.r.d. Basal slip in Mg alloys tends to be dominated in the process of plastic deformation at room temperature due to its low critical shear stress [32]. Grains with non-basal orientation effectively improve the Schmid factor of basal slip. Namely, the weakened texture of as-annealed alloy is favourable for the improvement of ductility. The alloy annealing with 19% cold-rolled reduction contains comparable RD and TD-orientated grains and exhibits high ductility and low anisotropy.

Static Recrystallization Behaviours

The low anisotropy and high ductility of the as-annealed alloy are closely related to the ring-like texture characteristic according to the above EBSD observations. It is well-known that static recrystallization behaviours primarily contribute to the formation of texture. In the following, the influence of static recrystallization during annealing is elaborated. Figure 4 shows the inverse polar figure and polar figure, twin map, KAM, and distribution of grain boundary misorientation of alloys after 19% cold-rolled reduction and annealing at 350 °C for 10 min. The high density of low-angel grain boundaries can be observed. The grain boundary misorientation shows relatively frequent proportions at 86 ± 5° and 56 ± 5°, indicating that tension twins and few compression twins remain after short-time annealing. Nevertheless, partial static recrystallization has been triggered as evidenced by the low-strain energy within the grains.

To get insight into the influence mechanism of static recrystallization, two representative grains are extracted, as shown in Fig. 5. Parent grains P1 and P2 with high-strain stored energy exhibit RD orientation in Fig. 5a and b, while a misorientation of ~ 86° between grain M1, M2, M3, and M4 and parent grains is observed. It indicates that these grains belong to tension twins, which are orientated toward TD. Tension twin boundary is characterized by good coherency and high mobility [33]. During annealing, the

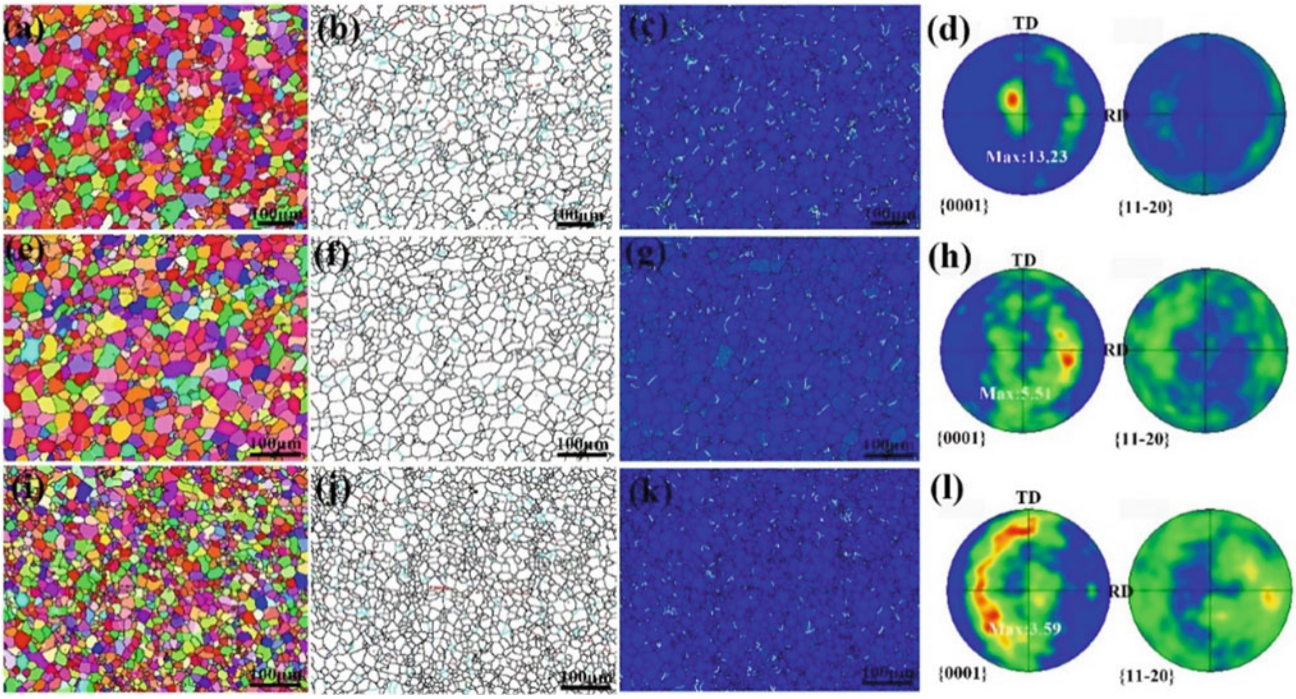

Fig. 3 Inverse pole figure, twin map, KAM, and pole figure of alloys at different rolling reductions with annealing: **a–d** 5%, **e–h** 8%, and **i–l** 19%

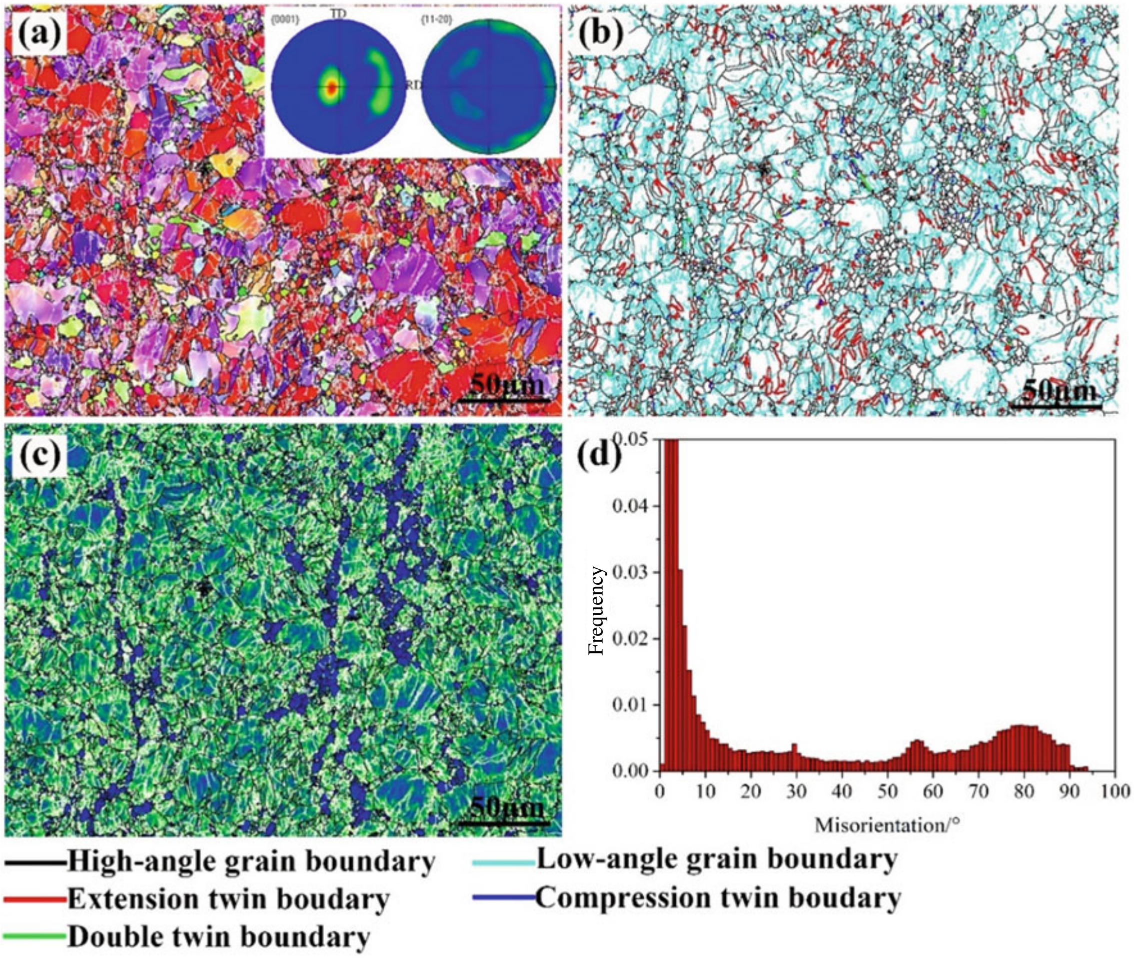

Fig. 4 Microstructure examination after short-time annealing: **a** inverse polar figure and polar figure, **b** twin map, **c** KAM, and **d** distribution of grain boundary misorientation

high-stress concentration accumulation is replaced by the region of low stored energy and tension twins are easy to grow. Therefore, the RD-orientated parent grains would gradually transform into TD-orientated recrystallized grains. In addition, it can be seen in Fig. 5d that TD-orientated grains (M6–12) with low stored energy are preferable to nucleate at the grain boundary of basal-orientated parent grain (P3). The basal-orientated grain with the *c*-axis paralleling the external force shows hard orientation for basal slip and tension twinning so that the plastic deformation is difficult to be accommodated. It results in high-strain energy stored in basal-orientated grains, which can provide the required driving force for recrystallization during annealing. The high proportion of ED-orientated grains is beneficial to tension twinning when cold rolling is conducted along ED. With the increase of rolling reduction, some completely twinning grains exist in basal orientation grains, and TD-orientated tension twins form in random and ED-orientated grains. The easy growth of tension twins and preferable nucleation of TD-orientated grains around basal-orientated grains during static recrystallization promote the formation of TD-split texture components. Therefore, at 19% cold-rolled reduction and annealing, the proportion of TD-orientated grains is significantly improved and even higher than that of RD-orientated grains, which ultimately results in the formation of ring-like texture and improves the ductility along TD to reduce plastic anisotropy.

Conclusion

The influence of thermo-mechanical process involving different cold-rolled reductions along extrusion direction combined with annealing treatment on plastic deformation and its anisotropy of Mg–1Zn–0.2Ce (wt%) alloy is studied. The primary results are summarized as follows:

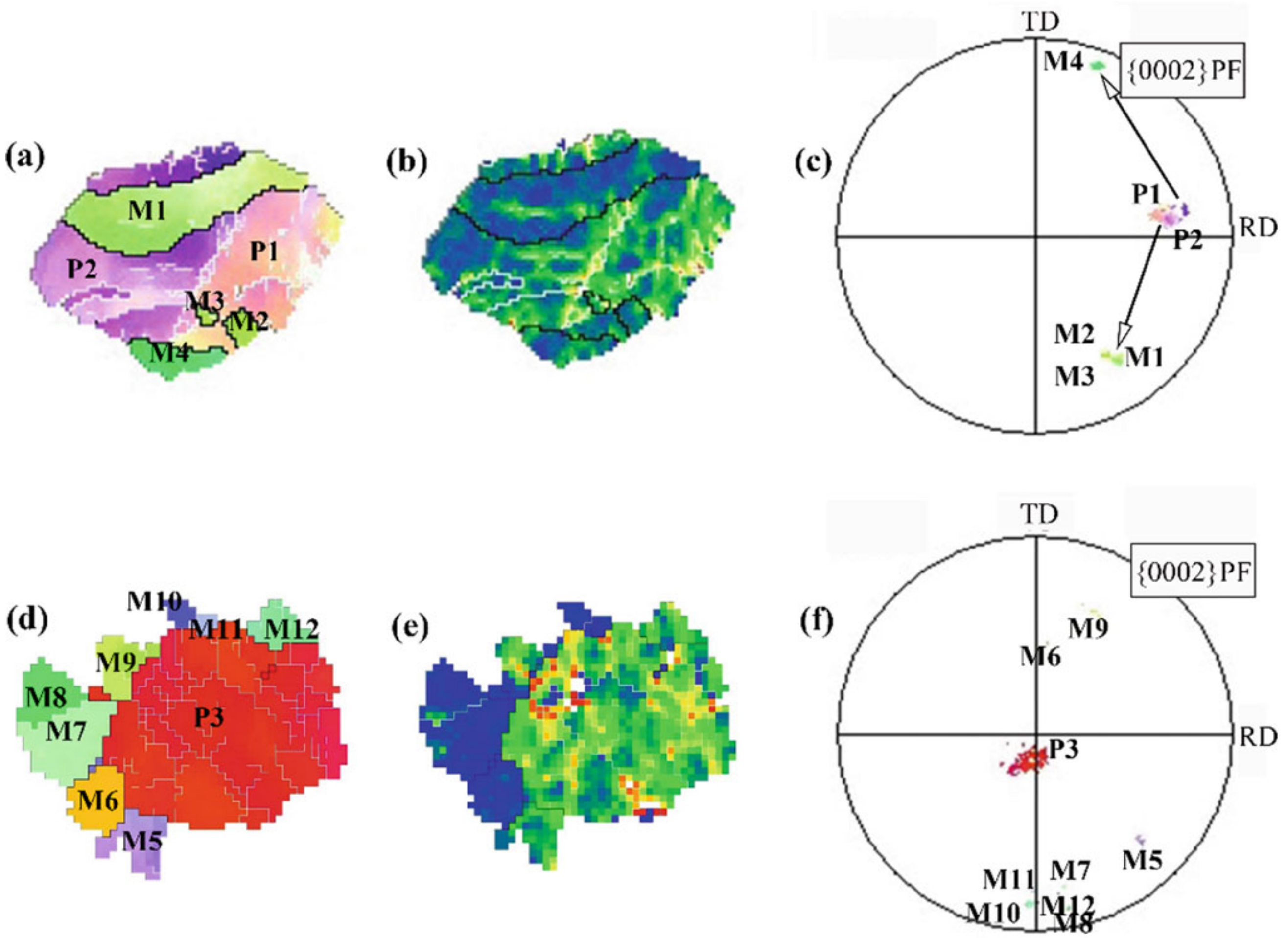

Fig. 5 Formation mechanism of TD-split texture component after one-passed cold rolling and annealing

1. Low anisotropy and excellent ductility with the elongation up to 41.6% along RD and 45.4% along TD are achieved by one-passed cold-rolled reduction of 19% in combination with the annealing at 350 °C for 1 h.
2. The microstructure characterization indicates that texture transformation from bimodal to ring-like type improves the TD-split texture component and contributes to low anisotropy.
3. The formation of a ring-like type texture during annealing is closely related to the static recrystallization mechanism including easy growth of TD-orientated tension twins and preferable nucleation of TD-orientated grains around basal-orientated grains with high stored energy.

Acknowledgements The authors are grateful to the National Natural Science Foundation of China (52101126, U1764253, U2037601, 52001037, and 51971044), the National Defense Basic Scientific Research Program of China, and the China Postdoctoral Science Foundation (2021M700566).

Conflict of Interest The authors declare that they have no conflict of interest.

References

1. S. Basu, E. Dogan, B. Kondori, I. Karaman, A. Benzerga (2017) Towards designing anisotropy for ductility enhancement: A theory-driven investigation in Mg-alloys. Acta Mater. 131: 349–362.
2. W. Huang, J. Chen, R. Zhang, X. Yang, L. Jiang, Z. Xiao, Y. Liu (2022) Effect of deformation modes on continuous dynamic recrystallization of extruded AZ31 Mg alloy. J. Alloys Compd. 897: 163086.
3. A.A. Luo, R. Shi, J. Miao, T. Avey (2021) Magnesium Sheet Alloy Development for Room Temperature Forming. JOM. 73: 1403–1418.
4. X. Qian, Z. Dong, B. Jiang, B. Lei, H. Yang, C. He, L. Liu, C. Wang, M. Yuan, H. Yang (2022) Influence of alloying element segregation at grain boundary on the microstructure and mechanical properties of Mg-Zn alloy. Mater. Des. 224: 111322.

5. M. Jiang, C. Xu, T. Nakata, H. Yan, R. Chen, S. Kamado (2016) Rare earth texture and improved ductility in a Mg-Zn-Gd alloy after high-speed extrusion. Mater. Sci. Eng. A. 667: 233–239.
6. X. Huang, M. Bian, Y. Chino (2022) Improvement of deep drawing formability of Mg-6Al-1Zn magnesium alloy sheets with high strength utilizing aging precipitation. Scripta Mater. 215: 114709.
7. P. Liu, H. Jiang, Z. Cai, Q. Kang, Y. Zhang (2016) The effect of Y, Ce and Gd on texture, recrystallization and mechanical property of Mg–Zn alloys. J. Magnes. Alloy. 4: 188–196.
8. Y. Du, M. Zheng, B. Jiang (2018) Comparison of microstructure and mechanical properties of Mg-Zn microalloyed with Ca or Ce. Vacuum. 151: 221–225.
9. T. Han, J. Zou, L. Ma, G. Huang, C. Che, W. Jia, L. Wang, F. Pan, Y. Zhang (2020) Microstructure evolution and mechanical properties of Mg-1.5 Zn-0.2 Ca-0.2 Ce alloy processed by accumulated extrusion bonding. JOM. 72: 2597–2602.
10. S.H. Lu, D. Wu, M. Yan, R.S. Chen (2023) Achieving texture randomization and yield anisotropy reduction in rolled Mg-Zn-Y-Zr alloy by multidirectional impact forging. Mater Charact. 195: 112540.
11. J. Bohlen, M.R. Nürnberg, J.W. Senn, D. Letzig, S.R. Agnew (2007) The texture and anisotropy of magnesium–zinc–rare earth alloy sheets. Acta Mater. 55: 2101–2112.
12. X. Qian, Y. Gao, Z. Dong, B. Jiang, C. He, C. Wang, A. Zhang, B. Yang, C. Zheng, F. Pan (2023) The enhanced Zn and Ca co-segregation and mechanical properties of Mg–Zn–Ce alloy with micro Ca addition. Mater. Sci. Eng. A. 867: 144712.
13. H. Yan, R. Chen, E. Han (2010) Room-temperature ductility and anisotropy of two rolled Mg–Zn–Gd alloys. Mater. Sci. Eng. A. 527: 3317–3322.
14. S. Wang, J. Ma, J. Yang, W. Zhang, Y. Sun, J. Pan, H. Wang, W. Chen (2021) Improving the ductility of Mg-2.5 Nd-0.5 Zn-0.5 Zr alloy by multi-pass hot rolling. J. Mater. Res. Technol. 14: 2124–2130.
15. M. Hashemi, R. Alizadeh, T.G. Langdon (2023) Recent advances using equal-channel angular pressing to improve the properties of biodegradable Mg–Zn alloys. J. Magnes. Alloy.
16. H. Wu, J. Jiang, H. Liu, H. Huang, Y. Li, J. Chen, A. Ma (2021) A novel method for improving the strength and ductility of Mg–Y–Er–Zn alloy using rotary-die equal-channel angular pressing. J. Mater. Res. Technol. 13: 1752–1758.
17. E. Mostaed, A. Fabrizi, F. Bonollo, M. Vedani (2015) Microstructural, texture, plastic anisotropy and superplasticity development of ZK60 alloy during equal channel angular extrusion processing. METALL ITAL. 11: 5–12.
18. M.M. Hoseini-Athar, R. Mahmudi, R.P. Babu, P. Hedström (2020) Tailoring the texture of an extruded Mg sheet through constrained groove pressing for achieving low mechanical anisotropy and high yield strength. Scripta Mater. 186: 253–258.
19. B. Shi, Y. Xiao, X. Shang, Y. Cheng, H. Yan, Y. Dong, A. Chen, X. Fu, R. Chen, W. Ke (2019) Achieving ultra-low planar anisotropy and high stretch formability in a Mg-1.1 Zn-0.76 Y-0.56 Zr sheet by texture tailoring via final-pass heavy reduction rolling. Mater. Sci. Eng. A. 746: 115–126.
20. S. Liu, C. Wang, H. Ning, Z.-Y. Meng, K. Guan, H.-Y. Wang (2023) Achieving high ductility and low in-plane anisotropy in magnesium alloy through a novel texture design strategy. J. Magnes. Alloy.
21. M. Bian, X. Huang, Y. Chino (2020) A combined experimental and numerical study on room temperature formable magnesium–silver–calcium alloys. J. Alloys Compd. 834: 155017.
22. M. Bian, X. Huang, Y. Chino (2020) A room temperature formable magnesium–silver–calcium sheet alloy with high ductility. Mater. Sci. Eng., A. 774.
23. M. Bian, X. Huang, M. Mabuchi, Y. Chino (2020) Compositional optimization of Mg–Zn–Sc sheet alloys for enhanced room temperature stretch formability. J. Alloys Compd. 818: 152891.
24. M. Yuasa, N. Miyazawa, M. Hayashi, M. Mabuchi, Y. Chino (2015) Effects of group II elements on the cold stretch formability of Mg–Zn alloys. Acta Mater. 83: 294–303.
25. W.-x. Fan, Y. Bai, G.-y. Li, X.-y. Chang, H. Hao (2022) Enhanced mechanical properties and formability of hot-rolled Mg–Zn–Mn alloy by Ca and Sm alloying. Trans. NonferusMet. Soc. China. 32: 1119–1132.
26. M. Bian, X. Huang, Y. Chino (2023) Improving the stretch formability of a heat-treatable magnesium–aluminum–calcium–manganese alloy by copper addition at the parts-per-million-level. Mater. Sci. Eng., A. 866: 144671.
27. X. Huang, M. Bian, I. Nakatsugawa, Y. Chino, M. Sato, K. Yamazaki, F. Kido, H. Ueda, M. Inoue (2023) Influence of aluminum content on microstructure and performance of Mg-Zn-Ca-Al-Mn magnesium alloys. J. Alloys Compd. 948: 169719.
28. Y. Chino, X. Huang, K. Suzuki, K. Sassa, M. Mabuchi (2010) Influence of Zn concentration on stretch formability at room temperature of Mg–Zn–Ce alloy. Mater. Sci. Eng., A. 528: 566–572.
29. M. Bian, Y. Matsuoka, X. Huang, Y. Ishiguro, Y. Tsukada, T. Koyama, Y. Chino (2023) Insights into the microstructures and mechanical properties of magnesium–calcium–transition elements: A combined experimental and simulation study. Acta Mater. 254: 118958.
30. M. Bian, X. Huang, Y. Chino (2021) Substantial improvement in cold formability of concentrated Mg–Al–Zn–Ca alloy sheets by high temperature final rolling. Acta Mater. 220: 117328.
31. T. Nakata, C. Xu, R. Abe, L. Geng, S. Kamado (2023) Unexpectedly formed strong basal texture in a rolled Mg-Zn-Ca-Mn alloy sheet. Mater. Charact. 203: 113101.
32. J. Zhang, S.P. Joshi (2012) Phenomenological crystal plasticity modeling and detailed micromechanical investigations of pure magnesium. J Mech Phys Solids. 60: 945–972.
33. L. Zhao, H. Yan, R. Chen, E.-H. Han (2020) Quasi-in-situ observations of low-angle grain boundaries, twins and texture evolution during continuous annealing in a cold-rolled Mg-Zn-Gd alloy. Mater Charact. 170: 110697.

Optimization of Bead Morphology for Cold Metal Transfer Wire Arc Additive Manufacturing of AZ31 Magnesium Alloy Wires

Suresh Goka, Manjaiah Mallaiah, and M. J. Davidson

Abstract

Wire arc additive manufacturing (WAAM) is a direct energy deposition additive manufacturing technology used for creating medium to large-scale components. This process involves the deposition of multiple layers of beads to fabricate a component from 3D CAD data. By controlling various process parameters, the fabrication of a component can be achieved through the deposition of multiple beads and layers. Therefore, the selection of suitable process parameters for efficient bead geometry, and bead-on substrate trials were conducted for the magnesium alloy (AZ31) using Taguchi L9 orthogonal array of experiments and a cold metal transfer (CMT) T400i welding power source. The input parameters chosen were wire feed, arc length correction, and travel speed, while the response parameters chosen were bead width, bead height, wetting angle, and dilution. The results were analyzed using analysis of variance (ANOVA) and regression equations. The R^2 and Adj R^2 values were both found to be above 90% for all the responses demonstrating the fitness of the model. Mean response optimization was employed to optimize the process parameters. To address the conflicting nature of the multiple responses, a Grey relation approach was applied to provide a unique solution for all responses. The validation of optimum process parameters was also conducted to determine the ability and suitability of the Grey relation approach. It was found that the predicted optimum process conditions were feasible settings for multi-layer deposition, with a deviation of less than 5% for experimental trials.

Keywords

WAAM • CMT • Magnesium alloy • Optimization • ANOVA • Desirability function

Introduction

Direct energy deposition (DED) is an additive manufacturing (AM) process that has been used to produce single-unit, complex-shaped components with less manufacturing lead time and more buy-to-fly ratios in various fields, viz. aerospace and automobile industries. Hence, the technology is moved to the next level by overcoming the conventional manufacturing process. During the last three decades, arc-based additive manufacturing has been exploring manufacturing large components enormously because the technology provides higher deposition rates, enlarged build envelop, lower capital cost, etc. The leading industry aerospace sector appears to be good at working with low-density and high-specific strength materials such as aluminium and magnesium alloys over the top usage of steel and other metal alloys. The wire feed-stock systems are useful in encouraging the arc welding process by supplying the wire-shaped raw material to the welding machine. Thus, the wire arc additive manufacturing (WAAM) process is a unique term that stormed the market as well as drawing the huge attention of users to work.

There are various WAAM processes that emerged in the industries due to their capability of producing components with high deposition rates and ensuring near-net shapes. Those are gas metal arc welding (GMAW), gas tungsten arc welding (GTAW), and plasma arc welding (PAW)-based layer-wise fabricating processes. Interestingly, cold metal transfer (CMT) is a modified technique of the GMAW process, which has attracted large-scale industries and many researchers because it is a phenomenal process that provides special benefits such as no spatter and low heat input [1].

S. Goka · M. Mallaiah · M. J. Davidson (✉)
Department of Mechanical Engineering, National Institute of Technology Warangal, Warangal, Telangana 506004, India
e-mail: jd@nitw.ac.in

A. Leonard et al. (eds.), *Magnesium Technology 2024*, The Minerals, Metals & Materials Series,
https://doi.org/10.1007/978-3-031-50240-8_27

The process has played a significant role in producing WAAM-based components [2]. MIG-based WAAM process was also used for thin wall preparation with ER70S-6 carbon steels [3], 316L steels [4], alloys H08Mn2Si [5] at variable layer width control. A second-order Hammerstein model is established to deal with the layer width and travel speed. A multi-material layered MIG/MAG-based WAAM welding has been carried [6] to investigate the material properties such as hardness and bond strength. Here, the materials used are YS308L and Ni6082, deposited alternatively one after another to make the thin walls. Hence, these methods are hugely appreciable in processing almost all the metals avail for industrial applications.

Among the materials, the lightest metals like aluminium, magnesium and their alloys are predominantly used due to their good specific strength and excellent machinability. Specifically, the magnesium-based WAAM components have been used in the aerospace and transportation fields. So, there is a need to analyse the basic operational parameters, other measurable factors, and their effect on the response parameters. Thus, the preliminary study is to be carried out in the contest of the weld deposition phenomenon (termed as cladding) to quantify the quality in the manufacturing process.

Firstly, it is important to know how the optimal operating conditions of the machine lead to depositing accurate bead profiles, which in turn decides the proper welding phenomenon and that implies the proper fabrication of the components. Many authors have followed the same phenomenon and got succeeded in producing favourable fabricated welded components [7, 8]. Therefore, the current work is focusing on optimizing the operating parameters using various sets of experiments. Subsequently, a relation between input and output parameters can be formed, and it can quantify the most appropriate parameters.

Secondly, in wire arc additive manufacturing deposition, focus on identifying the optimal deposition-related parameters and characterizing them. For that, conducting the design of experiments (DOE) is a crucial step before fabricating the bead geometries or components. These techniques are used in optimizing geometric parameters [9], machining parameters [10–12] welding parameters [13], topology optimization [14], and WAAM process parameters [15] also. Thus, statistical studies through the design of experiments also play a vital role in many areas such as design and manufacturing.

Experimental Procedure

Method and Material

In the process of simplification of the computed parameters, the experiments are carried out using the cold metal transfer (CMT)-based welding process (model type: Fronius TPS400i). The welding machine used is Trans Puls Synergic type, where the current, voltage, and wire feed used for operating the machine are correlated to each other. The feed-stock system is supplied with AZ31 type magnesium wire with a 1.2 mm diameter, which is used for depositing the preliminary beads. The beads of approximate length each 100 mm are deposited over a substrate of the same material, i.e., AZ31 type of plate with a thickness of 6 mm.

Table 1 illustrates the composition of the raw material, in terms of percentage of the weight. A high ultra-purity of 99.99% Argon gas is served as shielding gas operated at a flow rate of 15 l/min. During deposition, the nozzle tip-to-work piece distance (NTWD) is maintained at 16 mm. Bead samples of 10 mm in length are cut down using a wire electric discharge (EDM) machine (model type: EZEEWIN EW 300).

The bead deposition process is carried out using a CMT gun that is retrofitted to a gantry *X*–*Y* motion table. The arrangement of the experimental setup is shown in Fig. 1. The basic trail experiments are conducted to produce the simple single pass beads by using the input parameters over a certain range, namely current in the range of (90–126) A, voltage (13.2–15.1) V, and the torch travel speed maintained over (0.4–0.6) m/min. The consistency of arc stability is used to produce the proper cladding occupancy over the flat surface of AZ31-based magnesium alloy samples is tried to produce.

The input parameters used for the preliminary bead geometry analysis are wire feed, arc length correction, and travel speed. Table 2 is formulated with the parameters and their levels. For analyzing the bead geometry and proper coalescence of the welding phenomenon, the output parameters considered are bead height, bead width, contact angle, and dilution. These are treated as the main responses for optimizing analysis. The response values corresponding to input parameters are detailed in Table 3.

Here, dilution is representing the amount of material penetrated into the base plate. Dilution is one of the important parameters in estimating the fused weld quality. It

Table 1 Constituents of the raw material (as per AWS 5.19)

Wire particulars	Chemical composition							
Element type	Al	Mn	Zn	Si	Cu	Ni	Fe	Mg
Weight (wt%)	3.06	0.31	0.99	0.02	0.0023	0.0009	0.0026	Bal

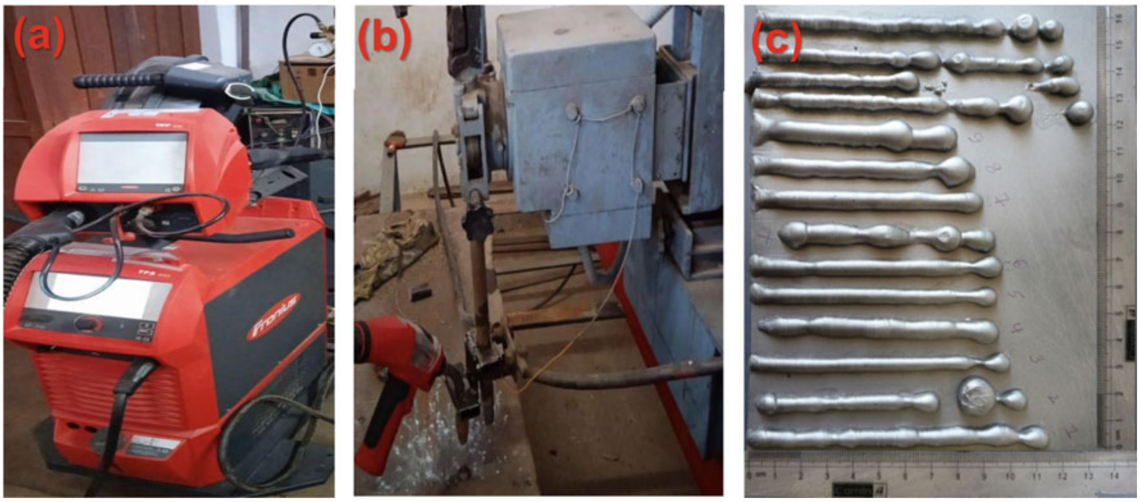

Fig. 1 Welding method **a** setup of CMT machine and **b** welding gun fixed to *X*–*Y* gantry table **c** deposited beads

Table 2 Factors and levels of the L9 orthogonal array

Input parameters	Levels of parameters		
	Level 1	Level 2	Level 3
Wire feed (m/min)	6.4	7.4	8.4
Arc length correction	− 2	0	+ 2
Travel speed (m/min)	0.4	0.5	0.6

Table 3 Input and output parameters corresponding to CMT bead deposition

S. No.	Input parameters			Output parameters			
	Wire feed (m/min)	Arc length correction	Travel speed (m/min)	Height (mm)	Width (mm)	Contact angle (°)	Dilution (%)
1	6.4	− 2	0.4	4.44	4.65	64.35	4.035
2	6.4	0	0.5	3.97	4.07	66.79	3.115
3	6.4	+ 2	0.6	3.96	3.99	65.35	5.388
4	7.4	− 2	0.5	4.14	5.47	75.96	4.711
5	7.4	0	0.6	4.01	4.98	72.15	4.183
6	7.4	+ 2	0.4	4.77	6.32	60.06	4.929
7	8.4	− 2	0.6	3.71	6.16	68.83	9.814
8	8.4	0	0.4	5.1	6.9	67.75	11.69
9	8.4	+ 2	0.5	4.45	6.22	59.58	16.83

results in change of weld metal chemistry due to mixing of the filler wire and base metal after fusion. The dilution percentage represents the amount of base material gets diluted due to depositing a bead on its surface. It is given by the following formula, as depicted in Fig. 2.

$$\text{Dilution} = \left(\frac{\text{Area of BOCFB}}{\text{Area of BOCFB} + \text{Area of BACOB}}\right) \times 100 \tag{1}$$

Hence, optimal results are observed by producing well-constructed beads for which the spatter formation is very less and an almost perfect bead profile is obtained without crater and any other weld defects.

Study of Design of Experiments

For precise weld outcomes quality, it is required to explore the optimizing techniques. Taguchi method and Grey

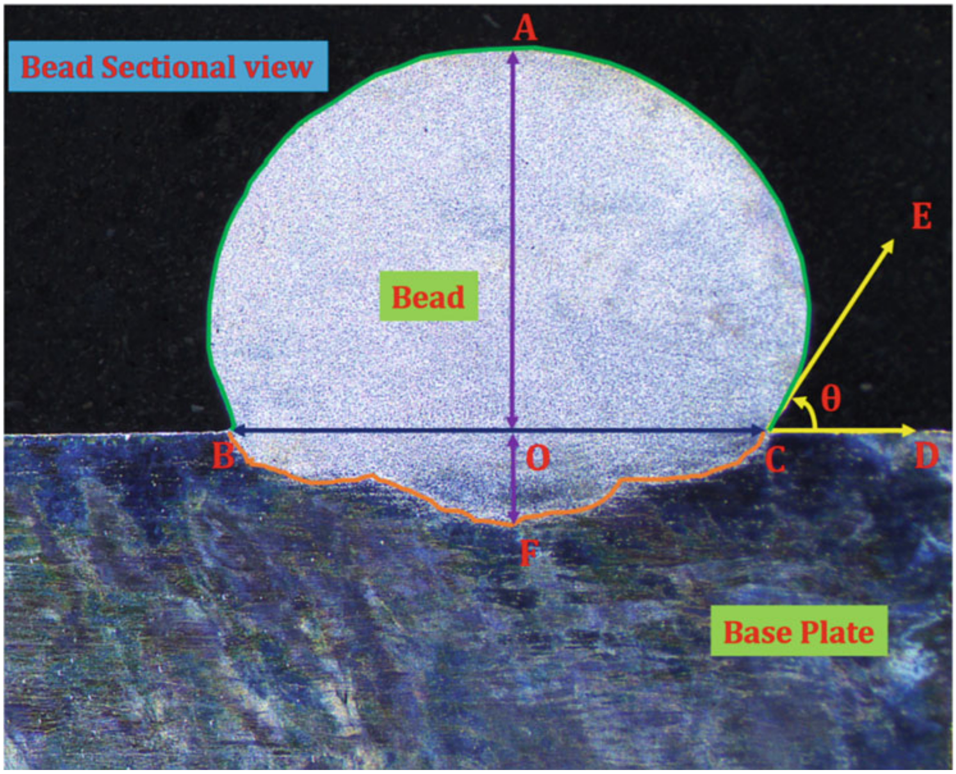

Fig. 2 Cross section of a bead: AO = bead height; BC = bead width; OF = penetration; $\theta = \angle DCE$ = contact angle

relational analysis are used to analyse and optimize the input process parameters based on the responses. The collected data is transferred into mean values and quantified as percentage of contribution. In our context, mean values, lower the better and higher better options are considered to optimize the data. The process parameters were analyzed using Minitab software.

ANOVA Method

The ANOVA test is used to figure out the percentage of impact of control factors/output parameters. Table 2 represents the actual L9 orthogonal array for the basic bead geometry analysis. The response of means of ANOVA is given in Table 4. The mean values is calculated using the following formula [11].

$$\text{Mean} = -10\log\left(\frac{1}{n}\right).\sum_{i=1}^{n} y_i^2 \tag{2}$$

where

$y_i, \ldots, y_n$	Response data
n	Number of observations.

Grey Relational Analysis (GRA) Method

For some cases, combined response of the output parameters is to be calculated to assess the effect of input parameters. In that case, GRA method is suitable with the design of Taguchi method. For determining the mean values, both higher the better and lower the better strategies are used. Higher the better is used to produce higher bead height, whereas lower the better is used to produce lower means of bead width, contact angle, and dilution also. Basically, three steps are involved in GRA method. First one is to normalize each output function. Secondly, the finding the deviation sequence. Then finally, acquiring Grey relational coefficient is to be done. In this way, both methods are used to identify and confirm the optimum process parameters. The following Eqs. (3) and (4) are used perform the first step.

In case of smaller the better,

$$z_{ij} = \frac{\max(x_{ij}) - x_{ij}}{\max(x_{ij}) - \min(x_{ij})} \tag{3}$$

In case of larger the better,

$$z_{ij} = \frac{x_{ij} - \min(x_{ij})}{\max(x_{ij}) - \min(x_{ij})} \tag{4}$$

here

x_{ij}	Experimental data obtained
$\max(x_{ij})$	Maximum of the experimental data obtained
$\min(x_{ij})$	Minimum of the experimental data obtained
z_{ij}	Normalized value for *i*th and *j*th experiments.

Table 4 Analysis of variance for means for **a** bead height, **b** bead width, **c** contact angle, and **d** dilution

Source	DF	Seq SS	Adj SS	Adj MS	*F*	*P*	Contribution (%C)
(a)							
Wire feed (m/min)	2	0.13447	0.13447	0.06723	1.42	0.414	8.50
Arc length correction	2	0.15847	0.15847	0.07923	1.67	0.375	10.01
Travel speed (m/min)	2	1.19487	1.19487	0.59743	12.58	0.074	75.49
Residual error	2	0.09500	0.09500	0.04750			6.00
Total	8	1.58280					
R^2 = 94.00%			Adj (R^2) = 76.00%				
(b)							
Wire feed (m/min)	2	7.32762	7.32762	3.66381	83.88	0.012	82.85
Arc length correction	2	0.05642	0.05642	0.02821	0.65	0.608	0.64
Travel speed (m/min)	2	1.37296	1.37296	0.68648	15.72	0.060	15.52
Residual error	2	0.08736	0.08736	0.04368			0.99
Total	8	8.84436					
R^2 = 99.01%			Adj (R^2) = 96.05%				
(c)							
Wire feed (m/min)	2	31.20	31.20	15.60	0.81	0.553	13.98
Arc length correction	2	117.79	117.79	58.90	3.05	0.247	52.77
Travel speed (m/min)	2	35.58	35.58	17.79	0.92	0.521	15.94
Residual error	2	38.63	38.63	19.31			17.31
Total	8	223.20					
R^2 = 82.69%			Adj (R^2) = 30.77%				
(d)							
Wire feed (m/min)	2	140.853	140.853	70.426	16.30	0.058	82.78
Arc length correction	2	15.619	15.619	7.809	1.81	0.356	9.18
Travel speed (m/min)	2	5.049	5.049	2.525	0.58	0.631	2.97
Residual error	2	8.643	8.643	4.321			5.08
Total	8	170.164					
R^2 = 94.92%			Adj (R^2) = 79.68%				

Grey relation coefficient is given by

$$\alpha\left(z_{0j}, z_{ij}\right) = \frac{\delta_{\min} + \gamma\delta_{\max}}{\delta_{ij} + \gamma\delta_{\max}} \tag{5}$$

where

δ_{ij}	$\lvert z_{0j} - z_{ij} \rvert$
$\delta_{\min}$	$\mathrm{Min}(\delta_{ij})$
$\delta_{\max}$	$\mathrm{Max}(\delta_{ij})$
i	1, 2, 3, …, m
j	1, 2, 3, …, n
δ_{ij}	The deviation sequence of the mentioned and the analogy sequence
γ	Distinguish coefficient in the range 0–1 0.5 (in this study).

The smaller the value γ, the more distinct it is. The summation of Grey relation coefficients is the Grey relational grade and it is given by below formula.

$$\wedge(Z_0, Z_i) = \sum_{i=1}^{n} Y_j \alpha\left(z_{0j}, z_{ij}\right) \tag{6}$$

where

$\sum_{j=1}^{n} Y_{jj}$	1 (for i = 1, 2, …, m)
$\wedge(Z_0, Z_i)$	The Grey relational grade between mentioned sequence Z_i and analogy sequence Z_0.

Results and Discussion

It is important to understand the influence of process parameters in achieving good weld quality. The summarized results of the L9 arrayed bead geometry are analyzed and discussed in this section in detail. The experimental values are tabulated for cross sectional geometry of each single bead. Figure 2 represents the sectional view of a bead and the corresponding terminology used for further analysis. The output parameters and their notations are mentioned in detail here.

The experimentally obtained output parameters corresponding to the welding operating input parameters are tabulated in Table 3.

ANOVA Analysis

The experimental information calculated from the geometry of beads can be analysed and optimized using ANOVA. This analysis makes possible to estimate how the input factors affect the bead height, width, contact angle, and dilution individually. The influence of input parameters and their interactions is studied in terms of percentage of contribution (%C). The information is given in Table 4, where DF stands for degree of freedom, Seq SS stands for sequential sums of squares, Adj SS stands for adjusted sum of squares, Adj MS stands for adjusted mean squares, F stands for statistics of test, and P stands for probability of the test.

The performance of ANOVA test in finding the interactions between the input parameters and the output parameters is presented in Table 4a–d, respectively. The observed data is quantified as mean values data so that it can be useful for estimating how successfully the process parameters being influenced the response values. Based on the calculated mean values for the bead height, width, contact angle, and dilution, their correlation is depending on the various levels of process parameters as mentioned above. The information is obtained using the Minitab software. As a result, the obtained numerical for individual output parameter is explained in detail.

The most influenced parameter in estimating the bead width is wire feed (82.85%), then followed by travel speed (15.52%) and arc length correction (0.64%). Similarly, in estimating the dilution, the most influenced parameter is wire feed (82.78%), then followed by arc length correction (9.18%) and travel speed (2.97%). That means, wire feed has to be focused more while selecting the operating process parameters. In addition, travel speed had significant effect (75.49%) in estimating the bead height. Here, the contribution of wire feed is 8.5%, and arc length correction is 10.01%. Subsequently, to estimate the contact angle, the arc length correction factor had 52.77% influence followed by the contribution of travel speed is 15.94% and wire feed is 13.98%.

Therefore, wire feed had the highest effect on the response factors, in terms of percentage of contribution, whereas the arc length correction and torch speed have significant effect. It is obvious that the wire feed had the most influence on the response factors such as bead width and dilution of base plate. The calculated results are converted to mean values to represent the effectiveness of the process parameters. The same information can be analyzed in better way by considering the plots made for input parameters versus mean values of the output parameters as shown in Fig. 3.

Figure 3 depicts the impact of multiple test input parameters (plot for main effects for mean) on the output parameters. If a specific parameter line is close to the horizontal reference line, that means, the parameter has no influence. Otherwise, in case the parameter line is greatly inclined to the horizontal reference line, then the parameter has good enough influence/impact. With the existing evidence, the travel speed has greatest impact on bead height, arc length correction has the greatest impact on contact angle, whereas other parameter wire feed has greatest impact on bead width and dilution. Nevertheless, the subsequent impact of the other input parameters on bead geometry, contact angle, and dilution is observed measurably.

In response to the bead height, parameter line is highly inclined to reference line in the range of 4.8–3.8 mm, with the change in travel speed from 0.4 to 0.6 m/min. Thus, travel speed is most influencing factor of the responses, followed by wire feed and arc length correction. In case of bead width, the parametric line is more inclined to the mean reference line in the range of 4.2–6.45 mm, with the change in wire feed 0.64–0.84 m/min, further followed by arc travel speed and arc length correction. Similarly, in case of dilution the parametric line is more inclined to the mean reference line in the range of 4–13% approximately, with change in wire feed 0.64–0.84 m/min, followed by arc length correction and torch speed. Whereas for the response of contact angle, the mean response line is more inclined in the range of 69.5–61.5° with the change in arc length correction in the range of -2 to 2 and is more than the effect of wire feed and travel speed.

Thus, from the analysis of variance (ANOVA), it can be concluded that wire feed is the most influencing input parameters among the considered three parameters. Then, travel speed is preferred to arc length correction.

GRA Study of Experimental Data

This study results in finding the best combination of the three input factors by treating the combined influence of all the four output parameters. The process is initiated with

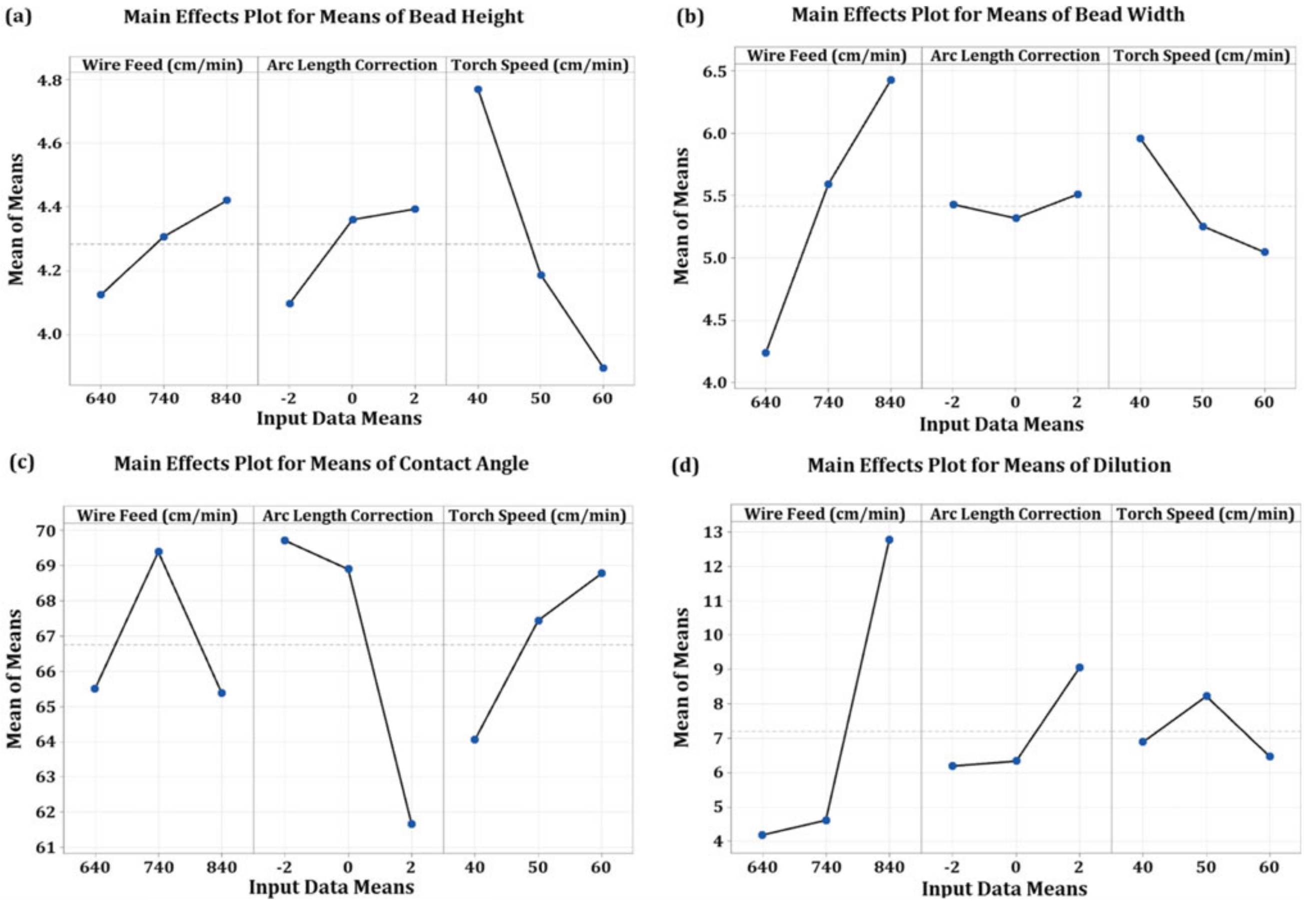

Fig. 3 Plots of input data means versus mean values: **a** for bead height, **b** for bead width, **c** for contact angle, and **d** for dilution

considering L9 array to represent the input data. Then after, the normalization, deviation sequence, Grey relational coefficient values followed by the Grey relational ranks are found out and tabulated the values corresponding to the values of each level and factor. Tables 5 and 6 are formed with complete calculation procedure involved in the GRA method.

The smaller the better performance and larger the better performance are two options used for the further step analysis in this optimization process. The overall process steps are considered and calculated the corresponding values to the 9 array combinations. The bead height is assigned to larger the better performance category, whereas the bead width, contact angle, and dilution are assigned to smaller the better performance category.

From the obtained results by following the three steps of GRA method, the calculated Grey relation grade is confirming that the 2nd combination is preferred as best combination of the three input factors. Further, the analysis can be extended to draw the best input parameters among the three factors.

The above response table is formed by considering the Grey relation grade of the three input parameters and their combinations. From the obtained (max–min) values and corresponding rankings, it can be confirmed that wire feed (0.172) is the most affecting input parameter, followed by arc length correction and travel with nearly stood with same values.

By conducting the GRA test, it is proved that wire feed is one of the most affecting operating parameters. And the best combination of input process parameters is obtained as the second combination. Hence, the second combination experiment is the optimal result. The combination is formed with wire feed is 6.4 m/min, arc length correction zero, and the travel speed is 0.5 m/min. The corresponding voltage and current are 90 A and 13.2 V, respectively.

Conclusion

CMT welding is one of the safe and comfortable welding processes, which can produce complex geometries to meet the industry requirements of near net shaping. Optimizing process parameters plays a vital role in conducting preliminary study of bead deposition. ANOVA offers a statistical framework for examining and measuring the impact of

Table 5 Stepwise procedure of GRA optimization

S. No.	Output parameters				Normalization				Deviation sequence				Grey relation coefficient				Grade	Order
	Height (mm)	Width (mm)	Contact angle (°)	Dilution (%)	Height (mm)	Width (mm)	Contact angle (°)	Dilution (%)	Height (mm)	Width (mm)	Contact angle (°)	Dilution (%)	Height (mm)	Width (mm)	Contact angle (°)	Dilution (%)		
1	4.44	4.65	64.35	4.035	0.525	0.773	0.709	0.933	0.475	0.227	0.291	0.067	0.513	0.688	0.632	0.882	0.679	4
2	3.97	4.07	66.79	3.115	0.187	0.973	0.560	1.000	0.813	0.028	0.440	0.000	0.381	0.948	0.532	1.000	0.715	1
3	3.96	3.99	65.35	5.388	0.180	1.000	0.648	0.834	0.820	0.000	0.352	0.166	0.379	1.000	0.587	0.751	0.679	3
4	4.14	5.47	75.96	4.711	0.309	0.491	0.000	0.884	0.691	0.509	1.000	0.116	0.420	0.496	0.333	0.811	0.515	8
5	4.01	4.98	72.15	4.183	0.216	0.660	0.233	0.922	0.784	0.340	0.767	0.078	0.389	0.595	0.395	0.865	0.561	7
6	4.77	6.32	60.06	4.929	0.763	0.199	0.971	0.868	0.237	0.801	0.029	0.132	0.678	0.384	0.945	0.791	0.700	2
7	3.71	6.16	68.83	9.814	0.000	0.254	0.435	0.512	1.000	0.746	0.565	0.488	0.333	0.401	0.470	0.506	0.428	9
8	5.1	6.9	67.75	11.69	1.000	0.000	0.501	0.375	0.000	1.000	0.499	0.625	1.000	0.333	0.501	0.445	0.570	5
9	4.45	6.22	59.58	16.83	0.532	0.234	1.000	0.000	0.468	0.766	0.000	1.000	0.517	0.395	1.000	0.333	0.561	6
Min	3.71	3.99	59.58	3.115														
Max	5.1	6.9	75.96	16.831														

Table 6 Response table for grade

Factor	Level1	Level2	Level3	Max–min	Rank
Wire feed (m/min)	0.691	0.592	0.520	0.172	1
Arc length correction	0.540	0.615	0.647	0.106	2
Travel speed (m/min)	0.649	0.597	0.556	0.093	3
	Average	0.600			

different variable factors on welding quality in terms of bead geometry, contact angle, and dilution. In this study of AZ31-based cladding process, the following conclusions are made:

- Form the ANOVA results, it is concluded that the wire feed had the highest effect on the both the bead width and dilution of base plate, respectively. Secondly, travel speed has significant effect on bead height, thirdly, arc length correction has moderate effect on contact angle.
- ANOVA method is concluded that the predicted optimum process conditions were feasible settings for depositing preliminary beads, with a deviation of less than 5% except for the mean values of contact angle response.
- GRA method confirms that the response is in good agreement with the ANOVA results.
- The optimal input process parameters obtained are wire feed as 0.64 m/min, arc length correction as zero, and travel speed as 0.5 m/min.

References

1. Ivántabernero, A. Paskual, P. Álvarez, and A. Suárez, "Study on Arc Welding Processes for High Deposition Rate Additive Manufacturing," *Procedia CIRP*, vol. 68, no. April, pp. 358–362, 2018, doi: https://doi.org/10.1016/j.procir.2017.12.095.
2. J. Wang, K. Zhu, W. Zhang, X. Zhu, and X. Lu, "Microstructural and defect evolution during WAAM resulting in mechanical property differences for AA5356 component," *J. Mater. Res. Technol.*, vol. 22, pp. 982–996, 2023, doi: https://doi.org/10.1016/j.jmrt.2022.11.116.
3. J. D. Kulkarni, S. B. Goka, P. K. Parchuri, H. Yamamoto, K. Ito, and S. Simhambhatla, "Microstructure evolution along build direction for thin-wall components fabricated with wire-direct energy deposition," *Rapid Prototyp. J.*, vol. 27, no. 7, pp. 1289–1301, 2021, doi: https://doi.org/10.1108/RPJ-04-2020-0085.
4. R. Mamedipaka and S. Thapliyal, "Data-Driven Model for Predicting Tensile Properties of Wire Arc Additive Manufactured 316L Steels and Its Validation," *J. Mater. Eng. Perform.*, 2023, doi: https://doi.org/10.1007/s11665-023-08071-5.
5. J. Xiong, Z. Yin, and W. Zhang, "Closed-loop control of variable layer width for thin-walled parts in wire and arc additive manufacturing," *J. Mater. Process. Technol.*, vol. 233, pp. 100–106, Jul. 2016, doi: https://doi.org/10.1016/j.jmatprotec.2016.02.021.
6. T. Abe and H. Sasahara, "Dissimilar metal deposition with a stainless steel and nickel-based alloy using wire and arc-based additive manufacturing," *Precis. Eng.*, vol. 45, pp. 387–395, 2016, doi: https://doi.org/10.1016/j.precisioneng.2016.03.016.
7. A. Sharma, N. Arora, and B. K. Mishra, "Mathematical model of bead profile in high deposition welds," *J. Mater. Process. Technol.*, vol. 220, pp. 65–75, 2015, doi: https://doi.org/10.1016/j.jmatprotec.2015.01.009.
8. S. Suryakumar and M. A. Somashekara, "Manufacturing of functionally gradient materials by using weld-deposition," *24th Int. SFF Symp. - An Addit. Manuf. Conf. SFF 2013*, pp. 505–508, Jan. 2013, doi: https://doi.org/10.1533/978-1-78242-164-1.505.
9. T. Markandeyulu, J. K. Devanuri, and K. Kiran Kumar, "Multi-Criteria Optimization of a PCM based Heat Sink—Effect of Geometric Parameters on Operational Time and Melt Fraction," *J. Therm. Sci. Eng. Appl.*, vol. 14, no. 3, Mar. 2022, doi: https://doi.org/10.1115/1.4051453.
10. M. Manjaiah, R. F. Laubscher, A. Kumar, and S. Basavarajappa, "Parametric optimization of MRR and surface roughness in wire electro discharge machining (WEDM) of D2 steel using Taguchi-based utility approach," *Int. J. Mech. Mater. Eng.*, vol. 11, no. 1, p. 7, Dec. 2016, doi: https://doi.org/10.1186/s40712-016-0060-4.
11. N. Bharat and P. S. C. Bose, "Optimization of tribological behaviour of TiO2nanoparticles reinforced AA7178 alloy matrix using ANN and Taguchi's methodology," *Surf. Topogr. Metrol. Prop.*, vol. 10, no. 2, p. 25032, 2022, doi: https://doi.org/10.1088/2051-672X/ac7a55.
12. N. Bharat and P. S. C. Bose, "Wear performance analysis and optimization of process parameters of novel AA7178/nTiO2 using ANN-GRA method," *Proc. Inst. Mech. Eng. Part E J. Process Mech. Eng.*, 2023, doi: https://doi.org/10.1177/09544089231156074.
13. S. C. Juang and Y. S. Tarng, "Process parameter selection for optimizing the weld pool geometry in the tungsten inert gas welding of stainless steel," *J. Mater. Process. Technol.*, vol. 122, no. 1, pp. 33–37, 2002, doi: https://doi.org/10.1016/S0924-0136(02)00021-3.
14. S. Satya Hanush and M. Manjaiah, "Topology optimization of aerospace part to enhance the performance by additive manufacturing process," *Mater. Today Proc.*, vol. 62, pp. 7373–7378, 2022, doi: https://doi.org/10.1016/j.matpr.2022.02.074.
15. M. Dinovitzer, X. Chen, J. Laliberte, X. Huang, and H. Frei, "Effect of wire and arc additive manufacturing (WAAM) process parameters on bead geometry and microstructure," *Addit. Manuf.*, vol. 26, pp. 138–146, Mar. 2019, doi: https://doi.org/10.1016/j.addma.2018.12.013.

Development of High-Strength Mg–Gd–Y Alloy Based on Machine Learning Method

Yunchuan Cheng, Zhihua Dong, Yuan Peng, Zhiying Zheng, Xiaoying Qian, Cuihong Wang, Bin Jiang, and Fusheng Pan

Abstract

A machine learning model is established to efficiently describe the relationship between mechanical properties and chemical composition and processing parameters of magnesium alloys. Among the implemented machine learning algorithms, the random forest model is demonstrated to show the high accuracy for the studied Mg–Gd–Y alloy family. By adopting the model, the optimal composition, thermal, and extrusion process parameters of a high-strength Mg–Gd–Y-based alloy are obtained. The ultimate tensile strength and elongation of the designed Mg–Gd–Y alloy are predicted to be 394 MPa and 8.7%, respectively, which is experimentally found to closely correlate to the formation of long period stacking ordered structure. Comparing with the experimental results, the prediction model gives relatively small error of 5.7% and 1.0% for the yield strength and ultimate tensile strength, respectively, and the poor prediction error of elongation is related to the quality of the prepared alloy. The findings are expected to provide helpful guidance for the intelligent design of advanced magnesium alloys.

Keywords

Magnesium alloys • Machine learning method • Mechanical properties

Introduction

Magnesium (Mg) alloys have broad application prospects in aerospace, transportation, electronic products, and other fields due to their low density, high specific strength, and stiffness [1–3]. However, its low strength and plasticity hinder the large-scale development and application of magnesium alloys [4, 5]. Developing high strength Mg alloys thus has been attracting the increased research interest. Alloying addition is one of the most effective methods to improve the mechanical properties of Mg alloys. Among them, rare earth elements such as Gd and Y are widely used to strengthen Mg alloys due to their exceptional solid solution strengthening and aging strengthening effects [6, 7]. With the development of Mg-RE alloys, a series of high-performance Mg–Gd–Y alloy families with multiple alloying elements such as Mg–Gd–Y–Zn–Zr and Mg–Gd–Y–Zn–Mn have been developed in recent years [8, 9]. In addition, the mechanical properties of Mg alloys can be further improved by different thermo-mechanical treatments such as hot extrusion, multiple rolling [10, 11], and equal channel angular extrusion [12, 13].

Nevertheless, extensive experimental efforts are usually required to optimize the chemical composition and processing parameters of Mg alloys to achieve the desirable properties, since the proper description of the complicated relationship between material composition, structure, process, and performance is generally missing. The machine learning (ML) method is a powerful tool to describe this type of complex relationships, which can effectively link the mechanical properties of the alloy with the composition and process based on data set [14]. In recent years, ML method

---

Y. Cheng · Z. Dong (✉) · Y. Peng · Z. Zheng · X. Qian ·
C. Wang · B. Jiang (✉) · F. Pan
National Engineering Research Center for Magnesium Alloys,
College of Materials Science and Engineering,
Chongqing University, Chongqing, 400044, China
e-mail: dzhihua@cqu.edu.cn

B. Jiang
e-mail: jiangbinrong@cqu.edu.cn

Y. Cheng · Z. Dong · Y. Peng · Z. Zheng · X. Qian ·
C. Wang · B. Jiang
National Key Laboratory of Advanced Casting Technologies,
College of Materials Science and Engineering,
Chongqing University, Chongqing, 400044, China

A. Leonard et al. (eds.), *Magnesium Technology 2024*, The Minerals, Metals & Materials Series,
https://doi.org/10.1007/978-3-031-50240-8_28

has been widely used in material property analysis and prediction [15], microstructure prediction [16], quantum chemistry, and discovery of new materials [17]. Nevertheless, there are few studies on the application of ML in Mg alloys, and the performance of different ML algorithms is also lack of in-depth research.

In the present work, four ML algorithms, i.e. bp-neural network (BP-NN), support vector machine (SVM), random forest (RF), and extreme gradient boosting tree (XGBoost), are implemented and their prediction accuracy are systematically compared based on the data set of Mg–Gd–Y alloys. The mapping model of alloy composition, process, and mechanical properties is established. The prediction of mechanical properties of high-performance Mg–Gd–Y alloy is realized, which is consistent well with the experimental measurement. The present findings are beneficial to the efficient development high-performance Mg alloys.

Machine Learning and Experimental Method

Data Preparation

The data set used in this paper is derived from the available publications of Mg–Gd-based alloys. It includes ~ 500 available data sets. In addition to the main alloying components, the solution temperature (ST), solution treatment time (St), and extrusion temperature (ET), and extrusion ratio (ER) are considered. The upper and lower limits of each feature variable in the data set are given in Table 1.

Model Method

In the present work, four ML algorithms including SVM [18], RF [19], XGBoost [20, 21], BP-NN [21–23] are considered, which were reported to be applicable for relatively small data set [24]. Four ML algorithms were established by Python programming language combined with Scikit-learn ML tool. The prediction model of mechanical properties of Mg–Gd–Y alloy was then established by comparing the prediction accuracy of different models.

The construction of ML model mainly includes data preprocessing, feature engineering, model training, model selection and evaluation, and model preservation [25]. In the present work, data processing methods such as missing value processing, outlier and repeated value removal were adopted to clean the Mg–Gd–Y alloy data [26]. In addition to eliminate the influence of feature inhomogeneity, the high-order features were scaled in the form of segmented coding. Specifically, the solution and extrusion temperatures starting from at 400 °C and 290 °C are coded every 20 °C and 30 °C, respectively. Then, the data are normalized.

The data set is divided into training set and testing set with the ratio of 8:2. The model is trained and selected using the training set combined with grid search and cross-validation; the model is evaluated using the testing set at the end [27]. The accuracy of the model is evaluated using R^2 and MAE, as follows:

$$R^2 = 1 - \frac{\sum (y_i - \hat{y}_i)^2}{\sum (y_i - \hat{y})^2} \quad (1)$$

$$\mathrm{MAE} = \frac{1}{N}\sum_{i=1}^{N} |y_i - \hat{y}_y| \quad (2)$$

where y_i is the actual value in the data set; $\hat{y}_i$ is the predicted value of the model; N is the total sample. The model with the highest accuracy is selected for the prediction of mechanical properties.

Experimental Method

The alloy designed using the ML method was prepared by gravity casting method, composition of which was determined by inductively coupled plasma analyzer (ICP). According to the designed thermo-mechanical process, the cast ingot was homogenized at 520 °C for 12 h and quenched into water. The homogenized ingot was preheated at

Table 1 Upper and lower limits of characteristic variables in Mg–Gd–Y alloy data set

Variables	Min	Max	Variables	Min	Max
Gd (wt%)	0	17.99	ST (°C)	0	550
Y (wt%)	0	9.11	St (h)	0	48
Zn (wt%)	0	10.6	ET (°C)	260	505
Zr (wt%)	0	2	ER	3.9	89
Mn (wt%)	0	2.23	UTS (MPa)	76	447
Nd (wt%)	0	6.48	YTS (MPa)	171	474
Er (wt%)	0	9.13	EL (%)	1.3	52

420 °C for 30 min and extruded into ingots with a diameter of 25 mm at the extrusion ratio of 12:1. Mechanical properties of the extruded alloys were measured by tensile tests performing at a CMT5105 test machine at room temperature (RT) with a crosshead speed of 1.5 mm/min. The microstructure was studied by scanning electron microscopy (SEM, TESCAN VEGA3 LMH SEM).

Results and Discussion

Data Analyzing

Figure 1 shows the distribution histogram of each characteristic variable in the adopted Mg–Gd–Y alloy data set. The results show that the distribution of Gd, Y, Zn, and Zr is relatively uniform owing to the relatively large data sets related to Mg–Gd–Y–Zn–Zr alloy system. In contrast, the data set containing other alloying elements are relatively small. For solution treatment, the temperature and time of the process are concentrated in the range from 500 °C to 540 °C and from 10 to 20 h, respectively. Similarly, the extrusion temperature is mainly concentrated at 430 °C, and the extrusion ratio is less than 20.

The Pearson correlation coefficient (PCC) is an effective measurement of the linear correlation between continuous variable pairs (x, y) [28]. It can reflect the dependence between different data features. Figure 2 is the PCC matrix between different data features for the Mg–Gd–Y alloy. The results show that the interdependence between the characteristics of the alloy is relatively weak, which reduces the possibility of feature confusion in the model. In addition, the relationship between the composition, process, and mechanical properties of Mg–Gd–Y alloy is characterized by a complex nonlinear relationship. The ML algorithms adopted thus should have the capability to deal with nonlinear processing.

Model Training, Evaluation, and Selection

After hyper-parameter optimization, the ML model was retrained on the entire training set to obtain a mapping model between chemical composition, process, and mechanical properties for Mg–Gd–Y alloy. The generalization performance of the model is verified using the test data set, which describes the ability to predict unknown data.

The comparison of prediction accuracy of the four established ML models is shown in Fig. 3. The results show that for the yield strength and tensile strength, the predicted values from the RF and XGBoost models are concentrated on the diagonal line, i.e. $y = x$ (Fig. 3g–l), the R^2 of which is as high as 0.91 and 0.89, relatively. The MAE is below ~ 23 MPa, indicating the higher prediction accuracy than those of SVM and BP-NN model for YTS and UTS. Furthermore, the RF model exhibits the best predictive performance for elongation (Fig. 3i), with a high R^2 of 0.87 and low MAE of 3.2%. Therefore, based on the predicted results of the three critical mechanical properties in the test data set, RF model is selected as the final prediction model for the mechanical properties of Mg–Gd–Y alloy.

Alloy Design and Model Prediction Performance Verification

With the target properties of UTS = 400MPa and EL = 10%, the chemical composition and processing parameters of Mg–Gd–Y–Zn–Zr alloy were screened by the established ML model. The results are given in Table 2. It is clear that combined the predicted chemical composition and thermos-mechanical properties, the UTS and EL are predicted to be in perfect line with the target properties, which will be further verified with the experimental measurements.

According to the prediction of the ML model, the target Mg–11.15Gd–5.41Y–1.05Zn–0.45Zr (wt%) alloy is prepared, and its tensile properties at room temperature were tested for the extruded samples. The engineering stress–strain curves are shown in Fig. 4. The yield strength, tensile strength, and elongation of the alloy are determined to be ~ 316 MPa, 398 MPa, and 3.2% (see Table 3), which are close to the prediction of the ML model except the relatively large deviation of elongation. Nevertheless, according to the ICP measurement, the actual composition of the prepare alloy is Mg–11.0Gd–5.4Y–1.0Zn–0.46Zr (wt%), which is slightly different from the designed one. To clarify, the actual alloy composition and process parameters are used as the input of the RF model to predict the mechanical properties of the alloy. The results in Table 3 show that the prediction error of yield strength, tensile strength, and elongation are 5.7% and 1.0% and 171.9%, respectively. Namely the established RF model has a good prediction ability on the strength for Mg–Gd–Y alloy, and the prediction of elongation is relatively poor, which the reason will be analyzed later.

Microstructure Characterization

To understand the mechanical properties of the designed alloy, microstructure at different states are investigated. Figure 5a, e shows the BSE-SEM image at as-cast state.

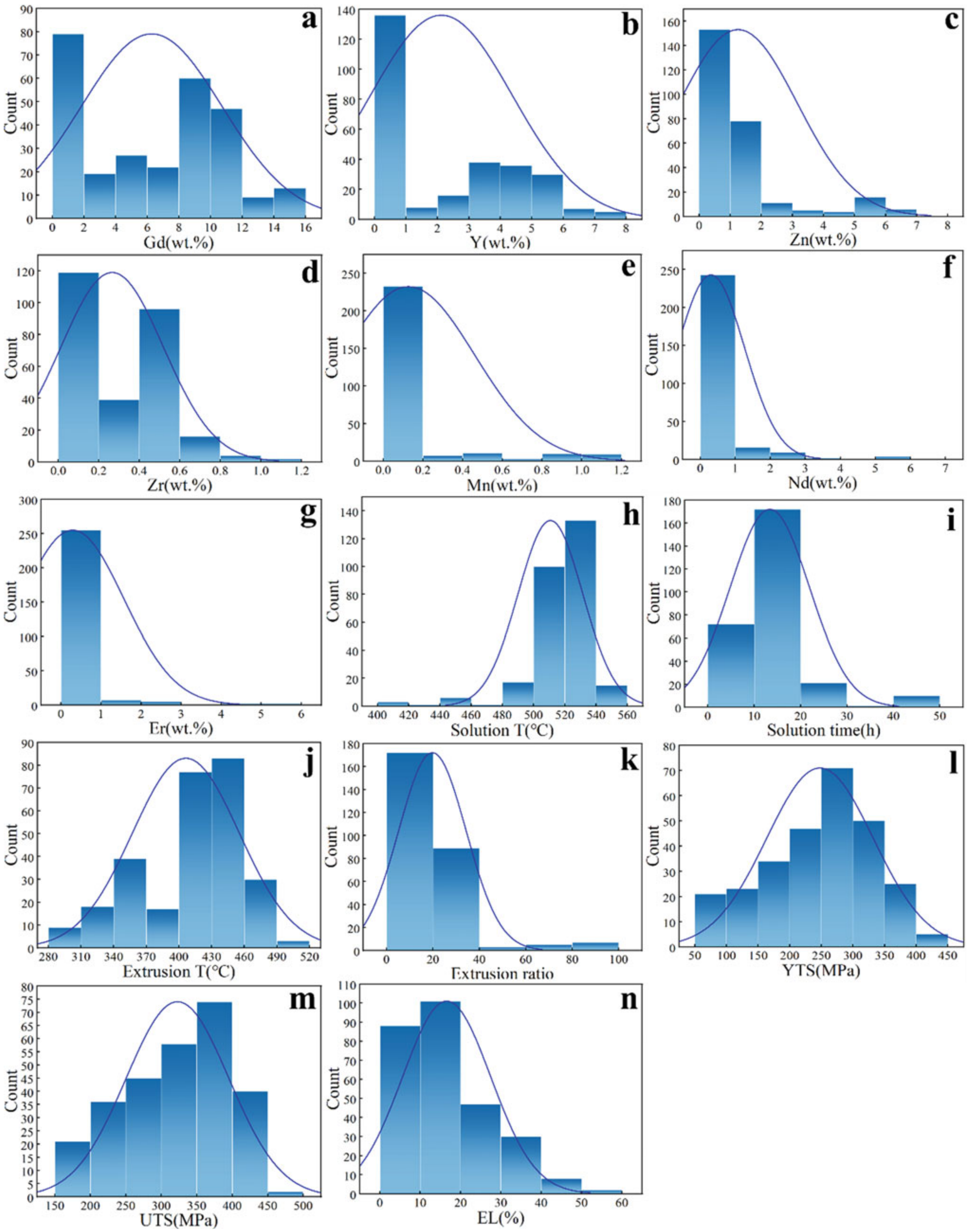

Fig. 1 Distribution histogram and density curve of each characteristic variable in Mg–Gd–Y data set. **a**–**g** Gd, Y, Zn, Zr, Mn, Nd, and Er, **h**–**i** solution treatment temperature and time, **j**–**k** extrusion temperature and ratio, **l**–**n** YTS, UTS, and EL

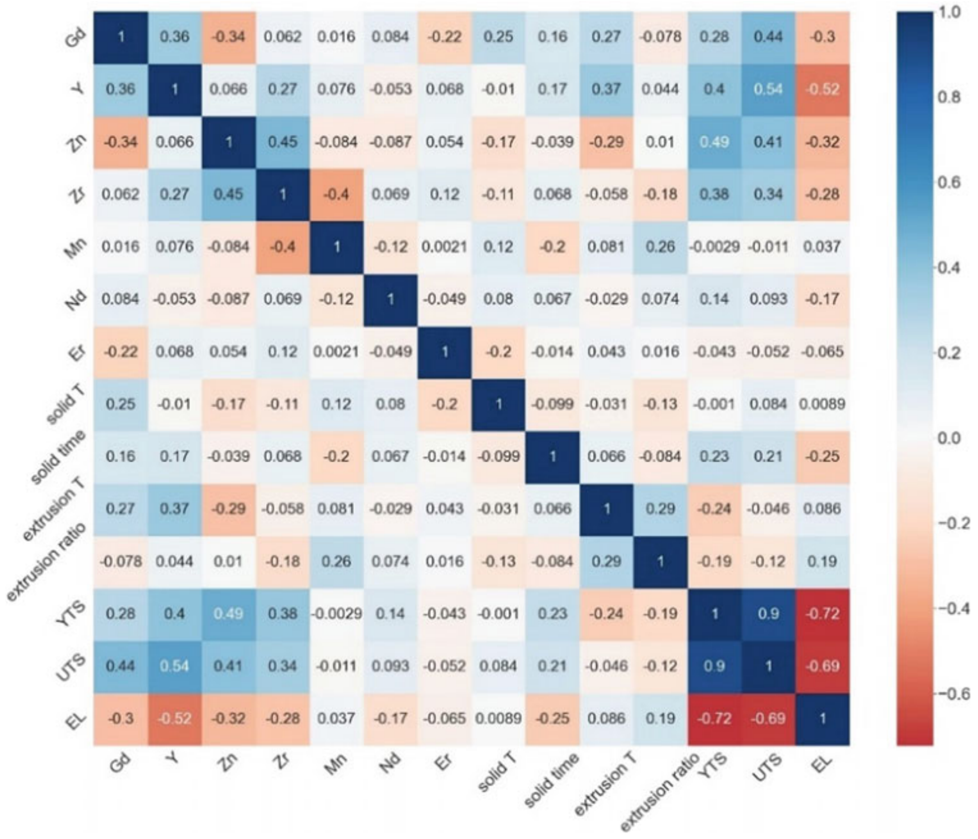

	Gd	Y	Zn	Zr	Mn	Nd	Er	solid T	solid time	extrusion T	extrusion ratio	YTS	UTS	EL
Gd	1	0.36	-0.34	0.062	0.016	0.084	-0.22	0.25	0.16	0.27	-0.078	0.28	0.44	-0.3
Y	0.36	1	0.066	0.27	0.076	-0.053	0.068	-0.01	0.17	0.37	0.044	0.4	0.54	-0.52
Zn	-0.34	0.066	1	0.45	-0.084	-0.087	0.054	-0.17	-0.039	-0.29	0.01	0.49	0.41	-0.32
Zr	0.062	0.27	0.45	1	-0.4	0.069	0.12	-0.11	0.068	-0.058	-0.18	0.38	0.34	-0.28
Mn	0.016	0.076	-0.084	-0.4	1	-0.12	0.0021	0.12	-0.2	0.081	0.26	-0.0029	-0.011	0.037
Nd	0.084	-0.053	-0.087	0.069	-0.12	1	-0.049	0.08	0.067	-0.029	0.074	0.14	0.093	-0.17
Er	-0.22	0.068	0.054	0.12	0.0021	-0.049	1	-0.2	-0.014	0.043	0.016	-0.043	-0.052	-0.065
solid T	0.25	-0.01	-0.17	-0.11	0.12	0.08	-0.2	1	-0.099	-0.031	-0.13	-0.001	0.084	0.0089
solid time	0.16	0.17	-0.039	0.068	-0.2	0.067	-0.014	-0.099	1	0.066	-0.084	0.23	0.21	-0.25
extrusion T	0.27	0.37	-0.29	-0.058	0.081	-0.029	0.043	-0.031	0.066	1	0.29	-0.24	-0.046	0.086
extrusion ratio	-0.078	0.044	0.01	-0.18	0.26	0.074	0.016	-0.13	-0.084	0.29	1	-0.19	-0.12	0.19
YTS	0.28	0.4	0.49	0.38	-0.0029	0.14	-0.043	-0.001	0.23	-0.24	-0.19	1	0.9	-0.72
UTS	0.44	0.54	0.41	0.34	-0.011	0.093	-0.052	0.084	0.21	-0.046	-0.12	0.9	1	-0.69
EL	-0.3	-0.52	-0.32	-0.28	0.037	-0.17	-0.065	0.0089	-0.25	0.086	0.19	-0.72	-0.69	1

Fig. 2 PCC matrix heat map between the characteristics of Mg–Gd–Y alloy data set

Combined with the EDS results (Table 4), it can be seen that the white phase (A point) and the white ash phase contain Mg, Gd, and Y elements, which should be Mg_5RE phase according to the thermodynamic calculations shown in Fig. 6. There is also a gray phase (C point) in the alloy. According to EDS, its composition is close to Mg_{12} (Gd, Y) Zn, which should be 14H-LPSO (Long period ordered stacking) phase [29]. As shown in Fig. 5b, f, after solution treatment, the second phase is significantly reduced, and a gray block LPSO phase appears. In addition, a rare earth-rich cubic phase composed entirely of Gd and Y is formed in the solid solution alloy. After extrusion at 420 °C, the broken block LPSO is distributed along the extrusion direction, and there are also some lamellar LPSO phases. In addition, some Mg-RE phases are precipitated along the extrusion direction [30]. Therefore, the relatively high strength of the designed alloy could be ascribed to the formation of LPSO phase. However, there are many large-sized second phases in the as-extruded alloy (Fig. 5h), and there are impurities in the alloy (Fig. 5d), which may be the reason for the low actual elongation of the alloy.

Conclusion

In the present work, through the construction and application of ML intelligent prediction model, the mechanical properties prediction of Mg–Gd–Y alloy based on alloy chemical composition and process parameters is realized. Firstly, the generalization performance of four ML algorithms is systematically compared, and the RF algorithm with the best comprehensive generalization performance is selected to construct the prediction model of mechanical properties of Mg–Gd–Y alloy. Secondly, the mechanical properties and microstructure of the designed alloy is measured experimentally. The yield strength, tensile strength, and elongation of the alloy are determined to be ~ 316 MPa, 398 MPa, and 3.2%, respectively. The microstructure analysis showed that the high strength of the alloy may be related to the formation of LPSO phase. Finally, a comparison of mechanical properties of the alloy from the established RF model and experimental measurement is made to verify the prediction accuracy. The prediction error of yield strength,

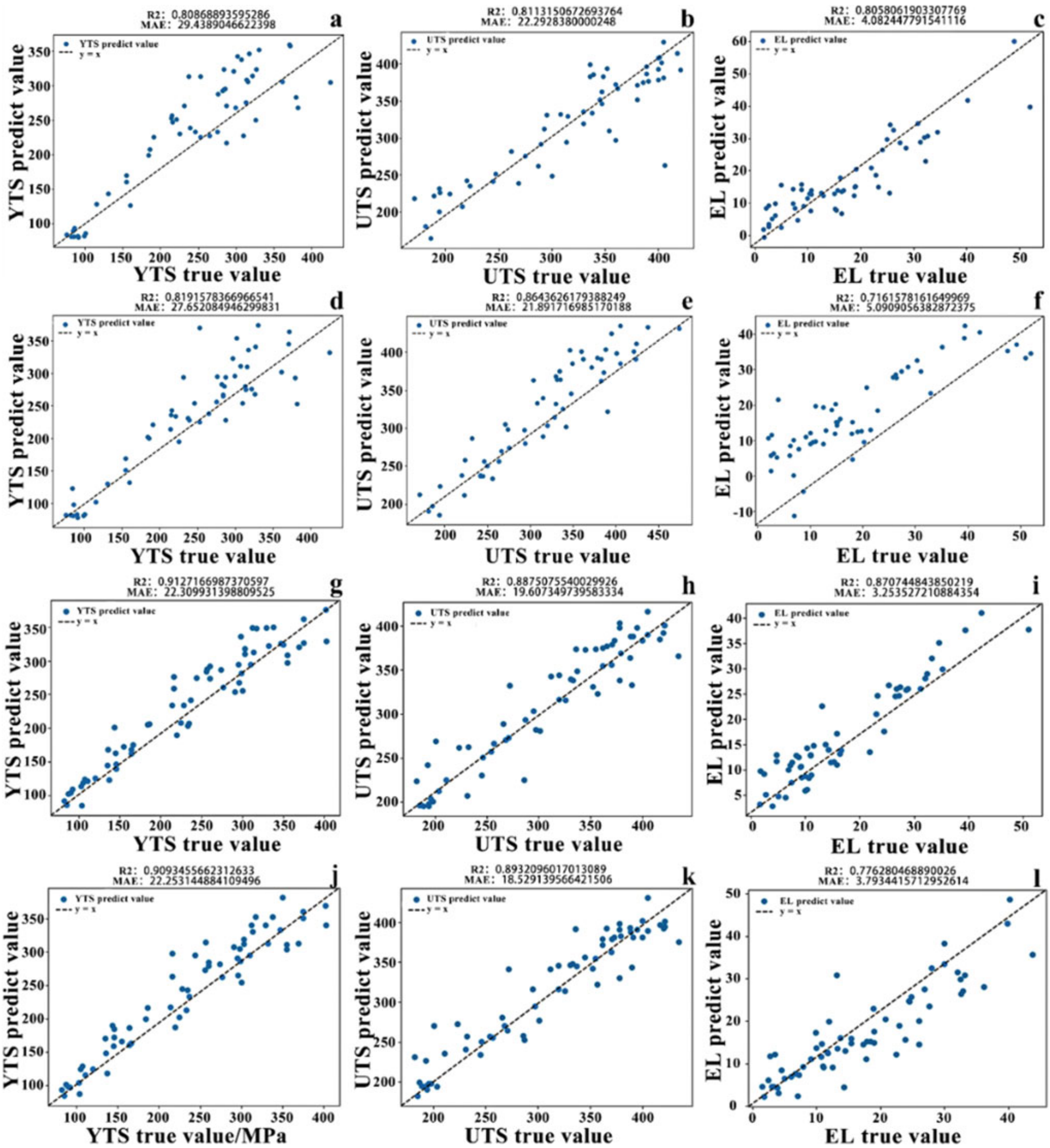

Fig. 3 Comparison of prediction accuracy of the four ML algorithms. **a**–**c** BP-ANN, **d**–**f** SVM, **g**–**i** RF, and **j**–**l** XGBoost

Table 2 Compositions and processing parameters designed by the established model

Gd	Y	Zn	Zr	ST	St	ET	ER	UTS	EL
11.15	5.41	1.05	0.45	520–540	11.50	420–450	13.00	400.01	10.00

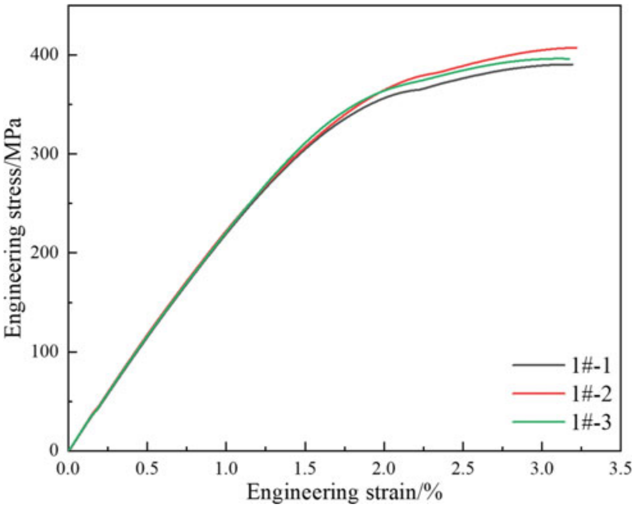

Fig. 4 Engineering stress–strain curves of the designed alloy

Table 3 Comparison of mechanical properties from the established RF model and experimental measurement

	YTS/MPa	UTS/MPa	EL/%
Experimental mean value	316	398	3.2
RF predicted value	298	394	8.7
Error = |Prediction − True|	18	4	5.5

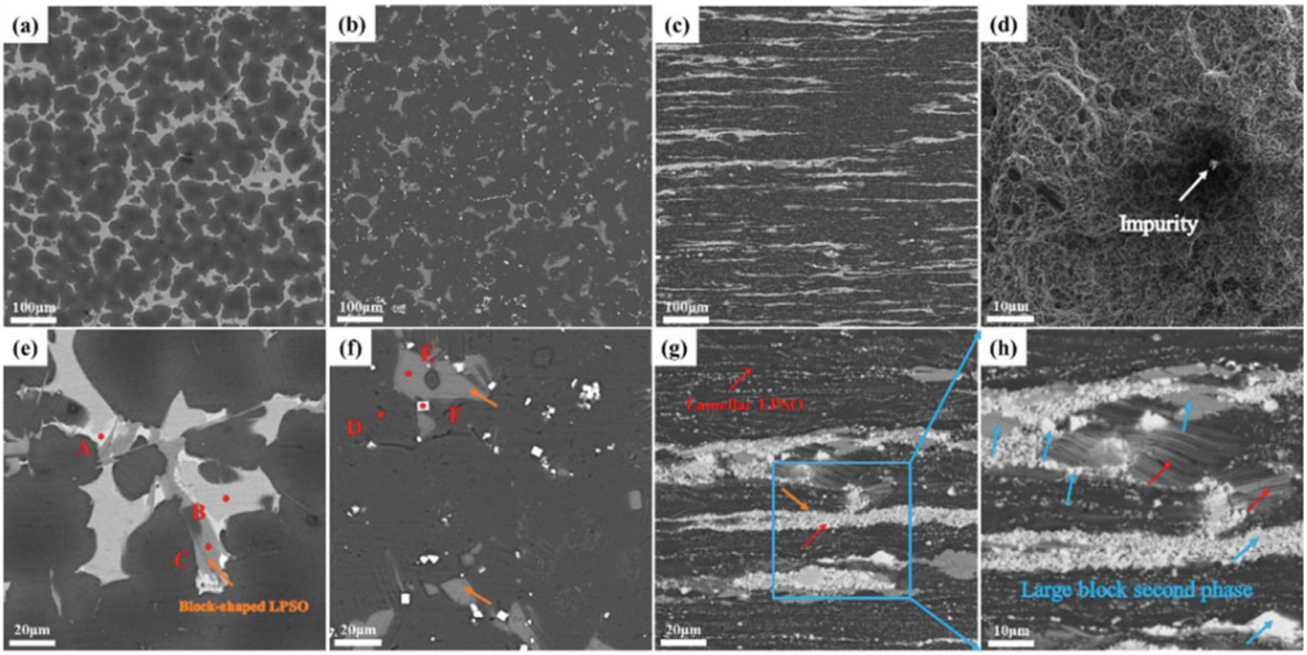

Fig. 5 BSE-SEM images of the alloys at different states: **a**, **e** as-cast, **b**, **f** solid solution, **c**, **g** as-extruded, and **d** the fracture morphology after tensile deformation

Table 4 EDS results of each phase of the alloy at different states

Alloy states	Position	Mg/at%	Gd/at%	Y/at%	Zn/at%	Zr/at%
As-cast	A	87.66	7.99	4.35	0	0
	B	88.04	6.43	5.53	0	0
	C	89.31	3.54	3.07	4.07	0
As-homogenized	D	97.82	2.18	0	0	0
	E	85.64	3.91	4.66	5.80	0
	F	0	29.37	90.63	0	0

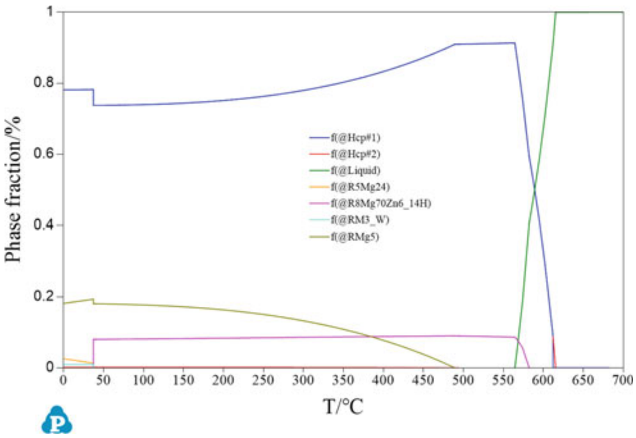

Fig. 6 Precipitation behavior of the alloy from Pandat thermodynamic calculations

tensile strength, and elongation is determined to be 5.7%, 1.0%, and 171.9%, respectively, showing a high prediction accuracy, and the large prediction error of elongation is related to the doping of impurities in the alloy.

Acknowledgements The authors are grateful to the National Natural Science Foundation of China (52101126, U1764253, U2037601, 52001037, and 51971044), the National Defense Basic Scientific Research Program of China, and the China Postdoctoral Science Foundation (2021M700566).

References

1. Qian XY, Dong ZH, Jiang B, et al (2022) Influence of alloying element segregation at grain boundary on the microstructure and mechanical properties of Mg-Zn alloy. Mater Des 224:111322
2. Qian XY, Gao YY, Dong ZH, Jiang B, He C, Wang CH, Zhang A, Yang BQ, Zheng CY, Pan FS (2023) The enhanced Zn and Ca co-segregation and mechanical properties of Mg–Zn–Ce alloy with micro-Ca addition. Mater Sci Eng A 867:144712.
3. Wang CH, Dong ZH, Jiang B, et al (2023) Lowering thermal expansion of Mg with the enhanced strength by Ca alloying. J Mater Res Technol 24:1293–1303.
4. Li YF, Zhang A, Li C, Xie HC, Jiang B, Dong ZH, Jin PP, Pan FS (2023) Recent advances of high strength Mg-RE alloys: Alloy development, forming and application. J Mater Res Technol 26:2919–2940.
5. Lei B, Dong ZH, Yang Y, et al (2022) Influence of Zn on the microstructure and mechanical properties of Mg-Gd-Zr alloy. Mater Sci Eng A 843:143136.
6. Ji ZK, Qiao XG, Hu CY, Yuan L, Cong F, Wang GJ, Xie WC, Zheng MY (2022) Effect of aging treatment on the microstructure, fracture toughness and fracture behavior of the extruded Mg-7Gd-2Y-1Zn-0.5Zr alloy. Mater. Sci. Eng. -Struct. Mater. Prop. Microstruct. Process. 849.
7. Wang J, Meng J, Zhang DP, Tang DX (2007) Effect of Y for enhanced age hardening response and mechanical properties of Mg-Gd-Y-Zr alloys. Mater Sci Eng -Struct Mater Prop Microstruct Process 456:78–84.
8. Jiang B, Dong ZH, Zhang A, Song JF, Pan FS (2022) Recent advances in micro-alloyed wrought magnesium alloys: Theory and design. Trans Nonferrous Met Soc China 32:1741–1780.
9. Zhang JH, Liu SJ, Wu RZ, Hou LG, Zhang ML (2018) Recent developments in high-strength Mg-RE-based alloys: Focusing on Mg-Gd and Mg-Y systems. J Magnes Alloys 6:277–291.
10. Yan H, Chen RS, Han EH (2010) Room-temperature ductility and anisotropy of two rolled Mg–Zn–Gd alloys. Mater Sci Eng A 527:3317–3322.
11. Wang S, Ma J, Yang J, Zhang W, Sun Y, Pan J, Wang H, Chen W (2021) Improving the ductility of Mg-2.5Nd-0.5Zn-0.5Zr alloy by multi-pass hot rolling. J Mater Res Technol 14:2124–2130.
12. Hashemi M, Alizadeh R, Langdon TG (2023) Recent advances using equal-channel angular pressing to improve the properties of biodegradable Mg–Zn alloys. J Magnes Alloys 11:2260–2284.
13. Wu H, Jiang J, Liu H, Huang H, Li Y, Chen J, Ma A (2021) A novel method for improving the strength and ductility of Mg–Y–Er–Zn alloy using rotary-die equal-channel angular pressing. J Mater Res Technol 13:1752–1758.
14. Hu MW, Tan QY, Knibbe R, Xu M, Jiang B, Wang S, Li X, Zhang MX (2023) Recent applications of machine learning in alloy design: A review. Mater Sci Eng R Rep 155:100746.
15. Fu ZY, Liu WY, Huang C, Mei T (2022) A Review of Performance Prediction Based on Machine Learning in Materials Science. Nanomaterials 12:2957.
16. Xie JX, Su YJ, Xue DZ, Jiang X, Fu HD, Huang HY (2021) Machine Learning for Materials Research and Development. Acta Met Sin 57:1343–1361.
17. Wei J, Chu X, Sun X, Xu K, Deng H, Chen J, Wei Z, Lei M (2019) Machine learning in materials science. InfoMat 1:338–358.
18. Min K, Choi B, Park K, Cho E (2018) Machine learning assisted optimization of electrochemical properties for Ni-rich cathode materials. Sci Rep 8:15778.
19. Li XC, Zheng MJ, Yang XY, Chen PH, Ding WY (2022) A property-oriented design strategy of high-strength ductile RAFM steels based on machine learning. Mater Sci Eng A 840:142891.

20. Lu ZX, Si SJ, He KY, et al (2022) Prediction of Mg Alloy Corrosion Based on Machine Learning Models. Adv Mater Sci Eng 2022:1–8.
21. Liu YW, Wang LY, Zhang H, Zhu GM, Wang J, Zhang YH, Zeng XQ (2021) Accelerated Development of High-Strength Magnesium Alloys by Machine Learning. Metall Mater Trans A 52:943–954.
22. Xu XN, Wang LY, Zhu GM, Zeng XQ (2020) Predicting Tensile Properties of AZ31 Magnesium Alloys by Machine Learning. JOM 72:3935–3942.
23. Xie BB, Fang QH, Li J, Liaw PK (2020) Predicting the optimum compositions of high-performance Cu–Zn alloys *via* machine learning. J Mater Res 35:2709–2717.
24. Xu P, Ji X, Li M, Lu W (2023) Small data machine learning in materials science. Npj Comput Mater 9:42.
25. Aurélien Géron (2019) Hands-On Machine Learning with Scikit-Learn, Keras, and TensorFlow, 2nd Edition. O'Reilly Media, Inc., Sebastopol.
26. Fu HD, Zhang HT, Wang CS, Yong W, Xie JX (2022) Recent progress in the machine learning-assisted rational design of alloys. Int J Miner Metall Mater 29:635–644.
27. Raschka S (2020) Model Evaluation, Model Selection, and Algorithm Selection in Machine Learning. arXiv:1811.12808.
28. Wang J, Xu P, Ji X, Li M, Lu W (2023) Feature Selection in Machine Learning for Perovskite Materials Design and Discovery. Materials 16:3134.
29. Hou XL (2012) Study on Structure and Mechanical Properties of Wrought Mg–Gd–Y–Nd–Zn(Zr) Alloy System. Ph.D. thesis, Jilin University.
30. Zhou JX, Luo XJ, Yang H, et al (2023) Introducing lamellar LPSO phase to regulate room and high-temperature mechanical properties of Mg-Gd-Y-Zn-Zr alloys by altering cooling rate. J Mater Res Technol S223878542300947X.

Part V

Primary Production, Recycling, and Modeling

A Succinct Method to Recycle WE43 Mg Alloys—From Wasted Chips to Consolidated Billets

Xingjian Zhao, Yanheng Xie, Joao Gandra, Matthew Murphy, William M. Rainforth, and Dikai Guan

Abstract

Spark plasma sintering (SPS) and friction stir processing (FSP) were used to recycle waste WE43 Mg alloy turning them into consolidated billets. Billets were firstly produced from machining chips using SPS. Metallurgical bonding between chips was achieved during the process, yet large second phase network and pores were observed. Then FSP was further applied to refine microstructures and remove pores confirmed by using electron backscattered diffraction (EBSD) and 3D X-ray computed tomography (3D XCT). Most of the large second phases were refined to 100 nm. The average grain size was reduced from around 30 µm to around 1–3 µm. The hardness of FSPed material reached HV0.2 = 83.5, which is comparable against commercial extruded bar (T5, HV0.2 = 90.2).

Keywords

Mg alloys • Recycling • Spark plasma sintering • Friction stir processing

Extended Abstract

A novel recycling method integrating spark plasma sintering (SPS) and friction stir processing (FSP) has been developed to rapidly turn WE43 (Mg-4Y-3RE, wt%) Mg alloy chips to consolidated billets. The entire flow of this recycling method is shown in Fig. 1. The chips were waste produced during machining process, and no pre-treatment was applied before the SPS. SPS and FSP were used in sequence, and an ageing treatment was carried out afterwards.

X-ray computed tomography (XCT) scanning (Fig. 2) indicates that pores (i.e., dark regions in Fig. 2) existed in the as-SPSed billet. Although the volume fraction of these pores was only about 1%, some of them were over 500 µm and had relative sharp tips. There were also some large inter-connected second phase particles as shown in Fig. 2b. The scanning electron microscopy (SEM) image and energy dispersive spectroscopy (EDS) maps in Fig. 3 reveal more detailed microstructure information of as-SPSed material. Two major second phases were identified, yet various other second phases were also observed. One of the major second phases has a network structure of a thin layer formed at the original chip surface. This type of second phase is rich in Y, Zr, and O. The other one has a eutectic structure and is rich in rare earth elements of Nd and Gd.

SEM images of FSPed material (Fig. 4a) show that the aforementioned second phase particles can no longer be observed. Instead, fine second phase particles were observed at both grain boundaries and within grains. In addition, electron backscattered diffraction images illustrate a gradient grain structure from the bottom to the top of the processed zone, with an average grain size ranging from 1 to 3 µm developed during FSP. No pores were identified in the as-FSPed material. Although the Vickers microhardness tests show that the hardness value of the billet after FSP was 83.5 HV, slightly lower than 90.2 HV of the commercial extruded T5 material, further ageing at 200 °C for 40 h successfully increased the hardness value to 94.6 HV, as

---

X. Zhao · D. Guan (✉)
Department of Mechanical Engineering, University of Southampton, Southampton, SO17 1BJ, UK
e-mail: dikai.guan@soton.ac.uk

Y. Xie · W. M. Rainforth
Department of Materials Science and Engineering, University of Sheffield, Sheffield, S1 3JD, UK

J. Gandra
TWI, Granta Park, Great Abington, Cambridge, CB21 6AL, UK

M. Murphy
Luxfer MEL Technologies, Elektron Technology Centre, Lumns Lane, Manchester, M27 8LN, UK

A. Leonard et al. (eds.), *Magnesium Technology 2024*, The Minerals, Metals & Materials Series,
https://doi.org/10.1007/978-3-031-50240-8_29

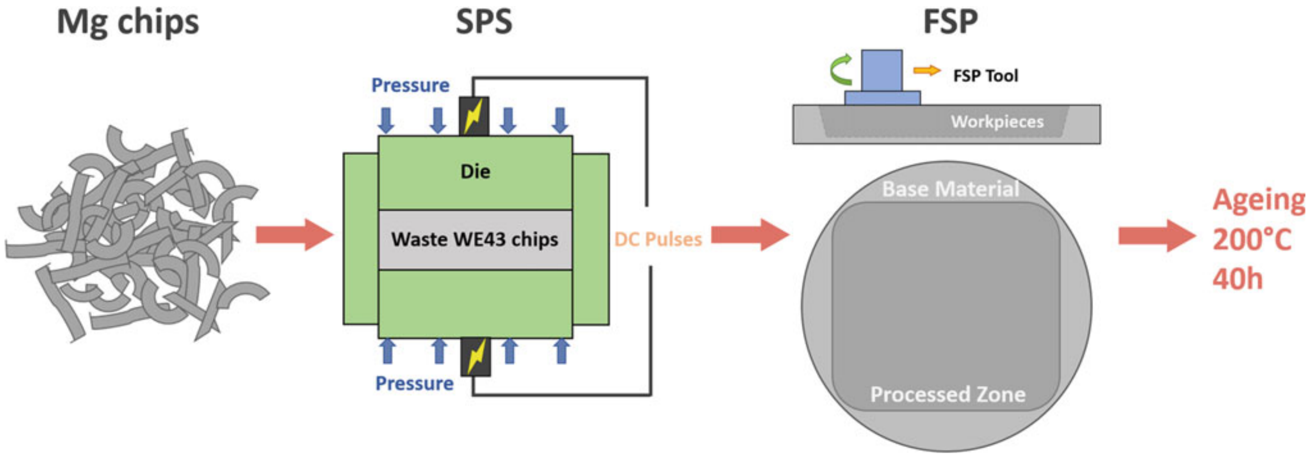

Fig. 1 Flow of the WE43 chip recycling method

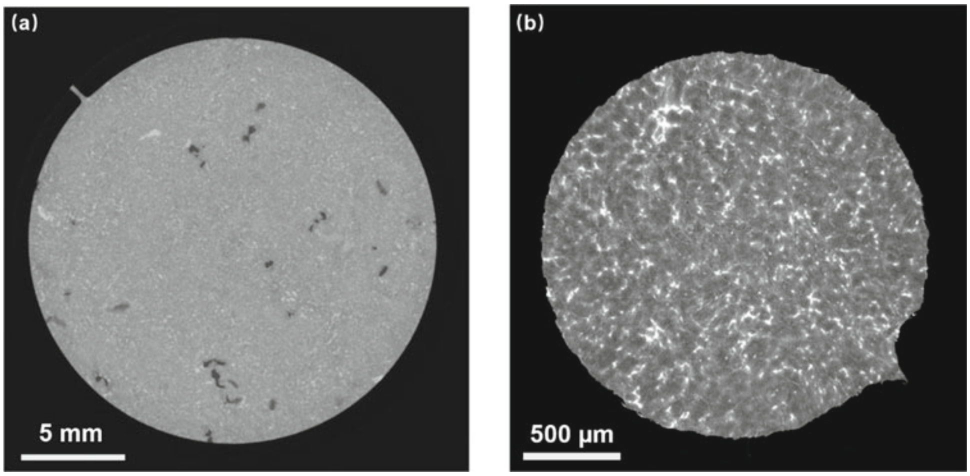

Fig. 2 **a** 2D XCT slice of as-SPSed WE43 (low resolution), **b** a 2D XCT slice of as-SPSed WE43 (high resolution)

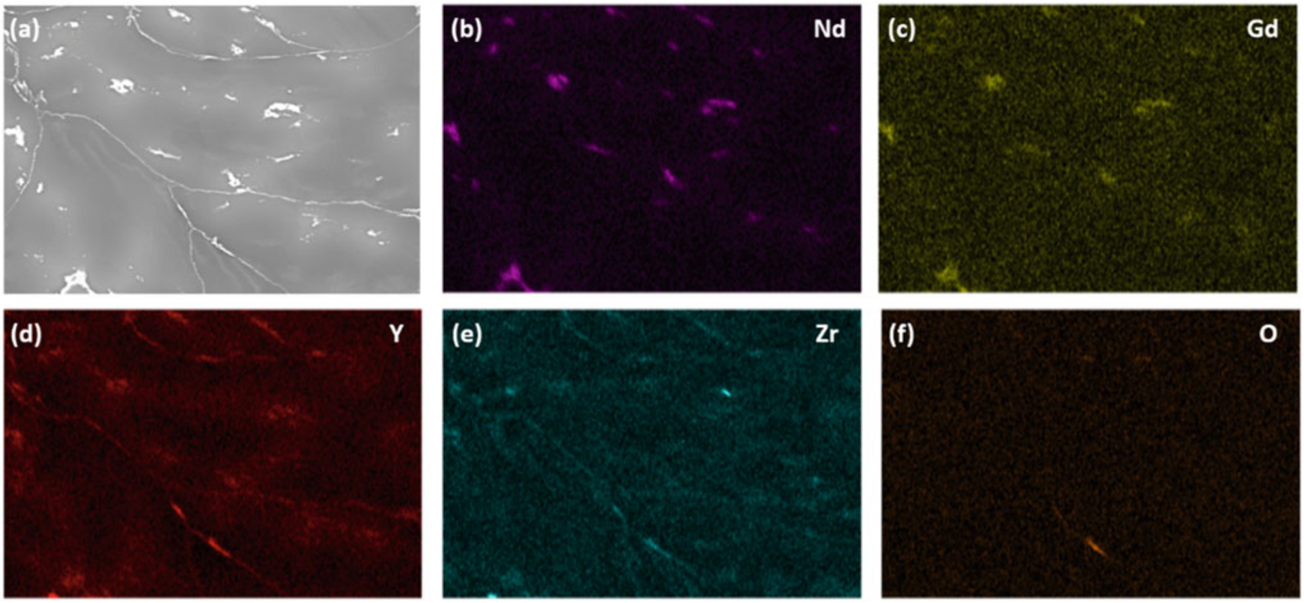

Fig. 3 **a** SEM image of as-SPSed WE43, **b**–**f** EDS maps of alloying elements in as-SPSed WE43

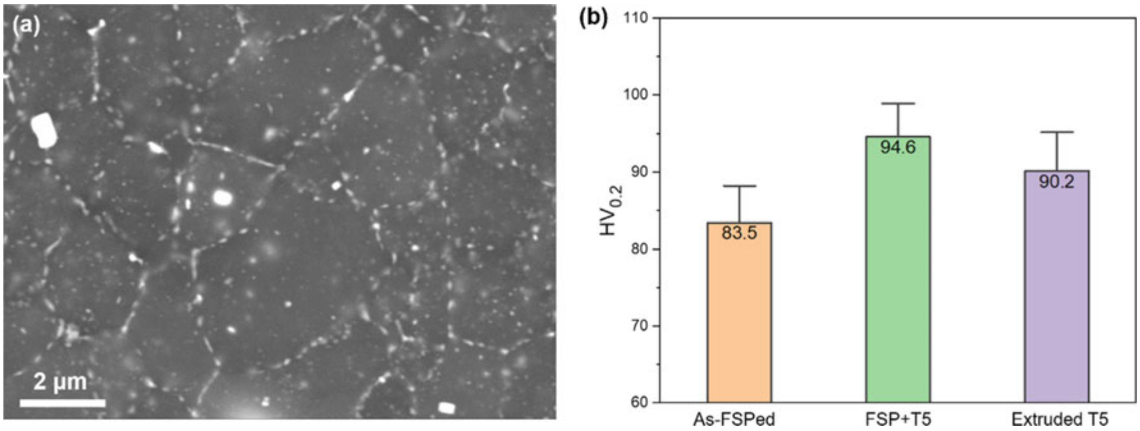

Fig. 4 **a** Backscattered electron image of a typical region in the as-FSPed WE43, **b** a bar chart of Vickers microhardness value of WE43 in three different states

shown in Fig. 4b. This indicates that by using this method, the recycled WE43 alloy can have equivalent or even better mechanical properties than commercial prime products.

In the SPS stage, although a vacuum condition was applied, porosity is inevitable due to the relatively big size and irregular geometry of waste WE43 alloy chips, compared to metallic powder which are usually used for SPS [1, 2]. The difference of affinity and diffusion rate between elements leads to the formation of diverse large second phases [3]. In the FSP stage, the strong material flow generated by the rotational tool plays a key role in the pore closure. With the assistance of heat generated by friction and deformation, dynamic recrystallisation enables the refinement of grains [4]. Most of the large second phases were broken, redistributed, partly re-dissolved, and precipitated again. The FSP can generate some effects of solid solution treatment, considering the processing temperature and cooling rate. Several factors are believed to contribute to the high hardness after ageing compared with the commercial alloy. Firstly, grains were refined to 1–3 μm. Secondly, higher cooling rate allows more alloying elements to dissolve in the matrix, and thus, a higher fraction of precipitates can form. Thirdly, the lower ageing temperature redistricted growth and further phase transformation of the effective precipitates.

References

1. Mondet M, Barraud E, Lemonnier S, Allain N, Grosdidier, T (2017) Optimisation of the mechanical properties of a Spark Plasma Sintered (SPS) magnesium alloy through a post-sintering in-situ precipitation treatment, J Alloys Compd 698:259–266, https://doi.org/10.1016/j.jallcom.2016.12.066.
2. Knapek M, Minárik P, Greš A, Zemková M, Lukáč F, Bohlen J, Chmelík F, Král R (2022) Spark plasma sintered Mg-4Y-3Nd with exceptional tensile performance, Mater Sci Eng A Struct Mater 849:143481–143492, https://doi.org/10.1016/j.msea.2022.143481.
3. Soderlind J, Cihova M, Schaublin R, Risbud S, Loffler JF (2019) Towards refining microstructures of biodegradable magnesium alloy WE43 by spark plasma sintering, Acta Biomater 98:67–80, https://doi.org/10.1016/j.actbio.2019.06.045.
4. Heidarzadeh A, Mironov S, Kaibyshev R, Çam G, Simar A, Gerlich A, Khodabakhshi F, Mostafaei A, Field DP, Robson JD, Deschamps A, Withers PJ (2021) Friction stir welding/processing of metals and alloys: A comprehensive review on microstructural evolution, Prog Mater Sci 117:100752–100818, https://doi.org/10.1016/j.pmatsci.2020.100752.

A New Method to Produce High-Purity Magnesium with a Low Aluminum Content

Rui Zheng, Bo Yang, Wei-Yi Yang, Bo-Yu Liu, Yue-Cun Wang, and Zhi-Wei Shan

Abstract

Magnesium is commonly used as a reducing agent to produce sponge titanium. And the aluminum impurities in magnesium will contaminate titanium, increasing the difficulty of producing high-purity electronic-grade titanium. Although our previous research has shown that eliminating the use of fluorite can effectively reduce aluminum impurities in the magnesium produced by silicothermic process, it also causes an increase in cost. Therefore, it is crucial to explore a new method to produce low aluminum magnesium in a cost-effective way. Since removing the sticking slag on the retort outlet is a long-standing challenge in industry, we analyzed its composition and found a substantial presence of Ca-Al-F-O compounds. Inspired by this observation, we propose a novel method that utilizes CaO to induce the deposition of aluminum impurities. Thermodynamic analysis confirms the feasibility, and experimental results demonstrate aluminum removal rates exceeding 90%. These findings pave the way for the cost-effective production of low aluminum high-purity magnesium.

Keywords

High-purity • Magnesium • Titanium • Aluminum impurity • Silicothermic reduction

Extended Abstract

Magnesium is a crucial reductant in sponge titanium production due to its strong reducing property [1, 2]. We found that almost 100% of the aluminum impurities in magnesium will be inherited to the sponge titanium [3] and are difficult to be removed in the subsequent titanium purification process [4–6]. Consequently, producing electronic-grade high-purity titanium requires low aluminum-containing magnesium as a reductant. Unfortunately, magnesium produced by silicothermic reduction process has long grappled with high and fluctuating aluminum impurity content [7] even though approximately 90% of the world's magnesium is produced by this method [8]. In our previous work, we have elucidated that CaF_2 is the chief culprit of the pest aluminum impurity in silicothermic magnesium, and AlF is the primary form of gaseous aluminum impurity [7]. Although reducing or abandoning the use of CaF_2 can significantly minimize aluminum impurity, it also reduces the yield of magnesium and therefore increases its costs. As a result, it remains a pressing need to discover new cost-effective solutions to produce magnesium with low aluminum impurities.

In this work, we first analyze the condensing behavior of AlF at temperature and pressure ranges where impurities commonly deposit. We found the AlF gas undergoes disproportionation reactions and finally condenses as Al and AlF_3 (Fig. 1) in the temperature range of 796–568 °C. This partly overlapped with the condense temperature of magnesium, i.e., 650–450 °C. As a consequence, the aluminum impurities are prone to condense together with magnesium. In order to minimize the aluminum impurities in magnesium, one potential solution is to remove AlF at a higher temperature range.

Considering that reducing the product concentration can enhance the equilibrium constant for a specific temperature, we propose to promote the disproportionation reaction of AlF as much as possible by eliminating its products, Al. This

R. Zheng · B. Yang · W.-Y. Yang · B.-Y. Liu · Y.-C. Wang · Z.-W. Shan (✉)
State Key Laboratory for Mechanical Behavior of Materials, Engineering Research Center for Magnesium-Based New Materials, Center for Advancing Materials Performance from the Nanoscale (CAMP-Nano), Xi’an Jiaotong University, Xi’an, 710049, China
e-mail: zwshan@xjtu.edu.cn

A. Leonard et al. (eds.), *Magnesium Technology 2024*, The Minerals, Metals & Materials Series,
https://doi.org/10.1007/978-3-031-50240-8_30

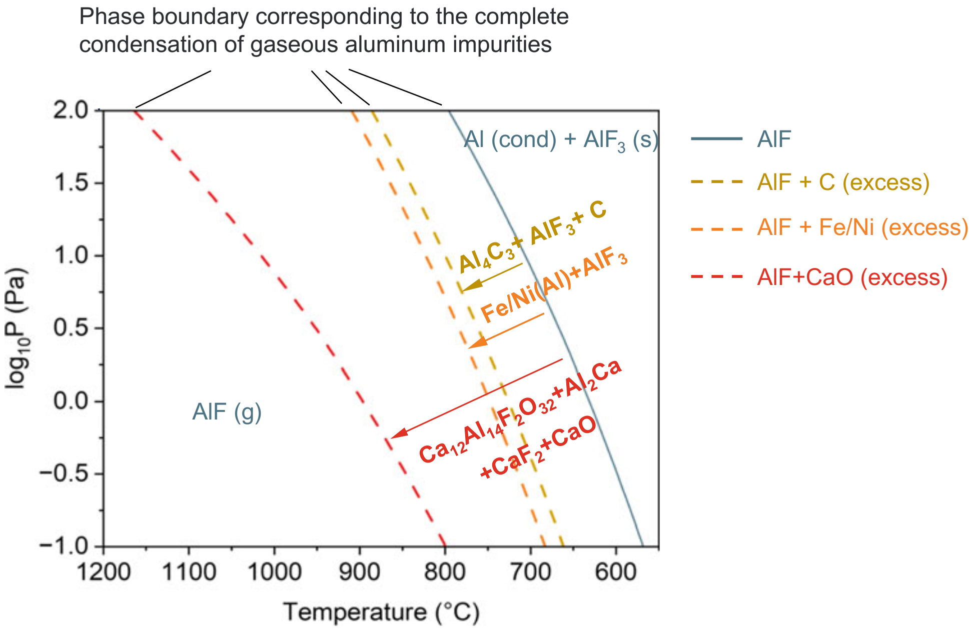

Fig. 1 Phase diagram of AlF, AlF-CaO, AlF-Fe/Ni, and AlF-C systems. Only phase boundaries corresponding to the complete condensation of gaseous aluminum impurities are shown here**.** During the cooling process, AlF undergoes disproportionation reactions, forming the Al and AlF_3 with condensed states. By introducing C, Fe/Ni, and CaO, the temperatures at which gaseous aluminum impurities completely condense are elevated, accompanied with the formation of Al_4C_3, Fe/Ni(Al) solid solution, as well as Ca-Al-F-O compound, respectively

Table 1 Main impurities in pure magnesium before and after using CaO filter material (wt.%, ppm)

	Al	Mn	Si	Fe	Zn
Without CaO	109.50 ± 5.36	12.00 ± 0.71	30.00 ± 6.71	9.50 ± 4.82	33.50 ± 6.10
With CaO	6.33 ± 0.47	10.67 ± 0.47	24.33 ± 14.01	8.67 ± 2.62	33.00 ± 1.63

is expected to increase the temperature required for the complete condensation of AlF. The substances for Al removal need to meet the following criteria: First, they should either react with Al or allow Al to dissolve into them; second, they would not react with magnesium under operating conditions; and third, they should be cost-effective. Then a batch of low-cost filter materials for aluminum removal was screened. We found that Al can react with C and CaO and has a significant solubility in Fe/Ni. To analyze whether the aforementioned materials can raise the temperature at which AlF gas transforms into condensed states, we performed thermodynamic calculations to examine the behavior of AlF in the presence of these filter materials. This involved calculating phase-temperature (*P*–*T*) phase diagrams for AlF-C (excess), AlF-Fe/Ni (excess), and AlF-CaO (excess). We found that after using the aforementioned filter materials, all the phase boundaries, which correspond to the complete condensation of AlF gas, shift to the bottom left corner (as depicted by arrows in Fig. 1). Meanwhile, Al_4C_3, Fe/Ni (Al) solid solutions, Ca-Al-F-O and Al_2Ca compounds appeared, respectively. This means AlF can be eliminated at higher temperatures or lower pressure, benefiting from the formation of the aforementioned aluminum-containing substances.

To validate the aluminum removal ability of the aforementioned method, we designed and established an experimental apparatus that enables us to mimic the silicothermic reduction process. We chose CaO as filter material because it results in the highest temperature elevation for aluminum removal (Fig. 1). It is surprising to find that the CaO filter can reduce aluminum impurity by more than 90% (Table 1). At the same time, other impurity elements are also reduced slightly. Our work offers a new and cost-effective approach to produce high-purity magnesium with low aluminum content.

Acknowledgements This work is supported by the National Natural Science Foundation of China (No. 52031011).

References

1. Fray DJ, Farthing TW, Chen Z (2000) Reducing the carbon footprint: primary production of aluminum and silicon with changing energy systems. Nature. 407: 361–363.
2. Froes F (2015) Titanium: physical metallurgy, processing, and applications. ASM International.
3. Yang B, Liu BY, Yang H, et al. (2020) Brief analysis of the importance of high-purity raw materials: taking magnesium as an example. Materials China. 39(7): 576–584.
4. Vutova K, Vassileva V, Koleva E, et al. (2010) Investigation of electron beam melting and refining of titanium and tantalum scrap. Journal of Materials Processing Technology. 210(8):1089–1094.
5. Weng QG, Li RD, Yuan TC, et al. (2014) Valence states, impurities and electro-crystallization behaviors during molten salt electrorefining for preparation of high-purity titanium powder from sponge titanium. Transactions of Nonferrous Metals Society of China. 24 (2): 553–560.
6. Yuan TC, Weng QG, Zhou ZH, et al. (2011) Preparation of High-Purity Titanium by Molten-Salt Electrolysis Process. Advanced Materials Research. 284–286:1477.
7. Yang B, Zheng R, Wu G, et al. (2022) Minimizing pest aluminum in magnesium for the production of high-purity titanium. Journal of Magnesium and Magnesium Alloys.
8. Yang B, Liu F, Liu B, et al. (2020) Producing High Purity Magnesium (99.99%) Directly by Pidgeon Process. Magnesium technology 2020. Springer International Publishing, 299–302.

Recycling of Magnesium Alloy Using the Gravity-Driven Multiple-Effect Thermal System (G-METS)

Daniel Mc Arthur Sehar, Armaghan Ehsani Telgerafchi, Artem Iurkovskyi, Emmanuel Opoku, and Adam Powell

Abstract

Magnesium metal has been significantly used in commercial applications from automobiles to aluminum alloys to defense weaponry. The surge in structural usage of magnesium over the past years has been due to high strength and excellent stiffness-to-weight ratio. Recycling magnesium scrap is a crucial aspect of the sustainability of the economy and environmental welfare. G-METS is an advanced distillation system used in the conversion of low-grade magnesium scrap into high-purity magnesium metal. This multiple-effect system uses the weight of magnesium as a compressor, to build pressure differences between each effect of the condenser-evaporator, modifying boiling points, and enabling transfer of vaporization enthalpy. This system is exceptionally efficient compared to the energy-intensive conventional distillation technique. This study compares experiments and models of one- and two-effect distillers.

Keywords

Magnesium • Distillation • Recycling • Extraction and processing

Introduction

Magnesium (Mg) is the fourth most commonly abundant structural metal ion available in the ocean and its various resources in the hydrosphere (encompassing the prominent sources of the Earth's water bodies and playing a vital role in sustaining Earth's natural ecosystem). Also, its been found that Mg is the eighth most copious element in the Earth's crust (lithosphere-underlining the presence of geological formations) [1]. Mg is remarkably noteworthy in the field of automotive and aeronautical transportation field due to its enhanced fuel efficiency. In comparison with aluminum (Al), magnesium is lighter in density and has the status of exceptional high specific strength. Additionally, Mg has a tremendous increase in the property in the strength-to-weight ratio [2]. It has been reported that from the 1990s, the Mg had a prominent role in the industrial application. Furthermore, Mg is considered to have low specific gravity which is the ultimate ground and foundation for the tremendous growth in the automobile industry, due to the advantage of lightweight. With the increase in Mg production, it has led to instantaneous growth in Mg die castings in the automobile market in recent years [3].

The Mg usage is increasing considerably with the increase in economic, technological, and environment impact in industrial growth and application [4]. According to the article International Magnesium Association, Mg alloy is used in fabricating most of the structural parts of automobile bodies by die casting method. However, there is a necessary emergence in the process of recycling the scraps consisting of Mg alloys into useful products. Also, they mention that the recycling process of the magnesium scraps into high-purity Mg requires only 5% of the minimal energy when compared to the energy-intensive primary production of Mg alloy. From September 2021, the smelter plant of US largest magnesium producers, US Magnesium LLC, Rowley, UT, was forced to shut down due to the failure of equipment. However, at recent records from the US Geological Survey 2023—it was observed that the Mg prices decreased in the first quarter due to restart manufacturing of primary production of Mg [5]. However, recycling and reprocessing have been emphasized constantly around the globe for the past few years due to environmental concerns.

D. Mc Arthur Sehar · E. Opoku · A. Powell (✉)
Materials Science and Engineering Program, Department of Mechanical Engineering, Worcester Polytechnic Institute, Worcester, MA, USA
e-mail: acpowell@wpi.edu

A. E. Telgerafchi · A. Iurkovskyi
Department of Mechanical Engineering, Worcester Polytechnic Institute, Worcester, MA, USA

A. Leonard et al. (eds.), *Magnesium Technology 2024*, The Minerals, Metals & Materials Series,
https://doi.org/10.1007/978-3-031-50240-8_31

The more the materials are recycled, consumption, and exhaustion of the natural resources will be minimized and depletion in the filling of the landfills with scraps and end-of-life waste products [6]. Mg recycling has noticeable benefit, firstly in reducing the energy demand for producing new magnesium, wherein results in reduce emissions in manufacturing. Secondly, it is beneficial in both sustainability and resource efficiency as recycling reduces drilling raw materials. Thereby mitigating the potential risks and environmental hazards during the extraction process. Moreover, there is also an urgent situation of magnesium and has been listed as critical materials according to the 2022 US Geological Survey report. Therefore, recycling of magnesium is a necessary requisite for reducing the high supply risk of magnesium metal [7]. Most of the installed Mg recycling capacity uses remelting, which cannot remove most of the impurities, Unlike Al, Mg is sensitive to small concentrations like Fe and Ni, for example AZ91B requires less than 50 ppmw for both.

As discussed in the previous paper, our technology of gravity-driven multiple-effect thermal system (G-METS) serves as the best method for refining and extracting high-purity magnesium metal from various forms of low-grade scraps, wastes, and impurities [8–10]. This technology uses the principle of low-cost vacuum distillation to distill pure Mg from the scrap alloys. This method and apparatus of G-METS was designed and patented by Adam Clayton Powell [11]. The idea of this technology used multiple effects of vertically stacked evaporator and condenser. The combined interaction between the evaporator and condenser is an "effect." This multiple-effect thermal system is used to distill the metals with different volatility and efficiently separate the alloys based on the vapor pressure and densities. This system uses gravity as the medium to initiate efficient distillation of Mg and other volatile metals by creating pressure difference between the effects. A detailed review and insights of this method were discussed in the previous papers of G-METS design TMS 2021 [9] and our team's future plan is to conduct continuous effect of G-METS system was assessed on TMS 2022 [8]. Currently, in this paper we have discussed a series of design changes and experiment run of Mg alloys using a single-effect of the G-METS distiller.

Experiments

One-Effect Distiller Experiments

The design and fabrication of one-effect distiller consist of an evaporator and condenser interconnected with a standpipe. The plates used for the experiment are 0.5″ thick carbon steel material [A572/A1018 HSLAS G50 Steel, HR] cut to specified 2-D drawings dimensions. The pipe is 10″ diameter SCH40 WELDED PIPE alloy 2205 from rolled alloys. The plates and the tube are welded together along with AZ31 (Al 3 wt.% and Zn 1 wt.%) alloy of 2 kg inside the evaporator. The design of the distiller has been mostly consistent with previous experiments, consisting of a condenser and evaporator connected by a vapor conduit tube (standpipe) between them, as shown in Fig. 1.

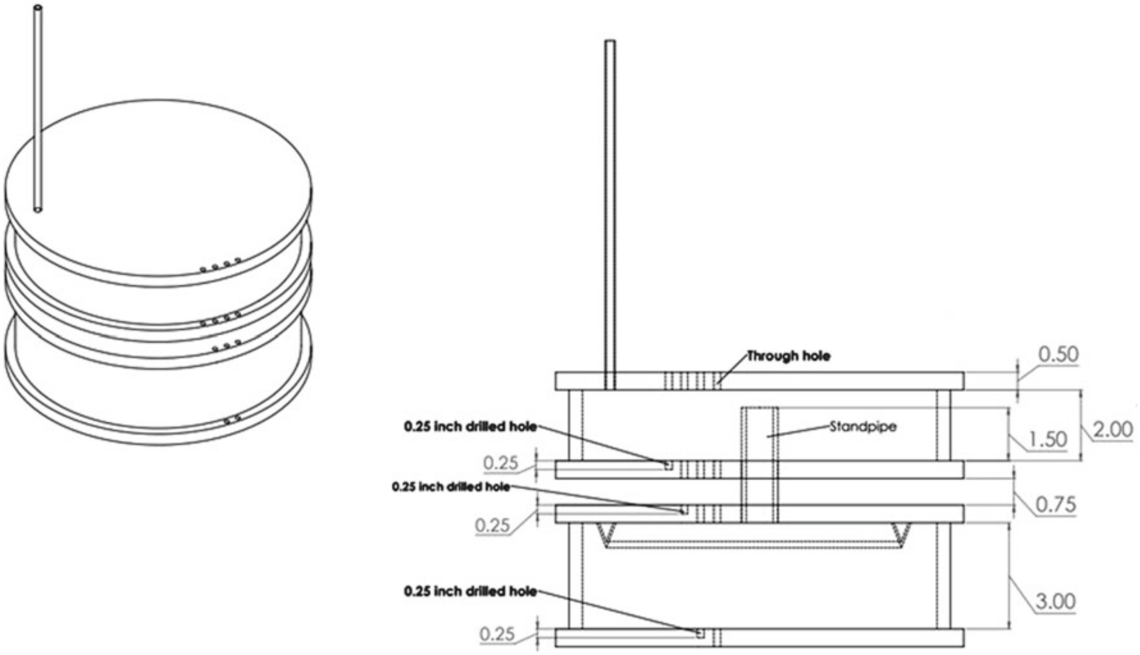

Fig. 1 10″ AZ91 Mg alloy distiller 2-D diagram

Fig. 2 Vacuum gauge and valve setup

Fig. 3 10″ distiller setup inside the insulation fiber

Some of the changes incurred in these experimental runs were changes in the design of distiller including the vacuum tube setup and changes in the thermocouple holders on the plates, from the grooves to through holes. The stainless-steel vacuum pressure pipe has been extended in length from 1 to 3 ft. This modification serves a primary purpose: replacing a previously employed crimped tube, which was a temporary measure to establish vacuum conditions. The new design incorporates a vacuum gauge affixed at the pipe's end, enabling continuous monitoring of chamber pressure during the entire experiment. Additionally, it includes a valve for occasional vacuum pumping in case the background pressure rises during the experiment. The extended length of the pipe provides protection to both the gauge and valve, safeguarding them from the elevated temperature within the distiller. Figure 2 depicts the elongated tube, the vacuum gauge, and the valve.

Correspondingly, the team practiced in these experiments to use leak checking to find problems with distiller vessel welds which may have caused problems with prior experiments. We figured out certain leaks by creating positive pressure inside the distiller using argon (Ar) gas. Such measures led to significant improvement of vacuum inside the distiller. Also, the ceramic insulation blanket was inserted in the region between the evaporator and condenser to initiate the temperature difference.

The team ran four one-effect distiller experiments with the AZ31 alloy. Wherein three failed to distill Mg, the final one succeeded. The successful experiment ran for nearly 10 h with the furnace temperature rising to around 1120 °C. The second experiment included a vacuum gauge, which indicated a maximum pressure of − 100 kPa. Pressure began increasing after the temperature rose above about 300 °C. Our hypothesis is that there may be organic compounds on the surface of the steel components which volatilized at elevated temperature, increasing pressure.

In the third experiment, the vacuum pump was attached once to pump down the chamber when its temperature was about 600 °C. However, we were not able to recover any magnesium from the top of the condenser. Figure 3 shows the distiller apparatus and the complete experimental setup with the distiller inside the furnace and insulation.

Again, in the third experiment, there was agglomeration of small globules of magnesium present on the top surface plate of the condenser, as shown in Fig. 4. Our hypothesis was that inadequate temperature difference between the top and bottom temperatures held back distillation.

During the final experiment, the procedure was mostly the same as that of the previous experiments, with two

Fig. 4 Mg nucleation at the condenser (top plate)—unsuccessful distillation

Fig. 5 10″ AZ91 distiller setup before (left) and during (right) the final successful experiment

significant changes. First, we used the vacuum pump on the distiller several times during the experiment when we saw an increase in the pressure on gauge reading. Second, we increased the temperature gradient by keeping the top temperature around 600–650 °C and the bottom temperature was around the working temperature of 1050–1150 °C. Figure 5 shows the distiller before and during the experiment. These changes resulted in the successful distillation of magnesium alloy from the evaporator to the top of condenser.

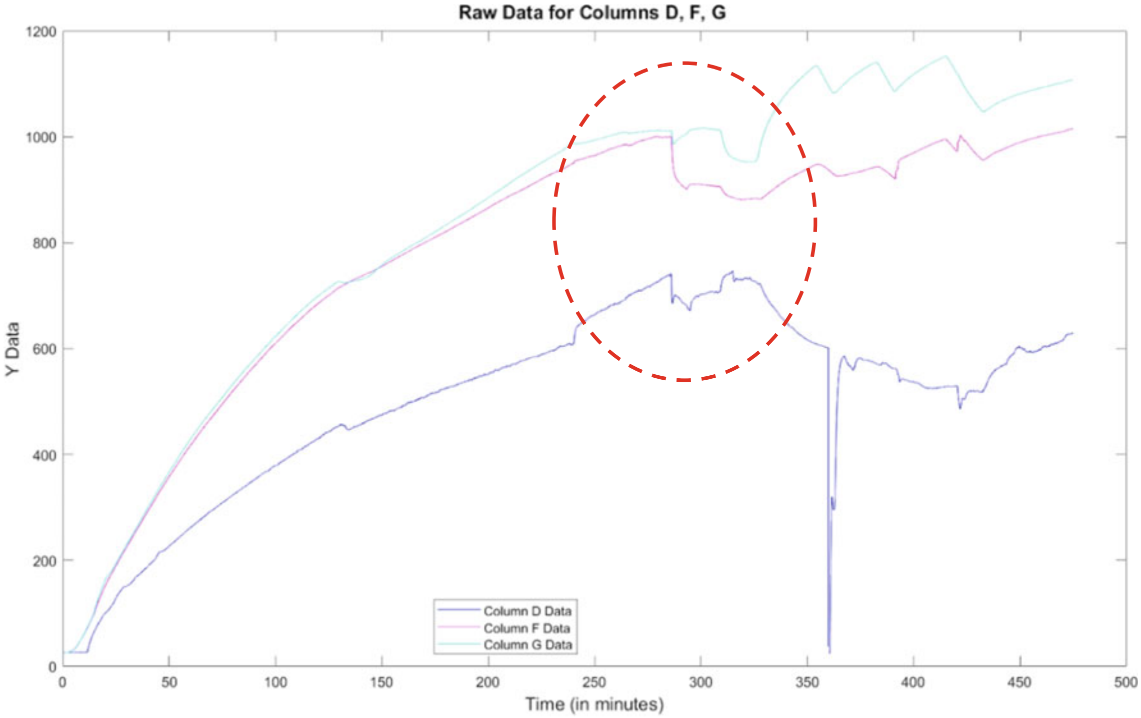

Fig. 6 Successful distillation experimental result temperature (y-axis) versus time (x-axis)

Results

The readings were calibrated of the temperature–time graph using data logger. Fig. 6 shows measured temperatures versus time during the experiment run. Our hypothesis is that distillation occurred mainly during the period highlighted with red dashes, when temperature difference decreased, and that the sudden divergence of temperatures—with the evaporator temperature rapidly rising and the condenser temperature falling—occurred at the end of distillation.

This time bottom evaporator chamber evaporator shrank inwards as shown in Fig. 7, likely because of low pressure inside the distiller due to multiple uses of the vacuum pump (Fig. 8).

We analyzed the composition of the alloy using X-ray fluorescence (XRF) analyzer. We planned to execute the analysis on the cross-sectional layer of the distilled Mg alloy to get accurate readings without the presence of oxidation. From the XRF results, we procured 97.02% of pure Mg, 1.34% of Al, and 1.122% of Zn on the top condenser. The values of the analyzed XRF are shown in Table 1.

Also, we performed XRF analysis on the small coating of black powder formation on the top surface of the distilled magnesium on the condenser, as shown in Fig. 9. From the results, there is the presence of strong oxidation on the top layer of Mg. The indication of light elements in Table 2 shows the presence of oxidation coating at surface.

Fig. 7 Shrinkage deformation of the evaporator in the final experiment

Fig. 8 Cut open condenser of the one-effect distiller

Table 1 XRF analyzed result

Element	Composition
Mg	97.02%
Al	1.34%
Zn	1.122%
Mn	1640 (ppm)
Si	550 (ppm)
Nd	290 (ppm)
Pr	220 (ppm)
S	920 (ppm)
Cu	85 (ppm)
Ni	233 (ppm)
Fe	974 (ppm)

Discussion

Some of the key highlights discussed for the successful distillation of magnesium were (i) Initial fast heating of distiller enabled to create a large temperature difference of around 300 °C and low temperature at the top condenser supported condensation of the Mg. (ii) Heating the distiller for a long time assisted in homogeneous melting of magnesium and volatile inorganics. (iii) Creating vacuum during the middle of experiment supported in Mg distillation by expelling the organics out of the distiller. (iv) Partially lifting the distiller inside the furnace helped in the consistent pre-melting of AZ31 alloy. (v) The stuffed ceramic fiber insulation between the evaporator and condenser aided in creating significant temperature differences to facilitate the distillation process.

Fig. 9 Black oxidation coating on top surface

Table 2 XRF results of black coating

Element	Composition
Mg	57.97%
Light elements	27.23%
Al	8.72%
Si	9930 (ppm)
Fe	2.599%
Nd	270 (ppm)
Cr	4260 (ppm)
Mn	5510 (ppm)
S	5270 (ppm)

Conclusion

The team's efforts during these four experiment run of AZ31 alloy was focused more on formulating hypotheses and adjusting the design and operation to achieve a successful distillation process. Additionally, we intend to install a new furnace that will enable the operation of a two-effect distillation setup. Notably, this upgraded furnace will feature significantly higher bottom heater power output and enhanced control capabilities for the experiment. This will aid in regulating the temperature gradient of both the one and two-effect distillers. If all proceeds as planned, our team plans to conduct some two-effect distillation experiments and validate the results in the future.

References

1. Neelameggham, R. *Primary production of magnesium*. 2013.
2. Jeoung, H.-J., et al., *Use of various MgO resources for high-purity Mg metal production through molten salt electrolysis and vacuum distillation.* Journal of Magnesium and Alloys, 2022. **11**.
3. Hanko, G., H. Antrekowitsch, and P. Ebner, *Recycling automotive magnesium scrap.* JOM, 2002. **54**: p. 51–54.
4. Brown, R., *Magnesium Recycling Yesterday, Today, Tomorrow.* 2013.
5. *Magnesium Metal in the First Quarter 2023*. 2023, US Geological Survey: Mineral Industry Surveys. p. 4.
6. Kramer, D.A., *Magnesium recycling in the United States in 1998.* 2002: US Department of the Interior, US Geological Survey.
7. *2022 Final List of Critical Minerals*. 2022, U.S Geological Survey, Department of the Interior: 02/24/2022.
8. McArthur Sehar, D., et al. *Design of the Continuous Gravity-Driven Multiple-Effect Thermal System (G-METS) for Efficient Low-Cost Magnesium Recycling*. In *Magnesium Technology 2023*. 2023. Cham: Springer Nature Switzerland, https://doi.org/10.1007/978-3-031-22645-8_31.
9. Espinosa, G., et al. *Design of Efficient Low-Cost Recycling of Magnesium Using Gravity-Driven Multiple Effect Thermal System (G-METS).* In *Magnesium Technology 2022*. 2022. Cham: Springer International Publishing, https://doi.org/10.1007/978-3-030-92533-8_22.
10. Telgerafchi, A.E., et al., *Magnesium production by molten salt electrolysis with liquid tin cathode and multiple effect distillation.* Frontiers in Chemistry, 2023. 11, https://doi.org/10.3389/fchem.2023.1192202
11. Adam Clayton Powell, David Dussault, Matthew Earlam, Aaron Tajima, *Method and Apparatus for Efficient Metal Distillation and Related Primary Production Process*. 2021, Worcester Polytechnic Institute, Worcester, MA: United States of America. p. 13.

Production of Mg-Mg_2Si Composites

Jessica Neuhaus, Björn Wiese, and Norbert Hort

Abstract

Mg_2Si is often used to improve creep resistance of Mg alloys, as an additive for aluminium alloys, as a negative electrode material in Li-ion batteries or in thermoelectric applications. In the Mg-Si system, Mg_2Si forms in an equilibrium exothermic reaction. However, during this reaction, the system is heating up, may overheat within a short time, and may run out of control. We will report on a powder metallurgy-based processing route where mechanical alloying, pressing, and heat treatments are used to produce Mg_2Si in a Mg matrix with different Si contents in a controlled manner. XRD is used to identify phases that form during processing.

Keywords

Stable/metastable phase • Cast/wrought processing • Heat treatments • Surface modification • Phase diagrams

Introduction

Mg_2Si is a well-known intermetallic phase in Si containing Mg alloys [1, 2]. It has a relatively high melting point, and the stoichiometric composition is fixed. It forms during solidification and is mostly used to improve creep resistance of Mg alloys. Unfortunately, the solubility of Si in Mg is low and has impact on the way castings can be made. However, besides this, there are also other possible applications, especially in electronics [3, 4].

Most applications of metallic materials are often produced by casting either as a feedstock material for further processing or to get a near net shape component that is ready for use. Casting is a highly dynamic process where composition and solidification conditions can become a challenge due to the appearance of porosity, shrinkholes, segregations, and the formation of intermetallic phases. Especially, Mg_2Si formation during solidification can be a challenge as it changes viscosity and mould filling to a large extent. If larger volume fractions of Mg_2Si in a component are required, casting might not be the best solution to produce such components, but powder metallurgical approaches could solve the problem. Moreover, this approach could also be transferred to the production of other pure intermetallic phases. The process used in this contribution is also known as mechanical alloying and is well introduced in numerous applications. Pure elements are mixed in high energy milling processes, consolidated by pressing and then often sintered. During sintering, the different constituents can react and can form intermetallic phases in a controlled manner. However, the question was: can mechanical alloying and sintering be used to produce Mg_2Si in various volume fractions?

Experimental

For the investigation of the PM process, Mg powder is first produced by mechanical milling in the PM 100 planetary ball mill from Retsch, Haan, Germany. The grinding container used is made of hardened steel and has a capacity of 500 ml. Steel (100Cr6) balls with 10 mm diameter were chosen as grinding media. After cleaning the grinding container and grinding media, pure magnesium is ground in one pass so that the grinding container and grinding media are covered with magnesium. This prevents contamination by the material of the grinding container and grinding media. Subsequently, 1 mol each of the respective mixing ratios (99:1, 90:10, 75:25, 67:33; 60:40, 50:50 in at%) was prepared. All

J. Neuhaus
Helmut-Schmid-Universität, Hamburg, Germany

B. Wiese · N. Hort (✉)
Helmholtz-Zentrum Hereon, Geesthacht, Germany
e-mail: norbert.hort@hereon.de

N. Hort
Leuphana Universität Lüneburg, Lüneburg, Germany

A. Leonard et al. (eds.), *Magnesium Technology 2024*, The Minerals, Metals & Materials Series,
https://doi.org/10.1007/978-3-031-50240-8_32

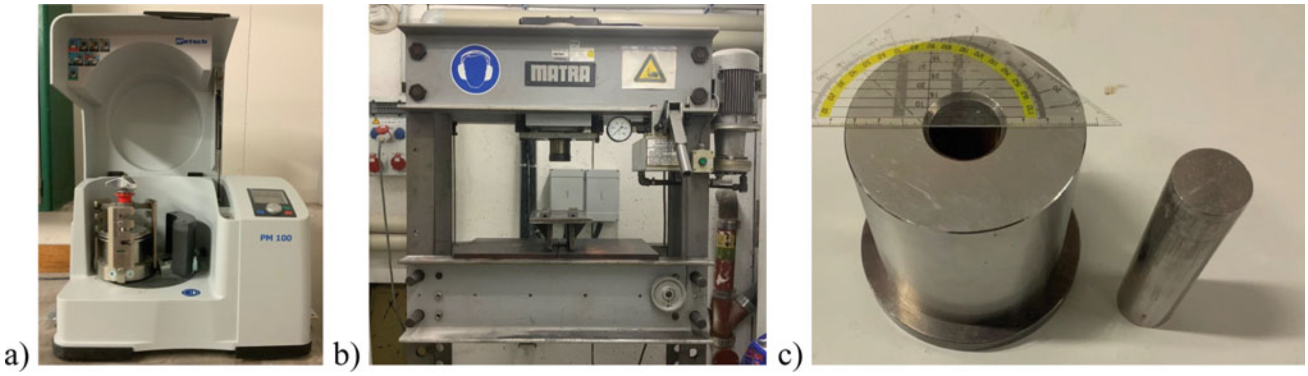

Fig. 1 **a** Retsch PM 100 planetary mill, **b** MATRA hydraulic press, **c** die for pressing specimen of 30 mm Ø

specimens underwent high energy ball milling with 150 rpm for 10 h. The powder mixtures were cold pressed in a hydraulic press (MATRA-Werke, Hainburg, Germany) in a die with an inner diameter of 30 mm using 450 kN. Figure 1 shows the different components of the experimental setup.

The final heat treatment takes place under an Ar inert gas atmosphere. The parameters used are based on a patent to produce magnesium sintered parts [5]. Here, parameter ranges of 600–642 °C and a process duration of 4–64 h are used. A temperature of 642 °C and a process duration of 4 h are used for the experiment. The furnace used is a chamber furnace from Carbolite Gero, Neuhausen, Germany. XRD investigations to identify phases were conducted by using a Bruker D8 Advance (Bruker AXS, Karlsruhe, Germany) with Cu kα radiation at an angle of 20–70°. The scanning speed was set to 1° min^{-1}.

Results and Discussion

While Mg reacts with Si in an exothermic reaction, the volume of the newly formed phase Mg_2Si has impact on the stability of the specimens (Fig. 2). Even when Mg_2Si forms, the specimens are losing their shape and integrity.

Fig. 2 Pressed samples prior (left) and after (right) heat treatment, **a** Mg-Si 99:1, **b** Mg-Si 90:10, **c** Mg-Si 75:25, **d** Mg-Si 67:33, **e** Mg-Si 60:40, **f** Mg-Si 50:50

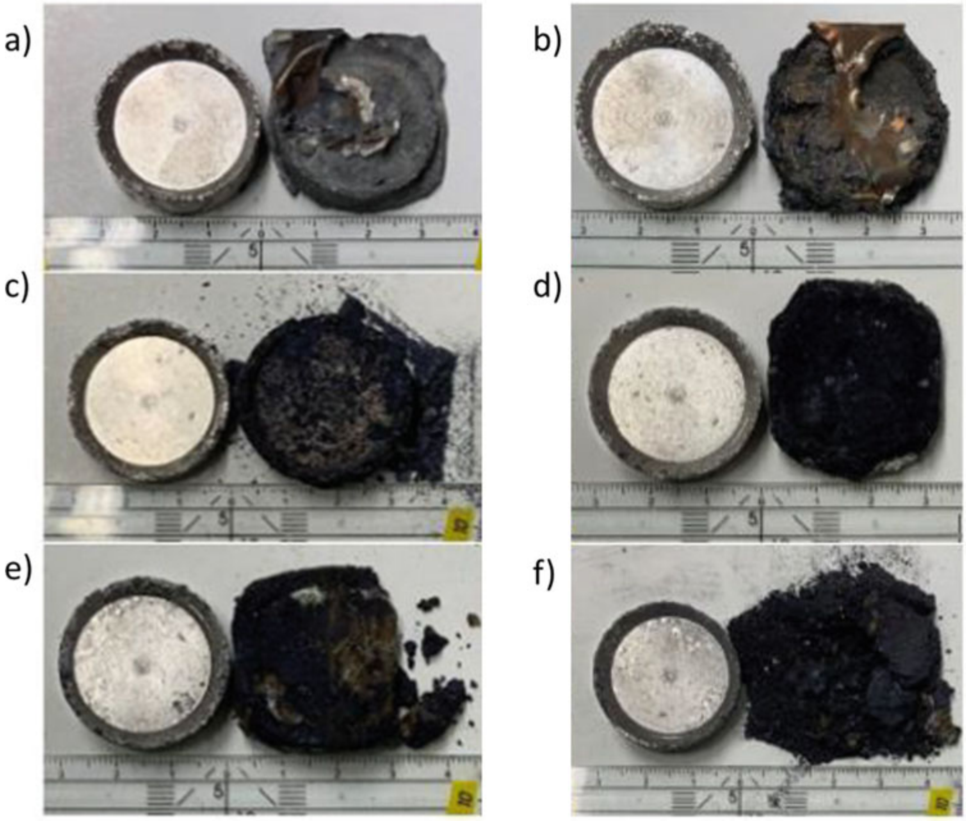

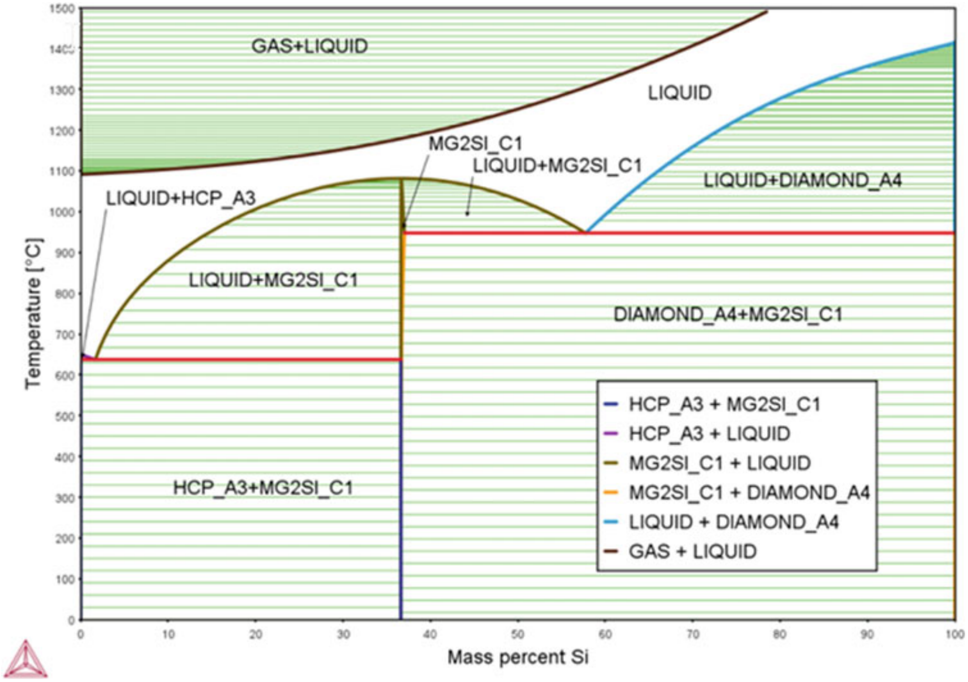

Fig. 3 Mg-Si phase diagram (Thermo-Calc 2021b, PCMg06)

From the Mg-Si phase diagram (Fig. 3), it is obvious that the solubility of Si in Mg is extremely low and that Mg_2Si forms in an early stage. Increasing amounts of Si will lead to increased amounts of Mg_2Si. This is also evident from the XRD investigations (Fig. 4).

According to the XRD results, all materials show after sintering the existence of Mg_2Si as well as MgO. Due to the chosen processing route and its parameters, it is not surprising that MgO forms. This could perhaps be avoided using vacuum or protective gases during high energy ball milling, compaction, and sintering. The presence of pure Mg and Si also indicates that the processing needs to be optimized for a full reaction of Mg with Si to form Mg_2Si. The results also indicate that the ratio Mg:Si can be properly varied to adjust the volume fraction of Mg and Mg_2Si with respect to the future application. A texture was not observed or expected due to the chosen processing route.

Summary

Mg and Si were successfully processed by high energy ball milling, compaction with a hydraulic press and sintering. Mg_2Si forms with respect to the different ratio of Mg:Si in different volume fractions. However, optimization of processing parameters is still necessary. It is also likely that this processing route can be adapted to other intermetallic phase which are difficult to be produced by standard routes like casting. However, due to the volume change during heat treatment, compact specimens are only possible at low volume fractions of Mg_2Si.

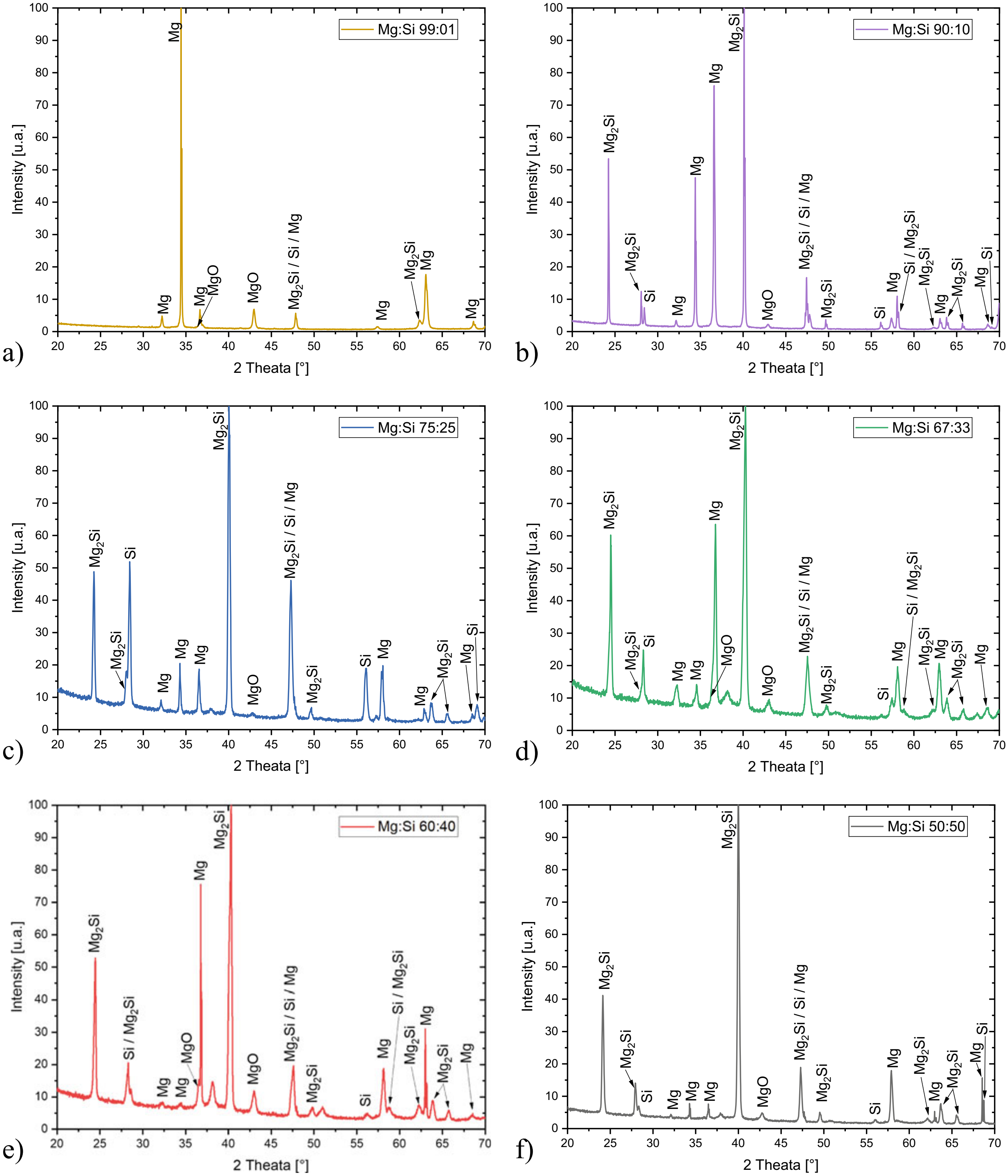

Fig. 4 XRD spectra of **a** Mg-Si 99:1 **b** Mg-Si 90:10, **c** Mg-Si 75:25, **d** Mg-Si 67:33, **e** Mg-Si 60:40, **f** Mg-Si 50:50

References

1. Neite G et al. (1999), Magnesium-based alloys, in: R. W. Cahn et al. (Eds.), Materials Science and Technology—A Comprehensive Treatment, Vol. 8, Structure and Properties of Non-Ferrous Alloys, 113
2. Mordike BL, Ebert T (2001), Magnesium – Properties-Applications-Potential, Mater. Sci. Eng. A 302:37–45
3. Iida T et al. (2021), Silicide materials: Thermoelectric, mechanical properties, and durability for Mg-Si and Mn-Si, Thermoelectric Energy Conversion - Theories and Mechanisms, Materials, Devices, and Applications, Woodhead Publishing Series in Electronic and Optical Materials: 389–427, https://doi.org/10.1016/B978-0-12-818535-3.00030-X
4. Hu XS et al. (2007), Low frequency damping capacities and mechanical properties of Mg–Si alloys, Materials Science and Engineering A 452–453(3):374–379, https://doi.org/10.1016/j.msea.2006.10.099
5. Wolff M et al. (2015), Method for producing components of Magnesium or Magnesium alloy by sintering, European Patent Office, EP 2 246 074 B1

Recent Advances in PRISMS-Plasticity Software for Simulation of Deformation in Mg Alloys

Mohammadreza Yaghoobi, Tracy Berman, Zhe Chen, Aaron Tallman,
Duncan A. Greeley, Michael Pilipchuk, John E. Allison,
and Veera Sundararaghavan

Abstract

An open-source parallel 3D crystal plasticity finite element (CPFE) software package, PRISMS-Plasticity, is presented here as a part of the overarching PRISMS Center integrated framework. A new PRISMS-Plasticity indentation module is integrated into the framework which can efficiently model indentation of large microstructures of Mg alloys. A new rate-dependent twinning-detwinning model is incorporated into the framework based on an integration point sensitive scheme to model Mg alloys. The model includes both kinematic and isotropic hardening in order to handle cyclic response of structural metals. PRISMS-Plasticity TM is incorporated to rapidly simulate the effects of alloying on texture development in Mg-Zn-Ca alloys. Finally, the PRISMS-Plasticity software has been integrated with the PRISMS-PF phase-field framework to model twinning within Mg alloys.

Keywords

PRISMS-Plasticity • Crystal plasticity finite element • Mg alloys

Extended Abstract

Crystal plasticity finite element (CPFE) is a powerful tool to simulate Mg alloys response at mesoscale incorporating several microstructural features such as grain size, texture, twinning, and precipitates [1]. However, the CPFE simulations are often computationally demanding and require very efficient numerical implementations. PRISMS-Plasticity [2] has been developed as a computationally efficient and highly scalable CPFE software as one of the major software tools of the PRISMS Center at the University of Michigan to investigate the Mg alloys response including several microstructural features. PRISMS-Plasticity is integrated well with other computational tools and experiments through a set of pipelines and computational platforms. DREAM.3D [3] and Neper [4] can be used to generate the microstructure, Matlab MTEX toolbox [5] can be used to generate pole figures and inverse pole figures, PRISMS-Fatigue package is introduced to conduct simulation-based fatigue analysis [6–11], PRISMS-Plasticity TM [12] is a method for performing rapid texture evolution analysis, and Materials Commons can be used as the PRISMS Center information repository. Different Mg alloys have been calibrated and modeled using PRISMS-Plasticity including unalloyed Mg, ZK60A [13], Mg-2.4wt.%Nd [14, 15], WE43 [16–18], and Mg-4wt.%Al [19–21]. PRISMS-Plasticity software version 1.5.0 will be released in Fall 2024 which includes new features such as an indentation module [22], a residual strain feature, and cell-centered user-defined visualization. A PRISMS-Plasticity forum has been established which is designed to answer user's questions. Additionally, PRISMS-Plasticity YouTube tutorials cover the basics of the software instructions.

PRISMS-Indentation module is the newly released feature which is able to perform indentation on microstructures of considerable size by implementing the contact using an efficient primal–dual active set strategy [22]. In the current work, the developed indentation module is used to indent the

---

M. Yaghoobi (✉) · T. Berman · Z. Chen · D. A. Greeley ·
J. E. Allison
Department of Materials Science and Engineering,
University of Michigan, Ann Arbor, MI, USA
e-mail: yaghoobi@umich.edu

A. Tallman
Department of Mechanical and Materials Engineering,
Florida International University, Miami, FL, USA

M. Pilipchuk · V. Sundararaghavan
Department of Aerospace Engineering, University of Michigan,
Ann Arbor, MI, USA

A. Leonard et al. (eds.), *Magnesium Technology 2024*, The Minerals, Metals & Materials Series,
https://doi.org/10.1007/978-3-031-50240-8_33

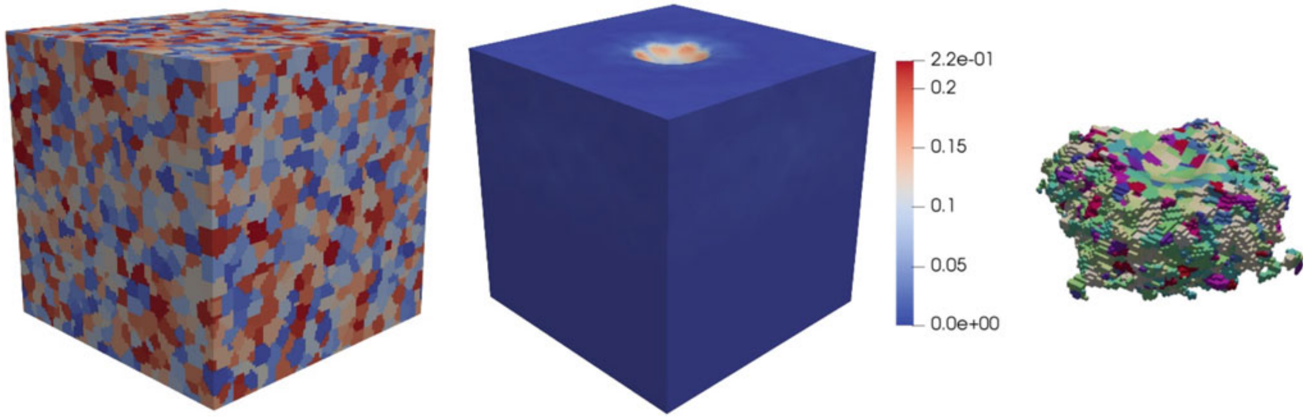

(a) Initial microstructure (b) abs$\left(\varepsilon_z^p\right)$ (c) zone of grains with $\varepsilon^{\mathrm{eq}} \geq 0.01$

Fig. 1 Indentation of a ZK60A Mg alloy with random texture composed of 7500 grains: **a** initial microstructure, **b** the absolute value of plastic normal strain component along the indentation direction, i.e., abs$\left(\varepsilon_z^p\right)$, **c** the zone of grains with the equivalent strain larger than 1%

Table 1 Values for initial slip resistance and corresponding hardening parameters for slip modes of ZK60A sample [13]

Mode	s_0^α (MPa)	h_0^α (MPa)	s_s^α (MPa)	a^α
Basal	20	10	21	2
Prismatic	140	20	155	2
Pyramidal <c + a>	240	1000	350	6

ZK60A sample with a random texture, which consists of ~ 7500 grains generated using DREAM3D as a 90^3 voxelized microstructure (Fig. 1). Each voxel is modeled using a hexahedral element. A frictionless spherical indenter with a radius of 0.2 mm is used. The centers of the sample and indenter are aligned. Fixed boundary condition is used for the bottom of the sample. The bottom of the sample is fixed in all three dimensions. Here, the response of ZK60A sample is simulated using three slip modes of Basal a $\left(\{0001\}11\bar{2}0\right)$, Prismatic a $\left(\{10\bar{1}0\}11\bar{2}0\right)$, and Pyramidal c + a $\left(\{\bar{1}\bar{1}22\}\bar{1}\bar{1}23\right)$. Twinning is not included in this simulation to enhance the convergence of the simulation. The elastic constants of pure Mg at room temperature are used here which are $C11$ = 59,400 MPa, $C12$ = 25,610 MPa, $C13$ = 21,440 MPa, $C33$ = 61,600 MPa, and $C44$ = 16,400 MPa. The CPFE parameters of ZK60A reported by Yaghoobi et al. [13] are used here for different deformation systems, as summarized in Table 1. In addition to initial microstructure, Fig. 1 shows the indented sample, along with the zone of grains with the equivalent strain larger than 1%. The results show the large ensemble of grains involved in the indentation response which can be further studied using the developed framework. The developed framework can be effectively used to investigate the response of Mg alloys during the indentation experiment.

Acknowledgements This work was supported by the US Department of Energy, Office of Basic Energy Sciences, Division of Materials Sciences and Engineering under Award#DE-SC0008637 as part of the Center for Predictive Integrated Structural Materials Science (PRISMS Center) at the University of Michigan. We also acknowledge the financial cost-share support of the University of Michigan College of Engineering. This work used the Extreme Science and Engineering Discovery Environment (XSEDE), which is supported by National Science Foundation grant number ACI-1548562, through the allocation TG-MSS160003.

References

1. M. Yaghoobi, G.Z. Voyiadjis, V. Sundararaghavan, Crystal Plasticity Simulation of Magnesium and Its Alloys: A Review of Recent Advances, Crystals 11(4) (2021) 435.
2. M. Yaghoobi, S. Ganesan, S. Sundar, A. Lakshmanan, S. Rudraraju, J.E. Allison, V. Sundararaghavan, PRISMS-Plasticity: An open-source crystal plasticity finite element software, Computational Materials Science 169 (2019) 109078.
3. M.A. Groeber, M.A. Jackson, DREAM. 3D: a digital representation environment for the analysis of microstructure in 3D, Integrating materials and manufacturing innovation 3(1) (2014) 56–72.
4. R. Quey, P.R. Dawson, F. Barbe, Large-scale 3D random polycrystals for the finite element method: Generation, meshing and remeshing, Computer Methods in Applied Mechanics and Engineering 200(17–20) (2011) 1729–1745.

5. F. Bachmann, R. Hielscher, H. Schaeben, Texture analysis with MTEX–free and open source software toolbox, Solid state phenomena 160 (2010) 63–68.
6. M. Yaghoobi, K.S. Stopka, A. Lakshmanan, V. Sundararaghavan, J.E. Allison, D.L. McDowell, PRISMS-Fatigue computational framework for fatigue analysis in polycrystalline metals and alloys, npj Computational Materials 7(1) (2021) 1–12.
7. K.S. Stopka, M. Yaghoobi, J.E. Allison, D.L. McDowell, Effects of Boundary Conditions on Microstructure-Sensitive Fatigue Crystal Plasticity Analysis, Integrating Materials and Manufacturing Innovation (2021) 1–20.
8. K.S. Stopka, M. Yaghoobi, J.E. Allison, D.L. McDowell, Simulated effects of sample size and grain neighborhood on the modeling of extreme value fatigue response, Acta Materialia 224 (2022) 117524.
9. K.S. Stopka, M. Yaghoobi, J.E. Allison, D.L. McDowell, Microstructure-Sensitive Modeling of Surface Roughness and Notch Effects on Extreme Value Fatigue Response, International Journal of Fatigue, In Revision (2022).
10. M. Yaghoobi, K.S. Stopka, D.L. McDowell, L. Graham-Brady, K. Teferra, Effect of sample size on the maximum value distribution of fatigue driving forces in metals and alloys, International Journal of Fatigue 176 (2023) 107853.
11. A. Lakshmanan, M. Yaghoobi, K.S. Stopka, V. Sundararaghavan, Crystal plasticity finite element modeling of grain size and morphology effects on yield strength and extreme value fatigue response, Journal of Materials Research and Technology 19 (2022) 3337–3354.
12. M. Yaghoobi, J.E. Allison, V. Sundararaghavan, PRISMS-Plasticity TM: An Open-Source Rapid Texture Evolution Analysis Pipeline, Integrating Materials and Manufacturing Innovation 11 (4) (2022) 479–496.
13. M. Yaghoobi, J.E. Allison, V. Sundararaghavan, Multiscale modeling of twinning and detwinning behavior of HCP polycrystals, International Journal of Plasticity (2020) 102653.
14. D. Greeley, M. Yaghoobi, D. Pagan, V. Sundararaghavan, J. Allison, Using synchrotron radiation to improve understanding of deformation of polycrystalline metals by measuring, modelling and publishing 4D information, IOP Conference Series: Materials Science and Engineering 580 (2019) 012017.
15. D. Greeley, M. Yaghoobi, D. Pagan, V. Sundararaghavan, J. Allison, Characterization of cyclic twin evolution in a Mg-Nd alloy using high energy X-ray diffraction microscopy, Journal of Magnesium and Alloys, In Revision (2022).
16. S. Ganesan, M. Yaghoobi, A. Githens, Z. Chen, S. Daly, J.E. Allison, V. Sundararaghavan, The effects of heat treatment on the response of WE43 Mg alloy: crystal plasticity finite element simulation and SEM-DIC experiment, International Journal of Plasticity 137 (2021) 102917.
17. Z. Chen, M. Yaghoobi, V. Sundararaghavan, J. Allison, S. Daly, The Effects of Microstructure on Deformation Twinning in Mg WE43, Materials Science and Engineering: A 859 (2022) 144189.
18. M. Yaghoobi, Z. Chen, V. Sundararaghavan, S. Daly, J.E. Allison, Crystal Plasticity Finite Element Modeling of Extension Twinning in WE43 Mg Alloys: Calibration and Validation, Integrating Materials and Manufacturing Innovation 10(3) (2021) 488–507.
19. M.T. Andani, A. Lakshmanan, V. Sundararaghavan, J. Allison, A. Misra, Quantitative study of the effect of grain boundary parameters on the slip system level Hall-Petch slope for basal slip system in Mg-4Al, Acta Materialia 200 (2020) 148–161.
20. M. Yaghoobi, Z. Chen, A.D. Murphy-Leonard, V. Sundararaghavan, S. Daly, J.E. Allison, Deformation twinning and detwinning in extruded Mg-4Al: In-situ experiment and crystal plasticity simulation, International Journal of Plasticity 155 (2022) 103345.
21. A. Lakshmanan, M.T. Andani, M. Yaghoobi, J. Allison, A. Misra, V. Sundararaghavan, A combined experimental and crystal plasticity study of grain size effects in magnesium alloys, Journal of Magnesium and Alloys (2023).
22. A. Tallman, M. Yaghoobi, PRISMS-Indentation: multi-scale elasto-plastic virtual indentation module, Integrating Materials and Manufacturing Innovation, In review (2023).

Energetic Terms Associated with Twin Nucleation in Magnesium

Enver Kapan, Sertan Alkan, C. Can Aydıner, and Jeremy K. Mason

Abstract

Molecular dynamics simulations are performed that follow the evolution of a tension twin embryo nucleating from an asymmetrically tilted grain boundary to investigate the energetics of twin nucleation. The line, surface, and volumetric terms associated with twin nucleation are identified. A micromechanical model is proposed where the stress field around the twin nucleus is estimated using the Eshelby formalism, and the contributions of the various twin-related structures to the potential energy of the twin are evaluated. The reduction in the grain boundary energy arising from the change in character of the prior grain boundary is found to offset the energy costs of the other interfaces. The defect structures bounding the stacking faults that form inside the twin are also found to possibly have significant energetic contributions. These results suggest that both of these effects could be more significant than has been assumed by many earlier continuum-scale twin nucleation models and are perhaps critical considerations when predicting twin nucleation sites in magnesium.

Keywords

Molecular dynamics • Magnesium • Twinning • Nucleation

Extended Abstract

The tensile twinning mechanism is central to our understanding of the deformation behavior of magnesium-based alloys. However, the development of an accurate deformation twin nucleation model for magnesium has proven to be challenging. Experimental studies [1–3] verified the role of grain boundaries as potential twin nucleation sites, but the absence of a heterogeneous twin nucleation model which provides rigorous energetic descriptions of twin-related structures indicates a need to understand twin energetics more deeply.

To address this problem, molecular dynamics (MD) simulations were performed to follow the energetic evolution of $\{10\bar{1}2\}$ tension twin embryos nucleating from an asymmetrically tilted grain boundary. A slab of Mg consisting of four grains (crystals) with a $[\bar{1}\bar{1}20]$ fiber texture (Fig. 1a) was compressed and, in response to the loading, a twin was nucleated (Fig. 1b) from a preexisting grain boundary that separated the twinned grain and a neighboring grain. Areas of stacking faults inside the twin, areas of interfaces between the twin and the neighboring grains, and the volume of the twinned region were all quantified (Fig. 1c), and the evolution of these structures was measured from atomic data as the twin embryo grew with further straining. A series of regression analyses is performed for the MD measurements of potential energy (Fig. 1d) to identify the contribution of each of these areas or volumes to the total twin energy (Fig. 1e). A micromechanical model is proposed where the twin is modeled as an inhomogeneity embedded inside an elastic medium. The total energy of the twin is expressed as the sum of major contributions from the twin-related defect structures in addition to the elastic strain energy from the presence of the twin inhomogeneity, with the contribution of the elastic fields around the twin nucleus estimated using the Eshelby formalism [4].

The energy of the grain boundary between the parent grain and the neighboring grain is found to be significantly

---

E. Kapan · S. Alkan · C. Can Aydıner
Department of Mechanical Engineering, Boğaziçi University,
Istanbul, 34342, Turkey
e-mail: enver.kapan@bogazici.edu.tr

S. Alkan
e-mail: sertan.alkan@bogazici.edu.tr

C. Can Aydıner
e-mail: can.aydiner@bogazici.edu.tr

J. K. Mason (✉)
Department of Materials Science and Engineering, University of
California, Davis, 1 Shields Avenue, Davis, CA 95616, USA
e-mail: jkmason@ucdavis.edu

A. Leonard et al. (eds.), *Magnesium Technology 2024*, The Minerals, Metals & Materials Series,
https://doi.org/10.1007/978-3-031-50240-8_34

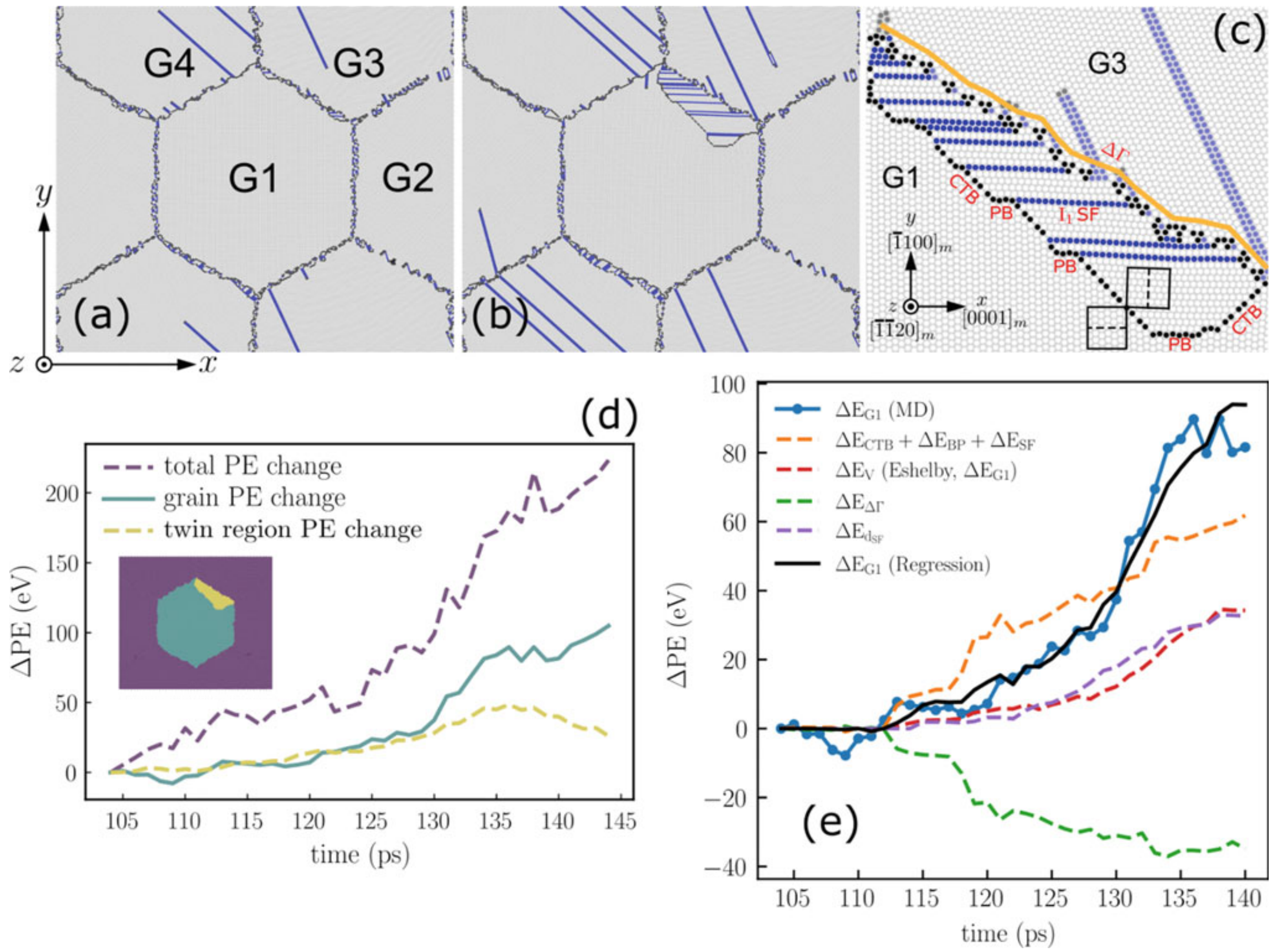

Fig. 1 **a** Simulation box configuration consisting of four different grains (labeled as G1, G2, G3, and G4, respectively). **b** A twin nucleated and grew from the G1–G3 grain boundary. **c** The structures associated with twin nucleation include the coherent (CTB) and prismatic/basal (PB) twin boundaries, stacking faults (I_1 SF), and the transforming grain boundary ΔΓ. **d** MD computations of the total potential energy of the atoms inside the whole simulation box, the parent grain, and the twinned domain. **e** Comparison of the individual contributions of twin-related structures (dashed curves), as obtained from the regression analysis, and the elastic strain energy (dashed red curve), as obtained from the micromechanical model, to the total twin energy (blue marked curve) measured from the MD output. Adapted from Ref. [5]

reduced during the twin reorientation, with the grain boundary changing from an asymmetric-tilt to nearly a symmetric-tilt configuration. This reduction in the energy of the grain boundary nearly offsets the energy cost of the other created interfaces (twin boundaries and stacking faults). However, the twin potential energy (blue curve with markers in Fig. 1e) must include a contribution from some term that scales with the twin volume apart from the elastic strain energy estimated using the Eshelby inhomogeneity theory (dashed red curve in Fig. 1e). It is proposed that the stacking faults inside the twin are bounded by line defects with Burgers vector content (disconnections) embedded in the twin boundary and the prior grain boundary. These line defects are expected to have interacting elastic strain fields that could contribute significant potential energy (dashed magenta curve in Fig. 1e) to that of the twin. These findings indicate that both effects could be key considerations when predicting likely sites for twin nucleation in magnesium. More generally, the intention is for the micromechanical model to be suitable as a way to evaluate the likelihood of observing twin nucleation at a given grain boundary among the grain boundary population in a polycrystal.

References

1. Beyerlein I.J., Capolungo L., Marshal P.E., McCabe R.J., Tome C. N., Statistical analyses of deformation twinning in magnesium, Philos. Mag. 90 (2010) 2161–2190. https://doi.org/10.1080/14786431003630835.

2. Khosravani A., Fullwood D.T., Adams B.L., Rampton T.M., Miles M.P., Mishra R.K., Nucleation and propagation of $\{10\bar{1}2\}$ twins in AZ31 magnesium alloy, Acta Mater. 100 (2015) 202–214. https://doi.org/10.1016/j.actamat.2015.08.024.
3. Paramatmuni C., Guo Y., Withers P.J., Dunne F.P.E., A three-dimensional mechanistic study of the drivers of classical twin nucleation and variant selection in Mg alloys: A mesoscale modelling and experimental study, Int. J. Plast. 143 (2021) 103027. https://doi.org/10.1016/j.ijplas.2021.103027.
4. Eshelby J.D., The determination of the elastic field of an ellipsoidal inclusion, and related problems, Proc. R. Soc. London. Ser. A. Math. Phys. Sci. 241 (1957) 376–396. https://doi.org/10.1098/rspa.1957.0133.
5. Kapan E., Alkan S., Aydıner C. C., Mason J. K., Energetic contributions to deformation twinning in magnesium, Model. Simul. Mater. Sci. Eng. 31 (2023) 075002. https://doi.org/10.1088/1361-651X/acec8c.

Thermodynamics of Mg–Y–O Alloys and Segregation at the Mg/MgO Interface

Rainer Schmid-Fetzer, Shihao Wang, and Zhongyun Fan

Abstract

Elemental segregation driven by the reduction of the total Gibbs energy of the system has been widely observed at the melt/substrate interfaces in various Al- and Mg alloys containing different inoculant particles. This study provides experimental observations, analyses, and identifications of the formation of Y-segregation 2DCs at the Mg/MgO interfaces in a solidified Mg–0.5Y (w%) sample. From an extended Gibbs adsorption isotherm, the interfacial segregation of solute Y in a dilute Mg alloy melt is quantitatively described. The thermodynamics of the elemental interactions, conditions for the formation of MgO and Y_2O_3 particles, and the contributions to the interfacial energy difference are detailed. A reasonable atomic segregation factor at the liquid/MgO interface from the bulk Mg–0.5Y melt is estimated. This changes the structural and chemical configuration at the interface, thus the nucleation potency of native MgO particles as well as the as-cast grain size.

Keywords

Thermodynamics • Nucleation potency • Grain refinement • ICME

Introduction

This study on elemental segregation driven by the reduction of the total Gibbs energy provides experimental observations, analyses, and identifications of the formation of Y-segregation two-dimensional-compounds (2DCs) at the Mg/MgO interfaces in a solidified Mg–0.5Y (wt.%) sample. It is shown that the segregation of Y occurs in the Mg–0.5Y melt, forming specifically Y_2O_3 2DC at the liquid-Mg/$\{111\}_{MgO}$ interface and Mg(Y)–O 2DC monolayer at the liquid-Mg/$\{100\}_{MgO}$ interface. That is proven by dedicated electron microscopy, and a summary is depicted in Fig. 1 [1].

This changes the nucleation potency of native MgO particles as well as the as-cast grain size. That is demonstrated by grain refinement of commercially pure Mg treated by high shear melt conditioning, HSMC, before casting (CP Mg-HSMC), shown as a basis in Fig. 2, left-hand micrographs. Segregation of Y towards the highly dispersed native MgO particles in the melt after addition of 0.5 wt.% Y is suggested to improve the observed grain refinement in Mg–0.5Y–HSMC, Fig. 2, right-hand micrographs. The average as-cast grain size is reduced from 235 ± 18 µm to 106 ± 4 µm [1]. The grain refining mechanism is attributed to the enhanced potency of {111} MgO particles (the predominant oxide in terms of population) modified by Y_2O_3 2DC, their dispersity and abundant number density, and the necessary growth restriction provided by 0.5 wt.% Y.

Thermodynamics and Interfacial Energy

The thermodynamics of the elemental interactions, conditions for the formation of MgO and Y_2O_3 particles, and the contributions to the interfacial energy difference are detailed below. From an extended Gibbs adsorption isotherm, the interfacial segregation of solute Y in a dilute Mg alloy melt is quantitatively described [1, 2]. It is suggested that

---

R. Schmid-Fetzer (✉)
Institute of Metallurgy, Clausthal University of Technology, Robert-Koch-Str. 42, 38678 Clausthal-Zellerfeld, Germany
e-mail: schmid-fetzer@tu-clausthal.de

S. Wang
SuperSTEM Laboratory, SciTech Daresbury Campus, Daresbury, WA4 4AD, UK
e-mail: swang@superstem.org

Z. Fan
BCAST, Brunel University London, Uxbridge, UB8 3PH, Middlesex, UK
e-mail: Zhongyun.Fan@brunel.ac.uk

A. Leonard et al. (eds.), *Magnesium Technology 2024*, The Minerals, Metals & Materials Series,
https://doi.org/10.1007/978-3-031-50240-8_35

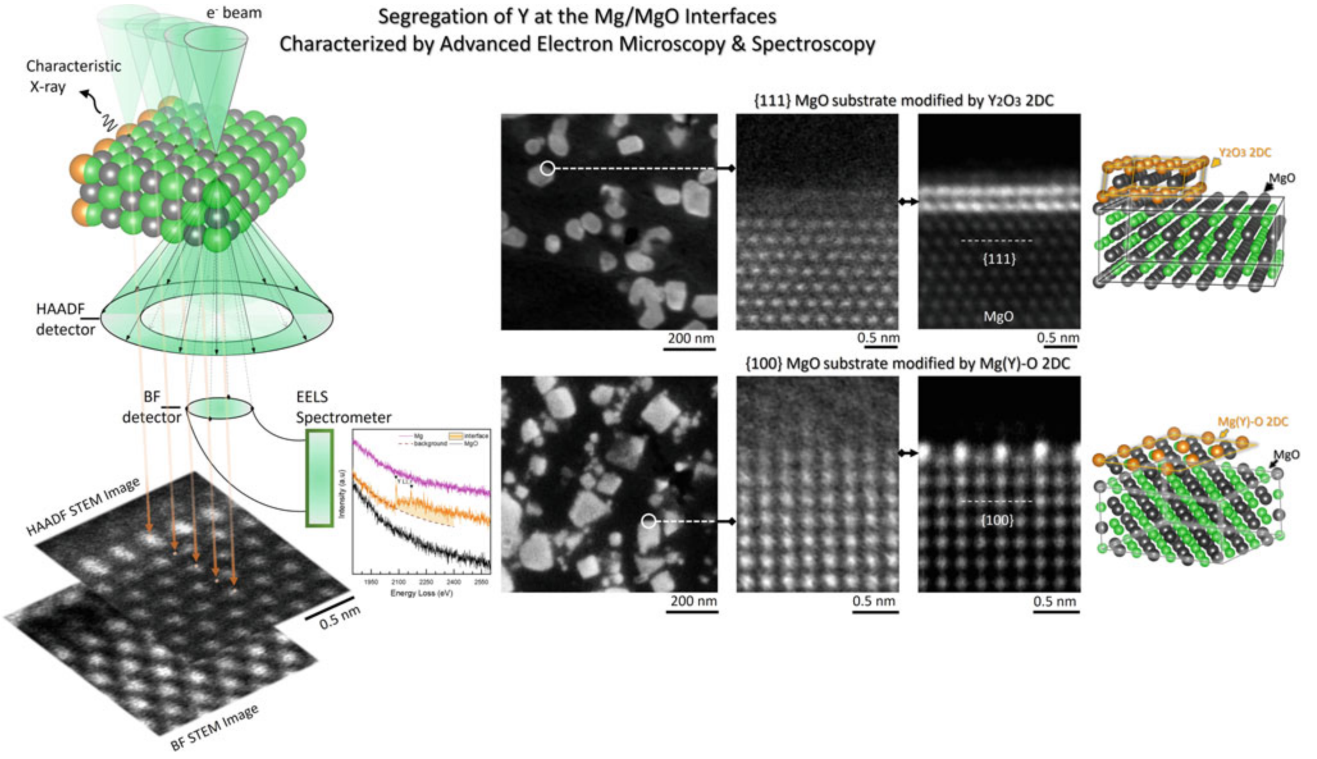

Fig. 1 Graphical sketch of the electron microscopic methods and results to determine and distinguish the Y_2O_3 2DC at the liquid-Mg/$\{111\}_{\mathrm{MgO}}$ interface and Mg(Y)–O 2DC monolayer at the liquid-Mg/$\{100\}_{\mathrm{MgO}}$ interface [1]

interfacial segregation is favored by (1) a negative difference in interfacial energies approximated by $\Delta\gamma = \gamma^i_{\mathrm{Y(L)/MgO}} - \gamma^i_{\mathrm{Mg(L)/MgO}}$ in this case, (2) a positive interaction term Ω of a regular solution between solvent and solute atoms related to a positive enthalpy of mixing $\Delta_{\mathrm{mix}}H^{\mathrm{Liquid}}_{\mathrm{Mg-Y}}$, and (3) a positive difference in entropies of fusion between pure solvent and solute $\Delta S^i = \Delta_{\mathrm{fus}}S_{\mathrm{Mg}} - \Delta_{\mathrm{fus}}S_{\mathrm{Y}}$. The three contributions are considered separately below.

Enthalpy and Entropy Contributions

A strong attractive interaction among Mg and Y in the melt is proven to exist from a comprehensive CALHAD assessment of that binary system [3] and the following data is calculated from these thermodynamic parameters using the Pandat software [4, 5]. A large negative value of the mixing enthalpy with the minimum value of $\Delta_{\mathrm{mix}}H^{\mathrm{Liquid}}_{\mathrm{Mg-Y}} = -10.6$ kJ/mol at 41 at.% Y is obtained from the subregular solution [3]. The approximation by a regular solution equation to fit the dilute, Mg-rich range results in $\Delta_{\mathrm{mix}}H^{\mathrm{Liquid,reg}}_{\mathrm{Mg-Y}} = -14$ kJ/mol at 50 at.% Y, corresponding to the interaction term Ω = − 56 kJ/mol. This strong negative term impedes the interfacial segregation of Y. The coordination numbers $Z_l = 9$, $Z_V = 12$, $Z = 13$, in the notation of Ref. [2], are used for the numerical calculations. Although the value of the entropy difference, $\Delta S^i = 2.837$ J/mol/K calculated from Ref. [3], is positive it only accounts for a small promotional contribution to the interfacial segregation of Y. At 700 °C its contribution is about 18 times smaller compared to the impeding Ω term.

Interfacial Energy Contributions

The remaining impeding effect can be canceled if the value of Δγ is negatively large enough. The interfacial energies of pure liquid elements/MgO are not known. However, the difference Δγ can be predicted by solving Eq. (25) in Ref. [2] with the data given above. At 700 °C the limit is $\Delta\gamma < -1.05$ J/m^2 to result in enrichment of Y. The value of $\Delta\gamma = -1.39$ J/m^2 is obtained for reasonable atomic segregation of factor 10 with 1.37 at.% Y (4.8 wt.% Y) at the Liquid/$\{111\}_{\mathrm{MgO}}$ interface from the bulk 0.137 at.% Y (0.5 wt.% Y) melt.

The sign of Δγ may be estimated to check the plausibility of assuming $\Delta\gamma < -1.05$ J/m^2. Clearly, the interface Mg(L)/MgO is non-reactive, whereas strong reactions are expected at the Y(L)/MgO interface as shown later by inspection of

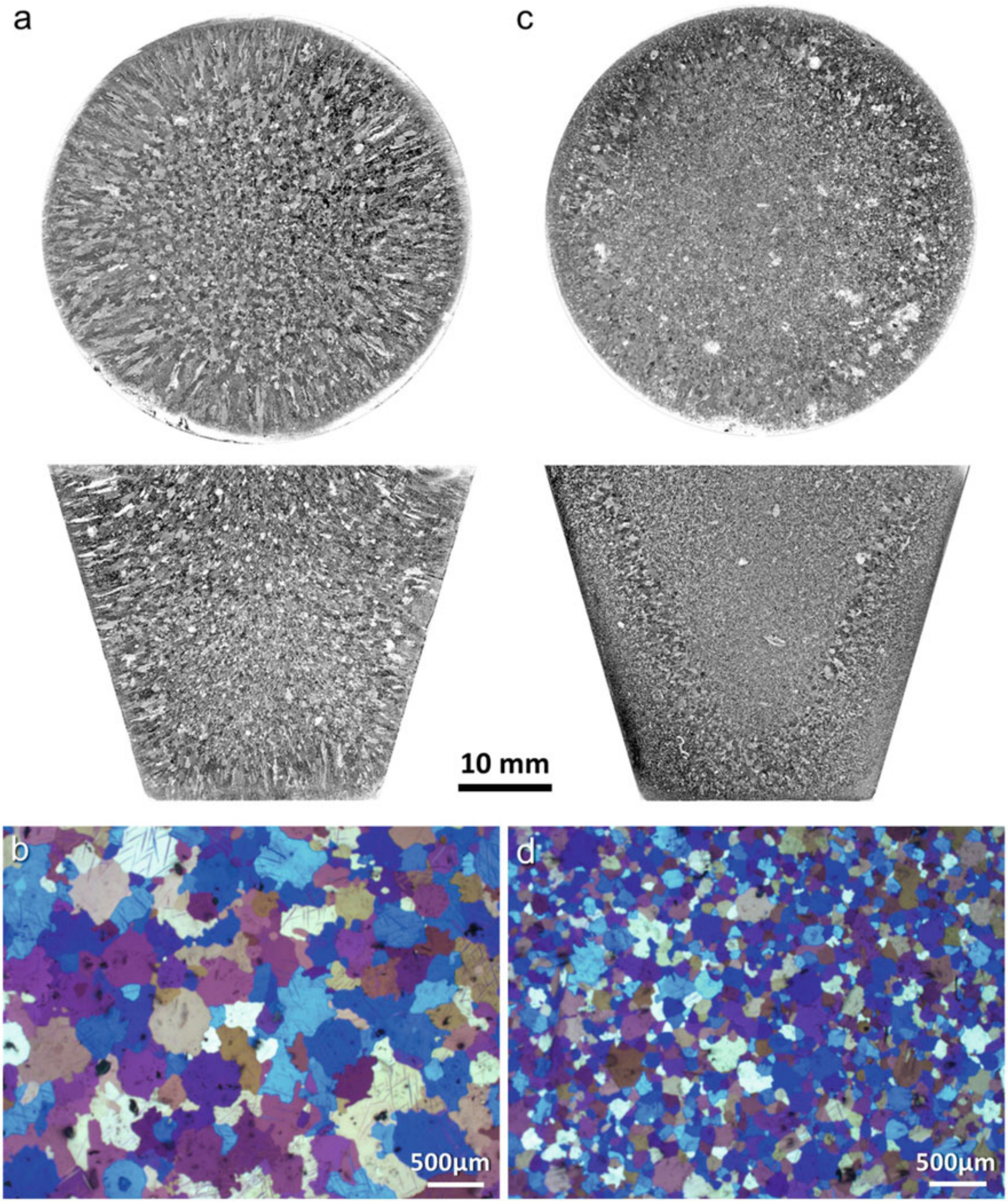

Fig. 2 Grain size of commercially pure Mg with highly dispersed native MgO particles, CP Mg–HSMC, left-hand micrographs (**a**, **b**), is significantly reduced by the addition of 0.5 wt.% Y enabling segregation of Y in Mg–0.5Y–HSMC right-hand micrographs (**c**, **d**). Both melts were treated by high shear melt conditioning, HSMC, before casting [1]

the Mg–Y–O phase diagram. If interfacial reactions occur in metal/oxide systems, the interfacial energies and wetting are difficult to analyze [6] but, in general, the wetting tendency and work of adhesion are increased significantly compared to the non-reactive case [7].

The work of adhesion, $W_{\mathrm{X}}^{\mathrm{ad}}$, is the work against surface forces required to separate the pure liquid element X from a ceramic substrate such as MgO. It is related to the three interfacial energies involved, $\gamma^{i}_{\mathrm{MgO/vapor}}$, $\gamma^{i}_{\mathrm{X(L)/vapor}}$, and $\gamma^{i}_{\mathrm{X(L)/MgO}}$ [7]:

$$W_{\mathrm{X}}^{\mathrm{ad}} = \gamma^{i}_{\mathrm{MgO/vapor}} + \gamma^{i}_{\mathrm{X(L)/vapor}} - \gamma^{i}_{\mathrm{X(L)/MgO}} \qquad (1)$$

and to the experimentally determined contact angle θ

$$W_X^{ad} = \gamma^i_{X(L)/vapor}(1 + \cos\theta) \tag{2}$$

Therefore, the difference in work of adhesion of reactive Y(L), $W_Y^{ad-react}$, and non-reactive Mg(L), $W_{Mg}^{ad-Non-react}$, on MgO is given as

$$W_Y^{ad-react} - W_{Mg}^{ad-Non-react} = \gamma^i_{Y(L)/vapor} - \gamma^i_{Mg(L)/vapor} + \gamma^i_{Mg(L)/MgO} - \gamma^i_{Y(L)/MgO} \tag{3}$$

Inserting the difference in interfacial energies of the condensed phases, $\Delta\gamma = \gamma^i_{Y(L)/MgO} - \gamma^i_{Mg(L)/MgO}$, we obtain

$$W_Y^{ad-react} - W_{Mg}^{ad-Non-react} = (\gamma^i_{Y(L)/vapor} - \gamma^i_{Mg(L)/vapor}) - \Delta\gamma \gg 0 \tag{4}$$

Assuming that the difference in surface tensions, the term in the brackets in Eq. (4), is not dominant compared to $\Delta\gamma$ we obtain at least $\Delta\gamma < 0$, as required to cancel the remaining impeding effect on Y-segregation detailed above. The value of $\Delta\gamma = -1.39$ J/m^2 related to a reasonable atomic segregation of factor 10 may not be quantitatively precise as it depends on the accuracy of input data and assumptions in the model. It is emphasized that a significant Y-segregation towards the Liquid/MgO interface from the bulk Mg–0.5Y melt is verified experimentally [1]. This changes the structural and chemical configuration at the interface, thus the nucleation potency of native MgO particles as well as the as-cast grain size.

Thermodynamics and Phase Diagram

The thermodynamic conditions for the formation of bulk Y_2O_3 particles in Mg–0.5Y, are revealed by the isothermal section at 700 °C and ambient pressure of the Mg–Y–O ternary equilibrium phase diagram. Figure 3 is calculated using Pandat and the PanMg database [4]. The oxygen solubility in liquid-Mg shown in the magnified Mg-rich part in Fig. 3b was verified by the detailed analysis of the experimental phase diagram and thermodynamic data [8]. It shows that the bulk Mg–0.5Y liquid alloy is saturated at 0.24 wt.% O with MgO. This small oxygen content is readily picked up from the ambient during melting because of the extremely low partial pressure of O_2, $p(O_2) = 5 \times 10^{-54}$ bar, calculated at the tie line Liquid + MgO. Therefore, MgO is the only stable native oxide in that Mg–0.5Y alloy which is also observed experimentally. This tie line also proves that the interface Mg(L)/MgO is non-reactive whereas no tie line exists from MgO to any Y-rich liquid indicating that strong reactions are expected at the Y(L)/MgO interface, as stated above. More than 3.9 wt.% Y in the liquid alloy is required to expect Y_2O_3 as the stable bulk oxide. The liquid phase from 3.9 to 46 wt.% Y is in equilibrium with Y_2O_3. It is interesting to note that under the assumed segregation of factor 10 with 4.0 wt.% Y in the liquid monolayer at the Liquid/$\{111\}_{MgO}$ interface one could obtain a local three-phase equilibrium with Y_2O_3 at that interface.

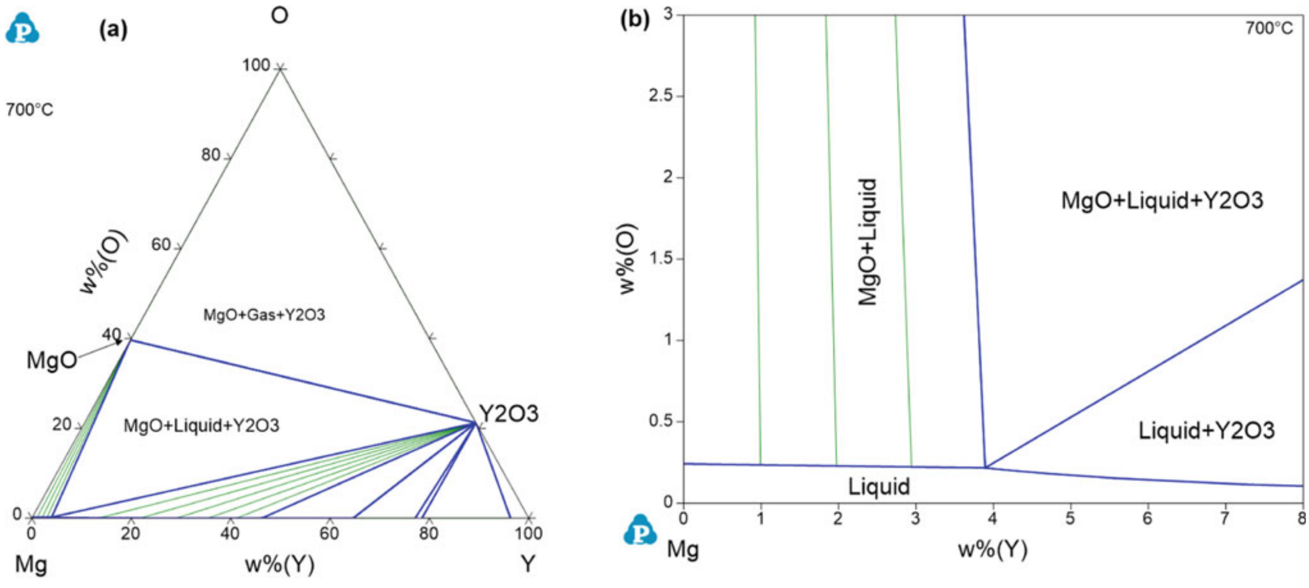

Fig. 3 Isothermal section at 700 °C of the Mg–Y–O equilibrium phase diagram calculated by Pandat and PanMg: **a** complete composition range and **b** Mg-rich corner with Y content up to 8 wt.%

Solidification Simulations

Finally, solidification simulations of the Mg–0.5Y–0.24O (wt.%) alloy, which is just saturated with MgO at 700 °C according to Fig. 3b, reveal the expected solid phases. The results obtained using the Pandat software are shown in Figs. 4 and 5.

Under equilibrium conditions, Fig. 4a, a tiny phase fraction of up to 0.2% of MgO grows from 700 to 647 °C due to the retrograde oxygen solubility in Liquid. From 647 to 643 °C, the bulk of (Mg) solid solution (Hcp) is formed (phase fraction from 0 to 99.27%) together with the growth of MgO from 0.2 to 0.73%. Solidification terminates in this monovariant eutectic reaction, Liquid → (Mg) + MgO at 643 °C without reaching an invariant ternary eutectic.

The distribution of solute Y between Liquid and (Mg) in Fig. 4b starts at the initial 0.5 wt.% in Liquid and increases rapidly from 0.5 to 2.3 wt.% Y during the bulk crystallization of (Mg). The (Mg) solid solution hosts from 0.1 to 0.5 wt.% Y in that secondary step from 647 to 643 °C. Only the two-phase equilibrium (Mg) + MgO exists from 643 to 490 °C. At 490 °C the solubility of 0.5 wt.% Y at the apex of the three-phase equilibrium (Mg) + MgO + Y_2O_3 is attained. Here we have a similarity to the 3.9 wt.% Y in the

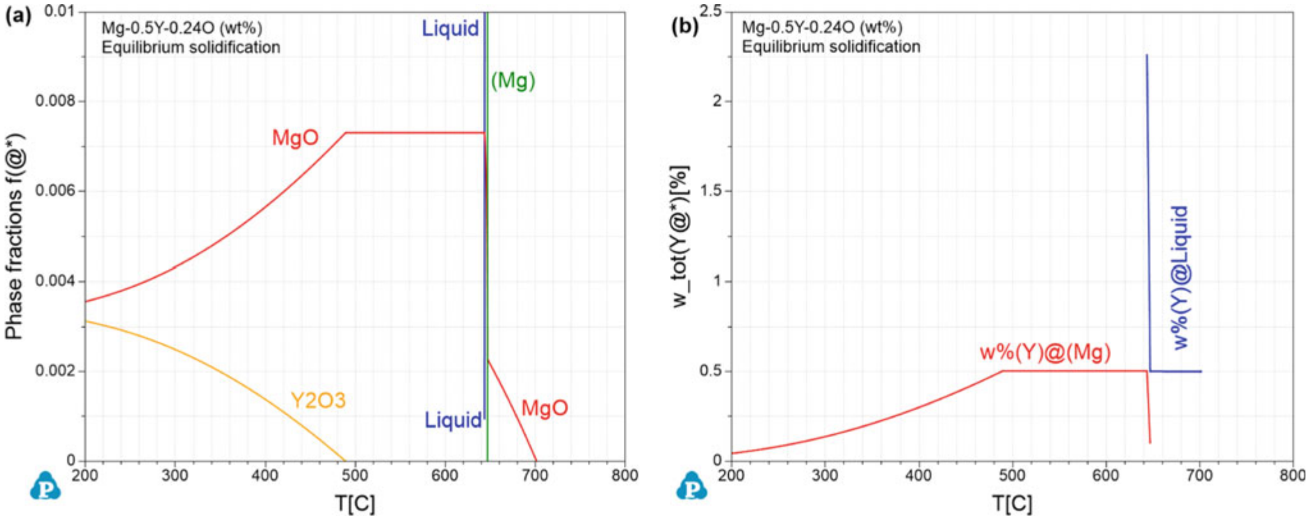

Fig. 4 Solidification simulation of the Mg–0.5Y–0.24O (wt.%) alloy under equilibrium conditions: **a** phase fractions shown up to 1% to reveal the minority phases, **b** distribution of solute Y between liquid and (Mg) phases

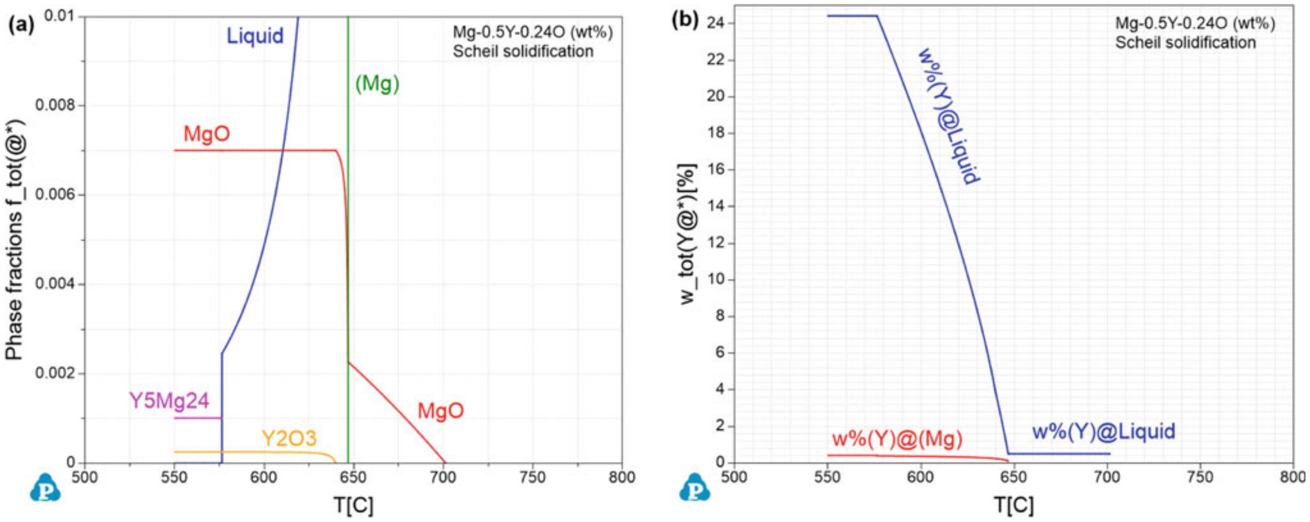

Fig. 5 Solidification simulation of the Mg-0.5Y-0.24O (wt.%) alloy under Scheil conditions: **a** phase fractions shown up to 1%, **b** distribution of solute Y between liquid and (Mg) phases; note that the average (total) wt.% of Y solute in (Mg) is plotted, ranging from 0.1 to 0.42 wt.% Y in the assumed layered growth of (Mg) under Scheil conditions

liquid alloy at the apex of the three-phase equilibrium Liquid + MgO + Y_2O_3 at 700 °C in Fig. 3b. Below 490 °C the solubility of Y at the three-phase equilibrium (Mg) + MgO + Y_2O_3 decreases as shown in Fig. 4b and the liberated Y forms Y_2O_3 at the cost of MgO in a solid-state reaction as given in Fig. 4a. The solubility of oxygen in (Mg) is negligibly small and both oxides MgO and Y_2O_3 are stoichiometric phases in this ternary system.

The results of solidification simulation of the same alloy under Scheil conditions, explained in Ref. [9], are given in Fig. 5. Initially the phase development in Fig. 5a is exactly the same as under equilibrium because there is no solid solution in the primary crystallizing MgO. At 647 °C the bulk of (Mg) starts crystallizing in the same monovariant eutectic reaction, Liquid → (Mg) + MgO. However, since back-diffusion of Y into the growing (Mg) phase is blocked the Y-enrichment in Liquid is huge, as shown in Fig. 5b. Below 640 °C Y_2O_3 starts growing while the phase fraction of MgO is frozen-in at 0.7%; the reaction switches to Liquid → (Mg) + Y_2O_3 until the ternary invariant eutectic reaction Liquid → (Mg) + Y_2O_3 + Y_5Mg_{24} terminates solidification at 576.4 °C. The solidified non-equilibrium constitution comprises four phases, the phase fractions are also plotted for better readability down to the arbitrary cut-off at 550°C in Fig. 5b: 99.17% (Mg) + 0.70% MgO + 0.10% Y_5Mg_{24} + 0.03% Y_2O_3. That is considered a good approximation of the as-cast microstructure of that alloy. The very small fraction of 0.1% Y_5Mg_{24} may be too small to be detected. Also, the initial alloy is certainly not single-phase Liquid at 700 °C but contains more oxygen in the form of MgO which was observed experimentally as highly dispersed native MgO particles after treatment by high shear melt conditioning before casting [1]. That phase fraction of MgO already present at 700 °C is simply added as inert basis to the MgO formed during the solidification simulations in Figs. 4a and 5a, at the cost of (Mg). This will reduce the tiny fraction of Y_5Mg_{24} even below 0.1%.

References

1. S. Wang, Y. Wang, Q.M. Ramasse, R. Schmid-Fetzer, Z. Fan, Segregation of Yttrium at the Mg/MgO interface in an Mg-0.5Y Alloy, Acta Materialia 257 (2023) 119147.
2. H. Men, Z. Fan, An Analytical Model for Solute Segregation at Liquid Metal/Solid Substrate Interface, Metallurgical and Materials Transactions A 45(12) (2014) 5508–5516.
3. O.B. Fabrichnaya, H.L. Lukas, G. Effenberg, F. Aldinger, Thermodynamic optimization in the Mg–Y system, Intermetallics 11(11) (2003) 1183–1188.
4. S.L. Chen, S. Daniel, F. Zhang, Y.A. Chang, X.Y. Yan, F.Y. Xie, R. Schmid-Fetzer, W.A. Oates, The PANDAT software package and its applications, Calphad 26(2) (2002) 175–188.
5. W. Cao, S.L. Chen, F. Zhang, K. Wu, Y. Yang, Y.A. Chang, R. Schmid-Fetzer, W.A. Oates, PANDAT software with PanEngine, PanOptimizer and PanPrecipitation for multi-component phase diagram calculation and materials property simulation, Calphad 33 (2) (2009) 328–342.
6. N. Eustathopoulos, Progress in understanding and modeling reactive wetting of metals on ceramics, Current Opinion in Solid State and Materials Science 9(4–5) (2005) 152–160.
7. M. Humenik Jr, W.D. Kingery, Metal-ceramic interactions: III, surface tension and wettability of metal-ceramic systems, Journal of the American Ceramic Society 37(1) (1954) 18–23.
8. S.-M. Liang, R. Schmid-Fetzer, Complete thermodynamic description of the Mg–Ca–O phase diagram including the Ca–O, Mg–O and CaO–MgO subsystems, Journal of the European Ceramic Society 38(14) (2018) 4768–4785.
9. R. Schmid-Fetzer, Phase Diagrams: The Beginning of Wisdom, Journal of Phase Equilibria and Diffusion 35(6) (2014) 735–760.

Part VI

Biomedical Applications

Assessment of Magnesium Wire Coatings for Absorbable Medical Devices

Adam J. Griebel, Cody J. David, Jeremy E. Schaffer, Weilue He, and Roger Guillory II

Abstract

Absorbable magnesium (Mg) wires have the potential to replace many permanent medical devices. Permanent devices endure as an unnatural material in the body whereas eventual staples, stents, and sternal wires made from absorbable magnesium can enable complete tissue healing by elimination of most long-term foreign material. Due to magnesium's relatively rapid degradation rate, thin devices may not provide adequate mechanical support during the entire healing phase without surface modifications or coatings to delay the onset of corrosion. This study aimed to assess the feasibility and effectiveness of absorbable coatings which could be suitable for a range of Mg-based biomedical devices, spanning cardiovascular, orthopedic, and wound closure implants. Mg alloy LZ21 wire was drawn to 0.3 mm and annealed to impart high ductility. A portion of the wire was then anodized in an experimental electrolyte. Anodized wire was then coated with an absorbable polymer jacket of polycaprolactone (PCL). Bare, anodized, and PCL-coated wire were then subjected to both in vitro and in vivo degradation testing to assess coating impact.

Keywords

Absorbable • Magnesium • Wire • Corrosion • Coating • Anodization • PCL • IVIVC

Introduction

Many medical devices such as stents, staples, sutures, and ligation clips are comprised of wires with diameters less than one millimeter. Often, these devices only serve a temporary purpose and their continued presence is unnecessary, and in some cases even harmful. Magnesium alloys, with an inherent ability to degrade and absorb into the body harmlessly, are an attractive material for new iterations of these medical devices. However, the relatively rapid degradation rate of magnesium may not allow for sufficient mechanical strength for a sufficient length of time, especially in these fine diameters [1].

Many studies have explored extending the lifetime of magnesium alloys with surface modification in the form of conversion coatings (e.g., anodization, plasma electrolytic oxidation (PEO), MgF_2) and polymeric coatings (e.g., PLA, PLLA, PLGA, PCL) with some success [2–4], though data on coated Mg wire is sparse. Ali et al. showed promising results with a continuous PEO coating on Mg wire [5, 6], but relatively hard and thick oxide layers may not be suitable in applications requiring flexural deformation of the wire. There is also some evidence that dual layer comprising a conversion coat and a polymer performs better than either coating alone [7]. An ideal coating would be pliable enough to withstand large wire bends, tough enough to withstand mild abrasion, and protective enough to delay corrosion past some critical time point, which will be application-specific.

A promising Mg alloy candidate, LZ21 [8, 9], possesses excellent ductility and moderate strength, properties which could lend it well to the aforementioned medical devices.

However, like most magnesium alloys, the degradation rate may not be sufficient without a coating.

The aim of the present study is to (1) determine the influence of anodization and polymer coating on the degradation of LZ21 wire, (2) determine for the first time an in vivo degradation rate of LZ21, and (3) establish an in vitro in vivo correlation (IVIVC) factor.

A. J. Griebel (✉) · C. J. David · J. E. Schaffer
Fort Wayne Metals Research Products Corp.,
Fort Wayne, IN, USA
e-mail: adam_griebel@fwmetals.com

W. He
Michigan Technological University, Houghton, MI, USA

R. Guillory II
Medical College of Wisconsin, Milwaukee, WI, USA

A. Leonard et al. (eds.), *Magnesium Technology 2024*, The Minerals, Metals & Materials Series,
https://doi.org/10.1007/978-3-031-50240-8_36

Materials and Methods

Magnesium alloy LZ21 wire preparation has been described previously [8]. In this study, wire was cold drawn to a final diameter of 0.3 mm and annealed. The wire was then divided into one of three surface conditions. Bare wire was left in the as-drawn, bright state. Anodized wire was prepared through a proprietary process which induced a thin surface layer containing Mg, F, O, and P. PCL wire was produced by melt extruding a thin layer (approximately 20 µm) of M_n 80,000 PCL (MilliporeSigma, Burlington, MA) onto the anodized wire.

Baseline mechanical properties of the three conditions were assessed via tensile testing (127 mm gauge length, 25.4 mm/min crosshead speed, N = 3).

In vitro corrosion properties of the wire were tested by using custom PVC and Nylon "kitewinder" test fixtures, in which multiple lengths of wire were wrapped across 250 mm spans. The wire sections experiencing bending stresses around the ends of the fixture were masked with paraffin wax, to prevent premature fracture at these locations during corrosion. Loaded kitewinders were fully submerged in 2 L of a modified Hanks's balanced salt solution, held in an incubator at 37 °C and 5% CO_2 to buffer the pH to 7.4 ± 0.2. Samples were then allowed to corrode for 3, 7, 14, and 28 days with 4 samples for each time point. Of the four samples, three were tensile tested as described above to determine residual mechanical strength while one sample was designated for cross-sectional analysis.

In vivo corrosion properties of bare and PCL wires were assessed via subcutaneous implantation of 10 mm lengths in mice for 7 and 33 days. Briefly, a subcutaneous pouch was created via blunt dissection after a midline abdominal incision. Materials were inserted into the pouch, and they would close with surgical staples. After euthanasia at the designated time points, the wires were carefully removed from the pouches and placed into 200 proof ethanol and desiccated overnight in a ventilated fume hood. The animal study was approved by the Michigan Technological University Institutional Animal Care and Use Committee (IACUC) and in accordance with guidelines set by the Panel on Euthanasia of the American Veterinary Medical Association. After each time point, the wires were explanted, and corrosion was assessed via cross-sectional analysis.

Cross-sectional analysis was conducted by mounting wire sections in a cold-curing epoxy and then progressively grinding and polishing to 4000 grit sandpaper with isopropyl alcohol lubricant. For each in vitro condition and time point, 11 sections were imaged. For each in vivo condition and time point, 16–26 sections were imaged. Residual area and pitting factor were measured for each cross section using ImageJ. Residual areas of both in vitro and in vivo samples were compared to establish a preliminary IVIVC.

Results

Representative tensile properties of the three wire conditions prior to corrosion are shown in Fig. 1. The triplicate testing revealed high consistency between samples. The bare wire exhibited an ultimate tensile strength of 245 MPa, a yield strength of 189 MPa, and an elongation of 15%. Neither coating process impacted the strength properties but the elongation to fracture did decrease slightly.

In vitro corrosion testing showed marked differences between coating types. As shown in Fig. 2, bare wire fell to 18% of its original strength within 7 days while anodized wire retained 60% of its original strength over the same time period. The PCL wire still had over 90% of its original strength out to 14 days. These strength values largely corresponded with cross-sectional area loss ($R^2 = 0.945$), illustrated in Figs. 3, 4, and 5 with representative images at each of the time points for which intact wire specimens remained. In the case of bare wire, no wires were intact at the 14 and 28 day time points. No anodized wire specimens were intact at the 28 day time point.

In vivo degradation testing of bare wires indicated a much slower degradation rate than the in vitro test (Fig. 6), with 84% of the metal cross section remaining after 7 days in the mouse as opposed to only 37% in Hank's solution. After 33 days in vivo, 60% of the cross section remained on average. The PCL wire showed almost no sign of corrosion at both 7 and 33 day time points (Fig. 7). Residual area over time for all 5 condition sets is shown in Fig. 8.

Taking the residual area measurements and assuming a uniform loss, average corrosion rates for the bare wire were 2.1 and 3.0 mm/yr at 3 and 7 days in Hank's solution, respectively, and 0.63 and 0.37 mm/yr at 7 and 33 days in mice, respectively. Taking the 7 day time point, we calculate an IVIVC factor of 8.1.

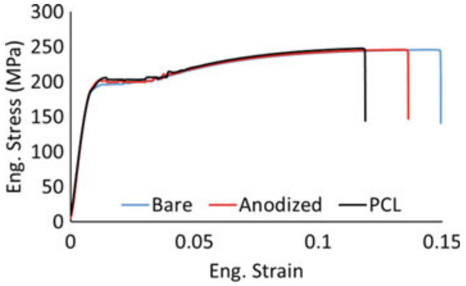

Fig. 1 Representative tensile curves of the three conditions prior to corrosion

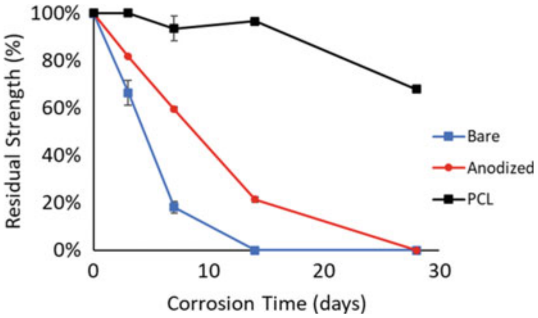

Fig. 2 Residual strength of wire over time after degrading in vitro. Data shown is mean values with standard deviation error bars

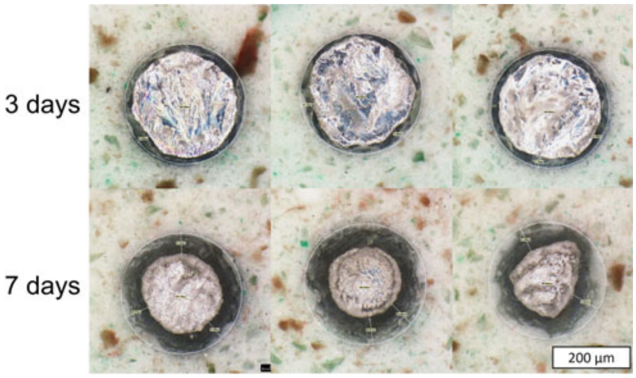

Fig. 3 Representative transverse cross sections of bare wire degraded 3 and 7 days in vitro

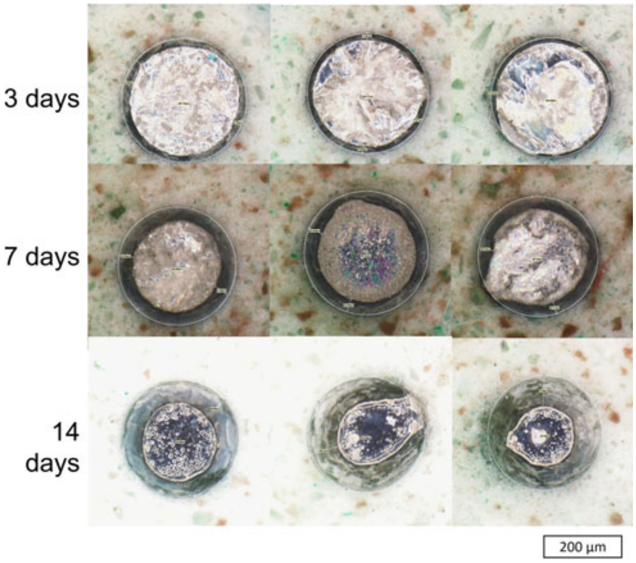

Fig. 4 Representative transverse cross sections of anodized wire degraded 3, 7, and 14 days in vitro

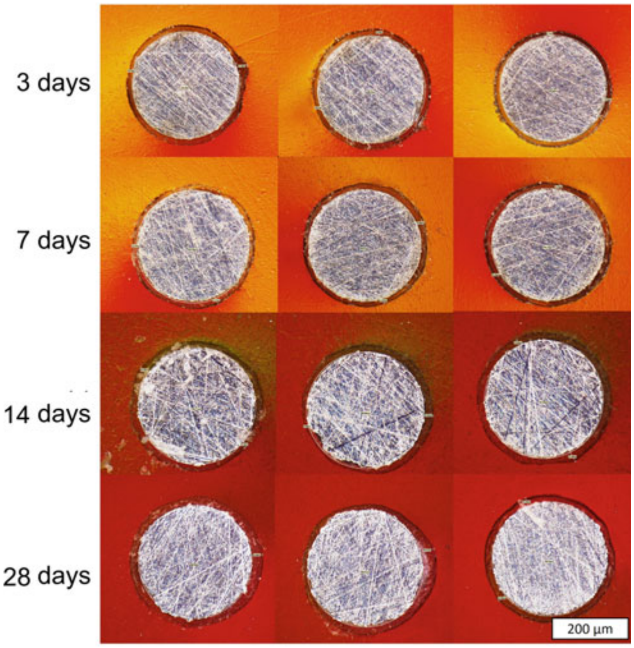

Fig. 5 Representative transverse cross sections of the PCL wire degraded 3, 7, 14, and 28 days in vitro

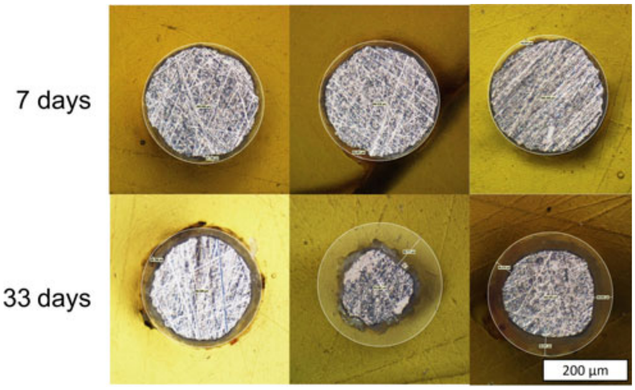

Fig. 6 Representative transverse cross sections of the bare wire degraded 7 and 33 days in vivo

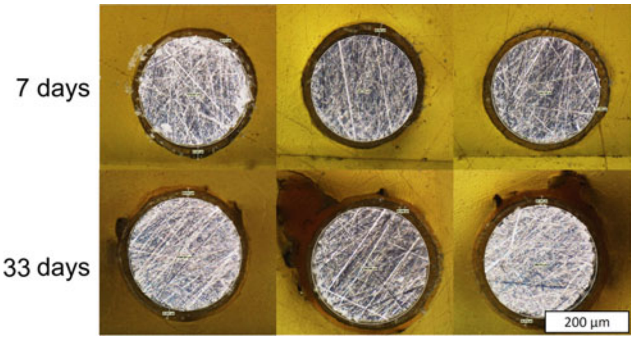

Fig. 7 Representative transverse cross sections of the PCL wire degraded at 7 and 33 days in vivo

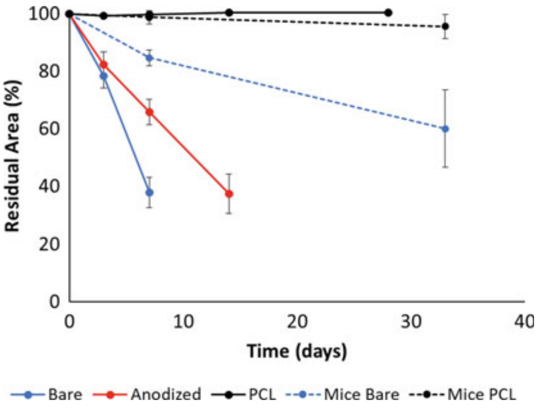

Fig. 8 Residual cross-sectional area (mean ± standard deviation) of the various wires in vitro (solid) and in vivo (dashed)

Discussion

The aim of this study was to (1) determine the influence of anodization and polymer coating on degradation of LZ21 wire, (2) determine for the first time an in vivo degradation rate of LZ21, and (3) establish an in vitro in vivo correlation factor. The data presented here substantially addresses each of these aims.

The in vitro testing clearly indicates that anodization surface treatment of Mg wire can offer some corrosion protection and extend functional lifetime. Incorporating a PCL jacket on top of this anodization layer can provide even further corrosion delay. The present results indicate that the PCL jacket used in this study might be too protective for some applications, as little to no degradation of the wire was seen in vitro or in vivo. It is possible that corrosion delay could be tuned by using a thinner layer of PCL or a different PCL grade [10]. Other polymer coatings might offer optimized degradation rates as well.

The in vivo degradation data indicate a relatively low and uniform corrosion rate for the LZ21 alloy, with no visible adverse histological effects. Lithium is primarily added to the alloy to enhance bending ductility, but it may be the case that this relatively small amount of Li is able to increase the passivity of the corrosion layer through the formation of a Li_2CO_3 film [11], inhibition of MgO to $Mg(OH)_2$ conversion [12], or some other mechanism. Additional work to elucidate the elemental composition and evolution of corrosion products on LZ21 wire is warranted.

The establishment of an IVIVC is an important step for the development of medical devices containing the LZ21 alloy. The factor of 8.1 determined here using 7 day time points is substantially higher than that reported by Bowen [1]. That study calculated an IVIVC factor of 1.2–1.9 for pure Mg, but the in vitro testing was conducted in DMEM rather than Hank’s solution. This indicates that in vitro testing in Hank’s can allow for effective accelerated corrosion testing. The high correlation between measured area and measured tensile strength of these wires aligns with other studies by Bowen [13, 14], and suggests that residual mechanical strength of a partially corroded device can be inferred by the remaining metallic cross-sectional area, provided corrosion is sufficiently uniform.

There are several areas of inquiry which are ripe for investigation. Future work should seek to understand the influence of thermomechanical processing on LZ21 degradation behavior. As many medical devices will undergo plastic deformation during implantation, testing corrosion properties of the coated materials after experiencing a relevant amount of plastic deformation may provide additional insights into the limitations of these coating strategies. Finally, a more in-depth investigation of the corrosion layer could explain the relatively low corrosion rate seen in this mouse model.

Acknowledgements U.S. National Institutes of Health, National Heart Blood Lung Institute (Grant 1R15HL167221-01 to RJG) is acknowledged for partially funding this work. The assistance of Dale Herndon, Lane Bailey, Sean Telley, and Harold Perez in wire preparation and testing is gratefully acknowledged.

References

1. P. Bowen, A. Drelich, J. Drelich and J. Goldman, “Rates of in vivo (arterial) and in vitro biocorrosion for pure magnesium,” *Society for Biomaterials,* vol. 103a, no. 1, pp. 341–349, 2015.
2. P. Wan, L. Tan and K. Yang, “Surface Modification on Biodegradable Magnesium Alloys as Orthopedic Implant Materials to Improve the Bio-adaptability: A Review,” *Journal of Materials Science & Technology,* vol. 32, no. 9, pp. 827–834, 2016.
3. J. Ma, M. Thompson, N. Zhao and D. Zhu, “Similarities and differences in coatings for magnesium-based stents and orthopaedic implants,” *Journal of Orthopaedic Translation,* vol. 2, no. 3, 2014.
4. Z.-Q. Zhang, Y.-X. Yang, J.-A. Li, R.-C. Zeng and S.-K. Guan, “Advances in coatings on magnesium alloys for cardiovascular stents – A review,” *Bioactive Materials,* vol. 6, no. 12, pp. 4729–4757, 2021.
5. W. Ali, M. Li, L. Tillmann, T. Mayer, C. Gonzalez, J. LLorca and A. Kopp, “Bioabsorbable WE43 Mg alloy wires modified by continuous plasma-electrolytic oxidation for implant applications. Part I: Processing, microstructure and mechanical properties,” *Biomaterials Advances,* vol. 143, 2023.
6. W. Ali, M. Echeverry-Rendón, A. Kopp, C. González and J. LLorca, “Effect of surface modification on interfacial behavior in bioabsorbable magnesium wire reinforced poly-lactic acid polymer composites,” *npj Materials Degradation,* vol. 7, 2023.
7. R. Menze and E. Wittchow, “In vitro and in vivo evaluation of a novel bioresorbable magnesium scaffold with different surface modifications,” *Journal of Biomedical Materials Research Part B,* vol. 109, no. 9, pp. 1292–1302, 2021.

8. A. Griebel and N. Romick, “In vitro degradation of magnesium wire in sternal-closure-like conditions,” *Magnesium Technology,* 2023.
9. A. Griebel and J. Schaffer, “Magnesium-based absorbable alloys”. WO Patent 2020/247383 A1, 3 June 2019.
10. M. Bartnikowski, T. Dargaville, S. Ivanovski and D. Hutmacher, “Degradation mechanisms of polycaprolactone in the context of chemistry, geometry and environment,” *Progress in Polymer Science,* vol. 96, pp. 1–20, 2019.
11. W. Xu, N. Birbilis, G. Sha, Y. Wang, J. Daniels, Y. Xiao and M. Ferry, “A high-specific-strength and corrosion-resistant magnesium alloy,” *Nature Materials,* vol. 14, pp. 1229–1235, 2015.
12. L. Hanke, L. Jessen, F. Weisheit and e. al, “Structural characterisation and degradation of Mg-Li thin films for biodegradable implants,” *Scientific Reports,* vol. 13, 2023.
13. P. Bowen, J. Drelich and J. Goldman, “A new in vitro-in vivo correlation for bioabsorbable magnesium stents from mechanical behavior,” *Materials Science and Engineering Part C,* 2013.
14. P. Bowen, J. Drelich, R. Buxbaum, R. Rajachar and J. Goldman, “New approaches in evaluating metallic candidates for bioabsorbable stents,” *Emerging Materials Research,* vol. 1, no. EMR5, 2012.

Processing and Characterization of Mg Microtubes for Biodegradable Vascular Stents

Joung Sik Suh, Chang Dong Yim, Byeong-Chan Suh, Ha Sik Kim,
Sang Eun Lee, and Hwa-Chul Jung

Abstract

Magnesium (Mg) alloys have attracted increasing attention as potential metallic biomaterials for temporary biodegradable implants in orthopedic and vascular applications due to their mechanical, electrochemical, and biological properties. However, Mg scaffolds still face some challenges such as high degradation rate, low mechanical properties, difficult fabrication method. Processing and alloying are key approaches to improving the comprehensive properties of Mg alloys for biomedical applications. This study investigated the microstructure, texture and mechanical properties of Mg-Zn-Ca (MZ01) microtubes fabricated by two-step extrusion for biodegradable vascular stents. Direct two-step extrusion at 400 °C produced seamless MZ01 microtubes with outer diameters of 3.5 and 2.5 mm, wall thickness of 250 µm, and maximum length of 2 m. Dimensional accuracy based on roundness improved as outer diameter decreased. Increasing the extrusion ratio made grains refiner and weakened texture intensity. The mechanical behavior of MZ01 microtubes was analyzed with respect to changes in microstructure and texture. Grain boundary strengthening and texture hardening were involved in the plasticity of as-extruded MZ01 microtubes.

Keywords

Magnesium • Biomaterials • Process technology

Introduction

Cardiovascular disease (CVD) is the leading cause of death worldwide, and the number of deaths is expected to increase to 23.6 million by 2030, according to the World Health Organization (WHO) report [1]. Currently, more than three million angioplasty procedures, primarily stent implantation, are performed annually to reopen blocked arteries [2, 3]. Bare metal stents are widely used in the treatment of arterial diseases to physically open stenosed blood vessels. However, these stents are proven to cause a long-term risk of in-stent restenosis and thrombosis [4, 5]. To overcome these side effects, biodegradable stents have been proposed and received intensive attention over the past decade [6, 7]. Biodegradable Mg alloys are of increasing interest as potential metallic biomaterials for temporary implants in vascular and orthopedic applications due to their mechanical, electrochemical, and biological properties [8–10]. However, Mg scaffolds still face some challenges such as high degradation rate, low mechanical properties, difficult fabrication method. Plasticity is especially important for biodegradable vascular stents, which need to crimp on a balloon and then expand with large deformation during implantation [11]. However, Mg alloys exhibit poor formability at room temperature due to the hexagonal close-packed crystal structure. This poses a serious challenge for fabricating Mg microtubes with high plasticity for biodegradable stent applications [11]. Processing and alloying are key approaches to improving the comprehensive properties of Mg alloys for biomedical applications. For instance, Li et al. [11] reported that Mg-Nd-Zn-Zr microtubes with high plasticity were successfully fabricated by double extrusion with large plastic deformation due to enhanced activation of non-basal slips by significant grain refinement.

In the present study, we focus on manufacturing technology necessary to realize patient-customized ultra-precision shapes and secure required physical properties for biodegradable vascular stents. For this purpose, a

J. S. Suh (✉) · B.-C. Suh · H. S. Kim · S. E. Lee
Advanced Metals Division, Korea Institute of Materials Science, Changwon, 51508, Republic of Korea
e-mail: jssuh@kims.re.kr

C. D. Yim
Materials Digital Platform Division, Korea Institute of Materials Science, Changwon, 51508, Republic of Korea

H.-C. Jung
R&D, Innosys Co., Ltd., Uijeongbu, 11781, Republic of Korea

A. Leonard et al. (eds.), *Magnesium Technology 2024*, The Minerals, Metals & Materials Series,
https://doi.org/10.1007/978-3-031-50240-8_37

two-step extrusion manufacturing process was developed involving extruded rods, hollow billets, and extruded microtubes. Direct two-step extrusion is applied to Mg-Zn-Ca (MZ01) alloy, which consists only of biocompatible alloying elements excluding Al and rare earths. This study investigates the microstructure, texture and tensile properties of MZ01 microtubes in terms of extrusion ratio.

Materials and Methods

Figure 1 presents the manufacturing process of two-step extrusion involving as-extruded rod, hollow billet, and as-extruded microtubes. MZ01 alloys were supplied by Innosys Co., Ltd. (Korea) in the form of rods with a diameter of 15.9 mm. The as-extruded rods were further machined into hollow billets with a diameter of 13.9 mm, a height of 30 mm, and a central hole size of 3.1 mm. These hollow billets were heat-treated at 400 °C for 1 h. Finally, direct two-step extrusion successfully fabricated seamless MZ01 microtubes using a 500-ton horizontal extruder at 400 °C. The dimensions of the MZ01 microtubes were 3.5 and 2.5 mm in outer diameter (OD), 250 μm in wall thickness (WT), and 1.3 and 2 m in length. Hereinafter, MZ01 microtubes with OD of 3.5 and 2.5 mm are denoted as OD35 and OD25, respectively. The second extrusion ratio for OD35 and OD25 is about 57:1 and 82:1, respectively. That is, this indicates that manufacturing microtubes involves large plastic deformation.

Microstructures and textures of as-extruded rod and microtubes were characterized by optical microscopy (OM, OLYMPUS GX51) and electron backscatter diffraction (EBSD, JEOL JSM-7800F). EBSD measurements were implemented with a step size of 0.3 μm over an area of 180 $\mu m^2 \times 180\ \mu m^2$ at an accelerating voltage of 15 kV. EDAX OIM analysis™ v8.6 processed EBSD data with a confidence index of above 0.08. Tensile tests were carried out at room temperature with a quasi-static strain rate of $1 \times 10^{-3}\ s^{-1}$ using a universal testing machine (INSTRON 5982). Based on ASTM E8, tensile specimens with a gauge length of 25 mm were prepared from the as-extruded rod and microtubes. Testing was performed at least three times in the extrusion direction (ED) for each condition.

Results and Discussion

Figure 2 compares the dimensional accuracy of two geometries of MZ01 microtubes. The comparison results are detailed in Table 1. The cross section of OD35 and OD25 was measured and analyzed to determine how accurately it was implemented. In principle, all diameters and thicknesses should be measured along the circumference, but in practice, the outer diameter, inner diameter (ID), and wall thickness

Fig. 1 Two-step extrusion for manufacturing MZ01 microtubes

were measured at four points: north (N), south (S), east (E), and west (W), as shown in Fig. 2. Based on this, out-of-roundness for OD and ID is defined as $OD_R = (OD_{NS} - OD_{EW})/OD_{avg}$ and $ID_R = (ID_{NS} - ID_{EW})/ID_{avg}$, respectively, where $OD_{avg} = (OD_{NS} + OD_{EW})/2$ and $ID_{avg} = (ID_{NS} + ID_{EW})/2$. WT_{avg} is the average of the wall thickness at four points. As a result, for OD35, OD_R and ID_R were 1.13 and 1.05%, but for OD25, OD_R and ID_R were slightly improved to 0.81 and 0.94%. Furthermore, WT_{avg} for OD35 and OD25 was 250.0 ± 15.8 µm and 249.8 ± 10.6 µm, respectively. Therefore, it can be seen that as OD decreases, the dimensional accuracy improves. Nevertheless, the variation in wall thickness needs to be significantly reduced to make more precise. Moreover, it is required to check the dimensional uniformity in the longitudinal direction.

Figure 3 shows the microstructures of the as-extruded rod and microtubes of MZ01 alloy utilizing inverse pole figure maps from EBSD measurements. In the cross section perpendicular to the ED, the microstructure of MZ01 rod is twin-free, but has a bimodal structure consisting of dynamically recrystallized (DRXed) fine grains and non-DRXed coarse grains. Therefore, the average grain size (GS) is 10.5 ± 10.1 µm, which shows a very large deviation. On the other hand, the microstructures of OD35 and OD25 exhibit fully DRXed grains. As the extrusion ratio increases, GS of OD35 and OD25 decreases from 18.4 ± 6.8 to 14.3 ± 5.8 µm. Despite severe plastic deformation, the grains of MZ01 microtubes become larger compared to MZ01 rod. The (0001) pole figures indicate that as stress is applied to the microtube from both the left and right sides at the measurement region, the c-axis of each grain rotates left and right to distribute the basal plane. The maximum pole intensity (I_{max}) also depends on process conditions. The basal texture was strengthened from 8.0 to 10.2 multiple random distribution (m.r.d.) for OD35 and weakened to 7.5 m.r.d. for OD25. As a result, the weighted average Schmid factor for basal <a> slip is 0.163 for the rod, increases to 0.279 for OD35, and decreases again to 0.241 for OD25. In two-step extrusion, increasing the extrusion ratio results in finer grains and weaker texture intensity.

Figure 4 presents the tensile properties at room temperature in the as-extruded rod and microtubes of MZ01 alloy. The as-extruded rod has superior tensile properties compared to OD35 and OD25. For MZ01 rod, tensile yield strength (TYS) is 209 ± 14 MPa, ultimate tensile strength (UTS) is 252 ± 6 MPa, and fracture strain (FS) is 23.7 ± 3%. On the other hand, the tensile properties of MZ01 microtubes rather deteriorate after two-step extrusion. For OD35, TYS and UTS decreased to 58% and 87% of MZ01 rod, respectively. As the extrusion ratio increased, TYS increased from 121 ± 3 to 139 ± 1 MPa, UTS increased from 121 ± 3 to 139 ± 1 MPa and FS decreased from 21 ± 3 to 18 ± 2%. The outstanding mechanical properties of MZ01 rod are attributed to the combined effects of grain boundary strengthening by fine DRXed grains and strain hardening by severely deformed grains. The reason why the strength of MZ01 microtubes decreased compared to MZ01 rod was fundamentally due to the coarsening of the grain structures of OD35 and OD25. Moreover, this is related to the fact that the basal <a> slip was more activated based on the Schmid factor calculated above rather than the pole intensity. To determine the mechanism of these results, it is necessary to

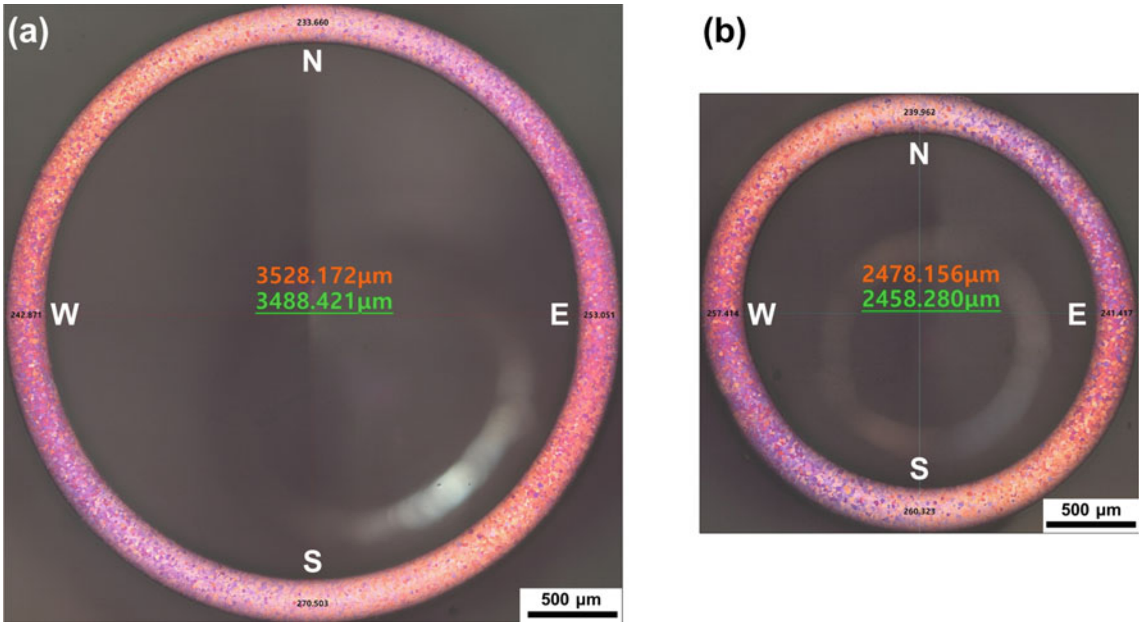

Fig. 2 Comparison of dimensional accuracy of MZ01 microtubes: **a** OD35 and **b** OD25

Table 1 Comparison of dimensional accuracy of MZ01 microtubes

In µm	OD_{NS}	OD_{WE}	OD_{R} (%)	ID_{NS}	ID_{WE}	ID_{R} (%)	WT_{avg}
OD35	3528	3488	1.13	3024	2992	1.05	250.0 ± 15.8
OD25	2478	2458	0.81	1978	1959	0.94	249.8 ± 10.6

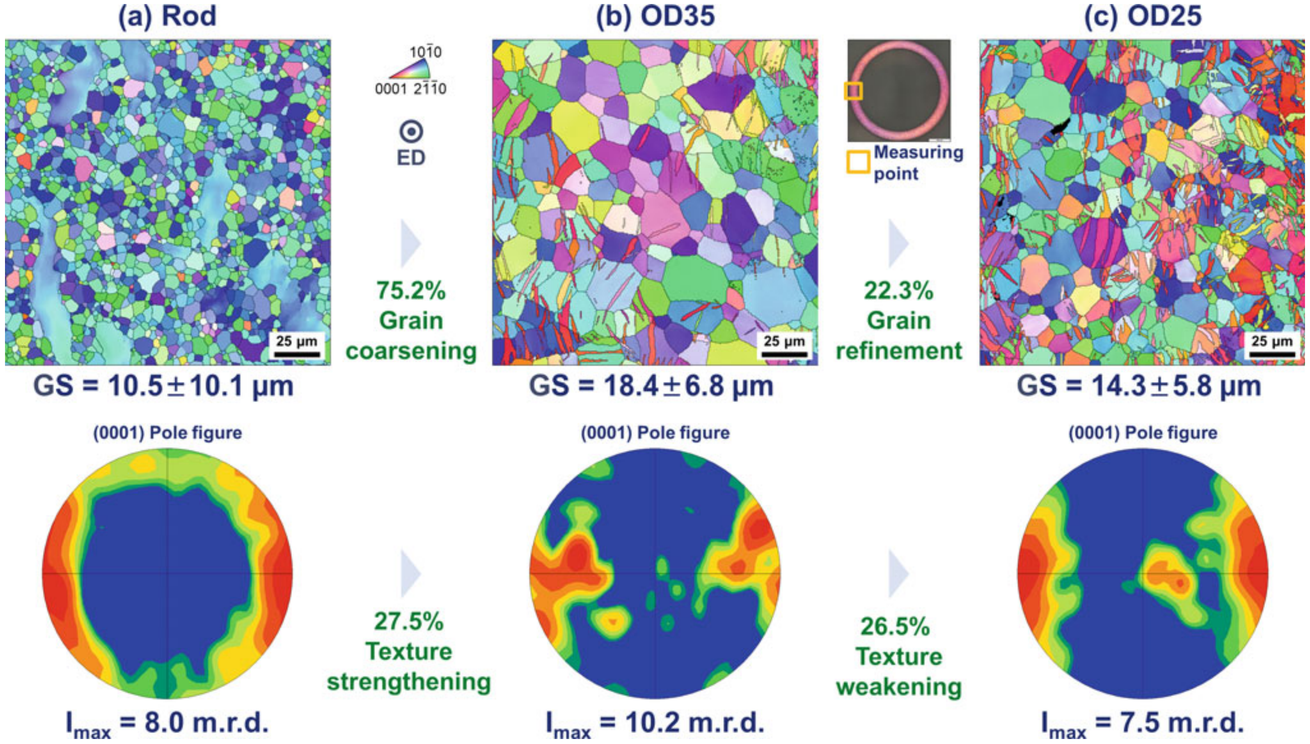

Fig. 3 Microstructure and texture of as-extruded rod and microtubes of MZ01 alloy: **a** rod, **b** OD35, and **c** OD25

further investigate the mechanical behavior in terms of microstructure, texture and reproducibility. Based on this, parametric studies on extrusion conditions, such as low extrusion temperature to induce grain refinement, should be conducted to improve the tensile properties of MZ01 microtubes.

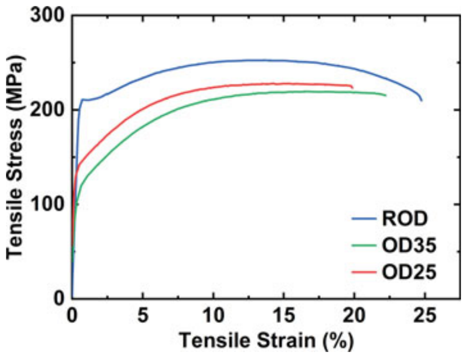

Fig. 4 Engineering stress–strain curves at room temperature of as-extruded rod and microtubes of MZ01 alloy

Conclusions and Outlook

The present study has performed direct two-step extrusion of Mg microtubes for biodegradable vascular stent applications. The effect of extrusion ratio on tensile properties at room temperature of the as-extruded MZ01 alloys was investigated in terms of microstructure and texture development. Direct two-step extrusion at 400 °C produced seamless MZ01 microtubes with outer diameters of 3.5 and 2.5 mm, wall thickness of 250 µm, and maximum length of 2 m. The second extrusion ratio for OD35 and OD25 is about 57:1 and 82:1, respectively. Dimensional accuracy based on roundness improved as outer diameter decreased. Increasing the extrusion ratio made grains refiner and weakened texture intensity. As the extrusion ratio increased, TYS increased from 121 ± 3 to 139 ± 1 MPa, UTS increased from 121 ± 3 to 139 ± 1 MPa and FS decreased from 21 ± 3 to 18 ± 2%. Grain boundary strengthening and the degree of the activation of basal <a> slip in the ED were involved in the plasticity of as-extruded MZ01 microtubes.

So far, we have focused on realizing the shape of Mg microtubes. Systematic study is currently underway to determine how much smaller and more precise it can be made through two-step extrusion. The variation in wall thickness must be significantly reduced to make more precise. Moreover, it is required to check the dimensional uniformity in the longitudinal direction. Above all, it is essential to investigate the mechanical behavior in detail in terms of microstructure, texture and reproducibility. Based on this, parametric studies on extrusion conditions, such as low extrusion temperature to induce grain refinement, should be conducted to improve the tensile properties of MZ01 microtubes.

Acknowledgements This research was supported by the Nano and Material Technology Development Program through the National Research Foundation of Korea (NRF) funded by Ministry of Science and ICT (2022M3H4A1A0408529).

References

1. Alfonso F, García J, Pérez-Vizcayno MJ, Hernando L, Hernandez R, Escaned J, Jiménez-Quevedo P, Bañuelos C, Macaya C (2009) New Stent Implantation for Recurrences After Stenting for In-Stent Restenosis: Implications of a Third Metal Layer in Human Coronary Arteries. J Am Coll Cardiol 54(8):1036–1038. https://doi.org/10.1016/j.jacc.2009.04.082
2. Van Beusekom HM, Serruys PW (2010) Drug-Eluting Stent Endothelium: Presence or Dysfunction. JACC Cardiovasc Interv 3 (1):76–77. https://doi.org/10.1016/j.jcin.2009.10.016.
3. Li S, Lei L, Hu Y, Zhang Y, Zhao S, Zhang J (2014) A fully coupled framework for in silico investigation of in-stent restenosis. Comput Methods Biomech Biomed Eng 22(2):217–228. https://doi.org/10.1080/10255842.2012.716830
4. Nordmann AJ, Briel M, Bucher HC (2006) Mortality in randomized controlled trials comparing drug-eluting vs. bare metal stents in coronary artery disease: a meta-analysis. Eur Heart J 27 (23):2784–2814. https://doi.org/10.1093/eurheartj/ehl282
5. Ota H, Mahmoudi M, Torguson R, Satler LF, Suddath WO, Pichard AD, Waksman R (2015) Safety and efficacy of everolimus-eluting stents for bare-metal in-stent restenosis. Cardiovasc Revasc Med 16(3):151–155. https://doi.org/10.1016/j.carrev.2015.02.005
6. Hermawan H, Dubé D, Mantovani D (2010) Developments in metallic biodegradable stents. Acta Biomater 6(5):1693–1697. https://doi.org/10.1016/j.actbio.2009.10.006
7. Witte F, Hort N, Vogt C, Cohen S, Kainer KU, Willumeit R, Feyerabend F (2008) Degradable biomaterials based on magnesium corrosion. Curr Opin Solid State Mater Sci 12(5–6):63–72. https://doi.org/10.1016/j.cossms.2009.04.001
8. Staiger MP, Pietak AM, Huadmai J, Dias G (2006) Magnesium and its alloys as orthopedic biomaterials: A review. Biomater 27 (9):1728–1734. https://doi.org/10.1016/j.biomaterials.2005.10.003
9. Xin Y, Hu T, Chu PK (2011) In vitro studies of biomedical magnesium alloys in a simulated physiological environment: A review. Acta Biomater 7(4):1452–1459. https://doi.org/10.1016/j.actbio.2010.12.004
10. Li D, Zhang D, Yuan Q, Liu L, Li H, Xiong L, Guo X, Yan Y, Yu K, Dai Y, Xiao T, Li Y, Wen C (2022) In vitro and in vivo assessment of the effect of biodegradable magnesium alloys on osteogenesis. Acta Biomater 141(15):454–465. https://doi.org/10.1016/j.actbio.2021.12.032
11. Lu W, Yue R, Miao H, Pei J, Huang H, Yuan G (2019) Enhanced plasticity of magnesium alloy micro-tubes for vascular stents by double extrusion with large plastic deformation. Mater Lett 245 (15):155–157. https://doi.org/10.1016/j.matlet.2019.02.114

Severe Plastically Deformed Mg–Zn–Zr–RE Alloy Developed as a Biomaterial

Vasanth C. Shunmugasamy and Bilal Mansoor

Abstract

Mg alloys have high corrosion rate that inhibits their application as biomaterial. For safe use as biomaterial, it is essential to control their corrosion rates. In Mg alloys, microgalvanic coupling between the α-Mg matrix and secondary precipitates can exist which results in increased corrosion rate. To address this challenge, we engineered the microstructure of a biodegradable Mg–Zn–RE–Zr alloy by severe plastic deformation process such as friction stir processing (FSP), improving its corrosion resistance and mechanical properties simultaneously. Subjecting the alloy to FSP resulted in refined grains, basal texture and broken and uniformly distributed secondary precipitates. In vitro corrosion of base material showed microgalvanic coupling between precipitate and matrix, resulting in unstable surface layer. The processed alloy showed uniform corrosion owing to formation of stable surface film formation, due to the refined grains, texture, and distribution of precipitates. The results show promising potential of Mg alloy as biomaterial.

Keywords

Microstructure • Friction stir processing • Microgalvanic corrosion

Introduction

Magnesium alloys containing biocompatible components show tremendous promise for applications as temporary biomedical devices. Mg-based alloys have been found to possess optimized properties for biodegradable material based on the following properties: (i) Mg is an essential nutrient in human body, naturally found in bone and act as simulator for new bone formation, also act as cofactor for many enzymes and the daily intake can be much higher compared to Fe or Zn metals [1–5], (ii) although excess intake of Mg can cause severe complications [6], it can be efficiently excreted [6, 7], and (iii) the stiffness of Mg is closest to that of bones which can help prevent stress-shielding [4, 5, 8].

Mg alloys have relatively higher corrosion rate that can impede their applications as biomedical devices. Mg has a low electrode potential of − 2.372 V [9] against normal hydrogen electrode, making it extremely active in aqueous media containing chloride ions, such as human body physiological condition. Mg corrodes in aqueous medium by anodic dissolution and cathodic reduction of Mg metal, with formation of $Mg(OH)_2$ and hydrogen gas [10]. The $Mg(OH)_2$ can offer a protective layer during corrosion through formation of surface film [11]. However, Mg also exhibits negative difference effect (NDE) during corrosion where in the curious effect of hydrogen evolution and magnesium corrosion rate increases with increasing potential [12, 13], leading to loss of protective film. The rapid corrosion can result in early loss of mechanical integrity of the implant before bone healing and hydrogen gas accumulation that can result in subcutaneous swelling [14, 15].

Several methods have been proposed in existing literature, to achieve an optimal biodegradable Mg-based alloy, such as grain refinement, alloying additions and coatings to improve its mechanical and corrosion properties [4]. Among the different alloying elements, elements such as Zn, Zr, and RE have shown to influence both mechanical and corrosion

V. C. Shunmugasamy (✉) · B. Mansoor
Mechanical Engineering Program, Texas A&M University at Qatar, Doha, Qatar
e-mail: vasanth.shunmugasamy@qatar.tamu.edu

B. Mansoor
e-mail: bilal.mansoor@qatar.tamu.edu

B. Mansoor
Department of Materials Science and Engineering, Texas A&M University, College Station, TX, USA

A. Leonard et al. (eds.), *Magnesium Technology 2024*, The Minerals, Metals & Materials Series,
https://doi.org/10.1007/978-3-031-50240-8_38

properties of Mg alloys [4, 10, 16]. Mg-Zn and Mg-RE alloys systems have shown to possess the highest mechanical properties (strength and ductility) [4, 17]. In the present work, Mg–Zn–Zr–RE alloy is utilized and is characterized for its corrosion and mechanical properties to be developed as a biomaterial.

In Mg alloys, a microgalvanic coupling between the α-Mg matrix and secondary precipitates can exist which results in increased corrosion rate [18]. The microstructure of Mg–Zn–RE–Zr alloy comprises RE $(Mg, Zn)_{11}$ T-phase precipitates along the grain boundaries and Zr-rich regions in the α-Mg grains [18, 19]. The presence of T-phase precipitates has been observed thorough X-ray diffraction analysis of the alloy [20]. In Mg–Zn–Zr–RE alloy, it was observed that the corrosion attack upon exposure to Hanks Balanced Salt Solution (HBSS) was intergranular due to the microgalvanic coupling between the T-phase precipitate and matrix, leading to dissolution of α-Mg around the precipitates resulting on loss of precipitates [21]. To address this challenge, we engineered the microstructure of a biodegradable Mg–Zn–RE–Zr alloy by severe plastic deformation process such as friction stir processing (FSP), improving its corrosion resistance and mechanical properties simultaneously.

Materials and Methods

3 mm thick cast Mg–Zn–Zr–RE alloy EZ33 was utilized in present work, and alloy composition is given in Table 1. The alloy was subjected to friction stir processing using an FSP setup (CFSWT, Beijing) having a tool with 12 mm shoulder diameter, 2.8 mm long conical pin (major dimeter—5 mm and minor diameter—3 mm). FSP was carried out using process parameters of tool rotational speed of 1500 rpm, translation speed of 20 mm/min and tool tilt angle of 2°. The alloy microstructure pre- and post-processing was revealed by etching with acetic picral solution [19, 22].

The alloy was characterized for in vitro corrosion characterization by immersion testing of base material and FSP stir zone (SZ) to Hanks Balanced Salt Solution (HBSS) at 37 ± 1 °C, to mimic human body conditions. Samples were removed at different time intervals, washed with distilled water, air-dried, and weighed. The calculated corrosion in mm/yr is given by NACE/ASTM G31-12a [24].

$$\text{Corrosion rate} = \frac{8760 \times \text{mass loss (g)}}{\text{Exposed area}\,(\text{mm}^2) \times \text{time (h)} \times \text{density}\,(\text{g/mm}^3)} \quad (1)$$

The base material (BM) and SZ specimens were evaluated for Vickers microhardness (Future Tech FM-310, Japan) using 100 gf load and a dwell time of 15 s, and at least 10 reading were carried out. Tensile testing was carried out using electromechanical MTS Insight 30 kN load tensile tester at ambient temperature with an initial strain rate of 10^{-3}/s. The tensile specimen had a nominal cross-sectional area of 3 mm^2 × 3 mm^2 and a gauge length of 12 mm. Two repetitions were carried out for tensile, and the microstructure of the alloy was observed using optical (OM, Zeiss Axiovert 40 Mat, Pleasanton, CA) and scanning electron microscope (SEM, Thermo Fisher Apreo Model).

Results and Discussion

The microstructure of Mg–Zn–RE–Zr alloy comprises RE $(Mg, Zn)_{11}$ T-phase precipitates along the grain boundaries and Zr-rich regions in the α-Mg grains [18, 19], as shown in Fig. 1a. The FS processed alloy resulted in refined grains (91% reduction in grain size compared to base material) and broken and relatively uniform distributed secondary precipitates as can be observed in Fig. 1b.

Texture analysis of the FS processed alloy showed strong basal texture compared to random texture observed in starting base material. Studies in existing literature have shown basal texture in Mg alloys, which shows improved corrosion resistance compared to non-basal textures [25–29]. The presence of refined grains, basal texture, and broken and uniformly distributed secondary precipitates due to subjecting the alloy to FSP can influence the alloy mechanical and corrosion response. Mechanical properties evaluated using Vickers microhardness and room temperature tensile testing on the processed alloy and compared with BM. The BM and FSP stir zone showed microhardness of 53.3 ± 3.8 HV and 59.5 ± 2.5 HV, respectively. The refined grains and broken-down precipitates resulted in 10.5% increase in microhardness of the FSPed SZ, compared to BM. Under tensile testing the FSPed material showed similar ultimate tensile strength (~175 MPa) to base material, while the ductility was increased by 85% (failure strain of 5.3% for BM and 9.9% for SZ) (Fig. 2).

Table 1 Chemical composition of EZ33A Mg alloy utilized in present work [23]

Element	Zn	Zr	Ce	La	Nd	Mn	Fe	Cr	Mg
Wt%	2.66	1.32	1.16	0.47	0.26	0.01	< 0.01	< 0.01	Balance

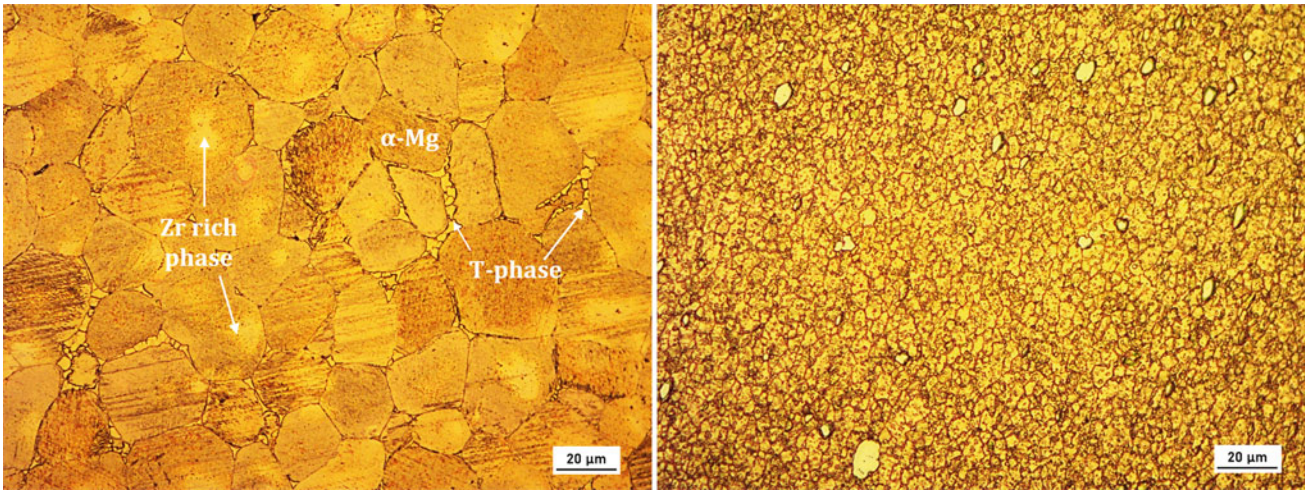

Fig. 1 Microstructure of EZ33 Mg alloy **a** base material and **b** stir zone post FSP

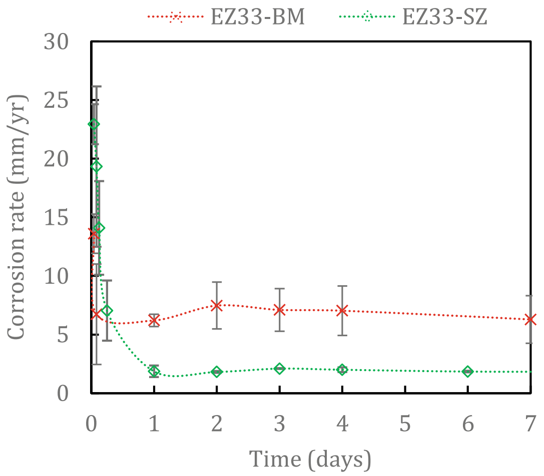

Fig. 2 Variation of in vitro corrosion rate of EZ33-BM and FSP stir zone material with respect to time immersed in HBSS

In vitro corrosion of the base material in HBSS showed, increasing OCP followed by plateau indicating of unstable passive layer formation. Microgalvanic coupling between the T-phase precipitate and α-Mg was observed as shown in Fig. 3a, resulting in trenching of the precipitates leading to unstable passive layer formation. In vitro corrosion of the FS processed alloy in HBSS showed stable OCP indicative of stable surface film formation. The FSPed alloy surface showed more uniform corrosion surface post exposure to HBSS corrosion medium (Fig. 3b).

Corrosion rate measured using weight loss method showed 0.35 ± 0.02 mm/yr for FSPed condition in comparison with 4.73 ± 1.27 mm/yr observed for base material. The refined grains, texture and breaking and uniform distribution of the precipitates resulted in more uniform corrosion in the FS processed Mg alloy compared to base material. The results from the present research show promising potential of Mg–Zn–Zr–RE alloy as biomaterial and will have profound benefit for utilization as biodegradable medical devices such as plates, screws, and stents.

Conclusions

Friction stir processing of Mg–Zn–Zr–RE alloy EZ33 resulted in refined grains, basal texture and breaking and relatively uniform distribution of secondary precipitates. These resulted in increase in mechanical properties (microhardness and ductility). The combination of broken, uniformly distributed precipitates, refined grains, and favorable texture resulted in reduced microgalvanic coupling leading to more uniform corrosion and reduced corrosion rate.

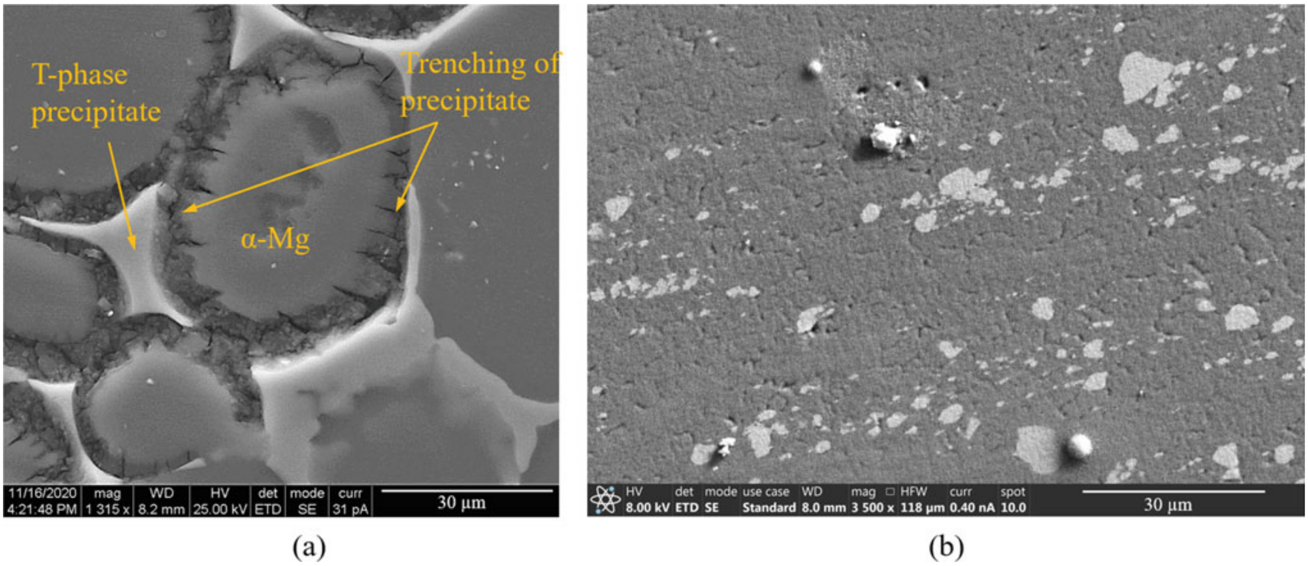

Fig. 3 Surface of **a** Mg–Zn–Zr–RE alloy base material showing microgalvanic coupling and **b** FSPed alloy surface showing relatively uniform corrosion, post exposure to HBSS medium

Acknowledgements This publication was made possible by the grant NPRP No.: 8-856-2-364 from the Qatar National Research Fund (a member of The Qatar Foundation). The statements made herein are solely the responsibility of the authors.

References

1. F. Witte, J. Fischer, J. Nellesen, H.A. Crostack, V. Kaese, A. Pisch, F. Beckmann, H. Windhagen, In vitro and in vivo corrosion measurements of magnesium alloys, Biomaterials. 27 (2006) 1013–1018. https://doi.org/10.1016/j.biomaterials.2005.07.037.
2. P. Trumbo, S. Schlicker, A.A. Yates, M. Poos, Dietary reference intakes for energy, carbohydrate, fiber, fat, fatty acids, cholesterol, protein and amino acids, J. Am. Diet. Assoc. 102 (2002) 1621–1630. https://doi.org/10.1016/S0002-8223(02)90346-9.
3. A. Hartwig, Role of magnesium in genomic stability, Mutat. Res. Mol. Mech. Mutagen. 475 (2001) 113–121. https://doi.org/10.1016/S0027-5107(01)00074-4.
4. Y. Chen, Z. Xu, C. Smith, J. Sankar, Recent advances on the development of magnesium alloys for biodegradable implants, Acta Biomater. 10 (2014) 4561–4573. https://doi.org/10.1016/j.actbio.2014.07.005.
5. M.P. Staiger, A.M. Pietak, J. Huadmai, G. Dias, Magnesium and its alloys as orthopedic biomaterials: A review, Biomaterials. 27 (2006) 1728–1734. https://doi.org/10.1016/j.biomaterials.2005.10.003.
6. N.-E.L. Saris, E. Mervaala, H. Karppanen, J.A. Khawaja, A. Lewenstam, Magnesium: An update on physiological, clinical and analytical aspects, Clin. Chim. Acta. 294 (2000) 1–26. https://doi.org/10.1016/S0009-8981(99)00258-2.
7. J. Vormann, Magnesium: nutrition and metabolism, Mol. Aspects Med. 24 (2003) 27–37. https://doi.org/10.1016/S0098-2997(02)00089-4.
8. K.F. Farraro, K.E. Kim, S.L.-Y. Woo, J.R. Flowers, M.B. McCullough, Revolutionizing orthopaedic biomaterials: The potential of biodegradable and bioresorbable magnesium-based materials for functional tissue engineering, J. Biomech. 47 (2014) 1979–1986. https://doi.org/10.1016/j.jbiomech.2013.12.003.
9. T. Ren, X. Gao, C. Xu, L. Yang, P. Guo, H. Liu, Y. Chen, W. Sun, Z. Song, Evaluation of as-extruded ternary Zn–Mg–Zr alloys for biomedical implantation material: In vitro and in vivo behavior, Mater. Corros. 70 (2019) 1056–1070. https://doi.org/10.1002/maco.201810648.
10. G.L. Song, A. Atrens, Corrosion mechanisms of magnesium alloys, Adv. Eng. Mater. 1 (1999) 11–33.
11. M. Pourbaix, Atlas of electrochemical equilibria in aqueous solutions - Translated from the French by JAMES A. FRANKLIN (except Sections I, III 5 and III 6, which were originally written in English), Second Edi, Houston, TX, 1974.
12. T.R. Thomaz, C.R. Weber, T. Pelegrini, L.F.P. Dick, G. Knörnschild, The negative difference effect of magnesium and of the AZ91 alloy in chloride and stannate-containing solutions, Corros. Sci. 52 (2010) 2235–2243. https://doi.org/10.1016/j.corsci.2010.03.010.
13. S. Bender, J. Goellner, A. Heyn, S. Schmigalla, A new theory for the negative difference effect in magnesium corrosion, Mater. Corros. 63 (2012) 707–712. https://doi.org/10.1002/maco.201106225.
14. S.S. Patil, R.D.K. Misra, M. Gao, Z. Ma, L. Tan, K. Yang, Bioactive coating on a new Mg-2Zn-0.5Nd alloy: modulation of degradation rate and cellular response, Mater. Technol. 34 (2019) 394–402. https://doi.org/10.1080/10667857.2019.1574956.
15. Y. Yang, C. He, Dianyu E, W. Yang, F. Qi, D. Xie, L. Shen, S. Peng, C. Shuai, Mg bone implant: Features, developments and perspectives, Mater. Des. 185 (2020) 108259. https://doi.org/10.1016/j.matdes.2019.108259.
16. Y. Ding, C. Wen, P. Hodgson, Y. Li, Effects of alloying elements on the corrosion behavior and biocompatibility of biodegradable magnesium alloys: a review, J. Mater. Chem. B. 2 (2014) 1912–1933. https://doi.org/10.1039/C3TB21746A.
17. S. Tekumalla, S. Seetharaman, A. Almajid, M. Gupta, H.F. Lopez, Mechanical Properties of Magnesium-Rare Earth Alloy Systems: A Review, Metals (Basel). 5 (2015) 1–39. https://doi.org/10.3390/met5010001.

18. W.C. Neil, M. Forsyth, P.C. Howlett, C.R. Hutchinson, B.R.W. Hinton, Corrosion of magnesium alloy ZE41 - The role of microstructural features, Corros. Sci. 51 (2009) 387–394. https://doi.org/10.1016/j.corsci.2008.11.005.
19. A. Marwa, C.A. Usman, V.C. Shunmugasamy, I. Karaman, B. Mansoor, Corrosion behavior of Mg-Zn-Zr-RE alloys under physiological environment – impact on mechanical integrity and biocompatibility, J. Magnes. Alloy. 10 (2022) 1542–1572.
20. V.C. Shunmugasamy, M. AbdelGawad, M.U. Sohail, T. Ibrahim, T. Khan, T.D. Seers, B. Mansoor, In vitro and in vivo study on fine-grained Mg–Zn–RE–Zr alloy as a biodegradeable orthopedic implant produced by friction stir processing, Bioact. Mater. 28 (2023) 448–466. https://doi.org/10.1016/j.bioactmat.2023.06.010.
21. A. Marwa, U. Ali, B. Mansoor, I. Karaman, In vitro corrosion and mechanical integrity of two different rare earth metals containing magnesium alloys, To Be Submitt. (2020).
22. A. Dorbane, B. Mansoor, G. Ayoub, V.C. Shunmugasamy, A. Imad, Mechanical, microstructural and fracture properties of dissimilar welds produced by friction stir welding of AZ31B and Al6061, Mater. Sci. Eng. A. 651 (2016) 720–733.
23. M. AbdelGawad, A.U. Chaudhry, B. Mansoor, The influence of temperature and medium on corrosion response of ZE41 and EZ33, in: V. V Joshi, J.B. Jordon, D. Orlov, N.R. Neelameggham (Eds.), Magnes. Technol. 2019, TMS - Miner. Met. Mater. Ser., Springer International Publishing, Cham, 2019: pp. 159–167.
24. NACE/ASTM G31-12a: Standard guide for laboratory immersion corrosion testing of metals, West Conshohocken, PA; ASTM International, 2012. https://doi.org/10.1520/NACEASTMG0031-12A, (n.d.).
25. Y. Luo, Y. Deng, L. Guan, L. Ye, X. Guo, A. Luo, Effect of grain size and crystal orientation on the corrosion behavior of as-extruded Mg-6Gd-2Y-0.2Zr alloy, Corros. Sci. 164 (2020) 108338. https://doi.org/10.1016/j.corsci.2019.108338.
26. S. Pawar, T.J.A. Slater, T.L. Burnett, X. Zhou, G.M. Scamans, Z. Fan, G.E. Thompson, P.J. Withers, Crystallographic effects on the corrosion of twin roll cast AZ31 Mg alloy sheet, Acta Mater. 133 (2017) 90–99. https://doi.org/10.1016/j.actamat.2017.05.027.
27. A. Atrens, G.-L. Song, M. Liu, Z. Shi, F. Cao, M.S. Dargusch, Review of recent developments in the field of magnesium corrosion, Adv. Eng. Mater. 17 (2015) 400–453. https://doi.org/10.1002/adem.201400434.
28. R. Xin, Y. Luo, A. Zuo, J. Gao, Q. Liu, Texture effect on corrosion behavior of AZ31 Mg alloy in simulated physiological environment, Mater. Lett. 72 (2012) 1–4. https://doi.org/10.1016/j.matlet.2011.11.032.
29. K. Hagihara, M. Okubo, M. Yamasaki, T. Nakano, Crystal-orientation-dependent corrosion behaviour of single crystals of a pure Mg and Mg-Al and Mg-Cu solid solutions, Corros. Sci. 109 (2016) 68–85. https://doi.org/10.1016/j.corsci.2016.03.019.

The Effect of Powder Size and Morphology on the Sinterability of Bioresorbable Mg-Sr/Ca Alloys

Ava Azadi, Eoin D. O'Cearbhaill, and Mert Celikin

Abstract

Possessing outstanding biocompatibility and bioresorbability, magnesium (Mg) alloys with strontium (Sr) and calcium (Ca) additions have shown potential to be used as temporary implants in orthopaedic applications. Having a low elastic modulus (45 GPa) close to the human bone lowers the stress shielding effects. Low temperature additive manufacturing (AM) techniques (e.g., Fused Deposition Modelling) have potential to be used for the fabrication of complex Mg components while avoiding safety concerns associated with high temperature AM. However, low sinterability of common Mg alloys is the main limiting factor. The objective of this work is to investigate the effect of powder particle size/morphology on the sinterability of Mg-Ca/Sr-based alloys produced via powder metallurgy. Laser diffraction and Scanning Electron Microscopy (SEM) were used to characterize particle size and morphology. The study also focused on assessing the role of liquid phase sintering (LPS) mechanism by thermodynamic calculations and microstructural characterisation (SEM). Porosity measurements using density analysis and image processing were employed to determine the effects of powder size and morphology on sinterability of the alloys. It was found that the non-homogeneous particle size distribution with more spherical powder particles, facilitated the compaction and accordingly higher densification was obtained. This was achieved for powders milled at higher speeds (900 rpm), resulting in significantly lower porosity levels (~ 6–8%) compared to the dry-milled state (~ 40–60%).

Keywords

Magnesium (Mg) alloys • Alloy design • Thermodynamic calculations • Materials characterisation • Sintering

Introduction

Magnesium (Mg) and its alloys have been receiving increased attention as emerging class of biomedical alloys due to their bioresorbability and biocompatibility [1, 2]. As temporary implants, they have proven high potentials in orthopaedic and cardiovascular applications, eliminating the need for the secondary surgical operations commonly conducted for conventional non-resorbable implants [3, 4]. Furthermore, the use of bioresorbable Mg implants decreases the risk of stress shielding effects thanks to the relatively low elastic modulus of Mg alloys (45 GPa) that is comparable to the human bone (1–30 GPa) [3–7]. However, current manufacturing processes have limitations for the customisation of Mg-based implants based on patients' requirements [8, 9].

Additive manufacturing (AM) of Mg-based alloys enables fast production of personalised implants with intricate designs, expanding the potential of Mg-based alloys for biomedical applications [10–12]. High temperature AM techniques such as laser powder bed fusion (LPBF) have been commonly used for Mg AM [13, 14]. However, safety concerns typically arise during the processing of Mg-based alloys via high temperature AM methods due to the inherent limitations of Mg, including low boiling temperature and high vapor pressure [15, 16]. Additionally, the chemical composition of the Mg-based alloys might undergo changes due to the temperature evolution exceeding the evaporation point of Mg [17, 18]. Hence, low temperature AM techniques such as fused filament fabrication (FFF) and binder jetting (BJ) are more compatible with the intrinsic properties of Mg-based alloys. However, one of the main challenges of

---

A. Azadi (✉) · E. D. O'Cearbhaill · M. Celikin
School of Mechanical and Materials Engineering,
University College Dublin, Dublin, Ireland
e-mail: ava.azadichegeni@ucdconnect.ie

A. Leonard et al. (eds.), *Magnesium Technology 2024*, The Minerals, Metals & Materials Series,
https://doi.org/10.1007/978-3-031-50240-8_39

low temperature Mg alloy AM is the low sinterability of the current Mg-based alloys, restricting the printability of Mg using FFF and BJ techniques [19–21]. Since Mg powder has high affinity for oxygen and upon exposure to air a stable oxide layer (i.e., MgO) is formed on the powder surface which has no solubility in solid Mg, acting as diffusion barrier during sintering [21, 22]. Therefore, liquid phase sintering (LPS) can be employed to improve Mg sinterability as the capillary force of the liquid phase causes the powder particles to come together. However, sintering of Mg is still challenging [23–25].

The aim of this study is to enhance the sinterability of Mg-Sr/Ca-based alloys by understanding the effect of powder size distribution and morphology. The study will focus on optimising liquid phase sintering (LPS) mechanism supported by thermodynamic calculations.

Experimental Procedure

Two binary alloys with nominal compositions of Mg-20Ca and Mg-20Sr (in weight %) were studied using the commercial master alloys supplied by Shanghai Xinglu Chemical Tech. China Company. Inductively coupled plasma (ICP) analysis was used to determine the chemical compositions of the cast ingots (Table 1). Therefore, the actual compositions are Mg-18.2Ca and Mg-20.9Sr.

The commercial ingots were dry milled in order to fabricate the starting material in the form of powder particles using slow speed Emill milling machine with following parameters: depth of cut 1mm, length of travel 200 mm per minute, without lubricant. Afterwards, the dry-milled particles were ball milled in a vertical lab planetary ball milling equipment (DECO-PBM-V-0.4L) using stainless steel jars and 10 mm balls under argon (Ar) gas. The ball milling variables are duration, ball-to-powder ratio (BPR), and speed, and accordingly 3 conditions were defined per composition, duration effect, BPR effect, and speed effect, respectively (Table 2).

To investigate the effect of ball milling variables on sinterability of the alloys, the powder size distribution and morphology of each ball milling condition was evaluated using Microtrac MRB TurboSync particle analyser laser diffractometer. Approximately, 2 g of ball-milled powders were used to fabricate discs of Mg-18.2Ca and Mg-20.9Sr compositions in a circular die with a diameter of 25 mm, using cold pressing setup (PA 260, Josef Lucas LTD Birmingham) under applied pressure of 60 bar and dwell time of 2.5 min. In order to determine the appropriate temperature range for sintering in terms of liquid phase fraction, thermodynamic calculations were performed on both compositions using ThermoCalc software package (TCMG6 Mg Alloys v6.3 database). In addition, differential scanning calorimetry (DSC) was conducted on Mg-18.2Ca and Mg-20.9Sr ball-milled powders using STA 1500 Rheometric Scientific equipment with the following profile: heating at 5 °C/min from ambient temperature to 700 °C under Ar gas. Sintering was performed on discs of Mg-18.2Ca and Mg-20.9Sr in a tube furnace (Lenton Tube Furnace 1600) in a controlled atmosphere of Ar from room temperature (RT) with heating rate of 5–575 °C/min, dwell time of 2 h and subsequent furnace cooling to the ambient temperature. Cross sections of sintered discs were cut and metallographically prepared following the standard procedure down to 1 µm diamond paste polishing step, and along with the ball-milled powders of both compositions were examined under scanning electron microscope (SEM) using TM4000Plus Tabletop Hitachi, Japan setup. To measure the densification of the sintered parts, image analysis was employed using MATLAB software package. In addition, density measurements were conducted based on Archimedes principle in ethanol medium.

Table 1 ICP analysis of alloy compositions, (wt%)

Alloy	Sr	Ca	Mg
Mg-20Ca	0.01	18.24	bal
Mg-20Sr	20.91	0.01	bal

Table 2 Ball milling parameters and conditions

BPR	Speed (rpm)	Time (h)	Condition
10:1	650	1	Duration effect
		4	
14:1	650	1	BPR effect
		4	
10:1	900	1	Speed effect
		4	

Results and Discussion

Powder Fabrication and Characterisation

SEM micrographs of the dry-milled Mg-18.2Ca and Mg-20.9Sr particles are shown in Fig. 1. Dry milling of cast ingots was the initial step of powder fabrication for both compositions. It is observed that the dry-milled particles exhibit sharp edges with irregular morphologies varying from µm to mm ranges in size. For more accurate analysis, size distribution of the dry-milled particles was studied, and D10, D50, and D90 values of the dry-milled particles are reported in Table 3, where Dx is defined as the size of X% of the particles being below a measured quantity. Both compositions have almost the same D50 value (50% of the

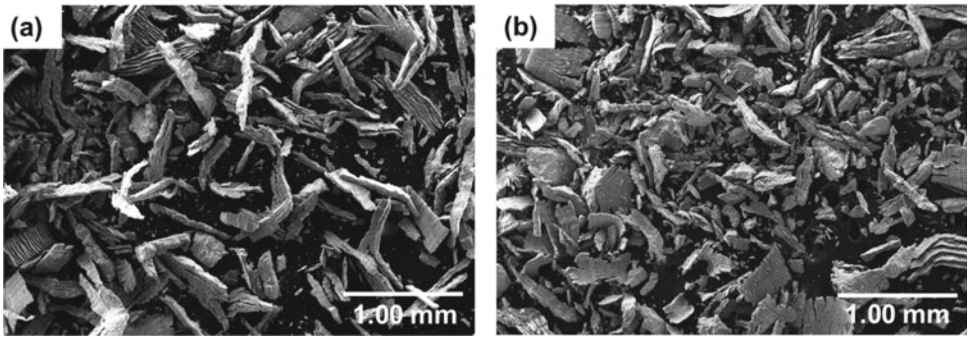

Fig. 1 SEM micrographs of dry-milled particles of **a** Mg-18.2Ca and **b** Mg-20.9Sr alloys showing the initial state of the produced particles

Table 3 Laser diffraction (LD) results representing the size distribution of dry-milled particles

Composition	D10	D50	D90
Mg-20.9Sr	44.39	366.5	1120
Mg-18.2Ca	116.9	367	672.2

particles have a particle size equal to or smaller than ~ 367 µm). However, particle size variation is more conspicuous for Mg-20.9Sr alloy with D10 of 44.39 µm and D90 of 1120 µm.

Figures 2 and 3 represent the SEM micrographs of dry-milled particles of Mg-18.2Ca and Mg-20.9Sr, respectively, after 1 and 4 h of ball-milling. It can be seen that after 1 h ball milling, the large, dry-milled particles (Fig. 1) of all conditions significantly reduced in size. Moreover, regardless of the conditions, the longer ball milling duration (i.e., 4 h) resulted in the finer particles for both compositions. Starting with Mg-18.2Ca composition, after 1 h of ball milling, it is determined that the speed increase (i.e., from 650 to 900 rpm) led to finer particles compared to the results of Duration and BPR Effects. Even after further 3 h of ball milling, the particles produced at higher speeds (900 rpm) became finer than those produced by Duration and BPR Effects. Furthermore, it can be asserted that the results of Duration and BPR variables are comparable. Similar trend can be observed for Mg-20.9Sr composition in terms of Duration and BPR Effects. However, it seems that the speed increase led to the agglomeration of the particles in Mg-20.9Sr composition; after 1 h ball milling the largest particles are correspond to the Speed Effect among all 3 conditions.

Size distribution of ball-milled Mg-18.2Ca and Mg-20.9Sr powder particles is summarised in Table 4. Generally, the quantitative size distribution values are in good agreement with the SEM micrographs for both compositions, confirming that the size of powders produced by BPR and Duration Effects are comparable, and there is not a remarkable difference between the resultant values. However, D10 and D50 values of Mg-20.9Sr powder particles are smaller than those of Mg-18.2Ca, considering the Duration and BPR Effects, whileD90 values of Mg-20.9Sr are larger than those of Mg-18.2Ca. Mg-20.9Sr powder particles have a bimodal size distribution which might be due to the agglomeration of the particles during ball milling or due to the higher oxygen content during powder processing. In addition, the laser diffraction technique is sensitive to outlier particles and the possible inclusion of a few large particles (as particles were not sieved before ball milling) affect D90 values.

Morphological transformation can be readily perceived comparing the SEM micrographs in Figs. 1, 2, and 3. The sharp-edged particles of both compositions became more spherical after 1 and 4 h of ball milling. Sphericity is a measure of the degree to which a particle approximates the shape of a perfect sphere, and it has a value of 1 representing a perfect sphere and 0 representing a totally non-spherical particle [26]. The sphericity indices (SI) of dry-milled and ball-milled particles are shown in Fig. 4. The mean SI of dry-milled particles is 0.522 and 0.504, corresponding to Mg-18.2Ca and Mg-20.9Sr, respectively. After ball milling, the average SI increased to 0.88 for both compositions, implying that the ball-milled particles became closer to the morphology of a sphere.

Sinterability Evaluation

Liquid phase fraction diagrams of Mg-Ca and Mg-Sr systems are illustrated in Fig. 5. The theoretical liquidus and solidus temperatures of Mg-Ca system are 572.3 °C and 518.27 °C, respectively, and 593.17 °C and 588.25 °C, respectively for Mg-Sr system. It can be seen that Mg-Sr system has a relatively narrower solidification temperature range compared to Mg-18.2Ca. The liquid phase volume fraction was calculated for both compositions. Theoretically, it can be seen that at 570 °C, Mg-18.2Ca system is approximately in fully liquid state while no liquid is expected in Mg-20.9Sr system.

DSC curves of Mg-18.2Ca and Mg-20.9Sr alloys are presented in Fig. 6. In Mg-18.2Ca system, there is an

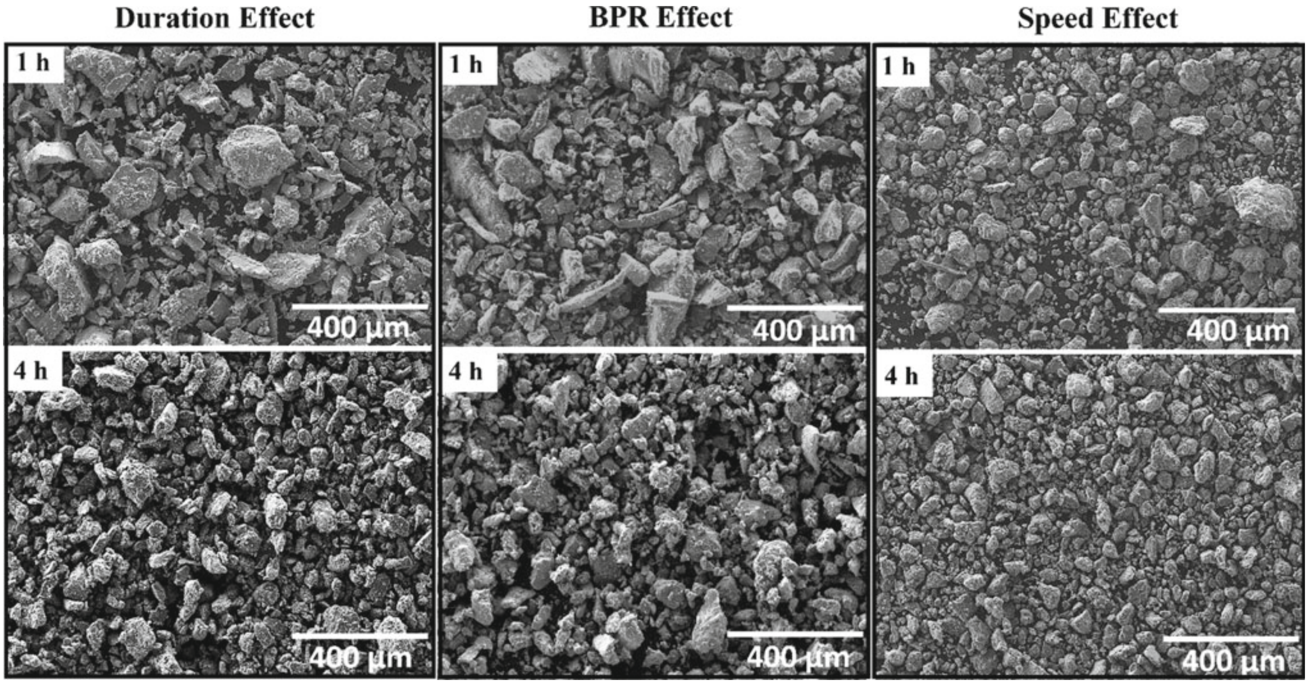

Fig. 2 SEM micrographs of Mg-18.2Ca after ball milling

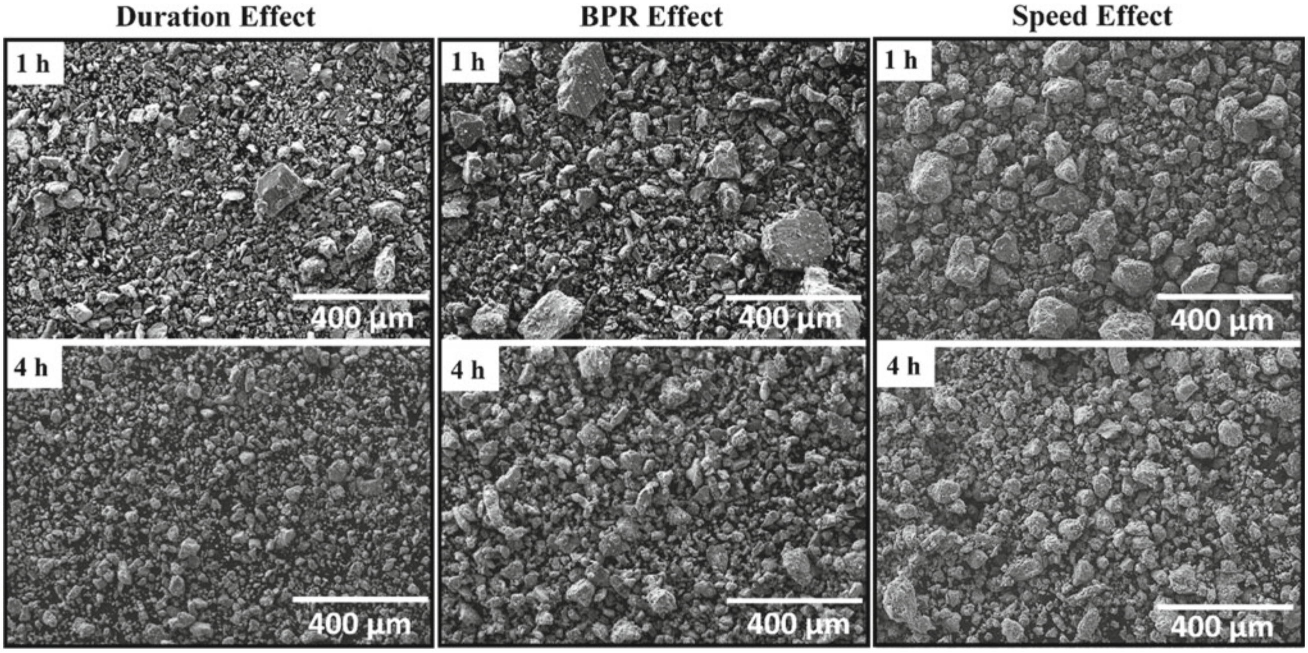

Fig. 3 SEM micrographs of Mg-20.9Sr after ball milling

endothermic peak in the temperature interval of 464–544 °C, with a minimum of 520.24 °C. The peak onset which represents the solidus, occurs at 464.17 °C, and the endset temperature representing the liquidus, occurs at 544.55 °C. In addition, in Mg-20.9Sr system, the endothermic peak appears in temperature interval of 556–590 °C, with a minimum at 582.55 °C. Therefore, the solidus of this system is determined as 556.17 °C, and the liquidus is 590.05 °C. Comparing the theoretical values obtained from the thermodynamic calculations (Fig. 5) and DSC results, the main reason for the difference in theoretical solidus and liquidus values with those obtained from the thermal analysis

Table 4 Laser diffraction results representing the size distribution of ball-milled particles

Composition	Condition	D10	D50	D90
Mg-18.2Ca	Duration effect	43.81	92.18	207.30
	BPR effect	40.95	89.76	264.80
	Speed effect	17.89	56.44	351.53
Mg-20.9Sr	Duration effect	21.48	61.82	261.60
	BPR effect	27.83	73.73	312.40
	Speed effect	6.60	29.21	214.20

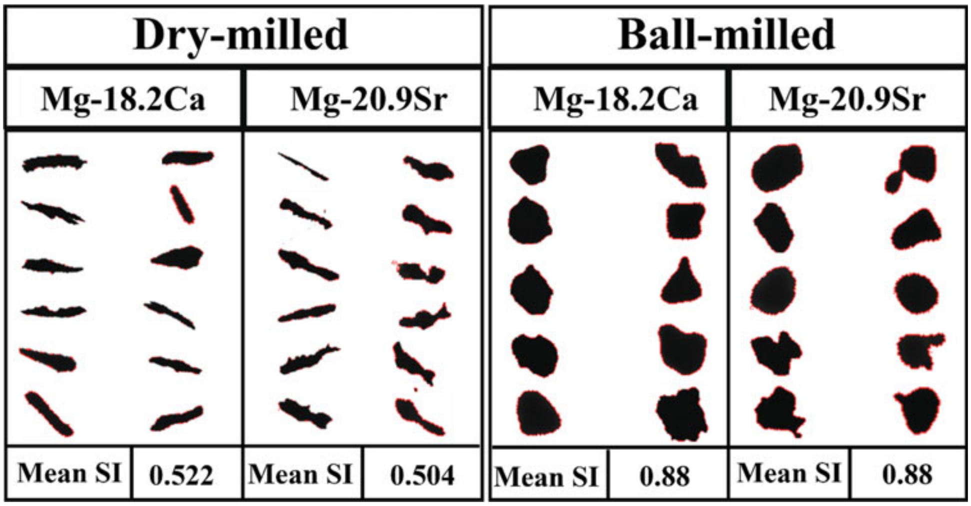

Fig. 4 Sphericity index results obtained by laser diffraction technique

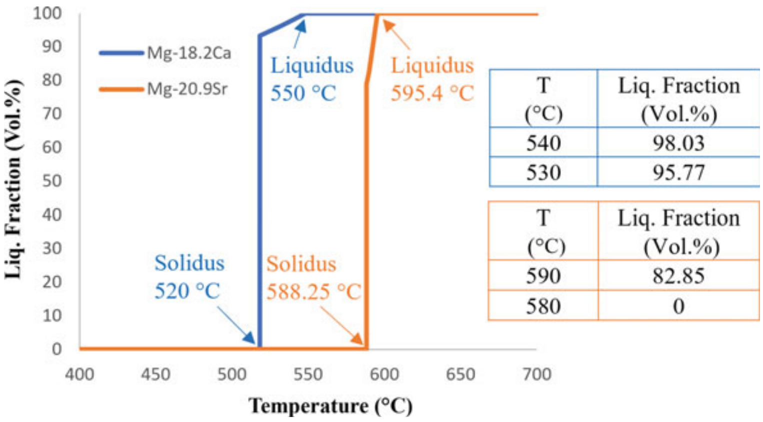

T (°C)	Liq. Fraction (Vol.%)
540	98.03
530	95.77

T (°C)	Liq. Fraction (Vol.%)
590	82.85
580	0

Fig. 5 Liquid volume fraction curves of Mg-18.2Ca and Mg-20.9Sr

originated from the fact that the thermodynamic calculations are based on the data of bulk materials. However, DSC was carried out on the powder particles surrounded by the MgO film. Additionally, the theoretical temperature calculations consider the thermodynamic equilibrium, while the thermal analysis is dependent upon the heating rate; with decreasing the heating rate the onset of a transformation shifts to lower temperatures [27]. In accordance with both thermal analysis and thermodynamic calculations, the sintering temperature was selected to be 625 °C for both compositions.

Figure 7 shows the SEM micrographs of the fully dense regions of ball-milled specimens of Mg-18.2Ca and Mg-20.9Sr after sintering. The presence of the liquid phase can be confirmed from the graphs. The lamellar microstructure is an indication of the solidified liquid phase within the microstructure. Unlike the sintering results of the dry-milled specimens of the same compositions previously investigated [28], the liquid phase formed during sintering at 575 °C was maintained within the microstructure, and the structural integrity was preserved. This might be due to the

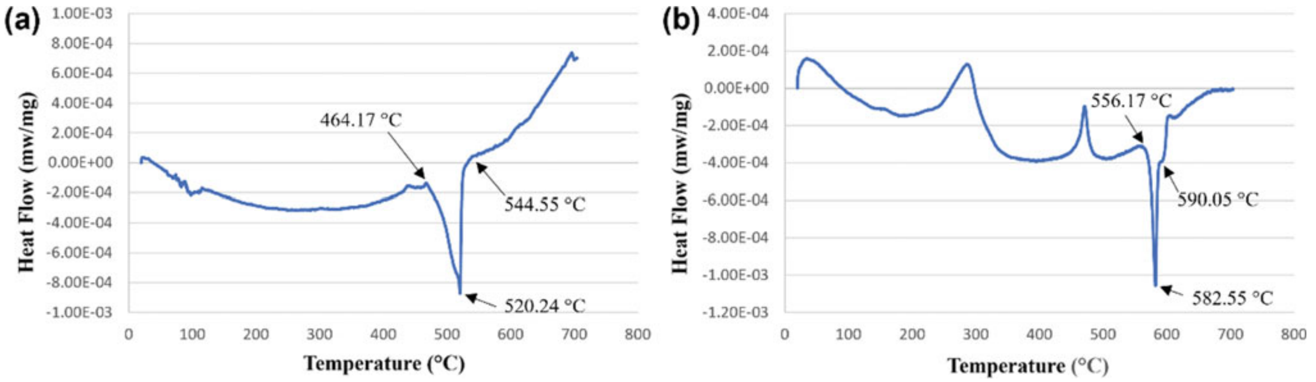

Fig. 6 DSC curves of **a** Mg-18.2Ca and **b** Mg-20.9Sr

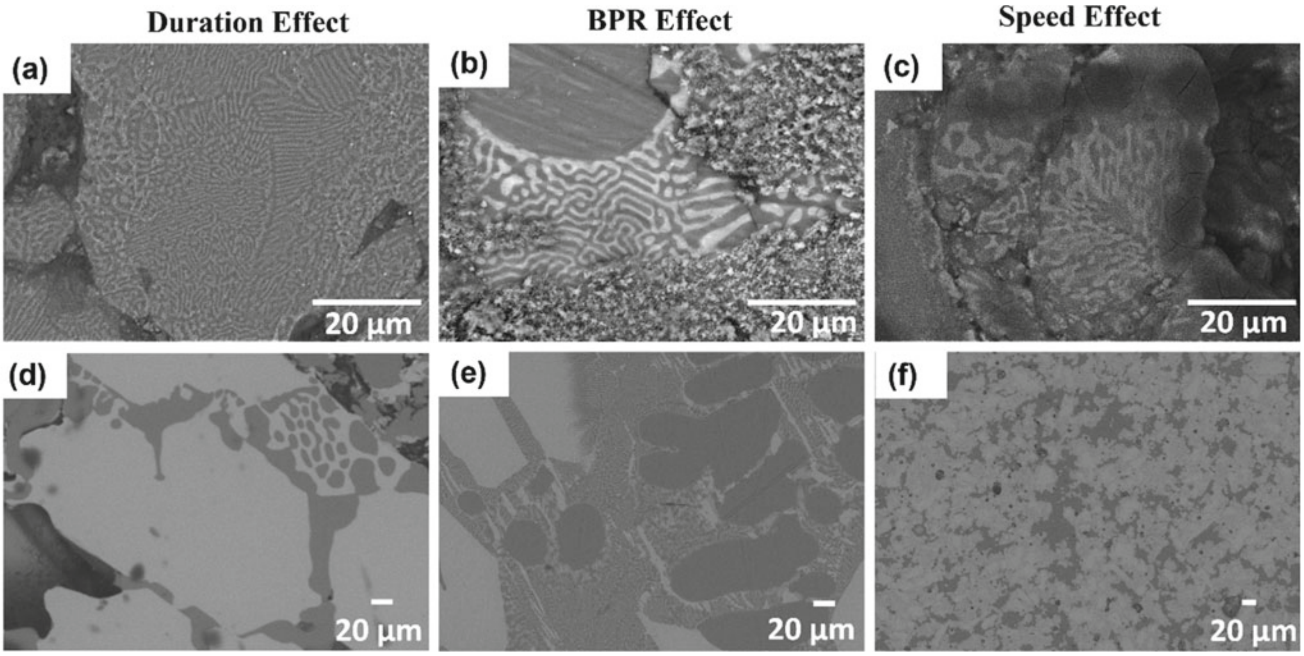

Fig. 7 SEM micrographs of **a**–**c** Mg-18.2Ca and **d**–**f** Mg-20.9Sr, indicating the liquid formation during sintering at 575 °C

finer size of the particles obtained after ball milling, and accordingly, the ease of compaction with finer powders compared to the dry-milled state. In addition, the liquid phase fills in the pores of the microstructure and thereby reduces the overall porosity level. As can be observed in Fig. 7, there is no porosity in the regions where the liquid phase solidified. However, the porosity was found to be in the regions where solid-state sintering is the controlling mechanism and no liquid phase was formed.

Porosity measurements were performed on sintered Mg-18.2Ca and Mg-20.9Sr specimens using both image analysis technique (Fig. 8a) and Archimedes density method (Fig. 8b). Generally, the porosity levels of the ball-milled specimens significantly dropped for both compositions compared to the dry-milled specimens (62.37 and 42.52% correspond to Mg-18.2Ca and Mg-20.9Sr in dry-milled state). In addition, a similar trend applies to both compositions with Speed Effect showing the lowest porosity level (6% and 8% correspond to Mg-18.2Ca and Mg-20.9Sr, respectively), and BPR Effect resulted in the highest porosity level (35% and 41% correspond to Mg-18.2Ca and Mg-20.9Sr, respectively) among 3 ball milling conditions. Furthermore, effects of Duration and BPR are comparable, with Duration Effect being slightly more effective in terms of densification in both compositions (29% and 39% correspond to Mg-18.2Ca and Mg-20.9Sr, respectively).

Archimedes density measurements of both compositions revealed that the porosity level of Mg-18.2Ca specimens

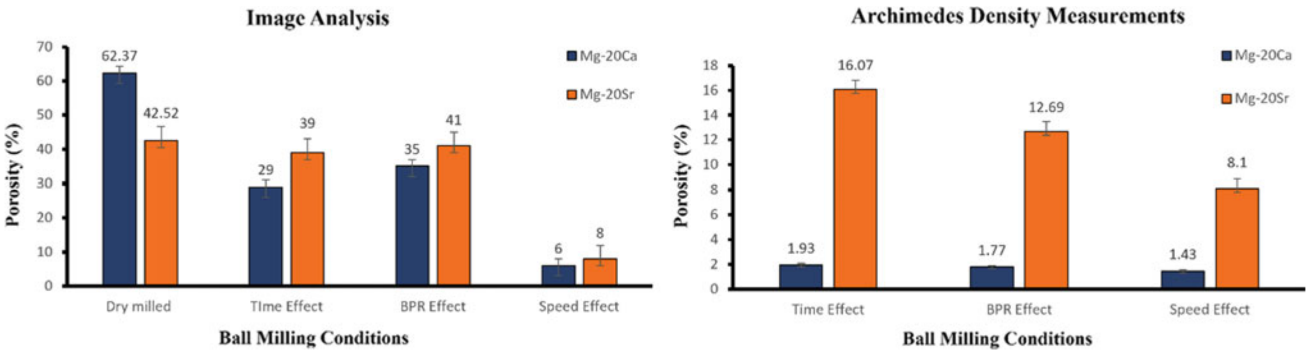

Fig. 8 Graphs of porosity measurements using **a** image analysis and **b** Archimedes density measurements

substantially decreased to 1.93%, 1.77%, and 1.43% correspond to Duration, BPR, and Speed Effects, respectively. In addition, the porosity of Mg-20.9Sr also decreased to 16.07 and 12.69% correspond to Duration and BPR Effects. However, the value of porosity remained unchanged for Speed Effect. On the basis of both density measurements and image analysis results, it was affirmed that Speed Effect resulted in less porosity levels and therefore more promising for achieving higher densification. This could be due to the presence of both fine and coarse powder particles which was obtained at higher speeds of ball milling and caused an improved green part compaction which resulted in higher densification.

Conclusion

This study investigated the sinterability of two binary alloys, namely Mg-18.2Ca and Mg-20.9Sr. Initial powders were fabricated using dry milling and ball milling techniques. The impacts of alloying elements (Ca and Sr) were evaluated by thermodynamic calculations and thermal analysis. The effect of ball milling parameters (Duration, BPR, and Speed) was also investigated. The following remarks can be derived from this study:

- After ball milling, particle size reduction and morphological transformation were observed; irregular and large dry-milled particles became more spherical and finer.
- Porosity levels of ball-milled specimens decreased compared to the dry-milled results.
- Particle size distributions as a result of Duration Effect and BPR Effect were approximately similar, and porosity levels of both conditions calculated by image analysis were comparable.
- Among ball milling conditions, Speed Effect resulted in non-homogeneous particle size distribution causing higher compaction and higher densification.

Acknowledgements Authors acknowledge the EU financial support received under Marie-Sklodowska Curie Fellowship (AMBIT 101029651). This publication has also emanated from research conducted with the financial support of Science Foundation Ireland under grant number 20/FFP-P/8868. For the purpose of Open Access, the author has applied a CC BY public copyright licence to any Author Accepted Manuscript version arising from this submission. Authors also thank South Eastern Applied Materials (SEAM) Research Centre for their support in conducting laser diffraction experiments.

References

1. Jamel MM, Jamel MM, Lopez HF (2022) Designing Advanced Biomedical Biodegradable Mg Alloys: A Review. Metals 12 (1):85. https://doi.org/10.3390/met12010085
2. Sharma SK, Saxena KK, Malik V, Mohammad KA, Prakash C, Buddhi D, Dixit S (2022) Significance of Alloying Elements on the Mechanical Characteristics of Mg-Based Materials for Biomedical Applications. Cryst. 12(8):1138. https://doi.org/10.3390/cryst12081138
3. Amukarimi S, Mozafari M (2021) Biodegradable magnesium-based biomaterials: An overview of challenges and opportunities. Med Comm. 2(2):123–144. https://doi.org/10.1002/mco2.59
4. Zhou H, Liang B, Jiang H, Deng Z, Yu K (2021) Magnesium-based biomaterials as emerging agents for bone repair and regeneration: from mechanism to application. JMA 9(3):779–804. https://doi.org/10.1016/j.jma.2021.03.004
5. Alam ME, Pal S, Decker R, Ferreri NC, Knezevic M, Beyerlein IJ (2020) Rare-earth- and aluminum-free, high strength dilute magnesium alloy for Biomedical Applications. Sci. Rep. 10 (1):15839. https://doi.org/10.1038/s41598-020-72374-z.
6. Maier P, Hort N (2020) Magnesium Alloys for Biomedical Applications. Metals 10(10):1328. https://doi.org/10.3390/met10101328
7. Yang Y, He C, Dianyu E, Yang W, Qi F, Xie D, Shen L, Peng S, Shuai C (2020) Mg bone implant: Features, developments and perspectives. Mater. Des 185:108259. https://doi.org/10.1016/j.matdes.2019.108259
8. Zamani Y, Ghazanfari H, Erabi G, Moghanian A, Fakic B, Hosseini SM, Mohammad BP (2021) A review of additive manufacturing of Mg-based alloys and composite implants. JCC 2(5):71–83. https://doi.org/10.52547/jcc.3.1.7
9. Kuah KX, Blackwood DJ, Ong WK, Salehi M, Seet HL, Nai MLS, Wijesinghe S (2022) Analysis of the corrosion performance of binder jet additive manufactured magnesium alloys for biomedical

applications. JMA 10:1296–1310. https://doi.org/10.1016/j.jma.2021.11.016

10. Zeng Z, Salehi M, Kopp A, Xu S, Esmaily M, Birbilis N (2022) Recent progress and perspectives in additive manufacturing of magnesium alloys. JMA 10(6):1511–1541. https://doi.org/10.1016/j.jma.2022.03.001
11. Allavikutty R, Gupta P, Santra TS, Rengaswamy J (2021) Additive manufacturing of Mg alloys for biomedical applications: Current status and challenges. Curr. Opin. Biomed 18:100276. https://doi.org/10.1016/j.cobme.2021.100276
12. Karunakaran R, Ortgies S, Tamayol A, Bobaru F, Sealy MP (2020) Additive manufacturing of magnesium alloys. Bioact. Mater. 5 (1):44–54. https://doi.org/10.1016/j.bioactmat.2019.12.004
13. Liu S, Yang W, Shi X, Li Bin, Duan S, Guo H, Guo J (2019) Influence of laser process parameters on the densification, microstructure, and mechanical properties of a selective laser melted AZ61 magnesium alloy. J. Alloy Compd. 808:151160. https://doi.org/10.1016/j.jallcom.2019.06.261
14. Niu X, Shen H, Fu J, Yan J, Wang Y (2019) Corrosion behaviour of laser powder bed fused bulk pure magnesium in hank's solution. Corros. Sci. 157:284–294, https://doi.org/10.1016/j.corsci.2019.05.026
15. Wei K, Zeng X, Wang Z, Deng J, Liu M, Huang G, Yuan X (2019) Selective laser melting of Mg-Zn binary alloys: Effects of Zn content on densification behavior, microstructure, and mechanical property. Mater. Sci. Eng. 756:226–236. https://doi.org/10.1016/j.msea.2019.04.067
16. Xu, R, Zhao MG, Zhao YC, Liu L, Liu C, Gao C, Shuai C, Atrens A (2019) Improved biodegradation resistance by grain refinement of novel antibacterial ZK30-Cu alloys produced via selective laser melting. Mater. Lette. 237:253–257. https://doi.org/10.1016/j.matlet.2018.11.071
17. Zumdick NA, Jauer L, Kersting LC, Kutz TN, Schleifenbaum JH, Zander D (2019) Additive manufactured WE43 magnesium: A comparative study of the microstructure and mechanical properties with those of powder extruded and as-cast WE43. Mater. Charact. 147:384–397. https://doi.org/10.1016/j.matchar.2018.11.011
18. Li Y, Zhou J, Pavanram P, Leeflang MA, Fockaert LI, Pouran B, Tumer N, Schroder KU, Mol JM, Weinans H, Jahr H, Zadpoor AA (2018) Additively manufactured biodegradable porous magnesium. Acta Biomater 67:378–392. https://doi.org/10.1016/j.actbio.2017.12.008
19. Somasundaram M, Uttamchand NK, Annamalai AR, Jen CP (2022) Insights on Spark Plasma Sintering of Magnesium Composites: A Review. J. Nanomater. 12(13):2178. https://doi.org/10.3390/nano12132178
20. Rotem R, Aghion E (2016) Innovative approach to protect magnesium powder during sintering. IJMR 107(6):553–557. https://doi.org/10.3139/146.111373
21. Wolff M, Ebel T, Dahms (2010) Sintering of Magnesium. Adv. Eng. Mater. 12(9):829–836. https://doi.org/10.1002/adem.201000038
22. Burke P, Kipouros Gj, Fancelli D, Laverdiere V (2013) Sintering Fundamentals of Magnesium Powders. Can. Metall. Q. 48(2):123–132. https://doi.org/10.1179/cmq.2009.48.2.123
23. Salehi M, Maleksaeedi S, Nai SML, Meenashisundaram GK, Goh MH, Gupta M (2019) A paradigm shift towards compositionally zero-sum binderless 3D printing of magnesium alloys via capillary-mediated bridging. Acta Mater. 165:294–306. https://doi.org/10.1016/j.actamat.2018.11.061
24. German RM, Suri P, Park SJ (2009) Review: liquid phase sintering. J. Mater. Sci. 44(1):1–39. https://doi.org/10.1007/s10853-008-3008-0
25. Johnson JL, German RM (1996) Solid-state contributions to densification during liquid-phase sintering. Metall. Mater. Trans. B. 27(6):901–909. https://doi.org/10.1007/s11663-996-0003-1
26. Mora CF, Kwan AKH (2020) Sphericity, shape factor, and convexity measurement of coarse aggregate for concrete using digital image processing. Cem. Concr. Res. 30(3):351–358. https://doi.org/10.1016/S0008-8846(99)00259-8
27. Salehi M, Seet HL, Gupta M, Farnoush H, Maleksaeedi S, Nai MLS (2020) Rapid densification of additive manufactured magnesium alloys via microwave sintering. Addit. Manuf. 37:101655. https://doi.org/10.1016/j.addma.2020.101655
28. Celikin M et al. (2023) Development of Magnesium-Strontium/Calcium (Mg-Sr/Ca)-Based Alloys with Improved Sinterability for Next-Generation Biomedical Implants. Paper presented at the 152nd TMS Annual Meeting, San Diego, California, 19–23 March 2023

Impact of Thermo-Mechanical Processing on Structure–Property Relationships for the Biodegradable ZX10 Mg Alloy

Sreenivas Raguraman, Ryan McGovern, Andrew Kim,
Veronica Ivanovskaya, Tram Nguyen, Tunde Ayodeji, Adam Griebel,
and Timothy Weihs

Abstract

Magnesium alloys offer immense potential as intelligent alternatives to traditional implant materials due to their inherent degradability, biocompatibility, and exceptional mechanical properties. However, their rapid deterioration hinders their practical applications, compromising their mechanical integrity. This study addresses this challenge by investigating the effects of thermo-mechanical processing, including extrusion, cECAP, rolling, and annealing, on the high-strength, dilute ZX10 Mg alloy. By subjecting the alloy to over thirty processing conditions, we identify an optimal combination of high-strength and low-corrosion rates. Simple characterization techniques like XRD, optical microscopy, and SEM were employed to rapidly evaluate the microstructural changes post-processing. The findings identify that grain boundary and strain hardening play pivotal roles in enhancing hardness, while factors such as texture, dislocation density, and precipitates impact corrosion significantly. This comprehensive investigation provides valuable insights into processing-structure–property relationships for Mg alloys, paving the way for developing superior biodegradable implant materials.

Keywords

Magnesium alloys • Thermo-mechanical processing • Biocorrosion • Mechanical properties

Extended Abstract

Magnesium-based alloys have surged to prominence in the realm of modern biomaterials due to their remarkable blend of absorbable, bone-equivalent mechanical properties, bone growth stimulation, and favorable cellular interactions. Particularly noteworthy is their inherent biodegradability, eliminating the requirement of additional surgical procedures to remove biomedical devices post-implantation. Despite these favorable properties, their clinical translation remains hampered due to their tendency to degrade quickly in physiological environments [1–5]. Numerous investigations [6, 7] over the past decade have demonstrated the impact of microstructural features on mechanical and bio-corrosion behavior. These microstructural features typically include grain size, crystallographic texture, dislocations, and

---

S. Raguraman (✉) · A. Kim · V. Ivanovskaya · T. Nguyen ·
T. Weihs
Department of Materials Science and Engineering, Johns Hopkins
University, Baltimore, MD 21218, USA
e-mail: sragura1@jhu.edu

A. Kim
e-mail: akim153@jhu.edu

V. Ivanovskaya
e-mail: vivanov4@jhu.edu

T. Nguyen
e-mail: nnguye59@jhu.edu

T. Weihs
e-mail: weihs@jhu.edu

S. Raguraman
Hopkins Extreme Materials Institute, Johns Hopkins University,
Baltimore, MD 21218, USA

R. McGovern
Department of Biomedical Engineering, Johns Hopkins
University, Baltimore, MD 21218, USA
e-mail: rmcgove3@jhu.edu

T. Ayodeji · T. Weihs
Department of Mechanical Engineering, Johns Hopkins
University, Baltimore, MD 21218, USA
e-mail: aayodej3@jhu.edu

A. Griebel
Research and Development, Fort Wayne Metals Research
Products Corp, Fort Wayne, IN 46809, USA
e-mail: adam_griebel@fwmetals.com

T. Weihs
Hopkins Extreme Materials Institute, Johns Hopkins University,
Baltimore, MD 21218, USA

A. Leonard et al. (eds.), *Magnesium Technology 2024*, The Minerals, Metals & Materials Series,
https://doi.org/10.1007/978-3-031-50240-8_40

secondary phases [8, 9]. However, the nature of these parameters is often determined by the processing methods.

In the recent past, there has been a significant push towards diluting magnesium-zinc-calcium alloys for implant application, as their secondary phases are limited in volume, thereby minimizing biocorrosion [10–12]. Earlier studies by Hofstetter et al. [11] and Bakhsheshi-Rad et al. [12] highlight the need for a balanced Zn and Ca composition to prevent the formation of noble micro-cathodic secondary phases. However, excessive Zn content promotes the creation of the detrimental $Ca_2Mg_6Zn_3$ phase [11, 12]. Reducing Zn content can enhance biocorrosion resistance, but doing so may limit the alloy's strength due to reduced solution hardening. Beyond alloying, processing routes, such as severe plastic deformation, can refine grain size and improve mechanical properties [13]. In this study, we investigate the impact of processing routes on both the mechanical and biocorrosion properties of the ZX10 Mg alloy. ZX10 is a high-strength low alloy composed primarily of Mg, with trace amounts of Zn, Ca, and Mn. A comprehensive investigation was conducted involving continuous Equal-Channel Angular Pressing (cECAP), solution treatment, and cold rolling processes to elucidate the influence of each process step on hardness and corrosion behavior. Microhardness measurements were carried out using a 200gf load, and immersion corrosion tests were performed in Earle's balanced Salt Solution at 5% CO_2, and 37.1 °C as per the ASTM G31-72 [14] to mimic the in-vivo conditions for a duration of one day as shown in Fig. 1.

The initial cECAP-processed sample exhibited impressive hardness but suffered from an elevated corrosion rate, as shown in Fig. 2. This phenomenon is attributed to multiple factors, including a heightened dislocation density, a refined grain size of 2 μm, and the presence of secondary phases [8, 9]. The secondary phases present in this alloy are $Ca_2Mg_6Zn_3$, α-Mn, and Mg_2Ca. The high dislocation density post-cECAP increases the material's hardness yet adversely affected corrosion resistance by offering many anodic sites

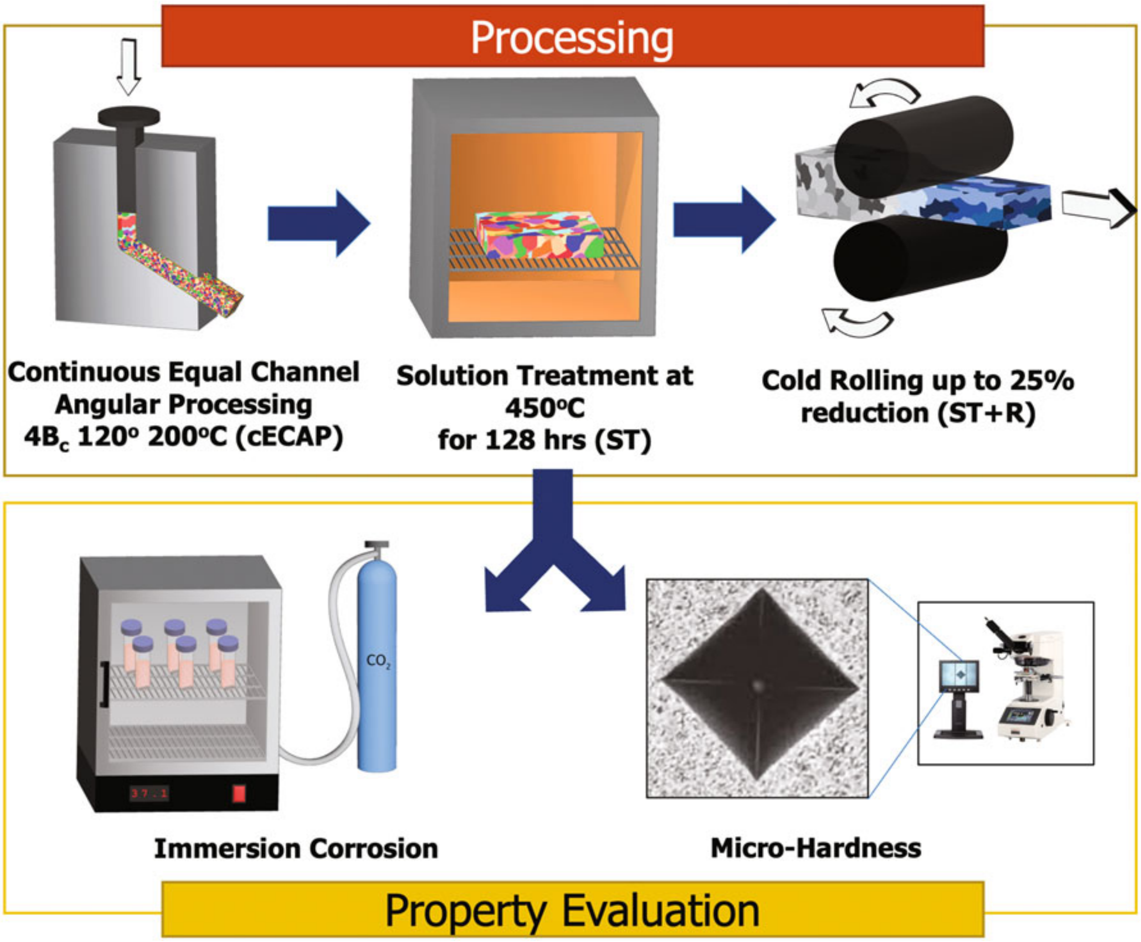

Fig. 1 Schematic depicting the workflow of this study. cECAP was carried out at 200 °C via the $4B_C$ route post-conventional extrusion at 350 °C as explained in [15]. Solution heat treatment (ST) was carried out at 450 °C for 128 h to dissolve the secondary phases on the cECAP samples. ST samples were cold rolled up to 25% reduction (ST + R). Mechanical and corrosion characterization post-processing was carried out using the LECO AMH55 Hardness Tester and Heraeus Heracell CO_2 150 incubator at 5% CO_2 atmosphere and 37.1 °C, respectively

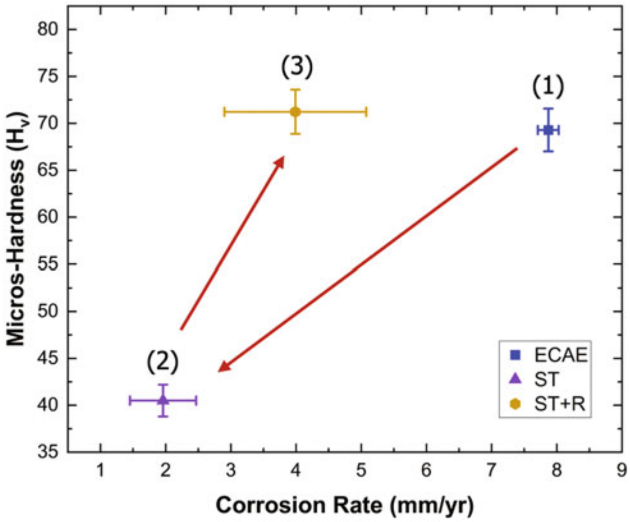

Fig. 2 Hardness and corrosion rate following three different sequential processing steps. The sequence of steps is identified by the arrows and numbers

for corrosion initiation [9]. Additionally, the refined grains resulting from the cECAP processing promoted accelerated corrosion due to excess grain boundaries, further promoting corrosion initiation.

To mitigate these challenges, a solution heat treatment at 450 °C for 128 h was employed, leading to a substantial reduction in dislocation density, a significant increase in grain size to ∼ 30 μm, and dissolution of secondary phases. Consequently, the corrosion rate decreased significantly, but the larger grain size resulted in a ∼ 43% drop in hardness (Fig. 2). The loss of secondary phases likely lowered the hardness as well, but the increase in grain size is thought to be the main factor in lowering hardness, per the Hall–Petch relation [16].

To regain resistance to plastic deformation without sacrificing corrosion resistance, the solution-treated sample was rolled to a 25% thickness reduction at room temperature. This process recovered most of the hardness lost during solution treatment with only a minor increase in the corrosion rate increased. Note that the corrosion rate for the cold rolled samples is still 50% lower than the rate observed for the cECAP-processed sample. The addition of excess dislocations due to cold rolling is thought to be the main factor in doubling the hardness as well as the corrosion rate. However, with limited secondary phases, the corrosion rate is still well below that of the cECAP-processed sample.

Future research directions include exploring a combination of mechanical processing and aging studies alongside detailed characterization of microstructural parameters. These investigations will elucidate the complex relationships between microstructural features, mechanical properties, and corrosion behavior. Ultimately, a comprehensive understanding of these interactions will contribute to developing Mg alloys with improved mechanical performance and enhanced corrosion resistance for potential implant applications.

Acknowledgements The authors thank Dr. Suhas Eswarappa Prameela, Michael Flickinger and Dr. Jenna Krynicki for their valuable insights. The authors would also like to thank Rich Middlestadt from WSE Manufacturing for technical support with sample preparation.

References

1. Witte F (2010) The history of biodegradable magnesium implants: A review. Acta Biomater 6:1680–1692. https://doi.org/10.1016/j.actbio.2010.02.028
2. Song G (2007) Control of biodegradation of biocompatable magnesium alloys. Corros Sci 49:1696–1701. https://doi.org/10.1016/j.corsci.2007.01.001
3. Prasadh S, Raguraman S, Wong R, Gupta M (2022) Metallic Foams in Bone Tissue Engineering. In: Pandey LM, Hasan A (eds) Nanoscale Engineering of Biomaterials: Properties and Applications. Springer Nature, Singapore, pp 181–205
4. Xue J, Singh S, Zhou Y, et al (2022) A biodegradable 3D woven magnesium-based scaffold for orthopedic implants. Biofabrication 14:034107. https://doi.org/10.1088/1758-5090/ac73b8
5. Prasadh S, Raguraman S, Wong R, Gupta M (2022) Current Status and Outlook of Temporary Implants (Magnesium/Zinc) in Cardiovascular Applications. Metals 12:999. https://doi.org/10.3390/met12060999
6. (2010) Revealing the relationship between grain size and corrosion rate of metals. Scr Mater 63:1201–1204. https://doi.org/10.1016/j.scriptamat.2010.08.035
7. Gerashi E, Alizadeh R, Langdon TG (2022) Effect of crystallographic texture and twinning on the corrosion behavior of Mg alloys: A review. J Magnes Alloys 10:313–325. https://doi.org/10.1016/j.jma.2021.09.009
8. Bahmani A, Arthanari S, Shin KS (2020) Formulation of corrosion rate of magnesium alloys using microstructural parameters. J Magnes Alloys 8:134–149. https://doi.org/10.1016/j.jma.2019.12.001
9. Bahmani A, Lotfpour M, Taghizadeh M, Kim W-J (2022) Corrosion behavior of severely plastically deformed Mg and Mg alloys. J Magnes Alloys 10:2607–2648. https://doi.org/10.1016/j.jma.2022.09.007
10. Hofstetter J, Rüedi S, Baumgartner I, et al (2015) Processing and microstructure–property relations of high-strength low-alloy (HSLA) Mg–Zn–Ca alloys. Acta Mater 98:423–432. https://doi.org/10.1016/j.actamat.2015.07.021
11. Hofstetter J, Becker M, Martinelli E, et al (2014) High-Strength Low-Alloy (HSLA) Mg–Zn–Ca Alloys with Excellent Biodegradation Performance. JOM 66:566–572. https://doi.org/10.1007/s11837-014-0875-5
12. Bakhsheshi-Rad HR, Abdul-Kadir MR, Idris MH, Farahany S (2012) Relationship between the corrosion behavior and the thermal characteristics and microstructure of Mg–0.5Ca–xZn alloys. Corros Sci 64:184–197. https://doi.org/10.1016/j.corsci.2012.07.015

13. Yan C, Xin Y, Chen X-B, et al (2021) Evading strength-corrosion tradeoff in Mg alloys via dense ultrafine twins. Nat Commun 12:4616. https://doi.org/10.1038/s41467-021-24939-3
14. G31 Standard Practice for Laboratory Immersion Corrosion Testing of Metals. https://www.astm.org/g0031-72r04.html. Accessed 21 Aug 2023
15. Davis CF, Griebel AJ, Lowe TC (2020) Isothermal Continuous Equal Channel Angular Pressing of Magnesium Alloy AZ31. JOM 72:2603–2611. https://doi.org/10.1007/s11837-020-04195-4
16. Yu H, Xin Y, Wang M, Liu Q (2018) Hall-Petch relationship in Mg alloys: A review. J Mater Sci Technol 34:248–256. https://doi.org/10.1016/j.jmst.2017.07.022

Examination of Cycling Rate Sensitivity in Magnesium Alloys in Fatigue and Corrosion Fatigue

Adam J. Griebel and Olivia Schuller

Abstract

Corrosion fatigue occurs when a metallic material undergoes mechanical cycling in the presence of a corrosive environment. Absorbable magnesium materials, intended to corrode in the body, may experience corrosion fatigue and must not fail prematurely because of it. Designing devices with appropriate data to predict how the material will behave is critical to success. Corrosion fatigue testing is complicated by mismatches between cycling frequency acceleration and corrosion acceleration. The aim of this study was to examine the fatigue and corrosion fatigue of three magnesium alloy wires (ZX10, LZ21, WE22) at a variety of strain levels and cycling frequencies. Baseline rotary beam ($R = -1$) fatigue testing was performed at three strain levels (0.5, 0.4, and 0.3%) and three frequencies (600, 3600, and 7200 rpm), in two environments (air, Hank's solution). In general, cycles-to-failure increased with decreasing strain in all conditions, increased with cycling frequency at high but not low strains, and decreased in Hank's solution compared to air. LZ21 displayed the highest corrosion fatigue durability, followed by WE22 and ZX10. These data will provide a baseline to aid designers in properly testing absorbable metal devices.

Keywords

Absorbable wire • Magnesium • Corrosion • Fatigue • Corrosion fatigue

Introduction

Absorbable medical devices are intended to provide some amount of structural support to local tissues during some critical period and then harmlessly degrade and absorb into the body. During this period of structural support, mechanical loads will be experienced by the device from the surrounding tissue. Often, these loads are cyclical in nature (e.g. beating of the heart for a coronary stent, walking stresses for a screw in the toe). Cyclical loading of a material introduces a phenomenon known as fatigue, wherein a material can fail at stresses well below the yield strength determined in a tensile test.

Fatigue of medical devices and their materials is a wide field of study with many intricacies [1, 2], but most of these analyses are on materials which do not corrode in the body. Absorbable metal devices which are corroding while undergoing mechanical fatigue are subject to a phenomenon known as corrosion fatigue. Corrosion fatigue is a complex phenomenon and has been identified as an important area to understand when attempting to use magnesium alloys as absorbable implant materials [3–6].

Many medical devices, including stents, staples, and sutures, could conceivably be made of magnesium wire. However, only limited data on the corrosion fatigue behavior of magnesium wire is available [7, 8].

A complicating factor in conducting corrosion fatigue tests involves the cycling rate. Often, mechanical fatigue testing is conducted at an accelerated rate compared to that experienced by the material in the body. This allows for efficient and timely data collection. Corrosion testing of magnesium alloys in various simulated body fluids tends to occur more quickly than corrosion seen in the body [9], though the magnitude of this acceleration can vary widely. Interpreting data where combined accelerated mechanical cycling and accelerated corrosion conditions are incorporated in a corrosion fatigue test can be challenging. An understanding of the impact of the mechanical cycling

---

A. J. Griebel (✉) · O. Schuller
Fort Wayne Metals Research Products Corp.,
Fort Wayne, IN, USA
e-mail: adam_griebel@fwmetals.com

A. Leonard et al. (eds.), *Magnesium Technology 2024*, The Minerals, Metals & Materials Series,
https://doi.org/10.1007/978-3-031-50240-8_41

frequency in a given media would help to inform this interpretation. Vinogradov et al. investigated the impact of cycling frequency on corrosion fatigue of 2 mm × 2 mm ZK60, showing a reduced cycle lifetime with reduced cycling rate (and higher corrosion time) [10]. Similar data in thin Mg wire materials, with substantially reduced cross-sections, have not yet been reported.

The aim of this study is to investigate the effects of cyclic frequency on three magnesium alloy wires, first in air and then in a simulated body fluid.

Materials and Methods

Wire samples used in this study were prepared from ZX10, LZ21 [11], and WE22 magnesium alloys. Alloy compositions were measured via spark OES and are reported in Table 1. Briefly, 50 mm ingots were cast, homogenized for 16 h, and extruded to 12 mm diameter rods. Homogenization and extrusion temperatures, respectively, were 450 °C and 300 °C for ZX10, 400 °C and 300 °C for LZ21, and 500 °C and 450 °C for WE22. Rods were cold drawn into wire using standard wire drawing practices with intermittent annealing until a final diameter of 0.25 mm. At the final size, wires were annealed to impart high ductility, representative of a condition useful in surgical stapling or balloon-expandable stenting. The annealing parameters for each alloy were tuned to impart a yield strength of approximately 250 MPa, to minimize wire strength as a potentially confounding factor.

Wire samples were longitudinally mounted, polished, and etched to expose the microstructure and allow for grain size measurement via Abram's three circle method. Wire surface roughness was documented with a Zygo 3D Optical Profiler. Mechanical properties of the wires were assessed by a simple tensile test (127 mm gauge length, 25.4 mm/min crosshead speed, N = 3).

Rotary beam fatigue testing was conducted in accordance with ASTM E2948-22 [12]. Strains are assumed to be fully reversed (R = −1), though tension–compression anisotropy may in fact shift the neutral axis. Testing was conducted for each alloy at three strain levels (0.3, 0.4, 0.5%), three frequencies (600, 3600, 7200 rpm), and in two environments (22 °C air and 37 °C Hank's balanced salt solution (HBSS)). A minimum of three tests were completed at each time point. Runout was set to 10,000,000 cycles.

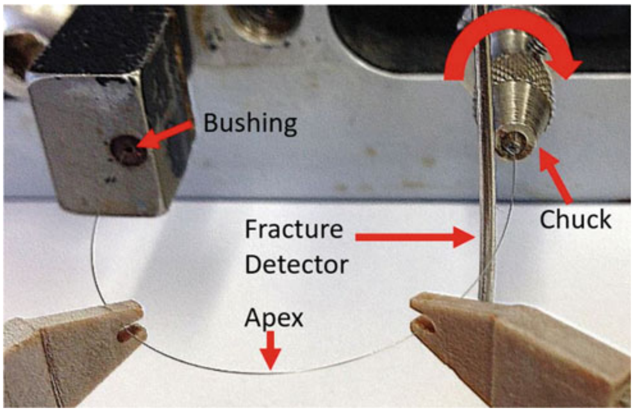

Fig. 1 Rotary beam fatigue testing apparatus. The wire is held at a predetermined strain by a rotating chuck, right, and a bushing, left. Fracture occurs at the apex and the wire trips the detector

After fatigue testing, select fracture faces were examined by SEM/EDS to look for any particles which contributed to fracture initiation (Fig. 1).

Results

Representative microstructures are shown in Fig. 2. Measured grain size for ZX10 was 2.87 ± 1.3 µm (mean ± standard deviation), LZ21 was 1.44 ± 0.61 µm, and WE22 was 1.7 ± 0.73 µm. 3D RMS surface roughness measurements were 0.114, 0.134, and 0.090 µm for ZX10, LZ21, and WE22, respectively.

Representative tensile properties of the three wires are shown in Fig. 3. Lüders-band-like yield point elongation is observed to some extent in all three alloys and is especially prominent in LZ21 and WE22. Studies in other Mg alloys [13] have indicated this is a twinning phenomenon, but that has not been investigated in the present work. 0.2% offset yield strengths were 258, 255, and 256 MPa, and elastic moduli were 30.3, 31.7, and 32.4 GPa for ZX10, LZ21, and WE22, respectively. Consequently, yield strains of approximately 0.8% were measured for each alloy, indicating that the selected strain levels for fatigue testing were safely in the elastic range.

Average cycle-to-failure and minimum cycles to failure are shown for each alloy at each condition in Tables 2, 3 and 4 for ZX10, LZ21, and WE22, respectively. Individual data points are also plotted in Figs. 4 (air) and 5 (HBSS).

Table 1 Alloy compositions via spark OES

Alloy	Mg	Zn	Ca	Mn	Li	Y	Nd
ZX10	Bal	1.01	0.30	0.15	–	–	–
LZ21	Bal	1.26	0.33	0.24	1.94	–	–
WE22	Bal	0.48	–	–	–	2.01	1.46

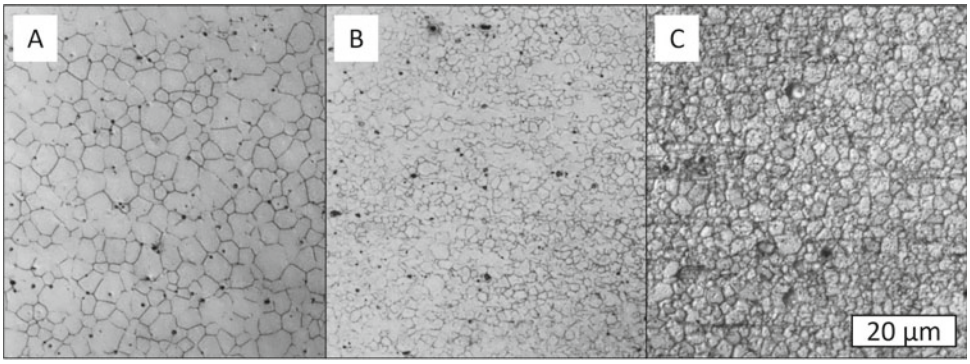

Fig. 2 Longitudinal microstructures of **a** ZX10, **b** LZ21, and **c** WE22 wires

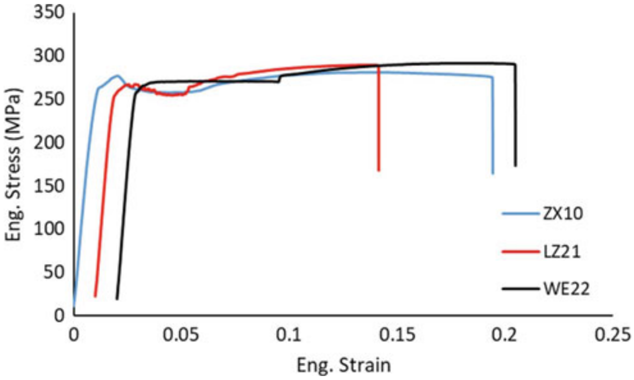

Fig. 3 Representative tensile curves of the three alloys used in the study. Subsequent curves are offset 0.01% for visual clarity

ZX10 in air showed generally increasing cycles to failure with increasing cycle frequency. While some samples at 0.3% strain did achieve runout, there was significant scatter, with many fracturing at much lower cycles. SEM analysis confirmed these samples fractured early due to silicon dioxide inclusions (Fig. 6). Running in HBSS reduced the cycles to failure, especially at lower strain levels, with no samples exceeding 100,000. Surprisingly, cyclic frequency had limited effect on the results in HBSS.

LZ21 in air at the highest strain level showed an increase in fatigue cycles with increasing frequency, but limited effect at lower strain levels. At 0.3%, all samples at all frequencies achieved runout except for one sample at 3600 rpm. SEM/EDS analysis revealed a MgO particle at the initiation

Table 2 Fatigue results for ZX10 wire

Strain (%)	Frequency (RPM)	Environment	Avg cycles	Min cycles
0.5	600	Air	6917	5389
0.5	3600	Air	7411	4292
0.5	7200	Air	11,070	10,430
0.4	600	Air	18,857	17,478
0.4	3600	Air	27,391	17,849
0.4	7200	Air	30,771	26,546
0.3	600	Air	4,221,027	1,527,700
0.3	3600	Air	2,974,179	23,173
0.3	7200	Air	7,079,602	117,347
0.5	600	Hank’s	6048	5615
0.5	3600	Hank’s	8119	7430
0.5	7200	Hank’s	8029	6156
0.4	600	Hank’s	12,073	10,664
0.4	3600	Hank’s	16,699	14,878
0.4	7200	Hank’s	18,956	16,942
0.3	600	Hank’s	28,438	24,059
0.3	3600	Hank’s	53,446	46,986
0.3	7200	Hank’s	46,681	29,741

Table 3 Fatigue results for LZ21 wire

Strain (%)	Frequency (RPM)	Environment	Avg cycles	Min cycles
0.5	600	Air	9058	8015
0.5	3600	Air	16,584	13,725
0.5	7200	Air	16,707	15,669
0.4	600	Air	42,009	25,342
0.4	3600	Air	71,407	36,113
0.4	7200	Air	52,557	42,072
0.3	600	Air	Runout	Runout
0.3	3600	Air	9,380,266	39,700
0.3	7200	Air	Runout	Runout
0.5	600	Hank’s	6386	6016
0.5	3600	Hank’s	9333	8448
0.5	7200	Hank’s	10,642	8771
0.4	600	Hank’s	17,370	16,687
0.4	3600	Hank’s	23,534	21,286
0.4	7200	Hank’s	35,593	32,646
0.3	600	Hank’s	545,438	496,452
0.3	3600	Hank’s	159,224	58,271
0.3	7200	Hank’s	359,060	266,763

Table 4 Fatigue results for WE22 wire

Strain (%)	Frequency (RPM)	Environment	Avg cycles	Min cycles
0.5	600	Air	12,962	11,301
0.5	3600	Air	18,152	8437
0.5	7200	Air	18,818	16,691
0.4	600	Air	121,912	122,207
0.4	3600	Air	70,641	29,027
0.4	7200	Air	209,797	36,327
0.3	600	Air	Runout	Runout
0.3	3600	Air	Runout	Runout
0.3	7200	Air	Runout	Runout
0.5	600	Hank’s	7419	7105
0.5	3600	Hank’s	10,312	9303
0.5	7200	Hank’s	10,253	7922
0.4	600	Hank’s	14,935	14,635
0.4	3600	Hank’s	19,848	17,920
0.4	7200	Hank’s	21,886	19,450
0.3	600	Hank’s	255,317	212,281
0.3	3600	Hank’s	53,097	46,315
0.3	7200	Hank’s	59,910	50,177

site. When testing in HBSS, lifetime was again reduced and consistent trends of increasing cycles to failure with increasing frequency were seen at 0.4 and 0.5% strain, but the high cycles achieved in the 0.3%/600 rpm data set disrupt the trend at the 0.3% strain level.

WE22 in air showed no trend with cycling frequency. All samples at all frequencies achieved runout at 0.3% strain. In HBSS, cycles to failure were reduced compared to air. At 0.4% strain, increasing cycles to failure were seen with increasing cycling rate, but no trends were seen at other

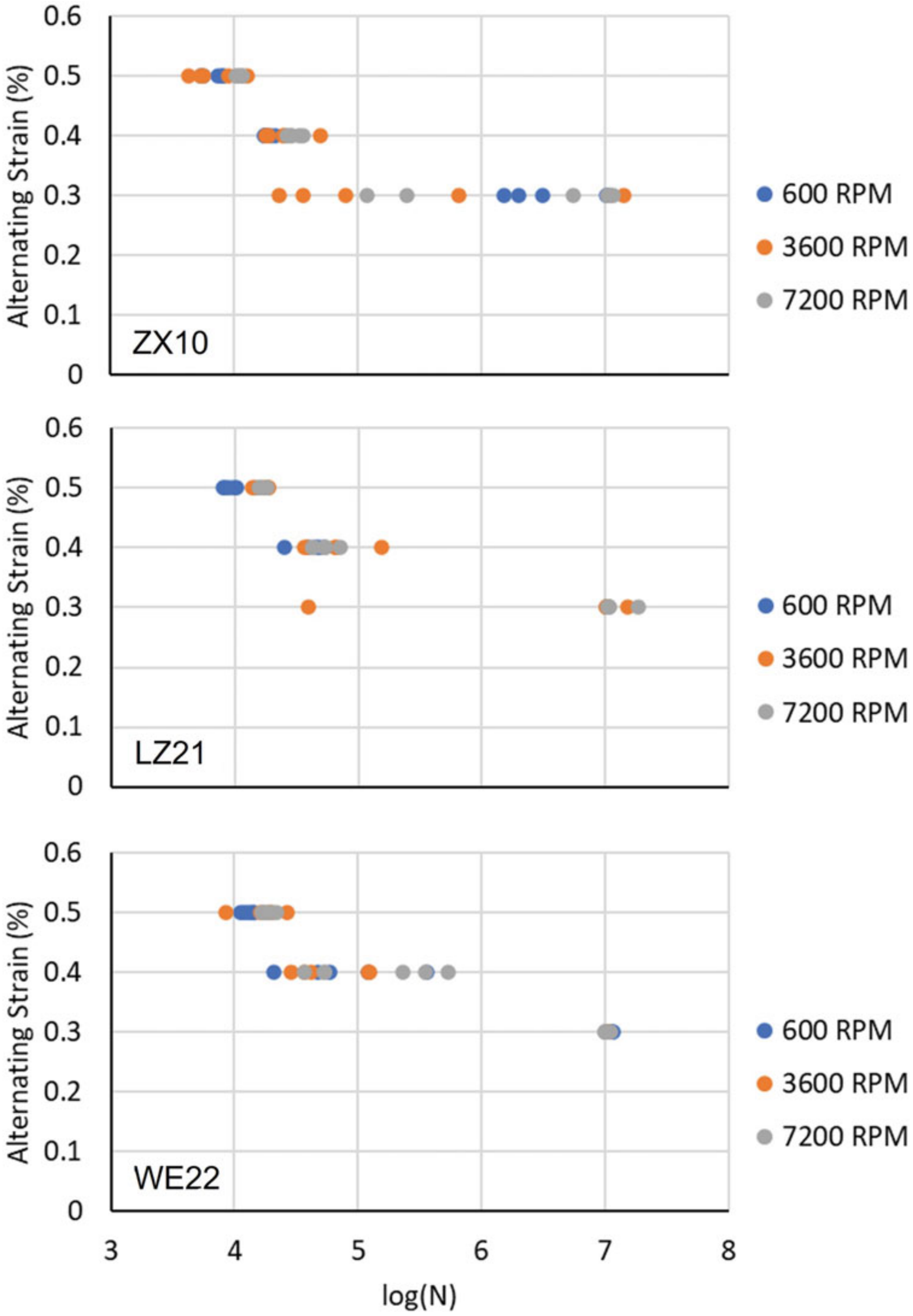

Fig. 4 Fatigue results for the three alloys in air

strain levels. Similar to the LZ21, a surprisingly high cycles to failure were achieved at 0.3% strain and 600 rpm.

Discussion

These data provide a first look at the impact of cycling rate in a corrosion fatigue test of magnesium alloy wire. Though it is premature to draw firm conclusions, the results provide some hints at likely trends and worthwhile future directions.

The author’s prior investigation of strain-rate sensitivity in magnesium alloy wire [14] revealed positive correlations of strength to strain rate in certain Mg alloys. This effect was prominent in alloys containing lithium, smaller but apparent in Mg-Zn-Ca alloys, and negligible in rare-earth containing alloys. Increasing the fatigue cycling rate, which increases the strain rate, could lead to higher strengths and higher fatigue resistance in high-strain, low-cycle regimes for the ZX10 and especially LZ21 alloys. This trend was seen in ZX10 at 0.5 and 0.4% strain levels. LZ21 showed a large

Fig. 5 Fatigue results for the three alloys in HBSS

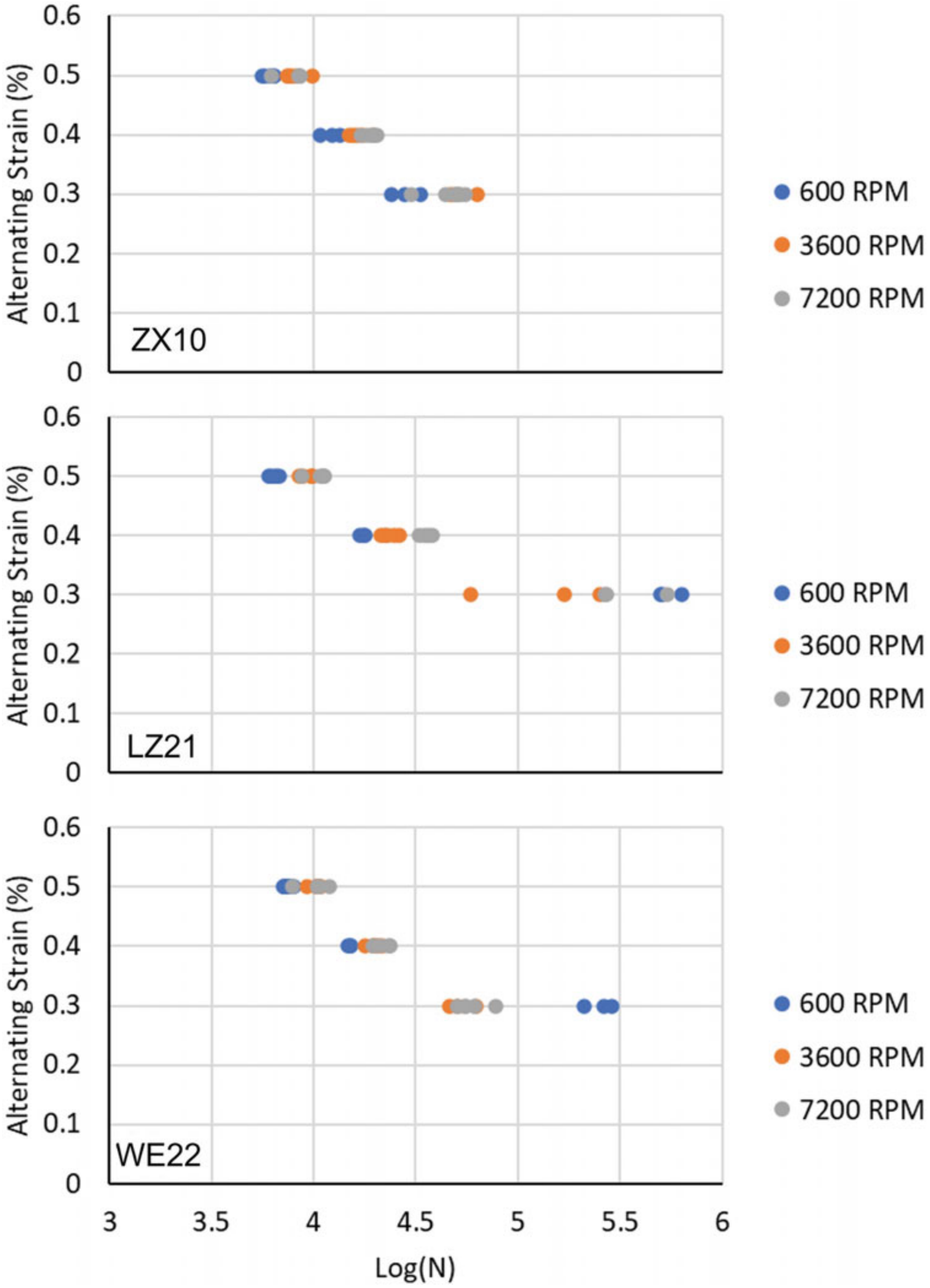

increase in lifetime at 0.5% strain by increasing frequency from 600 to 3600 rpm. WE22 did not show any appreciable trend.

With incorporation of corrosion via HBSS, it would be expected to see a decrease in lifetime with a decrease in cycling rate; slower cycles means more time corroding to reach a given number of cycles. The present results generally trend in this direction, with the notable exception of the 0.3% strain/600 rpm specimens of LZ21 and WE22, which both survived longer than their faster frequency counterparts. Reasons for this are unclear but it is possible that the reduced fluid shear stress from the slower cycling rate allowed a more passivating layer to develop. It is also possible that there was some unknown difference in the test conditions. These conditions are worthy of further testing.

Comparing the fatigue performance of the alloys across all conditions, it appears that LZ21 and WE22 are nearly equal in air, with LZ21 performing slightly better than WE22 in HBSS. ZX10, in this study at least, did not perform as well as either of the other alloys in air or HBSS. However,

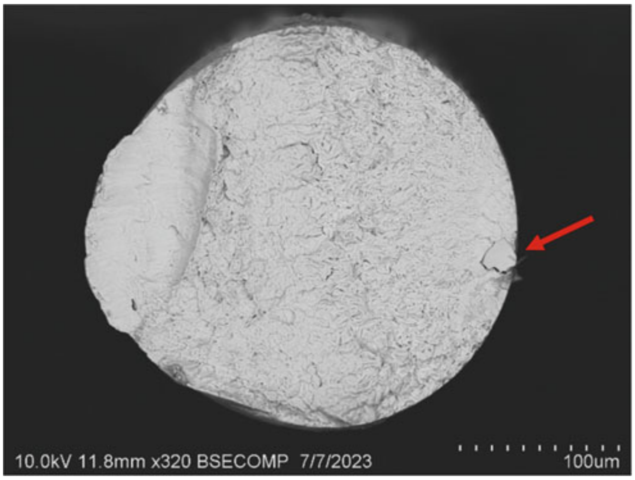

Fig. 6 SEM image of ZX10 fracture (0.3% strain, 3600 rpm, 655,933 cycles) which occurred at a ~ 20 µm inclusion (red arrow). EDS analysis confirmed it was a SiO_2 particle

due to the large SiO_2 inclusions found on several fracture faces, the overall poor fatigue performance of ZX10 in this study is likely a factor of the batch of material used, and not the alloy itself. These inclusions likely originated in the alloy melt preparation, and repeating these data with a batch free of these sorts of inclusions is warranted. It is also worth noting that the general fatigue life trends across the three alloys align with the measured grains sizes, where LZ21 and WE22, with grain sizes 1.44 and 1.70 microns, were finer than ZX10 at 2.87 microns. It is well established that finer grains tend to result in greater fatigue strength [15], so it is possible that some of the difference in fatigue performance in this study could be explained by grain size differences. Future work could target generating equivalent grain sizes rather than equivalent yield strengths.

It is difficult to assess the suitability of any of these materials for medical device applications due to the near-infinite stress profiles and corrosion conditions different types of medical devices might see. The authors have recently found that a similarly sized LZ21 wire has an in vitro-in vivo correlation factor of 8.1, when comparing corrosion in HBSS to subcutaneous mouse. If this holds, that would indicate that the 600 rpm condition in HBSS might allow for a proper match of corrosion acceleration to mechanical acceleration for a stent; a heart rate of 72 beats per minute accelerated by 8.1 times would give a cycling rate of 583 rpm, very near to the 600 rpm condition tested here. The LZ21 survived 600,000 cycles at 0.3% strain at 600 rpm in HBSS; this would translate to only 6 days of heart beats. This suggests a stent designed from the alloy would need to operate at much lower stresses (which is very likely) or the wire would need a coating of some sort to delay degradation. The authors have a second paper in these proceedings investigating potential coatings for this effect and invite the reader to peruse that study as well.

Conclusions

From this work, the following preliminary conclusions can be drawn:

- 250 µm wires of ZX10, LZ21, and WE22 magnesium alloys were produced with equivalent yields strengths of 250 MPa but varying grain sizes (1.4–2.9 µm).
- Cycles-to-failure increased with decreasing strain in all conditions.
- Cycles-to-failure increased with cycling frequency at high but not low strains.
- Cycles-to-failure decreased in Hank’s solution compared to air.
- LZ21 displayed the highest corrosion fatigue durability, followed by WE22 and ZX10.

Acknowledgements The assistance of Dale Herndon and Lane Bailey in preparation of wire materials and Drew Finan and Harold Perez in microstructural analysis and fatigue testing is gratefully acknowledged.

References

1. M. Chong, Y. Teo and S. Teoh, “Fatigue Failure of Materials for Medical Devices,” in *Degradation of Implant Materials*, Springer, 2012, pp. 303–328.
2. S. Teoh, “Fatigue of Biomaterials: a review,” *International Journal of Fatigue,* vol. 22, no. 10, pp. 825–837, 2000.
3. S. Jafari, S. Harandi and R. Singh Raman, “A Review of Stress-Corrosion Cracking and Corrosion Fatigue of Magnesium Alloys for Biodegradable Implant Applications,” *JOM,* vol. 67, pp. 1143–1153, 2015.
4. P. Das, S. Kumar, K. Sahu and S. Gollapudi, “Corrosion, stress corrosion cracking and corrosion fatigue behavior of magnesium alloy bioimplants,” *Corrosion Reviews,* vol. 40, no. 4, pp. 289–333, 2022.
5. Z. Shen, M. Zhao, X. Zhou, H. Yang, J. Liu, H. Guo, Y. Zheng and J.-A. Yang, “A numerical corrosion-fatigue model for biodegradable Mg alloy stents,” *Acta Biomaterialia,* vol. 97, pp. 671–680, 2019.
6. T. O. Olugbade, B. O. Omiyale and O. T. Ojo, “Corrosion, Corrosion Fatigue, and Protection of Magnesium Alloys: Mechanisms, Measurements, and Mitigation,” *Journal of Materials Engineering and Performance,* vol. 31, pp. 1707–1727, 2022.
7. A. J. Griebel and J. E. Schaffer, “Fatigue and Corrosion Fatigue of Cold Drawn WE43 Wires,” *Magnesium Technology,* pp. 303–307, 2015.
8. P. Maier, A. Griebel, M. Jahn, M. Bechly, R. Menze, B. Bittner and J. Schaffer, “Corrosion Bending Fatigue of RESOLOY® and WE43 Magnesium Alloy Wires,” *Magnesium Technology,* pp. 175–181, 2019.

9. P. Bowen, J. Drelich and J. Goldman, “A new in vitro-in vivo correlation for bioabsorbable,” *Materials Science and Engineering Part C,* vol. 33, no. 8, pp. 5064–5070, 2013.
10. M. Linderov, A. Brilevsky, D. Merson, A. Danyuk and A. Vinogradov, “On the Corrosion Fatigue of Magnesium Alloys Aimed at Biomedical Applications: New Insights from the Influence of Testing Frequency and Surface Modification of the Alloy ZK60,” *Materials,* vol. 15, no. 2, p. 567, 2022.
11. A. Griebel and J. Schaffer, “Magnesium-based absorbable alloys”. WO Patent 2020/247383 A1, 3 June 2019.
12. A. E2948-22, *Standard Test Method for Conducting Rotating Bending Fatigue Tests of Solid Round Fine Wire,* ASTM International, 2022.
13. M. Barnett, M. Nave and A. Ghaderi, “Yield point elongation due to twinning in a magnesium alloy,” *Acta Materialia,* vol. 60, no. 4, pp. 1433–1443, 2012.
14. A. J. Griebel and J. E. Schaffer, “Influence of Test Parameters on Tensile Testing of Magnesium Alloy Wire,” in *11th Symposium on Biodegradable Metals*, p. 51, Alicante, Spain, 2019.
15. M. Tsushida, K. Shikada, H. Kitahara, S. Ando and H. Tonda, “Relationship between Fatigue Strength and Grain Size in AZ31 Magnesium Alloys,” *Materials Transactions,* vol. 49, no. 5, pp. 1157–1161, 2008.

Magnesium Ion Embedded and Graphene Modified Vanadium Pentoxide Cathode for Superior Magnesium Storage Performance

Fu-Yu Chen, Hong-Yi Li, Wei-Wei Ren, Jin-An Wang, Dai-Bo Gao, Jiang Diao, Guang-Sheng Huang, Jing-Feng Wang, and Fu-Sheng Pan

Abstract

The strong interaction between Mg^{2+} and vanadium pentoxide deteriorates crystal stability, which restricts the highly efficient magnesium storage of vanadium pentoxide. In contrast to the typical strategy of introducing interlayer water, the establishment of a fast diffusion path and robust structure are crucial for enhancing the magnesium storage properties of vanadium pentoxide. Herein, we synthesize a new Mg^{2+} host of $Mg_xV_2O_5$@GO with Mg^{2+} pre-intercalation and graphene modification through a simple hydrothermal method. In $Mg_xV_2O_5$@GO, Mg^{2+} acts as a 'pillar' within the layered V_2O_5 to alleviate the crystal structure from collapse, while graphene serves as a conductive network to optimize the charge transfer efficiency. Remarkably, $Mg_xV_2O_5$@GO cathode achieves an outstanding cycling life of 5000 cycles at 1 A g^{-1} with an excellent capacity retention of 98.3%. Profited from the conductive graphene that offers a rapid charge transfer network, $Mg_xV_2O_5$@GO exhibits a considerable rate performance of 150.6/81.7 mAh g^{-1} at 0.02/3 A g^{-1}.

Keywords

Vanadium pentoxide • Cathode • Pre-intercalation

Introduction

With remarkable advances in novel energy storage systems, the global energy crisis has been significantly mitigated. Among them, lithium-ion batteries (LIBs) have garnered escalating research attention due to their relatively high voltage and energy density [1, 4, 6, 18]. However, uneven deposition of lithium metal anodes often leads to the formation of sharp lithium dendrites on the surface, resulting in cell failures. Consequently, researchers are prompted to explore other safe and energetic rechargeable metal-ion batteries like magnesium-ion batteries (MIBs) [5, 10, 14, 16]. Magnesium (Mg) anodes with a high theoretical volumetric capacity (3833 mAh cm^{-3}), low negative reduction potential (−2.73 V vs. standard hydrogen electrode), and abundant resources, exhibit promising development prospects [3, 8, 11]. Nevertheless, the strong interaction between Mg^{2+} and the host lattice is prone to irreversible volume changes, ultimately resulting in the collapse of the crystal structure [9, 13]. Therefore, establishing a fast ion diffusion pathway and robust construction for the cathode is paramount to pursue high-performance magnesium-ion batteries.

Vanadium pentoxide is extensively utilized in metal-ion batteries due to its notable specific capacity, abundant chemical valence, and adaptable crystal structure [21]. Zhou et al. successfully synthesized a Rod-like anhydrous V_2O_5 cathode through hydrothermal-calcination method, exhibiting an impressive reversible capacity of 449.8 mA h g^{-1} at 0.1 A g^{-1} in zinc ion batteries [22]. Although vanadium pentoxide demonstrates considerable charge storage potentials, the strong interaction between Mg^{2+} and vanadium pentoxide poses a challenge for long-term magnesiation/demagnesiation cycles in the host structure. Currently, pre-embedding cations or organic molecules within the V_2O_5 layer is considered an effective way to enhance the stability of host. For instance, $Mg_{0.34}V_2O_5·nH_2O$ nanobelts prepared through the pre-intercalation of Mg^{2+} into V_2O_5 layer, where Mg^{2+} serves as a 'pillar' within layers to

---

F.-Y. Chen · H.-Y. Li (✉) · W.-W. Ren · J.-A. Wang · D.-B. Gao · J. Diao · G.-S. Huang · J.-F. Wang · F.-S. Pan
National Magnesium Alloy Material Engineering Technology Research Center, Chongqing University, Chongqing, 400044, China
e-mail: hongyi.li@cqu.edu.cn

H.-Y. Li · J. Diao · G.-S. Huang · J.-F. Wang · F.-S. Pan
School of Materials Science and Engineering, Chongqing University, Chongqing, 400044, China

A. Leonard et al. (eds.), *Magnesium Technology 2024*, The Minerals, Metals & Materials Series,
https://doi.org/10.1007/978-3-031-50240-8_42

enhance its long-term cycle performance (∼97% capacity retention for at least 2000 cycles 5 A g^{-1}) [12]. Similarly, Xu et al. synthesized $Mg_{0.3}V_2O_5 \cdot 1.1H_2O$ nanowires via Mg^{2+} pre-intercalation and performed as a cathode for MIBs, delivering an unprecedented cycling lifespan of 80.0% capacity retention rate after 10,000 cycles [19]. Moreover, Joe et al. introduced an organic polymer molecule of poly (3,4-ethylenedioxythiophene) in V_2O_5 to mitigate the volume variation, resulting in a high specific capacity retention of 172.5 mA h g^{-1} after 500 cycles [7]. Obviously, the strategy of cation/molecule pre-intercalation can effectively promote the cycling performance of cathodes. Nevertheless, the inherent challenges of low conductivity and strong interaction between Mg^{2+} and V_2O_5 significantly impede the efficiency of magnesium ion diffusion.

Herein, we designed a composite cathode of $Mg_xV_2O_5$@GO, which involves the integration of Mg^{2+} intercalation and graphene oxide (GO) modification. Notably, Mg^{2+} serve as a stabilizing ‘pillar’ within the interlayers to reinforce the structural stability of host framework, while GO establishes a sophisticated conductive network, effectively augmenting the conductivity. This synergistic combination yields abundant storage sites and expedites the diffusion efficiency for Mg^{2+} ions, collectively enabling the $Mg_xV_2O_5$@GO cathode to exhibit an extraordinary performance in both of rate capability and cycling stability. Specifically, $Mg_xV_2O_5$@GO cathode achieves an impressive rate performance of 150.6/81.7 mAh g^{-1} at 0.02/3 A g^{-1}, and exceptional capacity retention of 98.3% after 5000 cycles at 1 A g^{-1}.

Experimental Methods

To synthesize $Mg_xV_2O_5$@GO, 2 mmol V_2O_5 powder is dissolved in 50 ml deionized water and stirred continuously for 30 min. Subsequently, 8 mL 30% hydrogen peroxide is added to the above solution and stirring continuously for 60 min. Then, an appropriate quantity of magnesium nitrate is dissolved in the homogeneous solution, and 35 mL with a concentration of 2.59 mg/mL of graphene oxide solution is added. After mixing, placed in the oven at 190 °C for 12 h. Finally, the prepared $Mg_xV_2O_5$@GO was freeze-dried for 60 h.

Materials Characterization

Morphology and microstructure of the as-prepared material were characterized by Environmental Scanning Electron Microscopy (ESEM, Thermo Fisher) and Field Emission Transmission Electron Microscopy (FETEM, Talos). X-ray diffractometer (XRD, Panalytical) with Cu-Kα radiation (λ = 0.15406 nm) was used to test the phase composition of the samples. Thermo Gravimetric Analyzer (TGA, Mettler Toledo) was conducted to calculate the mass of water. The functional groups of graphene oxide were confirmed by Raman spectroscopy (HORIBA).

Electrochemical Characterization

Active material, acetylene black, and polyvinylidene fluoride binder were grinded with the mass ratio of 7:2:1 to form a homogenous slurry, which was then coated on a carbon paper collector and vacuum dried at 80 °C for 12 h. Subsequently, the dried slurry is cut into disks with a diameter of 12 mm, carrying a loading mass of 1.5–2.0 mg. CR2032-type coin cells are assembled by active carbon (AC) anode, $Mg_xV_2O_5$@GO cathode, Watman GF/D separator, and 0.5 M $Mg(TFSI)_2$ in AN electrolyte in an Ar glove box (H_2O < 0.1 ppm, O_2 < 0.1 ppm). Galvanostatic charge–discharge and cyclic voltammograms (CV) are conducted on

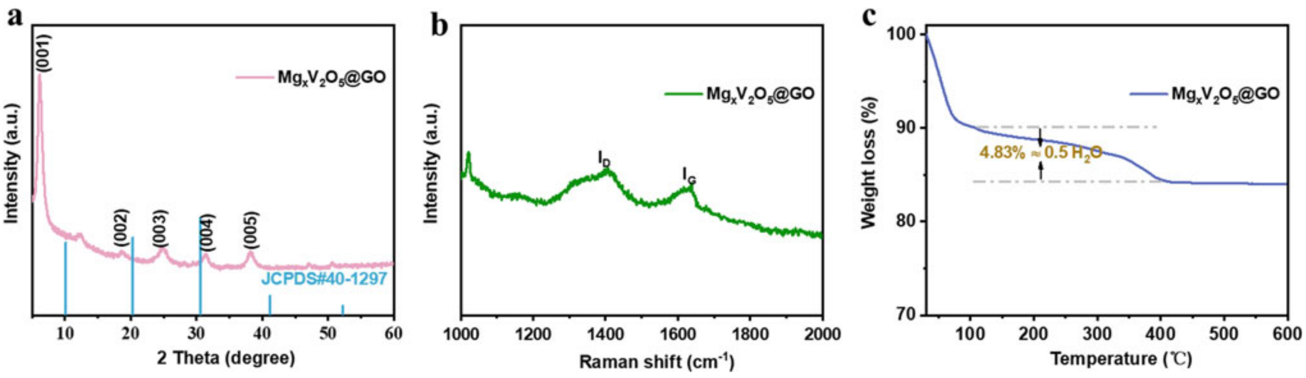

Fig. 1 **a** XRD pattern of $Mg_xV_2O_5$@GO. **b** Raman spectrum of $Mg_xV_2O_5$@GO. **c** TGA profile of $Mg_xV_2O_5$@GO

Neware-CT8000 and CHI660E electrochemical workstations, with a −1.2 to 1.4 V voltage window versus AC.

Results and Discussion

X-ray diffraction (XRD) diffraction patterns are depicted in Fig. 1a. $Mg_xV_2O_5$@GO shows a typical bilayer structure originating from the parent phase of $V_2O_5{\cdot}0.5H_2O$ (JCPDS#40-1297) [12]. Due to the insertion of Mg^{2+}, the (001) plane of $Mg_xV_2O_5$@GO has expanded from 10.2 to 14.5 Å compared to the parent phase, significantly increasing the interlayer spacing. Within the structure, Mg^{2+} act as pillars in V_2O_5 layers to stabilize the host lattice, and the successful embedding of Mg^{2+} will be confirmed by subsequent elemental mapping results. The combination of graphene oxide is demonstrated by successfully identifying I_D and I_G signals within the Raman spectra, as illustrated in Fig. 1b [2]. The content of interlayer water molecules in $Mg_xV_2O_5$@GO is quantified through Thermo Gravimetric Analysis (TGA), Fig. 1c. As highlighted in previous studies, interlayer water molecules can partly shield interaction forces between magnesium ions and the V_2O_5 lattice, effectively facilitating the transport of Mg^{2+} ions [15, 17, 19, 20].

Scanning Electron Microscopy (SEM) results are shown in Fig. 2a, b, where nanoribbon structures can be clearly observed and the nanoribbons are intertwined. Ultrathin GO establishes a conductive network and flawlessly composites with nanoribbons, culminating in a lamellar structure with the dimensions of micron scale. $Mg_xV_2O_5$@GO imparted exceptional structural robustness to accommodate the volumetric fluctuations during the magnesiation/demagnesiation process. Field Emission Transmission Electron Microscopy (FETEM) results are demonstrated in Fig. 2c, which further proves the presence of nanoribbon structure within $Mg_xV_2O_5$@GO. Selected Area Electron Diffraction (SAED) pattern exhibits a prototypical diffraction ring characteristic of polycrystalline materials, Fig. 2d. Subsequently, Energy Dispersive X-ray (EDX) analysis is employed to characterize the elemental distribution in $Mg_xV_2O_5$@GO. As shown in Fig. 2e–h, uniform distribution of the elements V, O, and Mg is achieved throughout the composites, confirming the successful embedding of Mg^{2+}. However, only a weak signal of C is detected, which is attributed to the GO sheets predominantly covering the surface of nanoribbons rather than lattice or interlayers.

In order to evaluate the electrochemical properties of the electrode, $Mg_xV_2O_5$@GO, AC, Watman GF/D, and 0.5 M $Mg(TFSI)_2$ in AN are respectively employed as cathode, anode, separator, and electrolyte to assemble the 2023-type coin cell in Ar-filled glove box ($H_2O < 0.1$ ppm, $O_2 < 0.1$ ppm). Figure 3a illustrates the cyclic voltammetric curve of $Mg_xV_2O_5$@GO at 1 mV s^{-1}, where the redox peaks at approximately 1.5 V/2.6 V are corresponded to the intercalation/deintercalation of Mg^{2+}. Benefiting from the Mg^{2+} pre-intercalation, which establishes a robust ion diffusion channel, while graphene oxide forms a continuous conductive network to facilitate the charge transfer behavior. Thus, $Mg_xV_2O_5$@GO cathode delivers an impressive discharge capacity of 150.6 mAh g^{-1} at 0.02 A g^{-1} and maintains a considerable discharge capacity of 81.7 mAh g^{-1} at a highly current density of 3 A g^{-1}, Fig. 3b. Furthermore, Fig. 3c delivers the remarkable capacity retention rate of 98.3% after 5000 cycles at 1 A g^{-1}, demonstrating the significant improvements in rate capability and cycling performance achieved by Mg^{2+} intercalation and graphene oxide composite strategies.

Conclusion

In summary, the introduction of Mg^{2+} serve to stabilize the host lattice, effectively mitigating volume fluctuations during the charge and discharge processes. Additionally, graphene oxide provides a continuous conductive network that address the intrinsic low conductivity of V_2O_5. The synergistic effect between the stabilizing Mg^{2+} struts and the conductive network enables $Mg_xV_2O_5$@GO cathode to achieve an excellent rate performance of /81.7 mAh g^{-1} at 0.02/3 A g^{-1}, along with outstanding long-cycle performance of 98.3% capacity retention rate after 5000 cycles at 1 A g^{-1}. Such cooperative strategy provides novel insights for energetic and enduring magnesium secondary batteries.

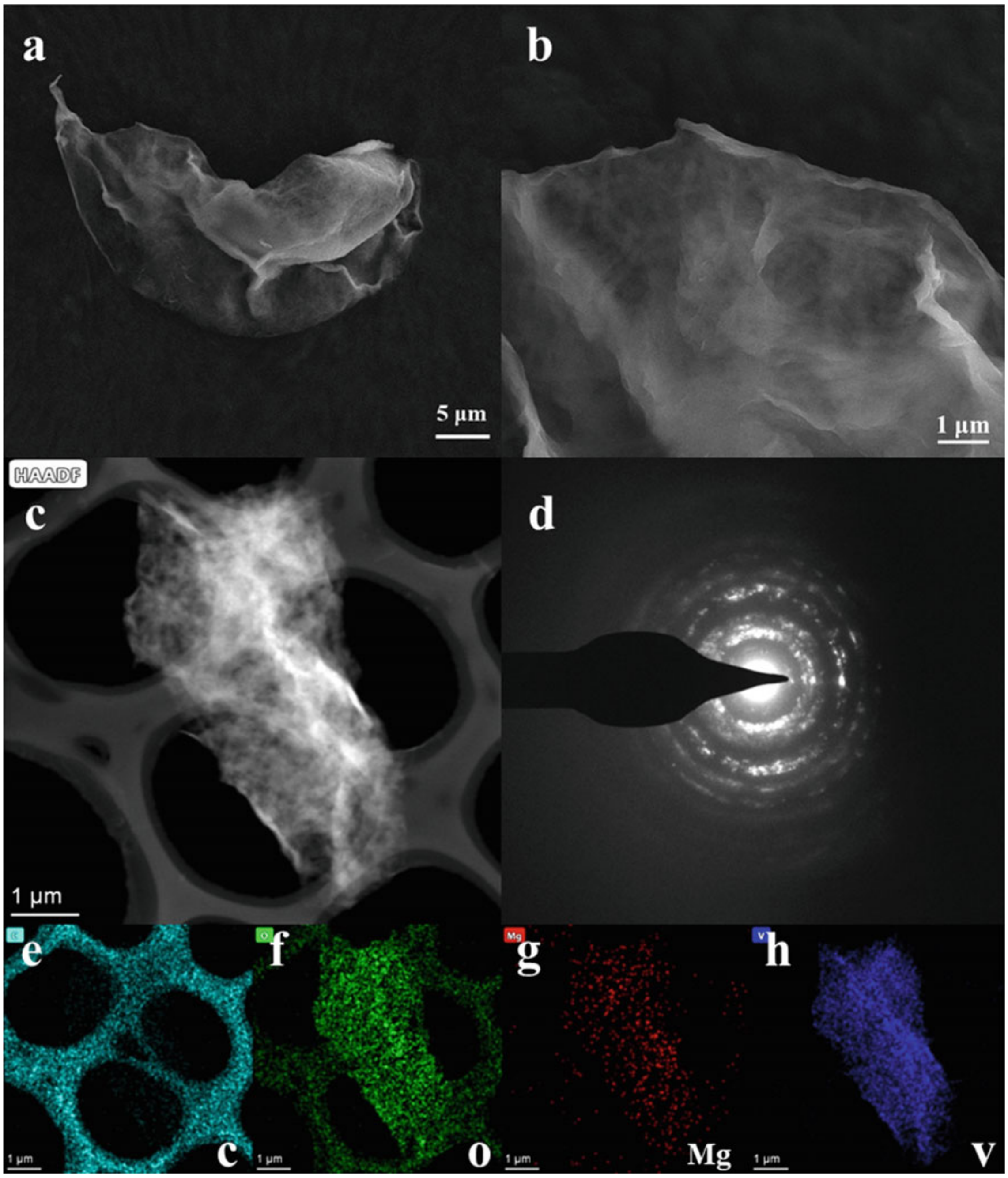

Fig. 2 Morphology characterization of $Mg_xV_2O_5$@GO. **a**, **b** SEM and corresponding elemental mapping of V, Mg, O, C. **c**, **d** HAADF image and SAED pattern. **e**–**h** Elemental mapping results of V, Mg, O, C

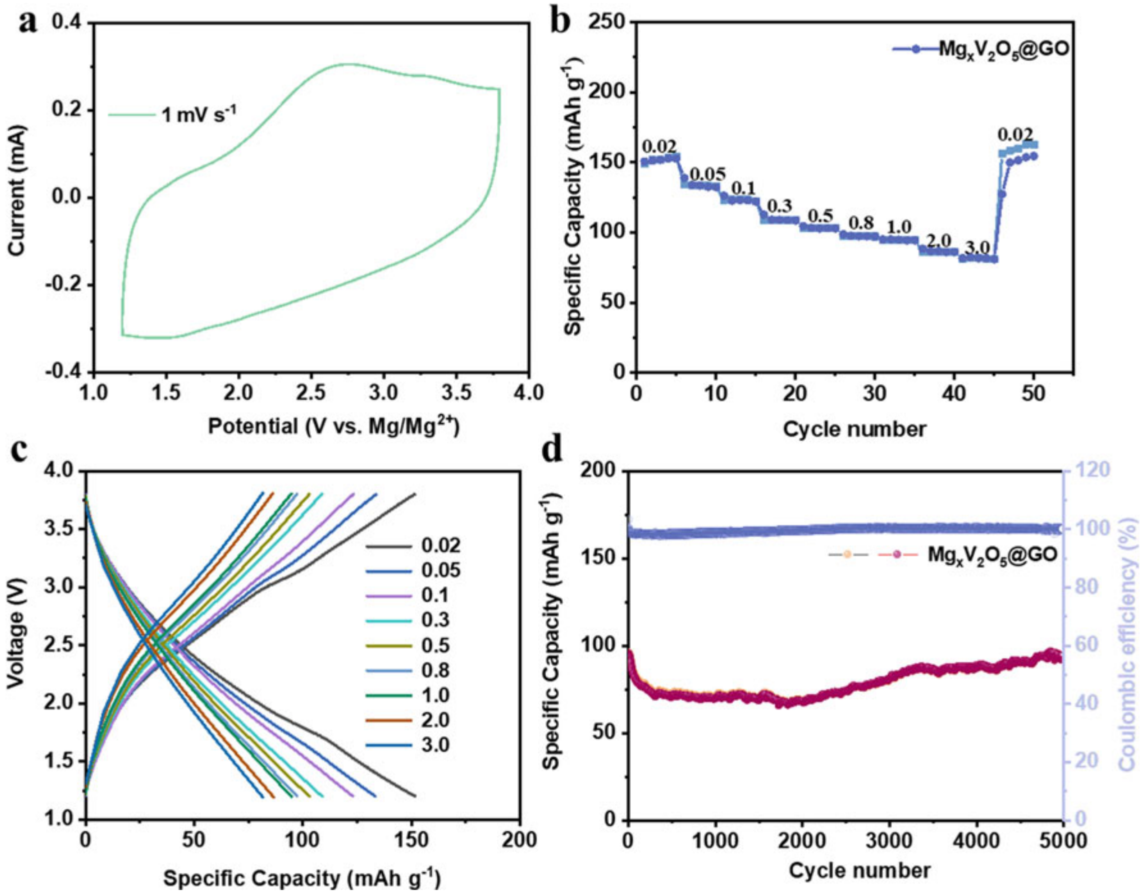

Fig. 3 Electrochemical performance of $Mg_xV_2O_5$@GO. **a** CV curves at 1 mV s^{-1}. **b**, **c** Rate performance and corresponding GCD curves with the current density range from 0.02 to 3.0 A g^{-1}. **d** Long cycling performance at 1 A g^{-1}

Acknowledgements This work was supported by the National Natural Science Foundation of China (52222407).

References

1. Bi J, Du Z, Sun J, Liu Y, Wang K, Du H, Ai W, Huang W (2023) On the road to the frontiers of lithium-ion batteries: A review and outlook of graphene anodes. Adv Mater 35(16):e2210734.
2. Chao Y F, Jalili R, Ge Y, Wang C Y, Zheng T, Shu K W, Wallace G G (2017) Self-assembly of flexible free-standing 3D porous MoS_2-reduced graphene oxide structure for high-performance lithium-ion batteries. Adv Funct Mater 27 (22):1700234.
3. Chen S, Fan S, Li H, Shi Y, Yang H Y (2022) Recent advances in kinetic optimizations of cathode materials for rechargeable magnesium batteries. Coord. Chem. Rev. 466:214597.
4. Chu Y, Shen Y, Guo F, Zhao X, Dong Q, Zhang Q, Li W, Chen H, Luo Z, Chen L (2019) Advanced characterizations of solid electrolyte interphases in lithium-ion batteries. Electrochem Energy Rev 3(1):187–219.
5. Duan J, Tang X, Dai H, Yang Y, Wu W, Wei X, Huang Y (2019) Building safe lithium-ion batteries for electric vehicles: A review. Electrochem Energy Rev 3(1):1–42.
6. Jia M, Zhao N, Huo H, Guo X (2020) Comprehensive investigation into garnet electrolytes toward application-oriented solid lithium batteries. Electrochem Energy Rev 3(4):656–689.
7. Joe Y S, Kang M S, Jang G, Lee S J, Nakhanivei P, Baek S H, Kim Y K, Jeong G, Kim H-s, Park H S (2023) Intercalation of bilayered V_2O_5 by electronically coupled pedot for greatly improved kinetic performance of magnesium ion battery cathodes. Chem. Eng. J. 460:141706.
8. Kotobuki M, Yan B, Lu L (2023) Recent progress on cathode materials for rechargeable magnesium batteries. Energy Storage Mater. 54:227–253.
9. Li Z, Häcker J, Fichtner M, Zhao-Karger Z (2023) Cathode materials and chemistries for magnesium batteries: Challenges and opportunities. Adv Energy Mater 13(27):2300682.
10. Liu Y, Wu X (2021) Hydrogen and sodium ions co-intercalated vanadium dioxide electrode materials with enhanced zinc ion storage capacity. Nano Energy. 86:106124.
11. Ma X-F, Li H-Y, Ren W, Gao D, Chen F, Diao J, Xie B, Huang G, Wang J, Pan F (2023) A critical review of vanadium-based electrode materials for rechargeable magnesium batteries. J Mater Sci Technol 153:56–74.
12. Ming F, Liang H, Lei Y, Kandambeth S, Eddaoudi M, Alshareef H N (2018) Layered $Mg_xV_2O_5 \cdot nH_2O$ as cathode material for high-performance aqueous zinc ion batteries. ACS Energy Lett 3 (10):2602–2609.

13. Mohtadi R, Tutusaus O, Arthur T S, Zhao-Karger Z, Fichtner M (2021) The metamorphosis of rechargeable magnesium batteries. Joule 5(3):581–617.
14. Pang Y, Pan J, Yang J, Zheng S, Wang C (2021) Electrolyte/electrode interfaces in all-solid-state lithium batteries: A review. Electrochem Energy Rev 4(2):169–193.
15. Sambandam B, Soundharrajan V, Kim S, Alfaruqi M H, Jo J, Kim S, Mathew V, Sun Y-k, Kim J (2018) $K_2V_6O_{16}\cdot 2.7H_2O$ nanorod cathode: An advanced intercalation system for high energy aqueous rechargeable Zn-ion batteries. J Mater Chem A 6 (32):15530–15539.
16. Sun X, Li Z, Liu Z, Lv X, Shi K, Chen R, Wu F, Li L (2023) A new candidate in polyanionic compounds for potassium ion battery anode: Mxene derived carbon coated π-$Ti_2O(PO_4)_2$. Adv Funct Mater 33(22):2300125.
17. Wang X, Ma L, Zhang P, Wang H, Li S, Ji S, Wen Z, Sun J (2020) Vanadium pentoxide nanosheets as cathodes for aqueous zinc-ion batteries with high rate capability and long durability. Appl. Surf. Sci. 502:144207.
18. Xiao J, Shi F, Glossmann T, Burnett C, Liu Z (2023) From laboratory innovations to materials manufacturing for lithium-based batteries. Nat Energy 8(4):329–339.
19. Xu Y, Deng X, Li Q, Zhang G, Xiong F, Tan S, Wei Q, Lu J, Li J, An Q, Mai L (2019) Vanadium oxide pillared by interlayer Mg^{2+} ions and water as ultralong-life cathodes for magnesium-ion batteries. Chem 5(5):1194–1209.
20. Yan M, He P, Chen Y, Wang S, Wei Q, Zhao K, Xu X, An Q, Shuang Y, Shao Y, Mueller K T, Mai L, Liu J, Yang J (2018) Water-lubricated intercalation in $v_2o_5\cdot nh_2o$ for high-capacity and high-rate aqueous rechargeable zinc batteries. Adv Mater 30 (1):1703725.
21. Zhang X, Xu X, Song B, Duan M, Meng J, Wang X, Xiao Z, Xu L, Mai L (2022) Towards a stable layered vanadium oxide cathode for high-capacity calcium batteries. Small 18(43): e2107174.
22. Zhou W, Chen J, Chen M, Xu X, Tian Q, Xu J, Wong C-P (2019) Rod-like anhydrous V_2O_5 assembled by tiny nanosheets as a high-performance cathode material for aqueous zinc-ion batteries. RSC Adv 9(52):30556–30564.

Part VII

Poster Session

Porosity and Mechanical Properties of Squeeze Cast and Permanent Mold Cast Wrought Mg Alloy AZ31

A. Dhaif, W. Shen, and H. Hu

Abstract

Wrought magnesium alloy AZ31 with a thick section of 20 mm was prepared by squeeze casting (SC) and permanent steel mold casting (PSMC). The yield strength (YS), ultimate yield strength (UTS), elongation (e_f), and strain-hardening rate of the cast AZ31 specimens were evaluated by tensile testing. The measured engineering stress versus strain curves showed that the SC AZ31 alloy exhibited 62 MPa in YS, 194 MPa in UTS, and 13.8% in e_f, while the YS, UTS, and e_f of the PSMC AZ31 specimen were only 58, 173 MPa, and 9.9%. The results of the tensile testing evidently showed that the YS, UTS, and e_f of the SC AZ31 alloy were 7, 12, and 39% higher than those of the PSMC counterpart. The calculated resilience and tensile toughness indicated that the SC AZ31 was more capable of resisting energy loads in elastic deformation and had an ability to absorb energy during plastic deformation without fracture than that of the PSMC AZ31. Also, the analyses of the true stress versus strain curves revealed that, upon the onset of plastic deformation, the strain-hardening rate of the SC AZ31 sample was 10,000 MPa, which was 25% higher than that (8000 MPa) of the PSMC AZ31 specimen. The obtained mechanical properties showcased the fit of the casting process to wrought magnesium AZ31 alloy, which was squeeze casting. The porosity measurements of the SC and PSMC showed that the SC AZ31 had a porosity of 1.13%, which was the 57% lower than that (2.66%) of the PSMC AZ31 counterpart. The low porosity level of the SC AZ31 alloy should be somewhat responsible for its high mechanical properties.

Keywords

Squeeze casting • Wrought magnesium alloy AZ31 • Permanent steel mold casting • Mechanical properties • Porosity

Introduction

As a replacement of gas or diesel-powered vehicles (GDVs), battery-powered electric vehicles (BEVs) are in high demand during this era due to greenhouse gas emissions causing environmental concerns [1–3], but BEVs are usually heavier than the GDVs in average. With the emergence of the BEV mass production, vehicle weight reduction becomes an urgent task for not only GDVs but also BEVs to achieve less energy for more mileage. Presently, the automotive industry is forced to develop advanced lightweight materials such as magnesium (Mg) alloys possessing a good combination of strengths and plasticity as well as their relevant manufacturing processes [4–6].

Mg is a two-third of aluminum's (Al) weight and one-fourth of steel's weight. Compared to other castable metallic alloys, Mg alloys hold the highest strength to weight ratio. Other advantages of magnesium-based alloys are good castability, high die casting rate, long tooling life, and excellent machinability that promote the optimization and utilization of the automotive industry. Mg has been used to make automotive components containing thin sections like instrument panels, steering wheel armatures, seats, and engine blocks which are mainly manufactured by conventional high pressure die casting processes (C-HPDC) [7]. The downside of the high pressure die casting of Mg parts is that the mechanical properties of cast components with thick sections are affected heavily by casting defects such as the

---

A. Dhaif · W. Shen · H. Hu (✉)
Department of Mechanical, Automotive and Materials Engineering, University of Windsor, Windsor, ON N9B3P4, Canada
e-mail: huh@uwindsor.ca

A. Dhaif
e-mail: dhaifa@uwindsor.ca

W. Shen
e-mail: shen12a@uwindsor.ca

A. Leonard et al. (eds.), *Magnesium Technology 2024*, The Minerals, Metals & Materials Series,
https://doi.org/10.1007/978-3-031-50240-8_43

entrapped gas porosity, shrinkage porosity, oxides, hot tearing, and cold shuts, which reduce the strength and ductility of the metal. These defects are greatly caused by the casting process [8–11]. To expand Mg applications into structural and safety–critical parts of gasoline or diesel-powered vehicles (GDVs) or battery-powered electric vehicles (BEVs), such as knuckles, control arms, subframe, unibody, door frame, and seat belt brackets, which experience a high cyclic mechanical loading during service, the development of cost-effective manufacturing processes along with high strength and ductile Mg alloys is essential to produce lightweight high-integrity structural automotive components.

AZ31 as a wrought Mg alloy can offer an excellent combination of strengths, elongation, and plasticity, but wrought Mg alloys are typically not castable. The major problem associated with casting these wrought alloys is their high tendency to form casting defects such as porosity, shrinkage, and hot tearing resulting from their inherent solidification characteristics, i.e., high liquidus temperatures, poor fluidities, hot tearing, and long freezing ranges [12–14]. Studies on casting of Mg alloy AZ31 with section thickness around 5 mm were attempted and focused on numerical simulation and solidification behavior of rapid cooling. The report on mechanical properties of cast AZ31 alloy with thick section (over 10 mm) is very limited, since the casting defects could easily form in the thick section of cast components [14–16]. The success in squeeze casting of wrought Al alloys 5083 and 7075 with varying section thicknesses and applied pressures has been demonstrated [17, 18]. This was because the fluidity and hot tearing were not critical process parameters in squeeze casting, and molten wrought Al alloys were solidified in the die cavity under high applied pressures to minimize defects associated with shrinkage cavities and porosity formation. However, work on SC of conventional wrought Mg alloys to produce high-integrity structural automotive applications with both high strength and excellent plasticity is scarce.

In this work, Mg alloy AZ31 was squeeze cast under a high applied pressure of 90 MPa to produce a casting with a thickness of 20 mm. The mechanical properties of the SC AZ31 alloy were evaluation by tensile testing. The porosity level of the SC alloy was determined by density measurements. For the purpose of comparison, the same alloy was also cast by permanent steel mold casting (PSMC) for evaluation.

Experimental Procedure

Casting and Material

The selected material was commercially available magnesium wrought alloy AZ31 with the chemical composition in weight percent (wt%) of 3.0% Al, 0.73% Zn, 0.25% Mn, 0.02% Sn, 0.005% Fe, 0.0014 Ca, and a balance of Mg. During melt preparation, 500 g of AZ31 was placed in a steel crucible inside an electric resistance furnace under the protection of a gas mixture of sulfur hexafluoride (SF_6) 0.5% with a balance of CO_2 with a flow rate of 3 standard liters per minute. AZ31 was molten to 720 °C and held for 20 min, stirred for 10 min to homogenize its composition, and the melt surface was skimmed before pouring. To prevent oxidation and burning, the AZ31 melt was covered by the protective gas during the transfer from the furnace to the die. The die cavity was also purged with the protective gas before pouring.

For squeeze casting (SC), the apparatus used was made from an upper and a lower die that are both preheated. The lower die is movable and has a piston to move molten into the upper die while the upper die is stationary. The liquid AZ31 alloy at 700 °C was poured into the preheated lower die preheated to 300 °C. After the dies were closed by lifting the lower die onto the upper die with a preheated temperature of 200 °C, the punch piston in the lower die pushed the melt in the upper die at 0.1 m/s. The pressure that was exerted by the punch piston on the molten metal was increased steadily to a predetermined level of 90 MPa and maintained until the entire casting was solidified. The dimensions of SC coupon were 20 mm in thickness and 100 mm in diameter.

In permanent steel mold casting (PSMC), the process is much simpler. The molten with the same weight from the same heating source was poured into a steel mold to produce a rectangular casting plate with the dimensions of 150 mm × 125 mm × 20 mm. The steel mold was preheated to 200 °C as well. The PSMC process used gravity to cast AZ31 and protective gas was also used.

Porosity Measurement

Porosity levels in the alloy was calculated using dry weight (W_d), wet weight (W_w), theoretical (Dt), and actual density (D_a). During porosity measurements, SC and PSMC specimens section from cast coupons sample were sanded and washed to prevent water entrapment on specimen surface. The cleaned specimens were weighted in the air and water to determine W_d and W_w. D_a of each specimen was calculated using Archimedes principle based on ASTM Standard D3800 [19].

$$D_a = \frac{D_w w_a}{W_a - W_w} \tag{1}$$

The porosity of each specimen was calculated from D_t and D_a by Eq. 2. Porosity of each specimen was calculated by the theoretical and actual density values using ASTM C948 [20].

$$\%\text{Porosity} = \left[\frac{D_t - D_a}{D_t}\right] \times 100\% \quad (2)$$

where D_t, the theoretical density of the AZ31 is 1.78 g/cm^3 [13]. The process was done with various specimens to obtain an average porosity for both the SC and PSMC alloys.

Tensile Testing

The mechanical properties of the SC and PSMC AZ31 alloys were evaluated by tensile testing. Samples of tensile specimens were taken out from the SC and PSMC coupons. The tensile specimens were machined with 0.025 m in gage length, 0.006 m in width, 0.004 m thickness, and 0.010 m in total length according to ASTM B557 subsize flat tensile specimens [21]. The prepared specimens were tensile tested at room temperature on a MTSTM Criterion (Model 43) Tensile Test Machine (Eden Praire, MN, USA) and equipped with data acquisition system. The tensile machine was set to strain rate of 0.5 mm/min with a sampling rate of 10 Hz. The tensile properties of ultimate tensile strength (UTS), 0.2% yield strength (YS), elongation to failure (e_f), and elastic modulus (E) were collected based on an average of five tests with a standard deviation of 5%.

Results and Discussion

Porosity

Figure 1 shows the porosity levels of the SC and PSMC AZ31 alloys. As can be seen from Fig. 1, the SC sample exhibited a porosity level of 1.13%, while the porosity in the PSMC was 2.66%. Compared to the data listed in [8], the porosity levels in both the SC and PSMC samples were much lower than that (3.57%) in the C-HPDC Mg alloy AZ91. The reason for the difference in the porosity level between the SC, PSMC, and C-HPDC was that the laminar melt flow was dominated in the SC and PSMC. In contrast, the turbulent flow prevailed in the C-HPDC process, which entrapped a large amount of air during cavity filling and resulted in the high porosity level. The air entrapment was reduced by the laminar flow in the SC and PSMC castings. The application of a high pressure (90 MPa) in the SC process squeezed last liquid metal into the porous and shrinkage regions of the solidifying AZ31 casting at the end of solidification, which further reduced the porosity level of the SC sample. Consequently, the SC alloy had the decreases of 135 and 216% in porosity compared to those of the PSMC and C-HPDC Mg alloys, respectively. The significant reduction in the porosity level should affect the mechanical properties of the cast Mg alloys. Moreover, the low porosity level implied that the SC AZ31 could be heat treated to further improve its mechanical properties.

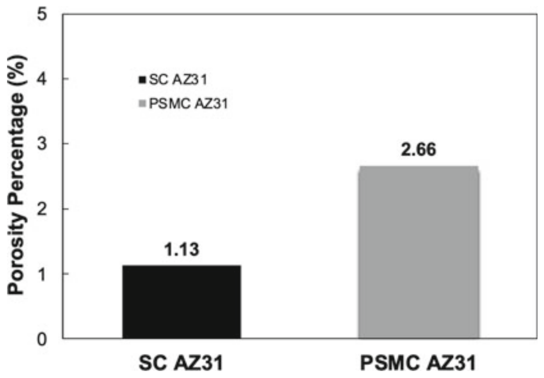

Fig. 1 Porosity levels (%) of the SC (1.13%) and PSMC (2.66%) AZ31 alloys with a section thickness of 20 mm, determined by Archimedes principle

Mechanical Properties

The engineering stress–strain curves of the as-cast PSMC and SC AZ31 alloys are compared in Fig. 2. Figure 2 clearly shows that SC has a higher UTS, a steeper slope of the linear portion of engineering curve, and a larger range of elastic and plastic deformation. Table 1 lists the mechanical properties of the PSMC and SC AZ31 alloys including the ultimate tensile strength (UTS), 0.2% yield strength (YS), elongation to failure (e_f), and elastic modulus (E), which were extracted from Fig. 2. The UTSs of the PSMC AZ31 alloy and SC AZ31 were 173 MPa and 194 MPa,

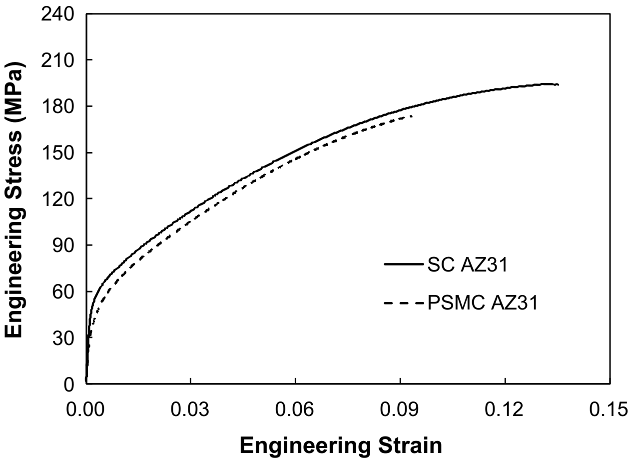

Fig. 2 Typical engineering stress versus strain curves of the SC and PSMC AZ31alloys

Table 1 Tensile properties of PSMC and SC AZ31 in room temperature

Method of casting	UTS (MPa)	YS (MPa)	e_f (%)	Modulus (GPa)
PSMC	173	58	9.9	38.9
SC	194	62	13.8	42.2

respectively, which signified an improvement of 12% from the PSMC to the SC AZ31. Moreover, the yield strength of the PSMC AZ31 was 58 MPa, which was 7% lower than that of the SC AZ31 with a YS of 62 MPa. The elongation of the PSMC alloy was only 9.9%, while the elongation of SC AZ31 was 13.8%, which showed an increase of 39%. The modulus of the SC AZ31 alloy was 42.2 GPa, which was 8% higher than that (38.9 GPa) of the PSMC AZ31.

Resilience

Resilience or the ability of material to absorb energy while it deforms elastically and then release it upon unloading. The resilience is usually measured by the modulus of resilience (U_r). U_r is the maximum strain energy absorbed per unit volume without producing permanent deformation. One way to calculate it is by integrating the stress–strain curve from zero to elastic limit. U_r can also be determined by Eq. 3 for uniaxial tension [8, 10].

$$U_r = \frac{(\mathrm{YS})^2}{2E} \tag{3}$$

where E and YS are the Young's modulus and yield strength, respectively. The modulus of resilience for the PSMC and SC AZ31 alloys are given in Table 1. The modulus of resilience for the PSMC AZ31 was 43.2 kJ/m^3 as the SC sample had an U_r of 45.6 kJ/m^3. The U_r results indicated that the SC AZ31 was more capable of resisting energy loads in engineering application where no permanent distortions were permitted.

Toughness

Toughness (U_t) is the ability of material to absorb energy during plastic deformation without fracture. This happens through static loading with a low strain rate. The material capacity to tolerate applied stresses higher than the yield strength without fracturing is customarily required for various engineering applications. U_t can be considered as the total area under the stress–strain curve, which is the total energy per unit volume before fracture. The area under the stress–strain curve can be approximated by Eq. 4 [8, 10].

$$U_t = U_{\mathrm{el}} + U_{\mathrm{pl}} = \frac{(\mathrm{YS} + \mathrm{UTS}) \times e_{\mathrm{f}}}{2} \tag{4}$$

where U_{pl} is the energy per unit volume of elastic deformation, U_{el} is the energy per unit volume for plastic deformation, YS is the yield strength, UTS is the ultimate tensile strength, and e_{f} is the elongation at fracture. Table 2 lists the calculated U_t for the PSMC and SC AZ31. The PSMC had a U_t value of 11.4 MJ/m^3 and SC had a U_t 17.7 MJ/m^3. The results signified that the SC AZ31 was tougher than the PSMC AZ31, because SC AZ31 alloy had a greater ultimate tensile strength, yield strength, and elongation.

Strain Hardening

The true stress and strain were calculated from the engineering stress and strain with Eqs. 5 and 6 to understand the strain-hardening effect.

$$\sigma_t = \sigma(1 + \varepsilon) \tag{5}$$

$$\varepsilon_t = \ln(1 + \varepsilon) \tag{6}$$

where σ is the engineering stress, ε is the engineering strain, σ_t is the true stress, and ε_t is the true strain. Figure 3 shows the true stress versus strain curves for the SC and PSMC AZ31 alloys.

The true stress and strain for plastic deformation can be related by the power law equation shown in Eq. 7.

$$\sigma_t = K\varepsilon_t^n \tag{7}$$

where K is the strength coefficient and n is the strain-hardening exponent [8, 10]. The regression analysis revealed that the power expression matched the tensile data. The numerical values of the derived constants in Eq. 7 with the regression coefficient R^2 are listed in Table 3. A higher strain-hardening exponent for the SC AZ31 alloy implied that the SC specimens would gain strength more quickly than the PSMC AZ31 during plastic deformation.

The strain-hardening rate is the first differential of Eq. 7 ($\mathrm{d}\sigma_t/\mathrm{d}\varepsilon_t$). The differential is found to be Eq. 8.

Table 2 Tensile toughness and resilience of PSMC and SC AZ31 at room temperature

Method of casting	Toughness (MJ/m^3)	Resilience (kJ/m^3)
PSMC	11.4	43.2
SC	17.7	45.6

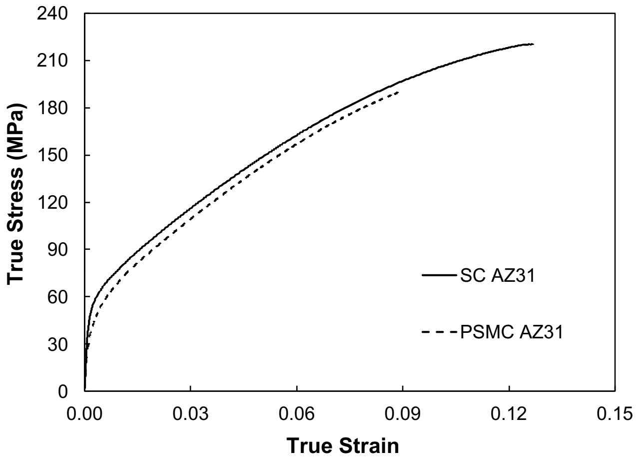

Fig. 3 Typical true stress versus strain curves for the SC and PSMC AZ31 alloys

Table 3 Best-fit parameters for power equations

Method of casting	K (MPa)	n	R^2
PSMC AZ31	508	0.41	0.99
SC AZ31	556	0.39	0.97

$$d\sigma_t/d\varepsilon_t = Kn\varepsilon_t^{n-1} \tag{8}$$

Figure 4 illustrates the curves of strain-hardening rate with respect to true plastic strain during the plastic deformation for the SC and PSMC AZ31 alloys, which were derived from the true stress to true strain curves shown in Fig. 3. Upon the onset of plastic deformation in Fig. 4 at a strain of 0.002, the strain-hardening rate of the SC sample was 10,000 MPa while the PSMC specimen revealed a strain-hardening rate of 8000 MPa. In the early stages of plastic deformation, the strain-hardening rate of the SC alloy was 25% higher than that of the PSMC specimen. As the strain increased, the strain-hardening rates of both the SC and PSMC AZ31 samples decreased. However, the SC alloy had a higher strain-hardening rate than that of the PSMC counterpart. The variation of strain-hardening rate with respect to true strain suggested that SC AZ31 could strengthen itself quicker in response to extended plastic deformation prior to fracture compared to the PSMC specimen.

The low porosity level of the SC AZ31 given in the preceding section as one of the key factors resulted in its mechanical properties higher than those of the PSMC AZ31. The preliminary microstructure analyses by optical and scanning microscopies revealed that, compared to that of the PSMC sample, the microstructure of the SC AZ 31 possessed a fine primary dendritic structure, and a large volume fraction of intermetallic phases. The difference in microstructure features between the SC and PSMC AZ alloys should be responsible for the resultant mechanical and electrical properties, as also indicated in [8–10]. The detailed results of microstructure analyses will be reported in future publication.

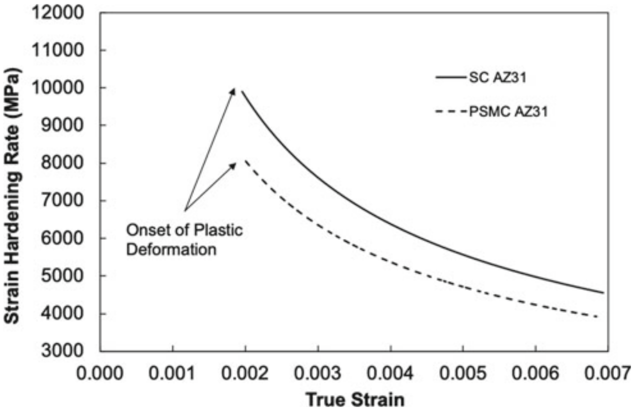

Fig. 4 Strain-hardening rates versus true strain curves for plastic deformation of the SC and PSMC AZ31 alloys

Summary

The SC and PSMC processes were employed to cast a wrought magnesium alloy AZ31. Due to the high applied pressure and laminar injection of molten alloy, the porosity level (1.13%) of the SC AZ31 alloy was only about half of that (2.66%) of the PSMC counterpart. The SC AZ31 alloy showed the enhanced YS (62 MPa), UTS (194 MPa), e_f (13.8%), E (42.2 GPa), U_t (17.7 MJ/m^3), and U_r (45.6 kJ/m^3), compared to the PSMC counterpart. The deformation analyses indicated that the straining hardening rate of the SC AZ31 was 25% higher than that of the PSMC AZ31. The porosity level should be partially responsible for the obtained mechanical properties. The SC AZ31 was more capable of resisting energy loads in elastic deformation and had an ability to absorb energy during plastic deformation without fracture than that of the PSMC AZ31.

Acknowledgements The authors thank the Natural Sciences and Engineering Research Council of Canada and the University of Windsor for supporting this work.

References

1. Li Y, Hu A, Fu Y, Liu S, Shen W, Hu H, and Nie X (2022) Al alloys and casting processes for induction motor applications in battery-powered electric vehicles: A review. Metals. 12:216–241.
2. Shen W, Hu A, Liu S, Hu H, (2023) Al-Mn alloys for electrical applications: a review. Journal of Alloys and Metallurgical Systems. 2:100008.

3. Liu S, Hu A, Hu H, Nie X, Kar NC (2022) Potential Al-Fe cast alloys for motor applications in electric vehicles: An overview. Key Eng. Mater. 923:3–19.
4. Wang GG, Weiler JP (2023) Recent developments in high-pressure die-cast magnesium alloys for automotive and future applications. J Magnes Alloy. 11(1):78–87.
5. Weiler JP (2021) Exploring the concept of castability in magnesium die-casting alloys. J. Magnes. Alloy. 9(1):102–111.
6. Weiler JP (2019) A review of Mg die-castings for closure applications. J. Magnes. Alloy. 7:297–304.
7. Luo AA (2013) Mg casting technology for structural applications. J Magnes Alloy. 1: 2–22.
8. Fu Y, Li Y, Hu A, Hu H, Nie X (2020) Microstructure, Tensile properties and fracture behavior of squeeze-cast Mg alloy AZ91 with thick cross section. J. Materi. Eng. Perform. 29:4130–4141.
9. Sun Z, Ren L, Geng X, Fang L, Wei X, Hu H (2019) Influence of wall stocks on mechanical properties of HPDC AZ91. Key Eng. Mater. 793:41–45.
10. Sun Z, Geng X, Ren L, Hu H (2020) Microstructure, tensile properties and fracture behavior of HPDC magnesium alloy AZ91. International Journal of Materials, Mechanics and Manufacturing. 8(2):50–56.
11. Song J, Pan F, Jiang B, Atrens A, Zhang M, Lu Y (2016) A review on hot tearing of Mg alloys. J Magnes Alloy. 4:151–172.
12. Lü Y, Wang Q, Ding W, Zeng X (2000) Fluidity of Mg–Al alloys and the effect of alloying elements. Zeitschrift für Metallkunde. 91 (6):477–482.
13. Avedesian, MM and Baker, H (ed) (1999) Magnesium and Magnesium Alloys. ASM International, Metals Park, OH.
14. Neh K, Ullmann M, Oswald M, Berge F, Kawalla R (2015) Twin roll casting and strip rolling of several Mg alloys. Mater. Today: Proc. 2:45–52.
15. Hadadzadeh A, Wells MA (2013) Mathematical modeling of thermo-mechanical behavior of strip during twin roll casting of an AZ31 Mg alloy. J Magnes Alloy. 1(2):101–111.
16. He Y, Javaid A, Essadiqi E, Shehata M (2009) Numerical simulation and experimental study of the solidification of a wedge-shaped AZ31 Mg alloy casting. Can. Metall. Q. 48(2):145–155.
17. Zhang X, Fang L, Hu H, Nie X, Tjong J (2017) Interfacial heat transfer of squeeze casting of wrought Al alloy 5083 with variation in wall thicknesses. Adv. Mater. Process. Technol. 3(3):407–417.
18. Zhang X, Fang L, Hu H, Nie X, Tjong J (2017) Determination of metal/die interfacial heat transfer coefficients in squeeze casting of wrought Al alloy 7075 with variations in section thicknesses and applied pressures. J. Heat Transfer. 139:022101-1-9.
19. Standard test method for density of high-modulus fibers, D3800-99. (2002) ASTM Standards. ASTM. 15.03:186–187.
20. Standard test method for dry and wet bulk density, water absorption, and apparent porosity of thin sections of glass-fiber reinforced concrete, C948-81. (2002) ASTM Standards, ASTM. 04.05:588–589.
21. Standard test methods for tension testing wrought and cast aluminum-and magnesium-alloy products, B557M. (2002) ASTM Standards, ASTM. 02 02:424–439.

Author Index

A. Leonard et al. (eds.), *Magnesium Technology 2024*, The Minerals, Metals & Materials Series,
https://doi.org/10.1007/978-3-031-50240-8

Subject Index

A. Leonard et al. (eds.), *Magnesium Technology 2024*, The Minerals, Metals & Materials Series,
https://doi.org/10.1007/978-3-031-50240-8